Charting Molecular Dynamics with Ultrafast X-ray Techniques

Philipp Lenzen

PhD Thesis

DTU

NEXMAP section
Technical University of Denmark
December 2022

DTU Physics
Department of Physics

Academic Advisors
Martin Meedom Nielsen
Klaus Braagaard Møller
Kristoffer Haldrup

Charting Molecular Dynamics with Ultrafast X-ray Techniques

Philipp Lenzen

Abstract

This dissertation investigates and discusses the structural and photophysical properties of the bi-metallic d^8d^8 transition metal complexes IrDimen and PtPOP, and their tri-metallic derivatives AgPtPOP, TlPtPOP and AgIrDimen using Time-Resolved X-ray Solution Scattering (TR-XSS).

This work has two main focuses. Firstly, the analysis and comparison of a broad range of experiments investigating the molecular structures and photophysical properties of the bi-metallic complexes. These experiments were conducted at the European Synchrotron Radiation Facility (ESRF), with a X-ray pulse length of $\sim$100 picoseconds, and the Linac coherent light source (LCLS) free electron laser, with an X-ray pulse length of $\sim$30 femtoseconds. The high energy X-ray pulses accessible at the synchrotron are utilized for ultra-fine structural refinement of IrDimen alongside an investigation of the structural implications of the intersystem crossing in this system. The femtosecond resolution of the Free Electron Laser (FEL) is used to investigate excitation wavelength dependent structural dynamics of PtPOP and IrDimen as well as structural parameter distribution in an ensemble of excited state molecules following photoexcitation. Secondly, this work investigates the formation as well as the molecular and electronic structures of tri-metallic complexes, alongside their structural dynamics and dissociation reactions on the femtosecond timescale.

Dansk Resumé

Denne afhandling undersøger og diskuterer de strukturelle og fotofysiske egenskaber af de bi-metalliske d8-d8overgangsmetalkomplekser IrDimen og PtPOP, og deres tri-metalliske derivater AgPtPOP, TlPtPOP og AgIrDimen ved brug af tidsopløst røntgen solventspredning (TR-XSS).

Dette arbejde har fokus på to hovedområder. Først og fremmest analysen og sammenligningen af en række eksperimenter, der undersøger de molekylære strukturer og fotofysiske egenskaber af de bi-metalliske metalkomplekser. Disse målinger er foretaget ved European Synchrotron Radiation Facility (ESRF), med en røntgenpulslængde 100 picosekunder, og ved en X-ray Free Electron Laser (XFEL) med røntgenpulslængde 30 fs. Den høje tilgængelige røntgenpulsenergi ved synkrotron-anlægget bruges til en ultrafin strukturforfinelse af IrDimen sammen med en undersøgelse af de strukturelle konsekvenser af intersystemkrydsning. Femtosekundopløsningen opnået ved XFEL-anlægget bruges til at undersøge afhængigheden af eksitations bølgelængdernes strukturrelle dynamik af PtPOP og IrDimen såvel som fordelingen af strukturelle parameter i et ensemble af eksiteret molekyletilstande som et resultat af en fotoeksitation. For det andet, undersøger dette arbejde dannelsen af molekylære og elektroniske strukturer af tri-metalliske komplekser, sammen med deres struktureldynamik og dissociationsreaktioner, der finder sted på femtosekundtidsskala.

Acknowledgements

First of all, I would like to thank my supervisors, Martin, Klaus and Kristoffer for their support of my PhD, for your knowledge, advice and motivation to meet the challenges of this field. Thank you for giving me the opportunity to travel the world for beamtimes and conferences, and also being prepared enough that a global pandemic and the shut down of all measurement facilities did not derail the project.

I would also like to thank the people I met during my external stay at ESRF in Grenoble, Michael, Matteo and Alix. I want to especially thank Michael for the many great discussions we had during that time and for our trip to film the stars.

I want to thank my colleagues in the ultrafast group for making the last years so enjoyable. Bianca, thank you for making me aware of the importance of walking 10000 steps a day, and walking so many of them together regardless of the UV levels outside. Verena, for all our trips to explore the world, both on beamtimes and in Denmark. Asmus for your help with all my programming questions and your culinary guidance through the world in general and Copenhagen in particular. Amke for sharing the fate of completing a PhD and philosophizing about what might come afterwards. The wild west awaits us. Diana, for introducing me to the danish system and for the company in times where the group was considerably smaller. Morten, for joining and supporting the PhD faction in times of great need and for showing me how far just a bit of mentoring can bring someone in life. Kerstin, for helping me carry the torch of the ultrafast group when no one else would, and Jaysree for our many great chats during the time. Mads L, for helping me to start with the programming in the world of X-ray solution scattering.

I would also like to thank all my other colleagues from the NEXMAP section and beyond. Mads for the enjoyable months we lived together in Grenoble and the many great times we had over the years. Wenjie and Mathias, for our endeavors and our shared enjoyment of Corona times in Denmark. Theodor, Anton, Anna Kristina, Thomas, Mathias and Matyas for the support and the many great moments we shared.

Finally, I would like to thank my friends who supported me through this time. Tim, for the uncountable hours we spend building together over the years. Daniel, for your perseverance on the Rift with me, no matter the cost. Sören, for your campaign to save the industry from me. Oliver, for sharing the good and the bad times that arise from doing a PhD, whether in Germany or Denmark. Thank you for our time over the years and your support for my cause on Catan! Last but not least, I want to thank my sister Julia for the competition with her and her own ambitions for a doctoral degree, and for motivating me to do my own globetrotting.

Publications

This thesis contains of the following research manuscript:

PAPER I: Ultrafast photoexcitation dynamics in tri-nuclear metal-metal bonded M-PtPOP (M = Ag, Tl) transition-metal complexes

Abbreviations

Here follows a list and short explanation of the different abbreviations used in this thesis.

TR-XSS	**T**ime **R**esolved **X**-ray **S**olution **S**cattering, structural measurement technique used at large scale facilities
ESRF	The **E**uropean **S**ynchrotron **R**adiation **F**acility, synchrotron in Grenoble, France
EBS	**E**xtremly **B**right **S**ource, name of the recently upgraded accelerator of the ESRF
ID09	Time-resolved beamline at the ESRF
LCLS	**L**inac **C**oherent **L**ight **S**ource, free electron laser in Menlo Park, California, USA
Å	**Å**ngstrom, unit of length, 10^{-10} m
ps	**P**icossecond, unit of time, 10^{-12} s
fs	**F**emtosecond, unit of time, 10^{-15} s
fwhm	**F**ull **W**idth **H**alf **M**aximum
ACN	**A**cetonitrile
DMSO	**D**i-**m**ethyl**s**ulf**o**xide
DMA	**DD**i**m**ethyl**a**cetamide
PtPOP	$[Pt_2(H_2P_2O_5)_4]^{4-}$, tetrakis (diphosphito) diplatinate(II) anion
IrDimen	$Ir_2(1,8$-diisocyano-p-menthane$)_4$
ISC	**I**ntersystem **C**rossing
IC	**I**nternal **C**onversion
S$_1$	lowest excited **S**inglet state
T$_1$	lowest excited**T**riplet state

Contents

Chapter 1

Introduction

Investigating chemical reactions on timescales of atomic movements has long been an objective in fundamental science, but for most of modern science measurement techniques were limited to much longer timescales. Lasers for the study of molecular dynamics have first been available in the optical range since the introduction of femtochemistry in the late 1980s by Ahmed Zewail [1]. For this work he was awarded the Nobel prize in 1999 [2]. Ultrafast laser-systems, delivering sub-picosecond pulses, have enabled the study of changes in energetic levels of molecules on the femtosecond scale through changes in their absorption and emission. The derivation of structural dynamics from these finding however requires a model of the coupling between electronic energy levels and structure, which is not a given for every molecule.

To gain the complementary structural information, methods to investigate the structure using X-rays have been developed. X-rays have been used to obtain structural information about matter since their discovery by Wilhelm Röntgen in 1895 [3]. But only in recent decades the construction of 3rd generation synchrotrons has enabled the usage of individual X-ray pulses with pulse lengths on the picosecond timescale, allowing the picosecond-resolved measurement of structural information. This temporal resolution has enabled the investigation of photoexcited samples and hydrodynamic processes, but is not sufficient to study the atom movement during structural rearrangements during chemical reactions.

The recent availability of X-ray free electron lasers (XFEL) has once again changed the field completely. The newly available X-ray pulse lengths ≥ 30 fs and unprecedented X-ray brilliance have opened up a whole new range of possibilities, opening the path to studying femtosecond structural dynamics with relatively short integration times.

The investigation on picosecond and sub-picosecond structural dynamics is of fundamental interest, as critical steps of all chemical reactions take place in that regime. To open up the field models and techniques have to be established with model systems to level the path for future experiments.

As a contribution to this endeavor, the work presented in this thesis has been focused on investigating the ultrafast structural dynamics in transition metal complexes with time-resolved X-ray solution scattering at free electron lasers and synchrotrons. This thesis summarizes the research

I have done at the Technical University of Denmark, and at the ID09 Beamline at the ESRF, during a 3 month external stay as part of this PhD.

Chapter 2

Photophysics

Visible light photons possess sufficient energy for inducing electronic excitations when absorbed by matter. These electronic transitions are entry points for investigating both the electronic as well as the molecular structure of materials. A comprehensive work on this phenomenon has been written by Lakowicz [4](chapter 1). In this chaptr, its key concepts are summarized, together with the development of techniques over the recent decades to study the electronic states and their implication on the properties in matter. The different electronic states and transitions between them are commonly depicted in a Jablonski diagram, as the one depicted in Fig. 2.1 A). The photon absorption process, in which a system is promoted from the ground state S_0 to a higher lying state occurs on the attosecond timescale 10^{-18}s. The promotion generally occurs into the higher lying singlet state S_1. The excitation also often occurs into a vibrationally excited level of a given electronic level, the energy of which is dissipated into the vicinity through vibrational relaxation (VR) on the femtosecond timescale into the lowest vibrational state of said electronic level.

The electronic state can change between states of different spin multiplicity by the flip of the spin of an electron. This spin-forbidden transition is called *intersystem crossing* (ISC). Depending on the number of unpaired electron spins in the system, the state is classified for instance as *Singlet* (S_N) or *Triplet* (T_N). The triplet states are energetically lower than their singlet excited state counterpart. Spin states of higher multiplicities, such as quintet states, have been observed other systems, but do not occur in the systems studied in this work.

The lowest energetic state of a given multiplicity can relax into the ground state through both optical and non-optical transitions. The non-optical transitions take place through internal conversion for the singlet and intersystem crossing for states of higher multiplicity. The optical transitions of the lowest singlet S_1 is known as *fluorescence*, while spin-forbidden transitions are referred to as *phosphorescence*, followed by vibrational relaxation. This barrier induced by the spin change commonly results in lifetimes orders of magnitude larger than those of singlet states.

Under sufficiently high photon densities a single molecule can absorb several photons in a process called multiphoton absorption. This process

can occur both simultaneously, where the energy of two photons is absorbed at the same time to promote an electron to a high electronic level, or sequentially, where a molecule that was previously promoted to S_1 absorbs an additional photon. When using femtosecond laser pulses with μJ intensities the electric fields created can facilitate this process and promote electrons into higher lying states S_2 to S_N [4].

This model to describe photophysical processes has been extended upon considerably since femtosecond techniques revolutionized the insight into photophysical processes. The changes in electronic structure change the potential energy surface of the complex, leading to structural deformation dynamics dissipating the excess energy. This relationship is often illustrated with a Frank-Condon diagram, shown in Fig 2.1 B), linking the energetic states to reaction coordinates. The reaction coordinate represents a primary structural parameter of the system, which is used to describe structural changes in an ensemble of molecules. With femtosecond resolution, the dissipation of energy of a molecule excited into a higher vibrational state can be tracked. The width and position of the distribution of an excited state ensemble along a given parameter r immediately after the photoexcitation depends on the interplay between the ground state distribution, the spectral profile of the laser pulse and the parameter dependent gap in the potential energy $\Delta V(r)$ between two electronic states. The shape of the distribution can be approximated with a Gaussian distribution. For pulses longer than 40 fs, as will be used in this work, the energy distribution can be sufficiently narrow that the maximum of the distribution is located at r^*, where $\Delta V(r)=\hbar\omega$ of the exciting photon [5], and as such defined by the excitation wavelength. The propagation of this distribution in the excited state ensemble depends on the excited state potential surface, on which it converges into the excited state minimum. In the case of a sufficiently harmonic potential and narrow population distribution, this results in an oscillation along the structural parameter that dephases over time. S_1 and T_1 are depicted as having their energetic minima at a similar value of the reaction coordinate, which is the case for the systems discussed in this work but not a given for all systems. Systems can have more than one reaction coordinate necessary for description, as will be discussed in chap. 7, resulting in a multidimensional description of the potential energy surface.
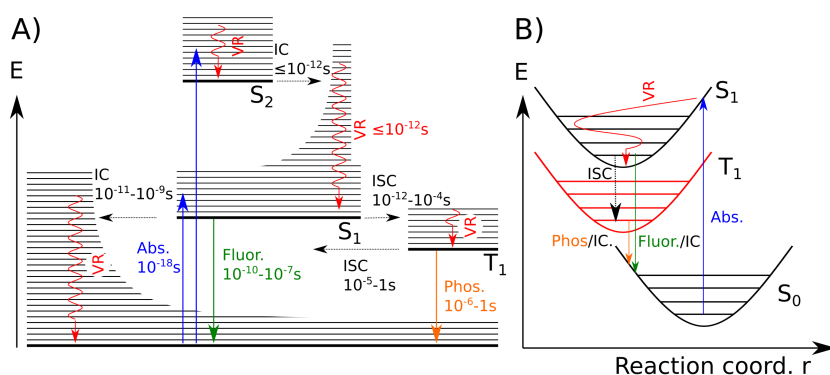
Figure 2.1: Jablonski diagram depicting a scheme of electronic states and the transitions between them. A) Adapted from [4, 6]. A system can be electronically excited by a visible photon into an excited state Singlet state S_n. Excessive energy stored in vibrational modes is dissipated through vibrational relaxation into the vicinity. Excited states can relax optically through fluorescence (green arrows), non-optically through internal conversion (dotted black arrows) or through a spin-forbidden intersystem crossing into a state of higher multiplicity T_n. This state relaxes optically through phosphorescence (orange arrows). B) shows the application of these electronic transitions as a Frank-Condon diagram, linking the energetic levels to a reaction coordinate. The excitation into a higher vibrational state results in an oscillation of the structure along the reaction coordinate. The vibrational relaxation dissipates energy from high vibrational states.

These electronic transitions, and potentially associated structural changes, can be reliably induced in all kinds of matter by femtosecond lasers. The probing of the system can in principle be done with neutrons, photons and electrons. Contemporary time-resolved neutron based measurement techniques offer a time-resolution in the millisecond regime [7], which is insufficient for the investigation of molecular dynamics.

Transient absorption spectroscopy probing the absorption of ultraviolet, optical or infrared light as a result of time following photoexcitation initially designed at longer timescales [8] can give excellent insight into the electronic structure, but, as discussed in the previous chapter, does not provide direct structural information. With the introduction of femtosecond lasers [1] the field has investigated structural dynamics both in solutions and solids [9].

Photons with shorter wavelength fall into the X-ray regime, for which the generation of short pulses is more difficult and generally requires *large scale facilities*. In earlier work at synchrotron facilities the time resolution in time-resolved experiments was limited to the millisecond regime [10] and later nanosecond regime [11]. This has allowed for time-resolved scattering experiment on crystals, both protein [11] and inorganic, as well as molecules dissolved in liquid solution. The implementation of high speed choppers introduced the selection of single pulses [12, 13] enabled a picosecond time-resolution through the selection of individual X-ray pulses. This allowed for the study of proteins [14, 15] and smaller molecules [16] on ultrafast time-scales. In addition to the structurally sensitive scattering, spectroscopic X-ray methods focusing on the electronic structure have been developed profiting from the same improvement of sources [17], investigating energy gaps and spin states [18].

The availability of free electron lasers (FEL) [19, 20] producing ultrashort and brilliant X-rays has increased the temporal resolution of these techniques by several orders of magnitude. This allowed for the investigation of molecules in solution, through both scattering [21] and spectroscopic methods [22], on crystals [23, 24] and solutions [25] on the femtosecond scale. These methodologies, in specific the *Time-resolved X-ray solution scattering* method discussed in chap. 5, and technical capabilities for time-resolved measurement provided by synchrotrons and free electron lasers will be the primary method of investigation in this thesis.

Electrons, as mentioned previously, can also be used for the probing of systems on ultrafast timescales. One of such techniques used for structural investigation on the femtosecond timescale is the emerging *Ultrafast electron diffraction* [26, 27], probing the structure through the scattering of electron pulses. Amongst others, the technique has been demonstrated for among other both ultrafast phase transition solids [28] and photophysical reactions in liquid [29].

Chapter 3

Transition metal complexes

A coordination complex, or complex from now on, are realized by a metallic *coordination center* forming a non-covalent bond to one or more ligands. This group of compounds will be the focus of this work. The ligands can be both organic or inorganic and are in principle only limited by the capabilities to synthesize them. As a result this class of compounds exhibits a very broad range of applications properties from catalysis, coloring or as chemically active centers in proteins [30].

Transition metals-complexes have been known and synthesized as dyes since modern times [31]. These procedures were later refined to industrial scale [32] due to the potential for modification in the modular setup of the complexes. They have also become more and more important in the field of catalysis over recent decades. Many contemporary catalysts rely on rare materials, fueling the search for new materials made out of abundant elements [33]. Despite many years of research, the direct interaction between catalytic activity, electronic structure and physical structure is not yet fully understood. A better fundamental understanding of the electronic structure on transition metals could be used to better understand the process catalysis by them as a whole and could help with the proposal and simulation of new materials with enhanced catalytic capabilities.

With the increased access to ever faster timescales discussed in the previous chapters, the path has opened to a more fundamental investigation of how their structure, both molecular and electronic, defines their properties. Such as the investigation of spin states [18, 34] with spectroscopic and structure with scattering based methods on the picosecond timescale. A recent review of scattering and spectroscopic method using X-rays, focused on iron based complexes, is published in [35].

This work will focus on complexes formed with d^8-transition metals. The *International Union of Pure and Applied Chemistry* (IUPAC) defines transition metals as "*an element whose atom has an incomplete d sub-shell, or which can give rise to cations with an incomplete d sub-shell*" [36]. This definition applies to more than 30 % of the discovered elements. Transition metals and their complexes have long been investigated for their catalytic properties [37]. They are commonly classified by the number of electrons in the outermost d-shell.

d^8-transition metals can be realized in ions from elements from the platinum group and other noble metals, such as Pd^{II}, Pt^{II}, Rh^I, Ir^I and

Au^{III}. They typically exhibit a square planar geometry translating to the formation of four bonds with ligands [38]. Together with the range of both inorganic and organic ligands that are available, an entire class of self-assembled materials with often fascinating photophysical and structural properties can be synthesized [39]. They have been investigated as mono-metallic [40], but also more recent in bi-metallic form [41] where the ligands bond to two metal ions in solution creating a distinct entity. A recent review on the group bi-metallic d^{8}d^8-transition metals has been published by Gray *et al.* [38]. If the reaction compounds or conditions favor the formation of continuous organic network structures rather than defined units, so called *metal organic frameworks* are formed instead. [42]

These bi-metallic transition metal complexes have been observed to form bonds with additional metal ions in solution, such as Ag$^+$ [43] and Tl$^+$ [44]. Uniquely, the bonding is not mediated by ligands enforcing proximity, but instead a *metal-metal* bond is formed between the atoms.

This thesis will focus on photoexcitation dynamics of bi-metallic complexes in chap. 7 and investigate this unique metal-metal bond in chap. 8.

Chapter 4

X-rays

X-rays are photons with a wavelength in the Ångstrom ($10e^{-10}$ m). As their wavelength is on the same order of magnitude as interatomic distances, the interaction is not limited to absorption or reflection, as commonly used with visible light, but instead is subject to interference effects on the structure of molecules.

The mathematical descriptions of their interactions with matter are derived and described in great detail by Jens Als-Nielsen and Des McMorrow [45] (chapter 4,5), and Warren [46] (chapter 1). This chapter will discuss the physical phenomenon and summarize the equations necessary for the interpretation of this work.

4.1 X-ray scattering

A wide range of experimental techniques has been proposed and applied in the investigation of structure and photophysical properties of transition metal complexes over the last decades. Time-resolved optical methods such as transient-absorption spectroscopy (TAS), which can probe the electronic states of molecules with femtosecond precision, core electron based techniques such as X-ray emission spectroscopy (XES), which is very sensitive towards spin states of atoms, or valence electron based techniques such as X-ray absorption spectroscopy (XAS) provide great insight into electronic structure or spin-state of the molecules, but do not provide direct structural information about the sample. Scattering techniques on the other hand directly probe the inter-atomic distances.

The available brilliance of large-scale facility X-ray has increased considerably over the last few decades with construction of 3rd generation synchrotrons and free electron lasers.

4.2 Interactions of X-rays with matter

A linear polarized X-ray photon propagating into the z direction can be described as a planar wave with the polarization $\hat{\epsilon}$, the wave-vector k=$\frac{2\pi}{\lambda}$ in direction of propagation and the frequency ω:

$$E(z, t) = \hat{\epsilon} E_0 \cdot e^{i(kz - \omega t)} \tag{4.1}$$

An electron, be it free or bound in the electronic shell of an atom, experiences the electric field of the incident electromagnetic wave, accelerates and emits an electronic wave itself. In a classical description of waves the process has to be elastic. This process is known as *Thomson scattering*. The intensity of light I scattered by an electron observed at a distance R is described by Eq. 4.2, with the electron charge e, the electron mass m_e, the speed of light c, the incident intensity I_0, and the scattering angle ϕ between $\vec{R}$ and z along the $E_{0,x}$ direction.

$$I = I_0 \frac{e^4}{(4\pi\epsilon_0)^2 m_e^2 c^4 R^2} \left(\frac{1 + \cos^2 \phi}{2} \right) \tag{4.2}$$

The constants in this equation are commonly expressed through the *Thomson radius* $r_e = \frac{e^2}{4\pi\epsilon_0 mc^2} \approx 2.818e^{-15}$ m.

The electrons of an atom can be interpreted as a distribution of charge density surrounding the nucleus. The scattering properties of this charge distribution can be described with the momentum transfer dependent *form factor* f(q), the first order term f_0 describing the coherent scattering shown in Eq. 4.3, with the electronic density $\rho(r)$. The momentum transfer vector q, defined as the difference between incoming (k_0) and outgoing (k) wave-vector, is given by q = k-k_0 = $\frac{4\pi \sin\theta}{\lambda}$ The form factor has dispersion correction terms f' and f'' describing the energy dependent inelastic scattering that may occur if the photon energy matches an electronic transition in the atom, which will not be discussed further in this work. The X-ray energies during the experiments have been intentionally chosen to be in regions where these effects are negligible for the sample.

$$f^0(q) = \int \rho(r) e^{iqr} dr \tag{4.3}$$

In practice the atomic form factors are approximated using tabulated coefficients using several Gaussian functions. Initially the form factors were tabulated by Cromer and Mann in 1968 [47]. These approximations have been extended by Waasmaier and Kirfel in 1995 [48] to comprise an additional term, resulting in Eq. 4.4, with the constants c, a_i, and b_i being tabulated for each element in the previously mentioned sources:

$$f(q) = c + \sum_{i=1}^{5} a_i \exp\left(-b_i \left(\frac{q}{4\pi}\right)^2\right) \tag{4.4}$$

The form factor approaches the electron number Z for q→0.

Similar as the electrons of an atom can be interpreted as a charge distribution, a molecule can be seen as a collection of atomic charge distributions. In the *Independent Atom Model*, which approximates the charge distribution as isotropic and only depending on the spherical distance r from the nucleus. The structure factor $F^{mol}(q)$ describes the scattering of a molecule and is given by:

$$F^{mol}(q) = \sum_{j}^{N} f_j(q) e^{iq \cdot r_j} \tag{4.5}$$

The absolute measured intensity is proportional to the flux, the scattering probability and the amount of material the beam is passing through. The measured intensity of X-ray for a given momentum transfer when scattering on N_α identical molecules can be calculated with Eq 4.6:

$$I(q) = N_\alpha I_0 \cdot r_e^2 |F^{mol}(q)|^2 \tag{4.6}$$

4.3   Debye equation

For a set of randomly oriented molecules, as will be the case for the transition metal complexes dissolved in solution discussed in this work, the Thomson scattering of a molecule with the structure factor $F^{mol}(q)$ can be rotationally averaged into the Debye equation, shown in Eq. 4.7. [45] This equation calculates the momentum transfer dependent scattering amplitude S(q) for a given rotationally averaged molecule, with the inter-atomic distance r_{ij}:

$$S_{orient.avg.}(q) = \langle |F^{mol}(q)|^2 \rangle_{orient.avg.}$$

$$= \sum_{i,j}^{N,N} f_i(q) f_j(q) \frac{\sin(qr_{ij})}{qr_{ij}} \qquad (4.7)$$

The Debye equation calculates the scattering for a single precisely known internal structure. Under finite temperature a range of vibrational and rotational modes will be populated, leading to an ensemble of individually deformed complexes, thus the discrete intermolecular distances used in Eq. 4.7 are a poor representation. In crystallographic experiments the positional uncertainty of atoms with regards to their perfect crystalline grid position induced by temperature is often modelled with a *Debye-Waller-factor* $\propto \exp(-u^2 q^2)$ [45], with the mean positional derivation u. A similar computationally economical approximation can be made for the calculation of a molecular structure ensemble with a distribution of interatomic distances. Eq. 4.8 shows this Debye-waller-esque description of uncertainty in structures with the positional uncertainty u_i [49, 50], with $u_i/2$ corresponding to the mean squared displacement:

$$S(q) = \sum_{i,j}^{N,N} f_i(q) f_j(q) \frac{\sin(qr_{ij})}{qr_{ij}} \cdot \exp(-(u_i^2 + u_j^2)q^2) \qquad (4.8)$$

4.4   Scattering from disordered systems

The rotationally averaged Debye equation allows for the calculations of the coherent isotropic scattering of an isolated structure with well-defined atom positions. For many disordered systems, such as liquids or very flexible compounds, such a description is insufficient to describe the distribution of interatomic distances, even if a *Debye-Waller-esque* blurring is applied to the position.

In liquids, the inter-atomic distances are much less well defined, making the discrete Debye formulation impractical due to the large amount of sampling required for an adequately averaged description. Disordered systems are commonly described with radial distribution functions (RDFs,

g(r)). These functions depict the correlation of inter-atomic distances of different types of atoms. For practical purposes, these different types entail both separation my atomic number as well as separation between solvent molecules and solute molecules [51].

The description of this problem has first been discussed by Zernicke and Prins and has seen increased interest with the improvement of simulations capabilities for solutions in recent decades [52]. Eq. 4.9 shows the calculation of the total scattering signal with the radial distribution function of N atom types, of which there are n_i in the Volume V, whose radial distribution functions $g_{i,j}$ towards atom type j converges towards $g_{0,i,j}$, 0 or close to 1, for large distances. g(r) is integrated until the discrete distance R. For very narrow distributions, this description has been shown to converge towards the Debye equation [51].

$$S(q) = \sum_i^N n_i f_i^2 + \sum_{i,j}^{N,N} f_i f_j \frac{n_i(n_m - \delta_{i,j})}{V}$$
$$\cdot 4\pi \int_0^R r^2 [g_{i,j}(r) - g_{0,i,j}] \frac{\sin qr}{qr} dr \tag{4.9}$$

4.5   Anisotropic scattering

Molecules that have a directed transition dipole moment are preferentially excited based on their transition dipole moment alignment when excited with linearly polarized light. The excitation probability follows a cosine squared pattern along the axis of the transition dipole moment. If the measurement occurs on timescales that are shorter than the rotational equilibration of the molecules in solution, this is reflected in the scattering pattern. The bi- and tri-metallic complexes discussed in this work generally exhibit such a preferential excitation axis and as such exhibit an anisotropic scattering component after photoexcitation with linearly polarized light.

Eq. 4.10 shows the calculation of the anisotropic scattering of a molecule with the second order Legendre polynomial P_2, the second order spherical Bessel function j_2, and the angle between transition dipole moment

and laser polarization ξ_{ij}, and the time dependent rotational alignment coefficient c_2 [53]:

$$S_2(q) = -c_2(t) \sum_{i,j}^{N} f_i f_j P_2[cos(\xi_{ij})] j_2(r_{ij}) \tag{4.10}$$

4.6   Inelastic scattering

In addition to the coherent scattering discussed previously, in which the energy of the photon remains identical, the X-ray photon may deposit energy in the electron during the scattering process. This process is known as the *Compton* effect [54] and gives rise to incoherent scattering. It has been tabulated for the first 36 elements by Hajdu et al. [55] using Eq. 4.11 with the empirically determined parameters M, K and L.

$$S_{inc}(q) = \left[Z - \frac{I_{coh}(q)}{Z}\right] \cdot \left(1 - M\left[e^{-Kq} - e^{-Lq}\right]\right) \tag{4.11}$$

The incoherent scattering of the heavier elements from Calcium onwards has been tabulated by Palinkas et al. [56] using Eq. 4.12 with the empirical parameters a,b and c.

$$S_{inc}(q) = Z\left[1 - \frac{a}{(1 + bq)^c}\right] \tag{4.12}$$

The incoherent scattering is sensitive to the electronic state of the atoms, but not to the structure of the molecules.

4.7   X-ray sources

Highly bright and temporally short X-ray pulses are needed for the experiments discussed in this work. A key index by which X-ray sources are compared is the *brilliance* B. Eq. 4.13 shows how this value is calculated with the photon flux n_{Photons}/s, the divergence, the diameter and the energy bandwidth.
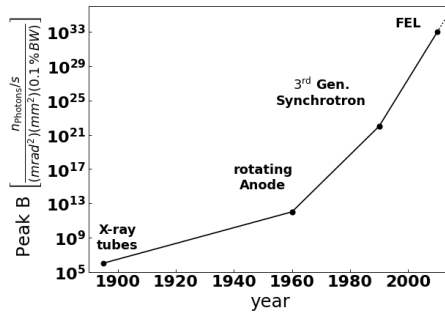
Figure 4.1: Peak brilliance of available X-ray sources over the last century [57]

$$B = \frac{n_{\text{Photons}}/s}{(\text{mrad}^2 \text{divergence})(\text{mm}^2 \text{source})(0.1\,\%\,\text{energy Bandwidth})} \quad (4.13)$$

For many contemporary applications of X-rays in science, such as time-resolved the X-ray solution scattering used in this work, laboratory sources cannot provide the necessary beam properties. These measurements can be conducted at large scale facilities. Fig. 4.1 depicts the improvement of the peak brilliance over time. The available peak brightness has increased by several orders of magnitude over the recent decades. Both the improvement of synchrotron sources and the construction of free electron lasers have elevated the available brilliance by several orders of magnitude.

This work discusses experiments done at both synchrotrons and free electron lasers. Synchrotrons are circular electron accelerators that can provide high intensity X-ray pulses with $\sim$100 ps time resolution Free electron laser are linear accelerators and can achieve femtosecond pulse resolution with even higher intensities.

Undulator Radiation

Large scale facilities sources generate X-ray radiation by changing the momentum of electrons that are accelerated close to the speed of light. This is commonly realized with two sets of alternating magnetic pols that oppose one another over the path of the electrons, so called undulators,
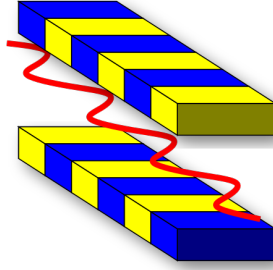
Figure 4.2: Generation of undulator radiation. Adapted from [45]

shown in Fig. 4.2. The electrons emit radiation while they are changing momentum in the alternating magnetic field. Eq. 4.14 shows the primary photon energy of the nth order harmonic frequency of an undulator with a magnetic pol length λ_0 and an electron energy E. Even-order harmonics are suppressed under ideal circumstances, but are present in the radiation generated at facilities:

$$E_n(\text{keV}) = n \cdot 0.95 \frac{E^2(\text{GeV})}{\lambda_0(\text{cm})\{1 + (0.934 B_0(\text{T})\lambda_0(\text{cm}))^2/2\}} \tag{4.14}$$

The magnetic field strength B_0 at the position of the electrons by changing the distance between the rows of magnets [45]. The equation describing the spectral and angular distribution of the beam are described elsewhere [45, 58] but exceed the scope of this work.

While a great number of synchrotron sources have been constructed over the recent decades, only a few have setups for picosecond time resolution experiments. The synchrotron source used for experiments in this work is the *European Synchrotron Radiation Facility* (ESRF) in Grenoble, whose time-resolved beamline ID09 can deliver the necessary time resolution.

Self Amplified Stimulated Emission

The radiation from synchrotrons has enabled excellent research over the recent decades. There are however a few properties of the X-ray beam

which limit their application is some areas, most notably the pulse length limiting the available time resolution to 100 ps and the limited brightness. Molecular structural dynamics and solvent molecules rearrangements occur on the femtosecond timescale, as observed with femtosecond resolved laser spectroscopy. As such they cannot be resolved at synchrotron sources.

Under sufficiently high electron densities, the electrons respond to the radiation fields of the other electrons within the electron bunch. This causes the electrons to oscillate coherently, resulting in the emittance of extremely bright coherent light. This process is known as *Self Amplified Stimulated Emission* (SASE). The electron gas density is a key parameter for the effectiveness of this process, which has been shown to be insufficient in contemporary circular synchrotron sources for this process. Linear accelerator facilities have been constructed to make use of this effect in *free electron lasers* (FEL), whose electron bunches can be compressed as low as 100 fs, which also improves the available time-resolution considerably [45].

A major downside of linear accelerators is that the electrons are only used for the generation of a single beam and as such can only be used for a single experiment at the same time. In direct comparison the circular ESRF accelerator can provide X-ray photons to all of its 50 [59] experimental hutches simultaneously. As a result, beamtime at FEL facilities is considerably more scarce than at synchrotrons.

Free electron laser facilities have been constructed among other places in Hamburg (European XFEL) [60], Switzerland (SwissFEL) [61] and Japan (SACLA) [62]. The FEL data shown in this work was measured at the *Linac Coherent Light Source* (LCLS) [20] at the SLAC National accelerator laboratory in California.

Chapter 5

Time-resolved X-ray solution scattering

X-ray solution scattering (XSS), also known as X-ray diffuse scattering (XDS), wide angle X-ray scattering (WAXS), and X-ray liquidography, is an X-ray based experimental method of determining the structure of molecules in solution.

As discussed in the last chapter, the wavelengths of X-ray photons in the energy range of $\sim$10 to $\sim$30 keV are on the same order of magnitude as the inter-atomic distances, and as such scatter elastic and coherent. The scattering produces a scattering pattern strongly dependent on the scattering angle 2Θ that can be captured with a 2-dimensional detector. The random orientation of the molecules in solutions results in a near isotropic scattering signal.

The time-resolved method introduces a change in system, in this work through photoexcitation with a laser pump pulse and probes the changes in inter-atomic distances as a result of it. In diluted sample solutions the scattering signal is dominated by the coherent and incoherent scattering of the solvent molecules, the magnitude of the difference between excited and non-excited sample is commonly less than 1 % of the total scattering signal [63]. The difference scattering image $\Delta S = S_{\text{Laser On}}$ - $S_{\text{Laser Off}}$ isolates changes induced by the laser while suppressing all other features. As a direct result this technique requires high photon flux rates and can only be employed at large scale facilities.

The measurements analyzed in this work have been conducted at the ESRF ID09 and the LCLS XPP endstation. I participated in the measurements at ID09, as the setup will be discussed in great detail in this chapter. I did not participate in any XPP measurements in person, as such there is no similarly detailed discussed on the setup.

5.1   Experimental setup

Fig. 5.1 depicts a schematic time-resolved X-ray solution scattering (TR-XSS) setup. The laser pump- and the X-ray probe-pulse are spatially overlapped on the liquid jet delivering the sample. They pass through the sample at a known time delay Δt. The X-ray photons scatter on the sample and are detected by the detector placed $\sim$5 cm behind the jet. The
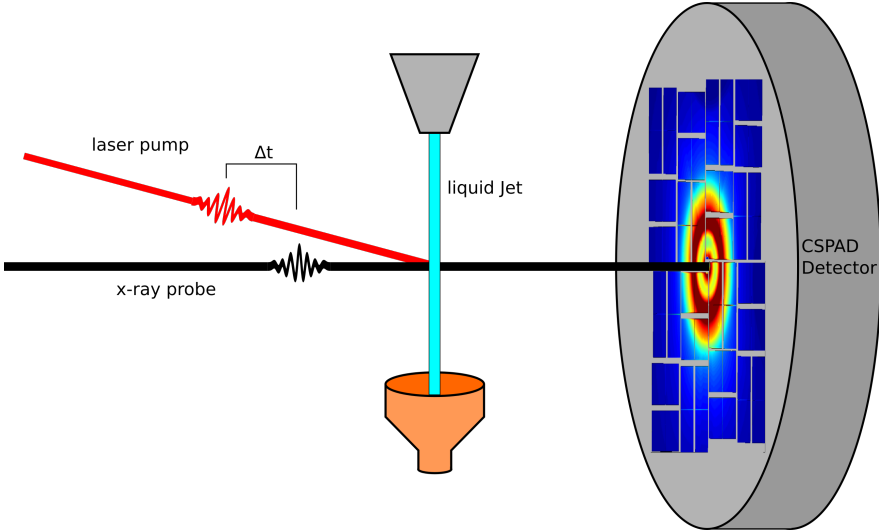
Figure 5.1: X-ray solution scattering setup sketch of the LCLS setup with the CSPAD detector

primary X-ray and laser pulses are blocked with beam stops to prevent detector damage.

The time resolution at a synchrotron facility is dominated by the pulse length delivered by the facility. The temporal X-ray pulse width of 70 ps at the ESRF ID09 is logged for each of the recorded detector images and is considerably greater than the 2 ps optical laser pulse length used in the experiments. The temporal X-ray pulse profile width was calibrated with a streak camera during the commissioning after the extremely bright source (EBS) upgrade in 2020.

This limitation in time resolution can partially be circumvented using the time-slicing technique applied in the experiment discussed in section 7.1.

The time resolution at free electron lasers can be determined with the instrument response function (IRF) in Eq. 5.1. The time resolution is a convolution of the pulse width σ_{xpw}, the temporal jitter of the X-ray pulse arrival time σ_{Jitter}, the temporal smearing σ_{jw} and the laser pulse width σ_{lpw}, which will be discussed in the following paragraphs:

$$\sigma_{\text{IRF}} = \sqrt{\sigma_{\text{xpw}}^2 + \sigma_{\text{Jitter}}^2 + \sigma_{\text{jw}}^2 + \sigma_{\text{lpw}}^2} \qquad (5.1)$$

$\sigma_{\text{X-ray Pulse width}}$ is generally around 30 fs at the LCLS. σ_{Jitter}, which has been as high as 100-200 fs after the commissioning of the LCLS but has since been continuously improved. The uncertainty temporal jitter can be reduced considerably through the usage of the timing tool, discussed in in sec. 5.1.2 [64].

The temporal smearing $\sigma_{\text{Jet width}}$ originates from the different group velocities of photons of different wavelength in a refractive medium. An optical pump pulse traverses a 50 μm jet of liquid water 55 fs slower than the X-ray pulse, limiting the possible time resolution. Finally, the laser pulse width σ_{lpw} contributes with about 30 fs. 30 or 50 μm thick Jets are commonly used during free electron laser experiments to take advantage of the short X-ray pulse lengths as much as possible. The considerably lower time resolution at synchrotrons allows for jet thicknesses between 100 and 300 μm. This increases the signal to noise with additional sample material being probed per photon pulse.

5.1.1   ESRF ID09 Beamline

The electrons in the ESRF synchrochroton circulate in the 844 m long storage ring close to the speed of light with an orbit frequency of 355 kHz.

The X-rays are however generated for all electrons passing the undulator, not only a single pulse. The selection of inciding pulses for the experiment therefor occurs on the generated X-rays. A sequence of choppers is employed to separate individual bunches from the pulse train. The experimental setup used for x-ray pump probe experiments at ID09 is depicted in Fig. 5.2.

Electron storage ring

The X-rays are generated with undulators, as discussed in sec. 4.7. Two different undulators were used for the experiments shown in this work, the u17 and the u27 undulator. The undulators are named based on the length of the magnetic poles in millimeters. The u17 undulator is used for the majority of experiments at the beamline providing X-rays with a tunable
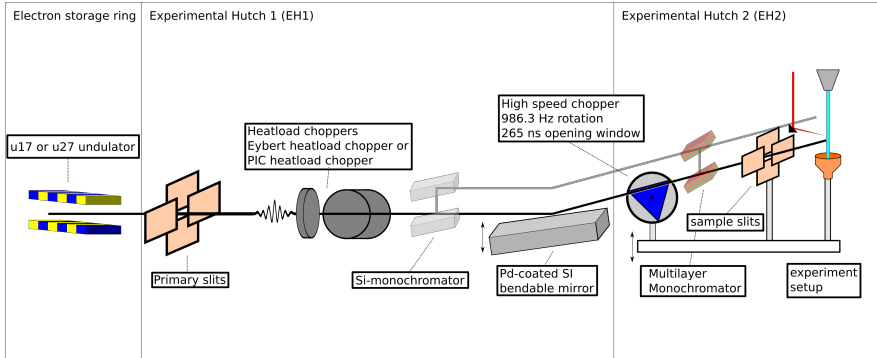
Figure 5.2: Simplified sketch of the beamline hutch setup at ESRF ID09. The X-rays are generated by the electrons in the electron storage ring passing through the undulators. The photons pass through a beryllium window and primary slits into the experimental hutch 1. A heatload chopper absorbs ∼90 % of the energy to reduce the load on subsequent equipment selecting single pulses. Following an optional silicon monochromator, a Pd-coated Si-111 mirror reflects the beam into the experimental hutch 2 where it hits the sample.

enery range from ∼12 to ∼19 keV. Section 7.1 contains a comprehensive analysis on the feasibility of using the u27 undulator, which can deliver up to 24 keV, for X-ray solution scattering experiments at ID09.

Experimental Hutch 1

The beam is initially defined using the primary slits. An initial chopper, called heatload chopper, selects μs wide windows and absorbing the majority of the total X-ray power generated by the undulators. The ID09 has two interchangeable systems for this process, the *Eybert* and the *Professional Instruments Company* (PIC) chopper. The Eybert chopper selects 96 μs wide windows at 986.23 Hz absorbing about 90 % of the beam, while the PIC chopper has additional modes at 82.19 and 2958.9 Hz. [13]

A silicon (111) monochromator can be inserted into the beampath to select individual wavelengths from the spectrum generated from the undulator. The small energy acceptance bandwidth of this monochromator $\sim \Delta E/E = 1.4e^{-4}$ reduces the photon flux considerably making time-resolved experiments using the monochromatic beam unfeasible. A

bendable Pd-coated Si mirror is then used to reflect the beam into the experimental hutch 2 (EH2). The mirror is reflective up to 25 keV and is used to focus the beam into the desired size at the sample position.

Experimental Hutch 2

In the second experimental hutch a high speed chopper selects a 265 ns wide window from the heatload chopper selection. To allow the selection of single pulses in experimental hutches, the ESRF has a range different electron bunch filling modes in the ring. The most common mode is the *7/8+1 (200 mA)* setting. During this mode 7/8th of the electron storage ring are filled with 2468 pulses each spaced ~2.84 ns. The remaining 352 ns are filled with a single centrally positioned 8 mA pulse. At the time of the experiments conducted in this work, the single pulse was limited to 4 mA by the facility. The high speed chopper consists out of a triangle with a tunnel rotating at high speeds, opening a 300 ns window for photons to pass. This windows is sufficiently small that the high speed chopper can select the single pulse. [65] The chopper system has been discussed in great detail by Cammarata*et al.* [13].

The beamline has multilayer monochromators that can be inserted into the beampath after the high-speed chopper. These monochromators have a considerably larger acceptance range and as such reduce the intensity less. Afterwards the beam reaches the sample position. The intensity of the single pulse is not sufficient for a good signal-to-noise ratio. As such several thousand pulses with identical delays between pump and probe pulse are integrated for each saved detector image.

5.1.2 Timing-tool

At the free electron laser LCLS, the production of the X-ray photons through SASE is a stochastic process, and the uncertainty of the start of the process results in a jitter in the delay at the sample position. It is also used, as will be shown later, as a tool to assess the quality of the X-ray pulse used in filtering processes. The timing-tool is an optical setup to measure the actual delay between X-ray and laser pulse at the LCLS implemented by Harmand *et al.*. The principal behind the detection is the
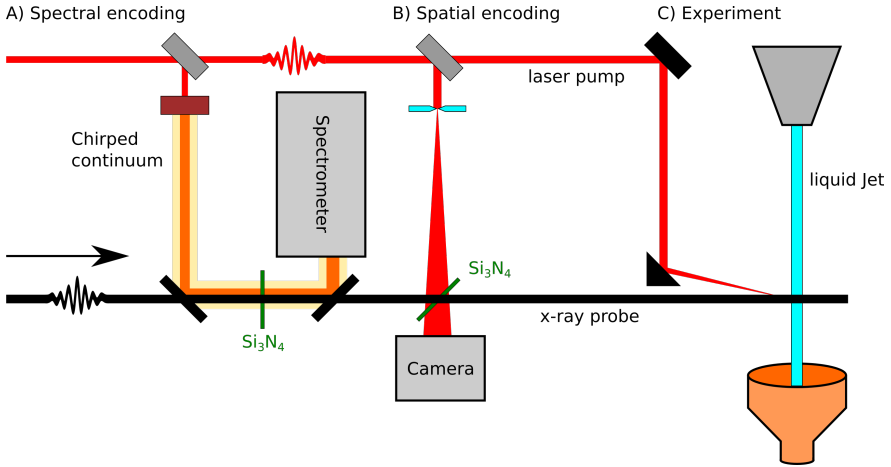
Figure 5.3: Timing tool setup adapted from [64].

change in the reflectivity of visible light in Si_3N_4 after photoexcitation by the probe X-ray pulse. [64]

Fig. 5.3 depicts the timing-tool with the three relevant subsections. In the *spectral encoding* section A), the pump laser is partially reflected onto a sapphire crystal, which *chirps* the pulse into a spectral continuum while increasing the pulse length. The chirped pulse is aligned with the X-ray pulse through a Si_3N_4 substrate whose reflectivity increases after the X-ray pulse passes. The residual pulse is analyzed by a spectrometer. The spectrometer will only be able to measure the spectral components which passed the Si_3N_4 before the X-ray pulse.

In the *spatial encoding* section depicted in Fig. 5.3 B), an additional part of the laser pulse is reflected through a pinhole onto a camera. An additional Si_3N_4 substrate is positioned inside and parallel to the X-ray beam crossing the laser pulse. The X-ray beam passes gain through the Si_3N_4 substrate and changes the reflectivity. The laser pulses crosses the substrate with the measured light detected by the detector depending on the reflectivity and thereby position of the X-ray pulse. The camera only detects the part of the laser pulse that passes through the not yet reflective substrate.

In both cases the detector measures a partially reduced signal with

a change at the position which corresponds the actual temporal delay between X-ray and laser pulse. This change can be fitted with a broadened step function on both detectors. By correcting with these values the uncertainty of the delay time can be reduced to ∼6 fs [64].

5.2   Data reduction

Large amounts of data are collected during an X-ray solution scattering experiment beamtime. The CSPAD detector used during the LCLS experiments [66] has 2.3 million, the Rayonix MX170-HS employed at Id09 has more than 14 million pixels. During an experiment typically thousands of images are taken at a synchrotron and more than 10 million at a free electron laser experiment. This amounts to several hundred gigabytes of data for synchrotron experiments and more than one hundred terabytes for free electron laser experiments. The sheer volume of data makes preprocessing compulsory before any further analysis can be conducted.

5.2.1   Synchrotron

The X-ray pulse length available at ESRF ID09 is about 70 ps, which is larger than the dephasing time of aligned molecules in solution, for the samples investigated in this work. As such there is no anisotropic solute difference scattering signal and each image can be azimuthally integrated. Each individual image is corrected for systematic errors before the azimuthal integration. Eq. 5.2 depicts the correction of an image taken at a synchrotron facility. The individual contributions of the equation will be discussed in the following paragraphs:

$$
\begin{aligned}
I_{\text{corrected}} =& (I_{\text{raw}} \cdot C_{\text{FF}} - I_{\text{Dark}}) \cdot C_{\text{mask}} \cdot C_{\text{Pol}} \\
& \cdot C_{\text{SA}} \cdot C_{\text{DA}} \cdot C_{\text{JA}}
\end{aligned}
\tag{5.2}
$$

The measured electronic signal I_{raw} is first corrected for the flat field C_{FF}, which corrects the individual pixels for their specific absorbance, and the electronic dark current I_{Dark}. The flat field correction has been calibrated by the ESRF detector group during commissioning and the dark
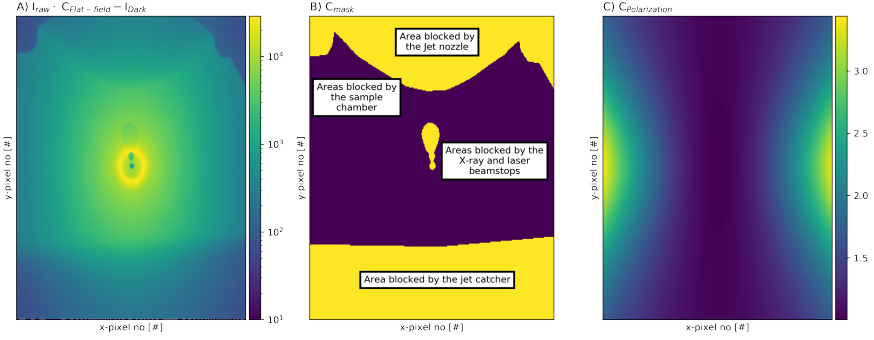
Figure 5.4: The partially corrected image saved from the detector A), the mask that is used to removed parts of the detector without solute scattering from the reduction B) and the polarization correction C).

current is measured by taking an image without X-ray exposure. The dark current image primarily consists out of read-out-noise as the increasing electronic charge is commissioned as 0.001 photons/pixel/second. These first two steps are carried out by the detector before the data is saved. [67]

The mask C_{mask} is used to filter out pixels that do not contain sample scattering signal. The detector is partially blocked from X-ray exposure by parts of the measurement setup, such as the sample chamber and the jet nozzle, or for its protection, such as the beam-stop. Pixels without sample scattering information are removed using Eq. 5.3:

$$C_{mask} = \begin{cases} \text{False,} & \text{if masked} \\ \text{True,} & \text{otherwise} \end{cases} \qquad (5.3)$$

Additionally, the scattering image is corrected for the difference in scattering probability based on the linear X-ray scattering angle and the azimuthal angle ϕ on the detector surface:

$$\begin{aligned} C_{Pol} = & 1/(P[1 - (\sin(2\theta)\sin(\phi))^2] \\ & + (1 - P)[1 - (\cos(2\theta)\sin(\phi))^2]) \end{aligned} \qquad (5.4)$$

with the x-ray polarization P, the x-ray scattering angle θ, and the azimuthal angle ϕ, as discussed by Hura et al. [68].

33

A solid angle correction C_{SA} is used to correct for the difference in relative area of a sphere each of the pixels covers, as discussed by Boesecke *et al.* [69]:

$$C_{SA} = \frac{1}{\cos(2\theta)^3} \tag{5.5}$$

Next, the image is corrected for the different absorbance of the material depending on scattering angle C_{DA}. The path length of an X-ray photon and thereby absorption probability through a pixel increases with its inciding angle compared to the perpendicular path. At larger photon energies where only a fraction of photons is detected this effect is considerable. Eq. 5.6 depicts this correction with the wavelength dependent detector material absorbance $\mu_{detector}$, the pixel thickness $d_{detector}$ and the scattering angle θ:

$$C_{\text{Detector Absorption}} = 1 - \exp\frac{-\mu_{detector}(\lambda) \cdot d_{detector}}{\cos\theta} \tag{5.6}$$

In a final step the image is corrected for the differences in self absorption of scattered photons based on the scattering angle. Based on absorption guided by the *Lambert Beer law*, larger scattering angle increases the path-length through the sample which scatters considerably stronger than the surrounding inert gas, as discussed by Paul *et al.* [70]. The jet absorption, with the jet width d and the sample X-ray absorption coefficient μ is given by:

$$C_{JA} = \frac{\mu d - \mu d / \cos(2\theta)}{\exp(\mu d)[\exp(\mu d / \cos(2\theta)) - \exp(\mu d)]} \tag{5.7}$$

The detector images also contain non-sample scattering contributions originating from the scattering of the surrounding air. X-Ray solution scattering experiments are commonly conducted under inert gas atmosphere to protect the sample from oxygen as much as possible and to reduce air scattering by flushing the chamber with gasses with low scattering strength. In practice these contributions may not necessarily be stable over longer time periods, as the gas composition is subject to change depending on the process of creating the inert gas atmosphere and evaporation of the solvent. As the contribution only change slowly, they are
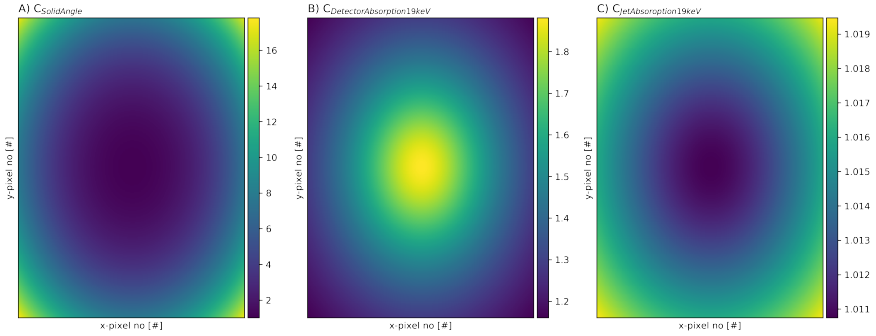
Figure 5.5: Solid angle correction A), detector absorption correction B) and the jet absorption correction C)

equally present in laser-on and laser-off images and are as such corrected for during the formation of the difference scattering images.

Formation of difference scattering images and filtering

The images taken at the ID09 Beamline each average between 4000 and 8000 pulses on each image, depending on the photon flux rate of the chosen wavelength. Thus, individual bad pulses cannot be rejected and are averaged alongside all other pulses. Each image is self-normalized to account for changes in the photon flux. The self normalization is done by dividing the azimuthally integrated total scattering signal by its average between higher q values such as 4 and $8 \text{\AA}^{-1}$. The range can influence the shape of the difference scattering signal and is ideally chosen between two isosbestic points in the difference scattering signal.

The difference scattering image is formed between each with laser pumping and the average of the two chronologically closest images without laser pumping. All difference scattering curves with the same pump-probe delay are gathered and outlier are rejected based on deviation from the median of the curves. The median of the curves that are not rejected, see sec 5.2.2, form the difference scattering signals.
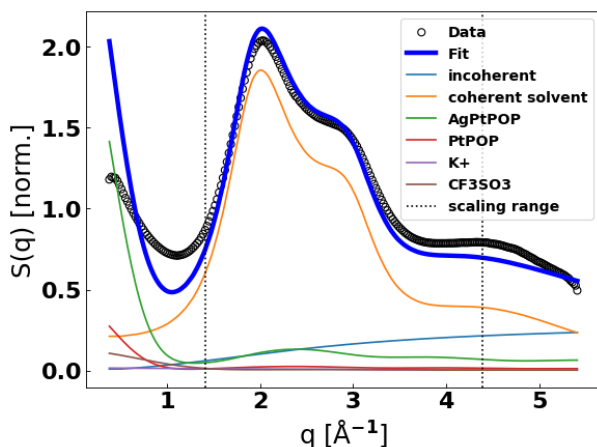
Figure 5.6: Liquid unit cell scaling of the 16.3 mM AgPtPOP sample in water used in the experiment discussed in sec. 8.1. Taken from sec. 9. Adapted from **Paper I**

Liquid unit cell

Any information about the signal magnitude is lost during the self normalization process of each image discussed in the previous section, in which the analogue detector units are converted to arbitrary units (a.u.). The liquid unit cell is the smallest representative unit of a solution that can be used to describe the sample of interest. It consists of 1 solute molecule, solvent molecules according to solute concentration, counter-ions, and stabilizing detergents according to sample preparation. The coherent and incoherent scattering of the solute, counter-ions and stabilizing detergents is calculated according to Eq. 4.7 and Eq. 4.11, the solvent signal is modeled with high precision reference measurements that have been scaled to single molecules [71].

Fig. 5.6 shows the liquid unit cell scaling of the AgPtPOP sample used in section 8.1. The sample consists of 16.3 mM AgPtPOP, 3.7 mM PtPOP synthesis residual, 20 mM K^+ counter ions and 30 mM triflic acid as stabilizing detergent. The scaling factor that is needed to match the simulated total scattering to the self normalized total scattering signal is

then applied to the difference scattering curves in the dataset. This process transforms the arbitrary units into electron units (e.u.). The analysis results from these scaled difference scattering curves, such as temperature and excitation fraction, are then directly extracted from the modeling.

Correction of the q-axis

The correct distance is paramount when converting pixel positions to scattering angles. Depending on the setup, the accuracy of the sample detector distance may be limited, and may vary by a millimeter or two from the nominal position. The correct detector distance can be found by comparing the total scattering or solvent contributions to literature positions. The q-axis can be corrected for an offset Δd using Eq. 5.8 [72]:

$$q_{d1+\Delta d,\theta} = q_{d1,\theta} \cdot \frac{\sin\left(\frac{1}{2}\tan^{-1}\left(\frac{1}{1+\frac{\Delta d}{d1}}\tan 2\theta\right)\right)}{\sin\theta} \tag{5.8}$$

5.2.2 Free electron laser

The high data acquisition rate at free electron laser creates a unique set of both opportunities and challenges for the data processing. Unlike the synchrotron experiments, where commonly detector images are integrated over several thousand pulses and several seconds, the scattering of a single XFEL pulse per detector exposure is sufficiently bright to generate detector images that are not dominated by detector noise.

The CSPAD used in the FEL experiments in this work has been shown to exhibit non-linear behavior towards the intensity and wavelength of the X-ray pulse. These effects result in differences between images that can be larger than laser induced differences and have not shown to average out with improved counting statistics, resulting in artifacts. These artifacts can be corrected for using the Singular Value Decomposition (SVD) based methodology developed by van Driel et al. [73], in which the entire measurement is decomposed into orthogonal components. Non sample signal components, which show a clear dependence on either pulse energy or intensity, are subtracted from each image based on the logged parameters. Eq. 5.9 shows the correction of the 2-dimensional for these artifacts

$$I_{\text{SVD corrected}} = I_{\text{Corrected}} - \sum_{m}^{n} I_{\text{Fit energy}} \cdot \gamma_{\text{X-ray energy}}$$
$$- \sum^{m} I_{\text{Fit intensity}} \cdot \gamma_{\text{X-ray intensity}}$$

(5.9)

Filtering

The machine parameters and information from monitoring diodes are logged for every X-ray pulse and as such for every detector images. This information allows for a more in-depth filtering approach compared to the synchrotron images averaging 1000s of pulses.

The timing-tool discussed in sec. 5.1.2 is the primary tool to reject images. To ensure the best possible time-resolution, all images that are either not associated with a valid hit detection, defined as more than 10 pixels away from the detector border, on the timing tool or whose fit error when determining said position is too large are rejected. Additionally images of X-ray pulses that deviate more than 20 % from the median X-ray intensity or deviate too much in energy are rejected. In a final step, similar to the synchrotron filtering, images are rejected based on their derivation from the mean of all images. Tab. 5.1 shows the filtering statistic of an FEL experiments discussed sec. 8.1. About half of all images that are taken are filtered out before the formation of difference scattering images.

Separation of isotropic and anisotropic components

A scattered photon k' position on the detector can be described with two angles, the scattering angle 2Θ and the azimuthal angle ϕ. Fig. 5.7 depicts these angles and their relation to the X-ray and laser polarization. The angle ϕ of k' and ϕ_q of the laser polarization are defined in relation to the X-ray polarization.

The X-ray solution scattering signal of an isotropic distributed ensemble of molecules is isotropic on the detector, when correcting for X-ray polarization as discussed sec. 5.2. As discussed in sec. 4.5, a molecule with a linear transition dipole will have a preferred excitation direction, resulting in an anisotropic distribution of excited state molecules and therefor

Table 5.1: Example of filtering statistics for the analysed datasets discussed in sec. 7.3.1 and 8.1. Adapted from **Paper I**

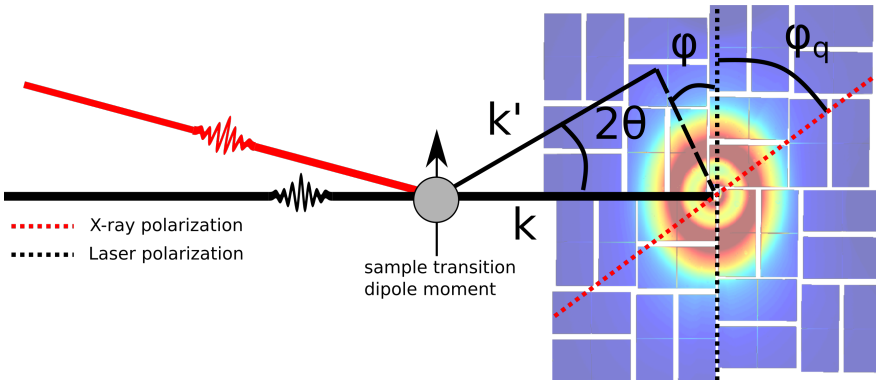|	Pt_2POP_4	$AgPt_2POP_4$	$TlPt_2POP_4$
Total Scattering images	554154	458346	361788
Low X-ray intensity	4877	8901	18402
Deviating X-ray energy	26955	26107	20129
Invalid position on timing-tool detector	76644	64369	51225
Error on timing tool position too large	143638	132269	95790
Scattering signal deviating from mean	17133	3926	3857
Scattering images after filtering	284907	222774	172385
Difference scattering images after filtering	208706	161001	125144

Figure 5.7: Anisotropy for a sample with a linear transition dipole moment with the laser polarization ϕ_q, the scattering angle 2θ and the azimuthal angle ϕ
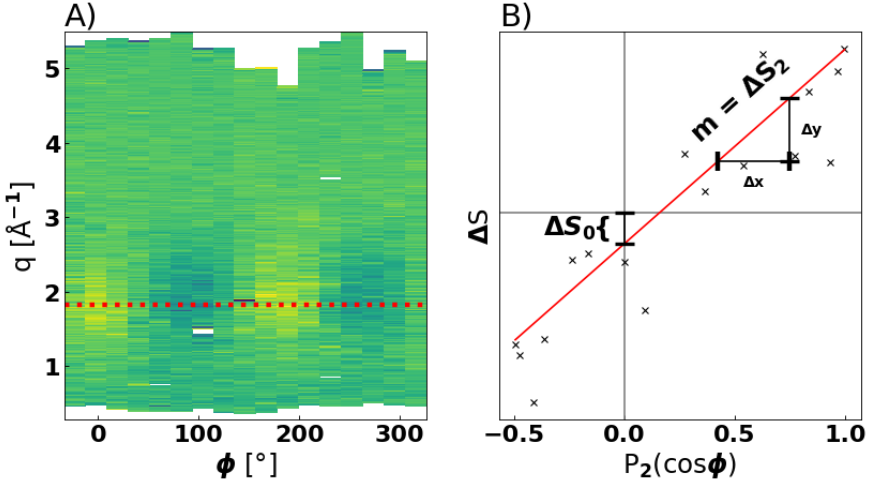
Figure 5.8: Illustration of decomposition of S_0 and S_2 in DMA. A) depicts the difference scattering image with 17 azimuthal slices after a delay of $\sim$130 fs. The dotted line depicts the q-bin at $1.8\,\text{Å}^{-1}$, which is decomposed with a linear fit according to Eq. 5.10 in B)

and anisotropic difference scattering signal, when probed on sufficiently short timescales.

To separate these the components, the 2D detector images, after correction according the Eq.5.2, are azimuthally integrated into n slices, with n being an odd number commonly between 11 and 17. These "caked" images are then used to form difference scattering images and temporally binned. Fig. 5.8 A) depicts the exemplary difference scattering image highlighting the dependence on ϕ of the difference scattering signal. Eq. 5.10 shows the composition of the difference scattering signal in each of the slices, with the second order Lagrange polynomial P_2.

$$\Delta S(q, \phi, t) \propto \Delta S_0(q, t) + P_2(\cos \phi)\Delta S_2(q, t) \qquad (5.10)$$

Using equation Eq. 5.10 the ΔS_0 and $\Delta S_2(q, t)$ can be separated by doing a linear fit of ΔS against $P_2(\cos \phi_q)$ for each q-bin, as depicted in Fig. 5.8 B). The slope of the line corresponds to $\Delta S_2(q, t)$, while the zero crossing corresponds to ΔS_0.

The process used for the separation of isotropic and anisotropic components was developed by Biasin et al. [53] based on theoretical work by Lorentz, Møller and Henriksen [74].

Chapter 6

Data Analysis

Once the measured data is sufficiently prepared it has to be analyzed to gain insight into the physical effects occurring in the sample. The common way for this is to calculate the signal of the assumed model and improve or discard it by comparing it to the measured data. Any modeling approach however always imposes assumptions onto the data, which may lead to the ignoring or creation of features as a result of an incomplete description of the system. Additionally, the modeling may be sensitive towards artifacts or noise. To avoid both over-interpretation of the data as well as missing components the modeling of the data is preceded by and combined with model-independent analysis methods. This chapter will introduce several key statistical and algorithmic methods used in this work, summarized from Press [75] (chapter 12,13,15).

6.1 Model independent analysis

There are three primary methods of model independent analysis used in this work, *Singular Value Decomposition* (SVD), already employed in sec 5.2.2, *Fourier transformation* and *autocorrelation*, which will be introduced in this section.

The Singular Value Decomposition is a method for identifying key components in a data matrix. The algorithm decomposes the N×M matrix A into the column-orthogonal N×N matrix U, the diagonal N×M matrix S and the M×M orthonormal matrix V according to Eq. 6.1 [75]:

$$A = U \cdot S \cdot V^{T} \tag{6.1}$$

These orthogonal components are commonly ordered by decreasing magnitude within the matrix, as shown in the *Singular Value* matrix S. In the case of the difference scattering matrices $q \times \Delta t$ the algorithm deconstructs the data into the left-singular components U_n each with their individual time trace V_n and their magnitude $S_{n,n}$. Fig. 6.1 depicts this procedure. This technique has been used in the past for XFEL data both to determine noise components [76] as well as signal contributions [77].

The Fourier transformation is a common method for spectral decomposition of a signal into periodic components. A time-resolved signal can be represented as a set of frequencies and vice versa. The interconversion
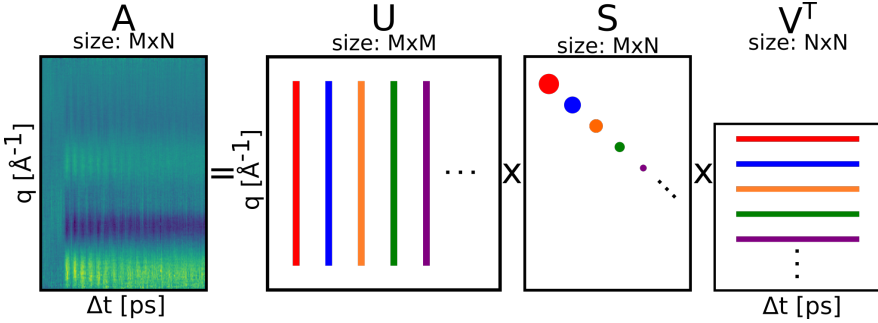
Figure 6.1: Singular Value Decomposition (SVD) of the PtPOP dataset ana-
lyzed in sec. 7.3.1. The data matrix A is decomposed into the matrix U, filled
with left singular components with contributions along the q-axis, the matrix
S, which contains only diagonal components describing the magnitude of each
component in descending order, and the matrix V^T, containing the right sin-
gular values representing time-traces along the Δt axis.

between these two representations is done by means of the Fourier trans-
formation. For an evenly sampled signal H with N points the frequency
representation is given by Eq. 6.2 [75].

$$H \equiv \sum_{n}^{N-1} a_n e^{i2\pi n/N} \tag{6.2}$$

In practice the excitation of the signal at $\Delta t = 0\,\text{ps}$ often introduces
a step function in signal magnitude. Sharp features in the temporal space
require access to high frequencies for adequate description during the
transformation. The maximal frequency f_c that can be resolved in a sig-
nal sampled discretely in the interval Δ is given by the *Nyquist critical
frequency* $f_c \equiv 1/(2\Delta)$. If the signal contains frequencies above f_c, they
create contributions in the spectrum in a process called *aliasing*, leading
to artifacts [75].

A way of suppressing these is to form the *Oscillatory Structural Signal*
(OSS) [53]. The signal that is to be Fourier transformed is first fitted
with a convolution of the IRF, a Heaviside function H and a selection of
low order polynomials and exponential functions, as shown in Eq. 6.3, to
match the shape with as few terms as possible. The residual of the fit

contains the periodic contributions of the initial signal which can then be extracted according to Eq. 6.2 without the artifacts originating from the excitation at Δt_0.

$$\Delta S(\Delta t) = IRF *$$
$$\left(H(\Delta t) \left(\sum_n a_n \Delta t^n + \sum_m b_m \exp(-c_m \Delta t) \right) \right) \quad (6.3)$$

The third model independent method used in this work is the auto-correlation. The correlation *Corr(g,h)* between two functions *g(t)* and *h(t)* is given by:

$$Corr(g, h)(t) = \int_{\inf}^{\inf} g(\tau + t) h(\tau) d\tau \quad (6.4)$$

with the *lag* t. Corr(g,h)(t) increases at lags t where *g(t)* and *h(t)* are very similar, and decreases of they are not. If *g(t)* and *h(t)* are the same function, this process is called autocorrelation. During the autocorrelation, Corr(g,h) converges fast towards small values , except if there are periodic contributions in the signals which are highlighted as peaks. The advantage that this method can provide is that the correlation identifies periodic contributions in scenarios where aliasing effects from discrete signals make the identification in Fourier transformations difficult [75](chap. 12, 13).

6.2 Modeling of X-ray solution scattering

The changes induced in the sample by the laser are isolated by forming the difference scattering signal ΔS in the data reduction process. During the modeling of X-ray solution scattering, a description must be found to match both the solute molecules and the solvent molecules in the sample. In practice this is realized with reference data, simulations of the solvent and scattering calculated from the assumed structure of the complex. The anisotropic contributions in the signal, as discussed in sec. 5.2, must be modeled with different contributions. A recent review on the modeling of TR-XSS data was made by Choi [25].

Isotropic contributions

The isotropic difference scattering signal in X-ray solution scattering in the picosecond range is commonly modeled with the contribution shown in Eq. 6.5. The solute contribution $\Delta S_{0,\text{Solute}}$ with the solute scaler α, the solvation shell term $\Delta S_{0,\text{Solvation shell}}$ with the solvation cage scaler β, and the isotropic heat term $S_{0,\text{Heat}}$ with the temperature change ΔT. For the difference scattering between a single ground and a single equilibrated excited state, the solute scaler α magnitude of the solute contribution of the molecules. For multiple ground states, or before the excited state equilibrium, the scaler describes both the phenomenon of the excited state formation as well as the population change in the ground state due to the photoexcitation. For a single ground and equilibrated excited state, α corresponds to the *excited state fraction*.

$$\Delta S_0 = \alpha \cdot \Delta S_{0,\text{Solute}} + \beta \cdot \Delta S_{0,\text{Solvation shell}} \\ + \Delta T \cdot S_{0,\text{Heat}} \tag{6.5}$$

Anisotropic contributions

The anisotropic data is modelled with two contributions as shown in Eq. 6.6, the solute term $\Delta S_{2,\text{Solute}}$ with the excitation fraction α_{ani}, and the optical Kerr effect term $\Delta S_{2,\text{Optical Kerr}}$ with its scaler γ.

The magnitude of the solute difference scattering signal α_{ani} is usually reduced in direct comparison to α. This can originate from both simultaneous multiphoton excitations, whose transition dipole moment might not follow the single photon geometry, or through a blurring of the for the calculation assumed perfect orientation along the molecule axis.

$$\Delta S_2 = \alpha_{\text{ani}} \cdot \Delta S_{2,\text{Solute}} + \gamma \cdot \Delta S_{2,\text{Optical Kerr}}(t) \tag{6.6}$$

6.2.1 Solute Structures

As part of the modeling process for optimizing Eq 6.5 and Eq 6.6 against the data, the structure of the complexes both before and after photoexcitation are optimized.

The scattering signals of a given structure are calculated with Eq. 4.7 for the isotropic and Eq. 4.10 for the anisotropic case. To contain the reduce of degrees of freedom, only the position of the metal atoms of the complex along a specific axis. In the case of the IrDimen molecule, the twist of the ligand cage is modeled through an additional parameter. These specific properties by which the complexes are parametrized, will be called *structural parameters*

The initial structures, used as a starting point for the structural optimization, were obtained from quantum computational computing calculations. Structures containing a large amount and heavier elements are generally computationally expensive to calculate due to the large amounts of electrons involved. An established method of reducing the computational load for large molecules is the density functional theorem (DFT). DFT predicts that the properties of a given system can be predicted from the electron density distribution of said system.

The structures that were used as starting points for the structural optimizations were calculated by Asmus Ougaard Dohn, Research Assistant Professor at University of Iceland, using DFT.

6.2.2   Bulk solvent contributions

Isotropic solvent contributions

A hydrodynamic system can be fully described by two variables out of temperature, pressure and volume. Here we use temperature and pressure to describe the system, as shown in Eq. 6.7 [78]:

$$\Delta S_{\text{bulk solvent}}(q,t) = \frac{\delta S(q)}{\delta T}\bigg|_\rho \Delta T(t) + \frac{\delta S(q)}{\delta \rho}\bigg|_T \Delta \rho(t) \qquad (6.7)$$

The heat is a measure of energy that is dissipated in the solvent and as such yields only isotropic scattering contributions. A standardized method to determine the solvent heat difference scattering signal has been introduced by Kjaer et al. [78]. A dye that quickly dissipates the absorbed energy into the solvent is used as a reference sample during an X-ray solution scattering experiment. Changes in the pressure occur on
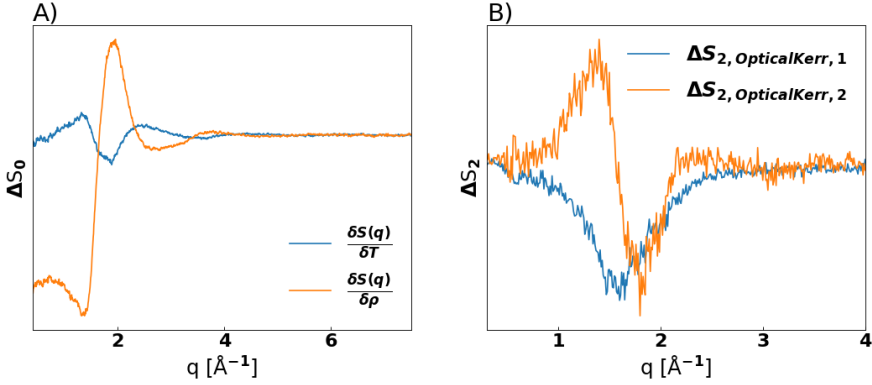
Figure 6.2: Bulk solvent contributions to the difference scattering signal of acetonitrile. A) Isotropic contributions heat and density. B) Anisotropic optical Kerr contributions, the two strongest orthogonal modes in the signal.

the timescale of nanoseconds, as such the measured signal after $\sim$100 ps only represents the changes from heat in the sample. [79] Fig. 6.2 A) depicts the difference scattering induced by heat dissipated and pressure changes. Most of this work focuses on timescales before 1 ns, thus the density contributions occurring at longer delays is not represented in the model described by Eq. 6.5.

Anisotropic solvent contributions

The solvent molecules are affected by the electrical field of the laser pump pulse when it passes through the liquid jet. This induces some transient alignment of molecules in solutions, which effects the difference scattering through the changes in inter-atomic distances within the solvent. This is known as the *optical Kerr effect*. For a linearly polarized laser this contribution follows the $\cos^2 \theta$ distribution, and as such the same pattern as the anisotropic scattering of transition metal complexes with a linear transition dipole moment.

The scattering optical Kerr effect in the solvent used during the experiment is obtained by performing a time-resolved XSS measurement on pure solvents using the same laser intensity. Fig 6.2 B) depicts the strongest two components determined by SVD-decomposition of the optical Kerr

effect in neat acetonitrile. The effect is only present within the first few hundred femtoseconds after the laser pump pulse but can be a dominant contribution especially in organic solvents in this period. Recent work on the interpretation of these anisotropic contributions has been done by Ki *et al.* [80] and Montoya-Castillo *et al.* [81].

6.2.3 Solvation cage contribution

Isotropic contributions

Upon solute molecule entry in a liquid, the surrounding solvent molecules rearrange to form solvation shells. The complexes discussed in this work are charged when dissolved in solution, and therefore align the surrounding solvent molecules according to their dipole moment. The complex rearranges structurally and electronically upon photoexcitation, which changes the distance distributions between solute and solvent molecules. This change in local structure yields a contribution to the difference scattering signal, and as such must be modelled, with often calculation heavy *molecular dynamics* (MD) simulations. These can be done with different set of potentials, quantum mechanical (QM) or molecular modeling (MM). This contribution is represented by $\Delta S_{0,\text{Solvation shell}}$, or $\Delta S_{0,\text{Cage}}$.

The QM/MM solvation cage for IrDimen, used in sections 7.1, 7.2 and 7.3, MM MD solvation cage for AgPtPOP and TlPtPOP, used in section 8.1 were calculated by A. O. Dohn. The QM/MM MD solvation cage for PtPOP, used in sections 7.3.1 and 7.3, was calculated by G. Levi [82], Postdoc at the University of Iceland. Information on the QM/MM MD used for the calculation of the cages can be found at [83, 84], information on the MM MD simulations can be found at [85].

6.2.4 Analysis of time-resolved signals

The structural parameters are optimized in sec 6.2.1 at a delay where the structural parameters have reached their excited state equilibrium. For a complete description of the photoexcitation dynamics, the structural parameters have to be determined for every time delay. Constraining some

of the structural parameters to values determined in the equilibrated excited state can be used to stabilize the optimizations. The time depentent paramter curves then describe the dynamics of the system.

The laser photon interacts with the sample at $\Delta t=0$ ps, from now on referred to as t_0. The excitation fraction is 0 for negative delays, grows in within the length of the laser pulse and remains constant from thereon, until the excited state relaxes through radiative or nonradiative decay. For practical purposes keeping α_1 constant even for negative delays may be practical to stabilize the parameters. This model however requires a certain degree of coherence in the motion of the molecules.

The time evolution of the parameters can be fitted with a function describing the path to identify the time constants of processes. These functions are in the following called *kinetic fits* or *kinetic functions*. An exemplary kinetic function is shown in Eq. 6.8, describing heat being dissipated with time constant $\tau_{\Delta T}$, the equilibrium temperature ΔT_{max}, and after a delay of t', convoluted with the *Instrument response function*:

$$
\begin{aligned}
\Delta T(\Delta t) =& IRF * (\Delta T_{max} \cdot H(\Delta t - t')\cdot \\
& (1 - \exp{(-(\Delta t - t')/\tau_{\Delta T})}))
\end{aligned}
\tag{6.8}
$$

The instrument response function is approximated by an error function with σ_i according to Eq. 5.1.

6.3 Confidence intervals

A fitting procedure such as the one used to model Eq. 6.5 and Eq. 6.6 to the data must provide three things to allow for an assessment of model quality and significance. Parameters, error estimates, and a statistical measure of goodness-of-fit, to be *genuinely useful* [75]. This section will discuss how these properties are derived for the structural optimizations in this work.

6.3.1 Confidence in data

To assess the error of a fitted parameter, the error of the data from which it is derived has to be assessed first. Especially for XFEL data sets, the number of photons detected can be so high that, depending on the temporal binning, the counting statistic can become so good that the data is no longer limited by signal-to-noise ratio but instead by signal-to-artifact ratio. These artifacts can range from detector non-linearities to reduction steps such as the self-normalization. As errors introduced by artifacts are difficult to estimate, the amount of difference scattering images averaged are limited to ensure the Poisson distributed counting statistic remain a dominant part of the error, which is relevant for the statistical consideration used in the following sections.

In this work, the error for each of the q-bins is estimated based on a method proposed by A. Filipponi [86] for X-ray absorption fine-structure data. The data is modelled with a low order polynomial in consecutive intervals. The error residual between fit and data is considered the error. The error is smoothed and used as the error σ_i associated with a given q-bin q_i.

6.3.2 Goodness-of-fit estimator

A common method of determining the quality a given model is the reduced goodness-of-fit estimator χ^2_{red}. It is given by Eq. 6.9 with the N data points y_i, the M free model parameters $a_1, a_2...a_M$, the error associated with each data point σ_i [75].

$$\chi^2_{red} \equiv \sum_{i=1}^{N} \left(\frac{y_i - y(x_i, a_1, a_2...a_M)}{\sigma_i \cdot (N - M - 1)} \right)^2 \tag{6.9}$$

2-dimensional detectors commonly have several millions pixels with unique distances towards the center of the beam. The number of azimuthal bins to integrate into can as a result be chosen to be as high as desired. The information content of the scattering signal however is finite. The amount of independent data points, also known as Shannon channels, has been assessed for small angle scattering in Eq. 6.10 [87] with the measured q-range q_{max}-q_{min} and the sample size D_{max}:

$$N_{idp} = 2 \cdot (q_{max} - q_{min}) \cdot D_{max}/\pi \qquad (6.10)$$

With the accessible q range between 0.3 and $5\,\text{Å}^{-1}$ at the free electron laser and 0.5 to $10\,\text{Å}^{-1}$ at the synchrotron in experiments used in this work, the amount of independent data points for the $6\,\text{Å}$ wide bimetallic complexes amounts to $\sim$18 at FELs and $\sim$36 at ID09. The data in this work is binned into 500 q-bins, which is an order of magnitude larger than these values. As such, the data can be interpreted as *oversampled*.

6.3.3 Confidence in fit parameters

Once parameters have been found for a model that minimizes Eq. 6.9 to a satisfying degree, an error has to be estimated to determine the confidence in a given set of fit parameters. They are commonly assessed in 1-σ to ... n-σ ranges, with the standard deviation σ, each of which being associated with an increased probability to measure a value with a normally distributed error around the expected value within its range. The 1-σ range, which is used in this work, encompasses $\sim$68.27 % of the probability. The Goodness-of-fit estimator χ^2 can be used to determine the confidence intervals of the model parameters. In this work, two primary techniques are used to derive uncertainty of the parameters, namely the Likelihood-method and the χ^2 convex-hull-method [75].

Likelihood-method

The relative probability P of a given set of parameters is given by Eq. 6.11. Fig. 6.3 A) depicts the determination of confidence intervals using this method, comparing the likelihood of the excited state platinum distance $d_{PtPt,ES}$ against the excitation fraction α in the transition metal complex PtPOP. The values are strongly correlated and as such the method yields large error bars. To assess a confidence interval, the probability is first calculated for a grid of N parameters each with M possible entries surrounding the most likely parameters determined by minimizing Eq. 6.9. The probability of this matrix is normalized to sum up to one. To obtain the confidence σ_i in a parameter a_i the normalized probability matrix is summed up along all axis except the one corresponding to the parameter
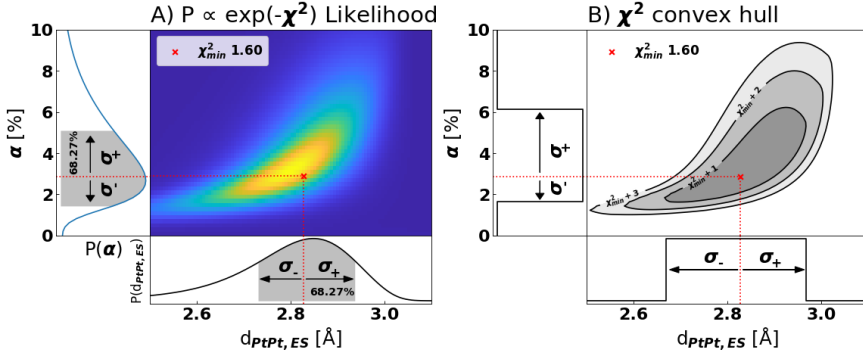
Figure 6.3: Assessment of the 1-σ confidence intervals for α and $d_{PtPt,ES}$ for PtPOP using A) a maximum Likelihood framework and B) a χ^2 convex hull method

a_i. The shortest range along the parameter range M_i that encompasses 68.27 % of the probability corresponds the 1-σ confidence interval. [75] This method has been established for the annalysis of XSS data for over a decade. [88]

$$P(a_1, a_2...a_n) \propto \exp\left(-\frac{\chi^2(a_1, a_2...a_n)}{2}\right) \qquad (6.11)$$

χ^2 convex-hull method

An additional method of determining confidence intervals for fit parameters using χ^2 is to use a constant χ^2 boundary. The confidence region is assessed as an N-dimensional ellipsoid in the M^N matrix, for which $\chi^2 \leq \chi^2_{min} + 1$, as shown in Eq. 6.12. This ellipsoid is projected onto each of the parameter axes. The confidence interval σ_i corresponds to the range of all entries along the parameter axis that contain at least one grid value inside the ellipsoid. Fig. 6.3 B) depicts the determination of confidence intervals using this method [75].

$$P(a_1, a_2...a_n) = \begin{cases} 0, & \chi^2(a_1, a_2...a_n) > \chi^2_{min} + 1 \\ 1, & \text{otherwise} \end{cases} \quad (6.12)$$

As shown in Fig. 6.3, both methods produce similar results for the same model. The main difference between them is the reduced dependence of the confidence interval on the size of the parameter space for the convex-hull method. The error bars determined with the likelihood method increase with an increasing parameter space, to encompass the necessary percentage generated by the improbable but non-zero outer space. The convex-hull on the other hand is immune to this. Both methods can be used to determine asymmetric error bars but have been used in symmetric approximation in this work.

Chapter 7

Bi-metallic complexes

There are two d^8d^8-complexes that will be discussed in this work, the tetrakis (diphosphito) diplatinate(II) anion $[Pt_2(H_2P_2O_5)_4]^{4-}$, from now on called *PtPOP*, and $Ir_2(1,8$-diisocyano-p-menthane$)_4]^{2+}$, from*IrDimen*. Each of them consists out of 2 metal ions of the platinum-group that are held together by bonding to each end of 4 ligands. Both of the structures are depicted in Fig. 7.1 as atomistic structures and as schematics describing the structural parametrization.

Both of these ligands have been, in addition to their photophysical and photochemical properties, investigated for their catalytic activity [89]. PtPOP has been demonstrated to dehydrogenate secondary alcohols $(CH_3)_2CHOH \xrightarrow[Pt_2]{\hbar\,\omega} (CH_3)_2CO + H_2$ [90, 91]. IrDimen has been shown to electro-catalytically reduce carbon dioxide $H_2O + 2e^- + 2CO_2 \xrightarrow[\text{IrDimen}]{} H_2 + 2CO_3^-$ [92]

The electronic structure of the complexes can be described by molecular orbital (MO) schemes, shown in Fig. 7.2. Panel A) depicts the electronic structure of PtPOP. The molecular orbitals are filled until the antibonding highest occupied molecular orbital (HOMO) $5d\sigma*$ orbital, resulting in no attractive forces between the platinum atoms. An excitation from the HOMO into the lowest unoccupied molecular orbital (LUMO) increases the bond order between platinum atoms, resulting in a contraction between them. Photons with higher energy can excite an electron from a lower lying orbital in a $d\pi p\sigma$ transition, also increasing the bond order [38].

Contrary to the rather stiff pyrphosphit ligands of PtPOP, the dimen ligands of the IrDimen are longer and more flexible. This stabilizes two ground state conformers in solution, a *long and eclipsed* and a *short and twisted* [94], shown in Fig. 7.2 B). The different structures exhibit a different HOMO-LUMO energy gap and can be preferentially excited with wavelength specific to their $d\sigma*p\sigma$ transition, highlighted by the red and blue arrows. The ratio of the two conformers is determined by a solvent dependent dynamic equilibrium. The complex can also be excited with a $d\pi p\sigma$ transition by a sufficiently large photon energy, resulting in excitation of both conformers [38, 95]. The absorption spectra for the HOMO-LUMO transition are depicted in Fig. 7.3 for both systems. The wavelengths associated with the transitions shown in Fig 7.2 are listed in Tab. 7.1.
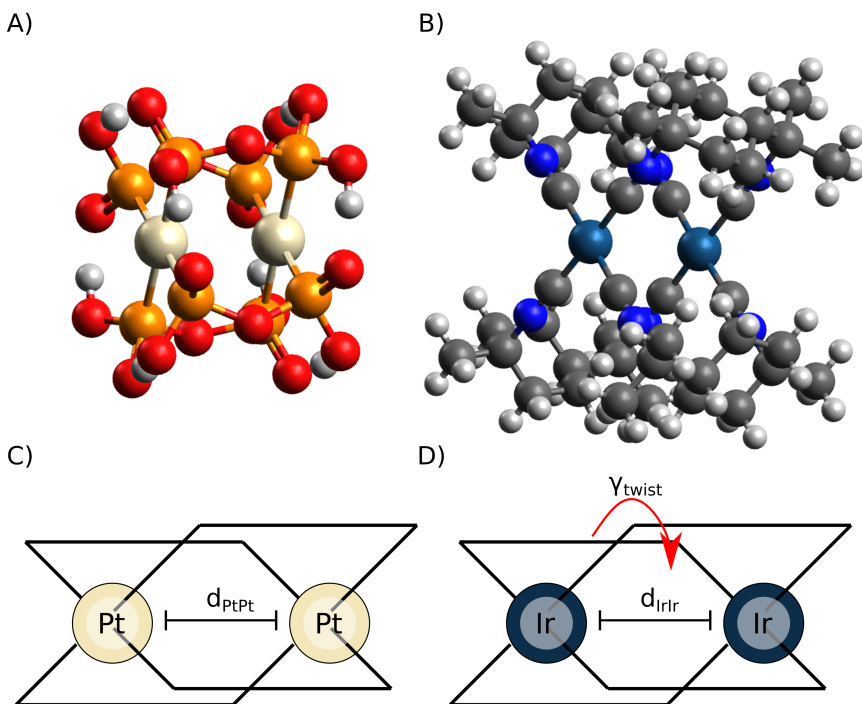
A)

B)

C)

D)

Figure 7.1: Molecular structure of A), C) PtPOP and IrDimen B),D). A) depicts the atomic structure of PtPOP, with C) depicting a simplified schematic reducing the ligand scaffolding to the bonding components and highlighting the d_{PtPt} axis. B) depicts the atomic structure of IrDimen with D) depicting the simplified sketch. The ligand scaffolding of the IrDimen has to be described with an additional parameter γ_{twist} parameterizing the adjustment of the flexible ligand reacting to changes in d_{IrIr}. The atomic structures were made using Avogadro [93]
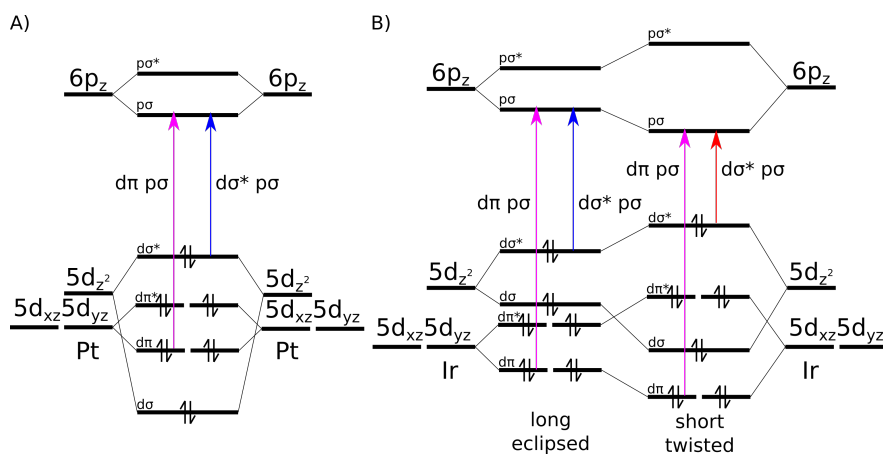
.

Figure 7.2: Molecular orbital schemes of PtPOP A) and IrDimen B). The more flexible dimen ligand stabilizes two ground state conformers in solution, one with a longer d_{IrIr} and one with a shorter d_{IrIr} and ligand scaffold twisted to accommodate the stress. Both complexes undergo a $d\sigma*p\sigma$ transition when excited with visible light, regardless of conformer. Additionally, a $d\pi p\sigma$ transition can be excited with UV-light. Adapted from [38] with information from [95,96].

Table 7.1: Absorption and emission spectra of PtPOP and IrDimen. The $d\sigma*p\sigma$ numbers correspond to the maxima of the broad peaks. The numbers in parenthesis correspond to spin forbidden transitions into the triplet state.

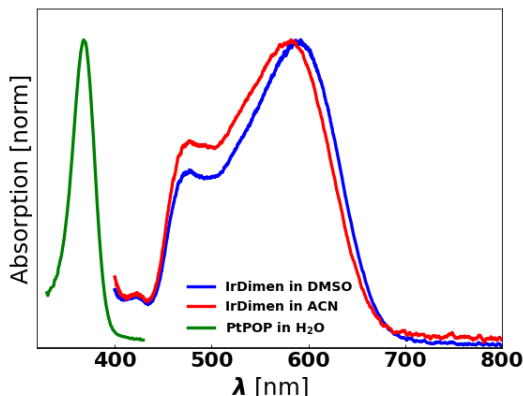|	PtPOP	IrDimen long, eclipsed	IrDimen short, twisted
Absorption [nm]			
dσ*pσ	368, (452) [44]	480 [95]	585 [95]
dπpσ	284, (315) [96]	316 , (375) [95]	316, (375) [95]
Emission [nm]		*(only 1*	*conformer)*
Flour.	400 [44]		
Phos.	513 [44]	710 [94]	

60

Figure 7.3: Absorption spectra of PtPOP in H_2O and IrDimen in ACN and DMSO. The peaks correspond to the dσ*pσ transitions in Tab. 7.1 Both the structures and the ratio between the two ground state conformers is solvent dependent, resulting in a solvatochromatic effect shifting both the peaks and the ratio. The flatter ground state potential surface of IrDimen results in the much broader peaks in comparison to the PtPOP.

Both of these complexes have been studied previously in X-ray solution scattering experiments investigating their structure [76, 88] and dynamics [77, 97]. With the recent and still ongoing improvement of X-ray sources, such as the upgrade to the *Extremely bright source* (EBS) at the ESRF and the upgrade towards LCLS-II, these compounds are once more subject to investigation to exploit these new beam properties to investigate fundamental phenomenons that could not be resolved previously. Among these are the structural changes potentially induced by intersystem crossing and the shape of the parameter distribution in oscillations following photoexcitation, which well be discussed in this chapter.

7.1 Ultrafine structural refinement of IrDimen

During the ongoing Extremely Brilliant Source (EBS) upgrade at the ESRf the properties of the electron bunches used for the time-resolved scattering experiments at ID09 was improved in several ways. This improvement

results among other things in a considerable reduction of the spectral width from the undulator radiation.

These new beam properties allow for more precise measurements especially at higher q values where the signal was previously smeared out by the beam spectrum and as such limiting the structural resolution. This can be used to gain additional insights into previously well studied systems, such as IrDimen, where the structural details and mechanisms guiding the intersystem crossing from the excited singlet state formed after photoexcitation into the long-lived triplet state are still unknown.

The intersystem-crossing process takes place on a timescale of 70 ps [98] with a quantum yield of almost unity. The energy rich singlet state can, as discussed by Durell et al. [99], be considered a precursor state in photochemical reactions. In similar Ir_2-complexes the reactivity has been observed to differ based on the spin-state of the complex. So far, the S_1 and T_1 were assumed to have the same distance between the Iridium atoms of ~ 2.90 Å [77], based on experiments on other $d^8 d^8$-complexes [38]. However, new density functional theory calculations suggested that the ISC would be associated with a further contraction of 0.04 Å. Establishing this connection between spin state and structure could lead to a better understanding of the $d^8 d^8$-complexes class as a whole.

The small structural change results in a small change in difference scattering signal, which would have been difficult to measure with the old beam profile of the ESRF. Fig. 7.4 A) shows the comparison of the old and the new beam profile after the EBS upgrade. The simulated difference scattering signals between the 3.6 Å and the S_1 and T_1 are depicted in Fig. 7.4 B) for the old beam profile and new beam profile are depicted as well as the range accessible when using 19 keV and 24 keV photons. The contraction of d_{IrIr} by 0.04 Å alters the shape of the difference scattering signal the strongest for q >8 Å^{-1}, which can be resolved with 19 keV photons of the new spectrum at commonly used angles of $2\theta \leq 65 \deg$. Increasing the photon energy up to 24 keV would result in the detection of an additional oscillation in the difference scattering signal, potentially improving the identification of the exact distance even further.
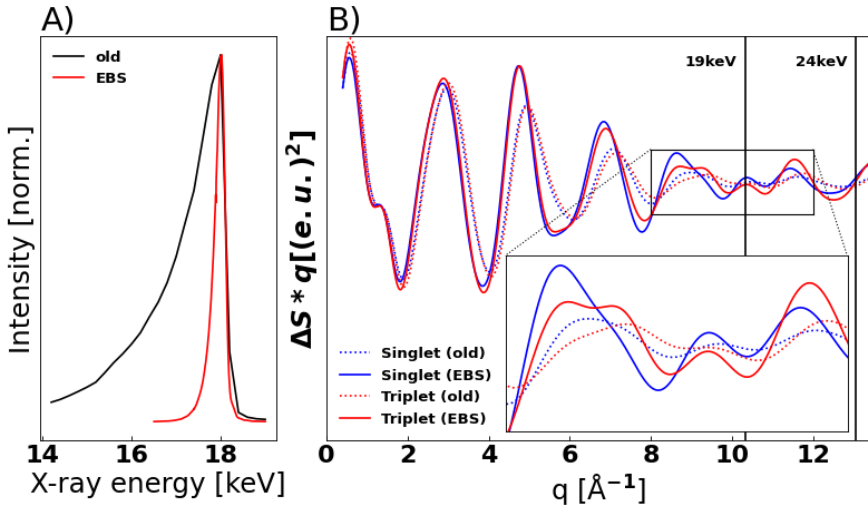
Figure 7.4: Comparison between old and new beam profile A) and a comparison between the difference scattering signals with the old and new beam profile B) for a contraction from the short ground state to the excited state of IrDimen.
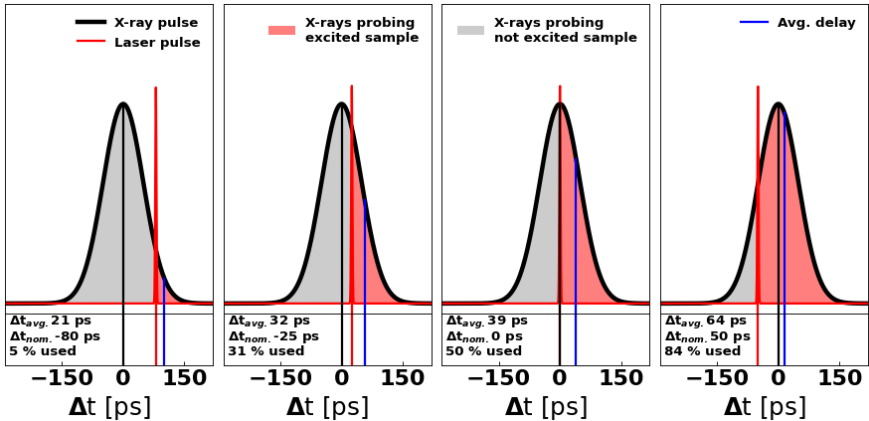

Figure 7.5: Time-slicing. The picosecond laser pulse in temporally positioned inside the much longer X-ray pulse. The X-ray pulse probes the sample primarily shortly after the laser pulse, as such a time resolution faster than the X-ray pulse duration can be reached, albeit of the cost of a worse signal to noise ratio. Adapted from [76].

7.1.1 Time-slicing

The lifetime of the IrDimen S_1 is, as previously discussed, 70 ps and as such similar to the temporal pulse width available at the contemporary synchrotron light sources, which is usually the limiting factor in the time-resolution. The time resolution, however, can be improved by using the so-called time slicing scheme, previously successfully applied at ID09 [76], which provides a time resolution of $\sim$20 ps.

The technique uses the smaller temporal width of the pump laser pulse, about $\sim$2 ps, to increase the available time resolution. The process is depicted in Fig. 7.5. The pump laser pulse is temporally positioned inside the X-ray pulse. This causes the X-ray pulse to only partially probe excited sample, and primarily temporally shortly after the photoexcitation. The average time delay of the probed sample t_{avg} can be calculated by forming the weighted average of the share of the x-ray pulse until the nominal time t_{nom}.

As only part of the X-ray pulse is used to probe the excited state sample, the overall signal-to-noise ratio measured is proportionally less than when measuring with the entire X-ray pulse. This must be compensated for by with increased integration times during the experiment.

7.1.2 Experimental parameters

This calculated contraction during the intersystem crossing of IrDimen was investigated with TR-XSS at ID09 at the ESRF in July of 2021 with the experiment number CH6002. The 652 nm laser was ovally shaped at the sample position with a vertical FWHM of 331 μm and a horizontal FWHM of 230 μm. The liquid jet ran at 0.873 m/s, or 885 μm between X-ray pulses, ensuring the replenishing of sample between measurements. The X-ray pulse was focused down to 25 x 25 μm. The sample was prepared was 6 mM solution, obtained by dissolving dimen and [Ir(1,5-cod)Cl]$_2$ in either acetonitrile (ACN) or dimethyl sulfoxide (DMSO).

The solvent heat responses of ACN was measured during the same beamtime measuring the heat released by a 5.13 mM solution 4-(N,N-diethylamino)-2-methoxy-40-nitro-azobenzene after photoexcitation with a 400nm laser. The dye releases its energy fast into the solvent as discussed
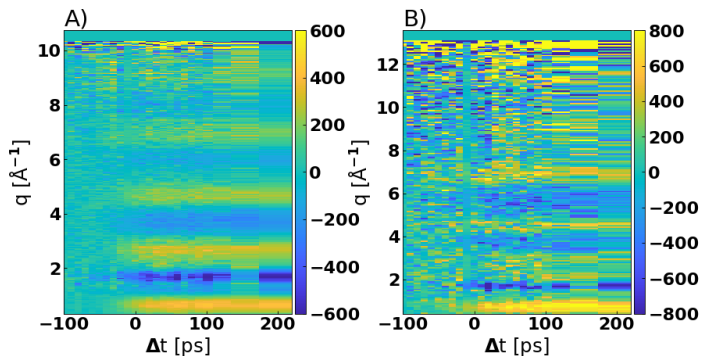
Figure 7.6: ΔS q colormaps of IrDimen in acetonitrile at A) 19 keV and B) 24 keV. The increase in photon energy increase the available q-range from <10 to $<12.5\,\text{Å}^{-1}$.

by Kjaer *et al.* [100]. The DMSO heat signal was measured as a 0.67 mM solution of 4-bromo-40-(N,N-diethylamino)-azobenzene in DMSO during the CH6318, *Solvation cage structures of aqueous iodide*, experiment in March of 2022. The measured $\Delta S_{Heat,ACN}$ was scaled in magnitude to the results from Kjaer *et al.*, allowing the extraction of ΔT from the fit parameter. There was no comparable reference for $\Delta S_{Heat,DMSO}$, which prevented a quantitative assessment of the dissipated heat in the DMSO sample.

7.1.3   Acquired data

The collected and reduced time-resolved data is depicted in Fig. 7.6. Panel A) shows the 19 keV and panel B) the 24 keV data of IrDimen in acetonitrile. The accessible q-range for 19 keV was 0.7 to $10\,\text{Å}^{-1}$, extending up to 12.5^{-1} for the 24 keV measurement.

As discussed in sec. 7.1.1, In addition to the fine temporal resolution shown in Fig. 7.6, specific delays were chosen to represent the structure of the triple state T_1, $\Delta t_{nom.} \geq 200$ ps ($\Delta t_{avg.} = 200$ ps), and the singlet state S_1, $\Delta t_{nom.} = 0$ ps ($\Delta t_{avg.} = 39$ ps), where around 57 % of molecules should still be in the S_1 state. These two states were the only delays measured for the DMSO sample. These delays were integrated for considerable longer
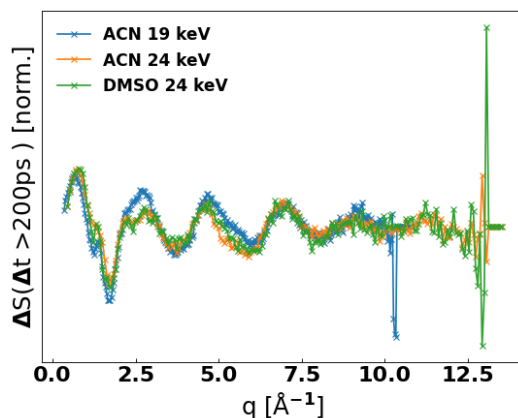
Figure 7.7: $\Delta S(T_1)$ of IrDimen in ACN and DMSO, measured with 19 keV photons and 24 keV photons. The measurements with 24 keV exhibit strong similarities to one another despite the different solvents. They differ from the 19 keV, specifically turning the peak at $\sim 2.7\,\text{Å}^{-1}$ into a double peak and in the shape of the peak at $4.5\,\text{Å}^{-1}$, suggesting am impure beam spectrum in the 24 keV measurement. The increased photon energy resolves signal until $12.5\,\text{Å}^{-1}$, resolving an additional oscillation in the difference scattering signal.

times among the entirety of measured delays shown in Fig. 7.6. Fig. 7.7 depicts the $\Delta S(T_1)$ of the measurements. Both of the 24 keV measurements appear similar in shape and differ from the 19 keV the strongest at the peak at $2.7\,\text{Å}^{-1}$, which splits into two for the 24 keV measurements, and the change in peak shape at $4.5\,\text{Å}^{-1}$. This suggests the presence of another wavelength in the 24 keV probe pulse spectrum.

7.1.4 Structural refinement 19keV

The structure of the IrDimen was optimized by optimizing Eq. 6.5 with the structural parameters shown in Fig. 7.1. The Iridium atoms were constrained to symmetric positions along the symmetry axis. The ligand scaffolding was taken from a structural matrix of DFT optimized structures, where the structure was relaxed for a range of Iridium distances and ligand scaffolding twists for both the ground and excited state. The matrix contains structural information for a grid of $2.5 < d_{IrIr} < 5.5\,\text{Å}$ and

$0 < \gamma < 45\,°$. The matrix was used in previous studies of IrDimen, where the computational details are discussed in detail [77]. The angular twist of the long ground state was fixed to $0°$. The solute scaler α_{long} and α_{short}, the temperature ΔT and the solvation cage scaler ϵ were free parameters in the fit. An uncertainty of $0.2\,\text{Å}$ was used in the scattering cross-term between ligand scaffolding and metal atoms according to Eq. 4.8 to simulate the flexibility, resulting in a distribution of structures, in the ligand scaffolding.

The most likely ligand structure strongly depended on the choice of self-normalization interval chosen during the data reduction. The data at present was reduced by normalizing all images between 3.25 and $7.5\,\text{Å}^{-1}$, for which a simulation of the difference scattering curve using the parameters from van Driel *et al.* [77] predicted a net difference scattering signal of zero in the interval ($\int_{q1}^{q2} \Delta S_0 = 0$). Data sets with different self-normalization intervals had yielded physically implausible larger contractions in the short ground state γ_{short} that the excited state γ_{ES}

The best possible fit achieved by the structural refinement of $\Delta S(T_1)$ is depicted in Fig. 7.8, with the structural parameters being listed in Tab. 7.2. The fit captures the structural signal well until the peak at $\sim 7\,\text{Å}^{-1}$, where the fit quality decreases. The fitted distances of $d_{IrIr,long}$ $4.45\pm0.13\,\text{Å}$, $d_{IrIr,short}$ $3.76 \pm 0.09\,\text{Å}$ and $d_{IrIr,ES}$ $2.91 \pm 0.03\,\text{Å}$ are slightly longer than previous studies ($d_{IrIr,long}$ $4.3\,\text{Å}$, $d_{IrIr,short}$ $3.6\,\text{Å}$, $d_{IrIr,ES}$ $2.90\,\text{Å}$) [101]. The twist angles of γ_{short} $16\pm13\,°$ and γ_{ES} $20 \pm 10\,°$ are slightly larger than previous results (compared to $15\,°$ $d_{IrIr,ES}$ and $<5\,°$ γ_{short}) [77]. There was no heat signal detected during the fitting. The small energy dissipation suggests that multi-photon excitation events were minimal.
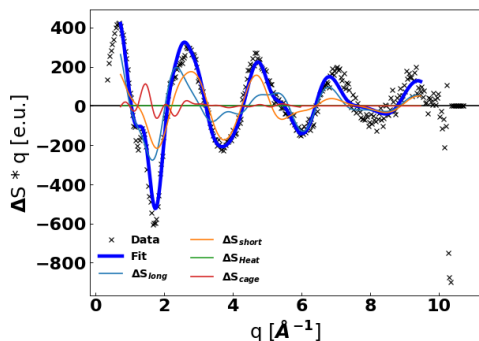
Figure 7.8: Fit used for the structural refinement of $\Delta S(\Delta t=200\text{ps}, q=0.7\text{-}9.5)$ according to Eq. 6.5. The oscillations until $7\,\text{Å}^{-1}$ are matched well by the fit, the fit quality decreases towards larger q-values. The heating component, measured in the same experimental setup, was not picked up by the fit.

Parameter	Value
$d_{IrIr,long}$	4.45 ± 0.13 [Å]
$d_{IrIr,short}$	3.76 ± 0.09 [Å]
$d_{IrIr,ES}$	2.91 ± 0.03[Å]
α_{long}	4.8 ± 0.1 [%]
α_{short}	4.8 ± 0.1 [%]
γ_{short}	16 ± 13 [°]
γ_{ES}	20 ± 10 [°]

Table 7.2: Structural parameters of the fit depicted in Fig. 7.8

This structural information about the ground state composition and structure obtained from the $\Delta S(T_1)$ optimization was used to refine the structure of the complex for every measured time delay. $d_{IrIr,long}$, $d_{IrIr,short}$, γ_{short} and γ_{ES} as well as the ratio between α_{long}, α_{short} and β cage were constraint to the values determin in Fig. 7.8. $d_{IrIr,ES}$ and the scaler α scaling the total solute scaler were optimized for each time step. The extremely large error-bars on the scaffolding twists γ made further time-resolved structural refinement of the ligand scaffolding unfeasible. The results of the structural optimization are depicted in Fig. 7.9. Panel A) depicts $d_{PtPt,ES}$ and the associated error. The black line corresponds to $d_{IrIr}(T_1)$. The solute scaler α, normalized to α_{T_1}, shown in B), follows the instrument response function dominated by the X-ray pulse length. The fit of $\alpha(t)$ with an error function yielded an X-ray pulse width of 66 ± 6 ps, which is well in line with previous investigations at the beamline.

The most likely $d_{IrIr,ES}$ for $\Delta S(S_1)$ and $\Delta S(T_1)$ are listed in Tab. 7.3. $d_{IrIr,ES}$ decrease with increasing Δt, but not larger than the error associated with each of the values. In both cases the error is, for the measurement points that have not received integration time, notably larger
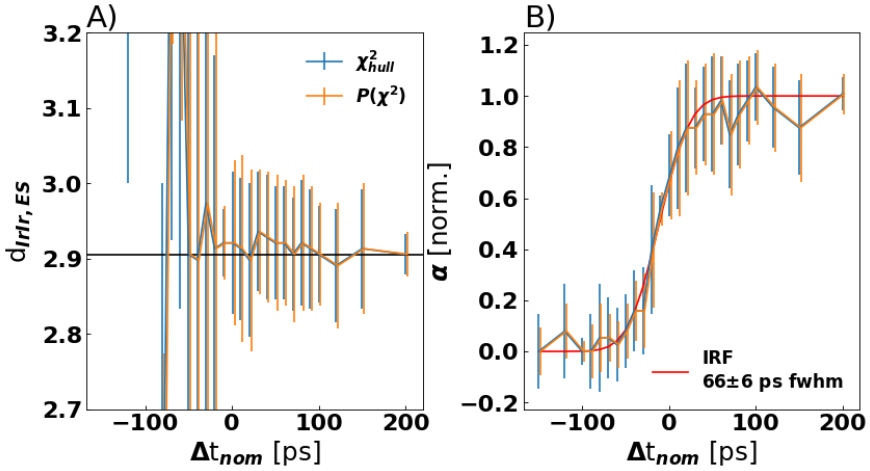
Figure 7.9: Certainty of structural parameters for A) $d_{IrIr,ES}$ and B) α. Both the likelihood and the χ^2 method have been used, yielding similar results.

Table 7.3: Structural parameters of the intersystem crossing of IrDimen in ACN, measured at 19 keV. Both error bar determination methods yield the same result when considering significant digits.

state	distance [Å]
$d_{IrIr,Es}$ (S_1)	2.92±0.05 Å
$d_{IrIr,Es}$ (T_1)	2.91±0.03 Å

than the actual spread of point, notably between 0 and 100 ps. This suggests that the uncertainty associated with each of the parameters is an overestimation.

The structural optimization of the 19 keV did not yield a contraction during the intersystem crossing larger than the confidence interval. In the next step, the same data analysis will be applied to the 24 keV measurements, to see if the additional q-range can be used to improve the structural precision.

7.1.5 Structural refinement 24keV

As discussed in sec. 7.1, access to higher q-values through the use of higher energy photons could improve the structural resolution during the analysis. The measured ΔS at 24 keV was shown in sec. 7.1.3. The change in the observed peak shape in between the 19 keV and the 24 keV measurements suggested that the 24 keV measurements contain significant amount of scattering from a different wavelength. A single peak splitting up into a double peak would not be expected from a simple increase in bandwidth, which would simply smear out features. The 24 keV photons are generated by using the third harmonic from the u27 undulator according to Eq. 4.14. This results the 8- and 16 keV first and second harmonics as expected continuations in the spectrum, which were intended to be suppressed with a 1.5 mm thick diamond window. The improvement of the source during the EBS upgrade has reduced the contamination of the second harmonic, which suggested the possibility of this high energy TR-XSS experiment.

   The actual share of scattering signal per wavelength was assessed by scaling contributions of 8, 16, and 24 keV to the measured signal. The contributions were calculated by taken the $S(q, 19\,keV)_{Sample}$ and interpolating it to match the $S(2\theta, n\,keV)_{Sample}$ of 8, 16 and 24 keV. The fit of the total measured scattering signal with these 3 simulated components is depicted in Fig. 7.10. The share of each of the contributions is tabulated in tab 7.4. The model suggests that 19.7 % of the scattering signal can be attributed to 16 keV photons and a potentially negligible amount of 8 keV scattering (1.4 %). The distribution of share in the scattering signal does not equivalate to the number of photons scattered at the sample, as the detector absorption efficiency decreases towards higher energies and detected signal magnitude per photon depends on the individual photon energy [67]. The composition of the of the 24 keV and the possibilities of improving the spectral purity will be further discussed in sec. 7.1.7.
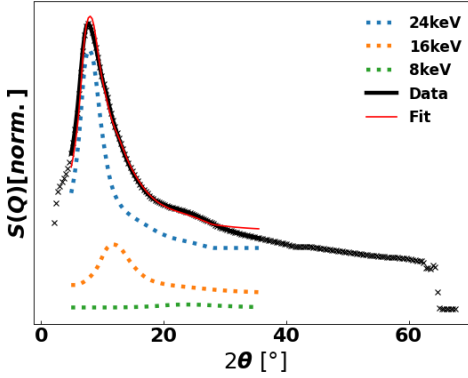
E [keV]	$n_{photons}$
8	1.4[%]
16	19.7[%]
24	78.9[%]

Figure 7.10: Determination of the composition of the 24 keV beam. The absolute scattering of the 19 keV IrDimen in ACN measurement is scaled to match the $S(2\theta)$ of the 8-, 16- and 24 keV modes of the u27 undulator. These 3 components are used to fit the measured azimuthal integrated S(q).

Table 7.4: Beam composition of the 24 keV beam according to Fig. 7.10. In total 21.1% of the photons are not from the target energy of 24 keV

This information about the spectral composition is then used to calculate the scattering components used in the modeling according to Eq. 6.5, as described for the 19 keV data. The individual components were calculated or interpolated to match the $S(2\Theta)$ curve represented by the q-axis. The q-axis is however only defined for a single wavelength. To maintain comparability, the q-axis for the 24 keV photons is used going forward, even if the signal and model contains contributions from different wavelengths. The fit of the structural optimization is depicted in Fig 7.11, with the results listed in Tab. 7.5. The d_{IrIr} parameters are similar to the ones determined in the 19 keV analysis, but γ presents an unphysical further twisting of the ground state than the excited state.

Table 7.6: Structural parameters of the intersystem crossing of IrDimen in ACN, measured with 24 keV photons.

state	distance [Å]
$d_{IrIr,Es}$ (Singlet)	2.93±0.07
$d_{IrIr,Es}$ (Triplet)	2.93±0.03
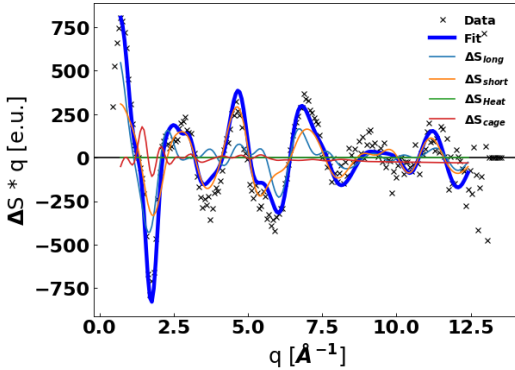
Figure 7.11: Fit used for the structural refinement of $\Delta S(\Delta t=200\,ps, q=0.7\text{-}12.5)$ according to Eq. 6.5. Sample was IrDimen in ACN measured with the 24 keV beam. The oscillations until $8\,\text{Å}^{-1}$ are matched well by the fit, the noise increases towards higher q considerably. The heating component, measured in the same experimental setup, was not picked up by the fit.

Parameter	Value
$d_{IrIr,long}$	4.52±0.11 [Å]
$d_{IrIr,short}$	3.76 ±0.09 [Å]
$d_{IrIr,ES}$	2.93 ±0.02 [Å]
γ_{short}	24 ± 12 [°]
γ_{ES}	16 ± 8 [°]

Table 7.5: Structural parameters of the fit depicted in Fig. 7.11

These ground state parameters were used to determine the most likely $d_{IrIr,ES}$ for all measured delays. The results are depicted in Fig. 7.12 A). The solute scaler α and their uncertainty are depicted in B), exhibiting a much larger spread than the 19 keV measurement. The error determined for the parameters for delays with low integration time greatly exceed the actual spread of the values, suggesting that the error might be assessed too high.

The values for then $\Delta S(S_1)$ and $\Delta S(T_1)$ are listed in tab 7.6. In this analysis, the two states have identical distances.
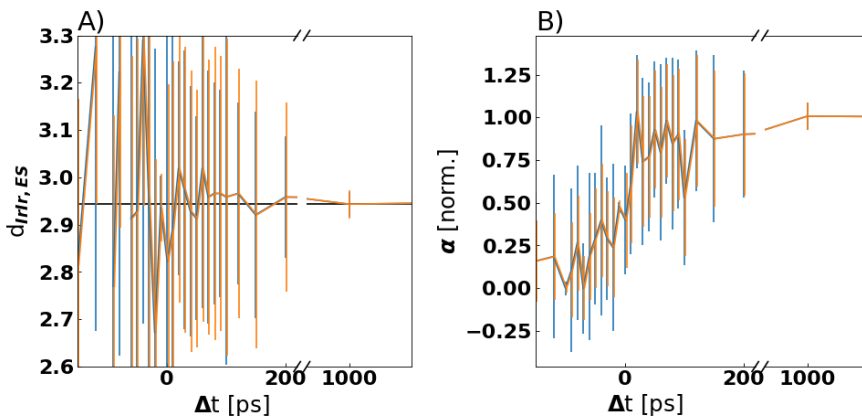
Figure 7.12: Certainty of structural parameters for A) $d_{IrIr,ES}$ and B) α for IrDimen in acetonitrile measured at 24 keV. Both parameter curves are associated with error bars much larger than the actual spread of the values for positive time delays.

In the end, the 24 keV measurement in IrDimen did not yield an improvement of the structural resolution and as such did not confirm the contraction upon intersystem crossing either. As shown in sec. 7.1.3, an additional measurement was done of IrDimen in DMSO. Given that the integration time of that experiment was less than the IrDimen in ACN sample, the resolution of the intersystem crossing is unlikely. The sample does exhibit a solvatochromatic effect as shown in Fig. 7.3. This change in absorption wavelength at the 580 nm peak could be reflected in the structural parameters.

7.1.6 Structural refinement of IrDimen in DMSO

The ΔS(Triplet) data was fitted, identical to the previous section and using the spectral distribution of the 24 keV beam determined in sec. 7.1.5. The result is depicted in Fig 7.13 with the structural parameters listed in tab 7.7. The data could not be scaled to the liquid unit cell as no reference was available to scale the total scattering of DMSO.
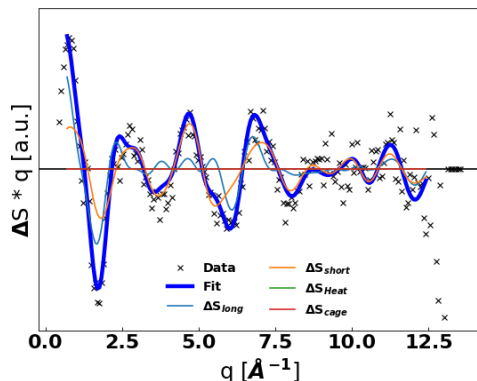
Figure 7.13: Fit used for the structural refinement of $\Delta S(\Delta t=200ps, q=0.7-12.5)$ according to Eq. 6.5. Sample was IrDimen in DMSO measured with the 24 keV beam. The oscillations until 8 Å^{-1} are matched well by the fit, the noise increases towards higher q considerably. No ΔS_{heat} or ΔS_{cage} was used.

Parameter	Value
$d_{IrIr,long}$	4.54±0.15 [Å]
$d_{IrIr,short}$	3.67 ±0.13 [Å]
$d_{IrIr,ES}$	2.93 ±0.06[Å]
γ_{short}	32 ± 12 [°]
γ_{ES}	16 ± 10 [°]

Table 7.7: Structural parameters of the fit depicted in Fig. 7.13

The $d_{IrIr,long}$ 4.54±0.15 Å and $d_{IrIr,ES}$ 2.93±0.06 Å are very close to the distances found in the acetonitrile measurement (4.45±0.13 Å and 2.91 ±0.03 Å). $d_{IrIr,short}$ is contracted to 3.67 ±0.13 Å (from 3.76 ±0.09 Å). The shorter distance could explain the absorption peak at longer wavelengths in DMSO, as shown in Fig. 7.3, as the ground state structure becomes more similar to the excited state structure in this solvent.

7.1.7 Investigation of the high-energy capabilities of ID09

Following the analysis results discussed in sec. 7.1.5 and sec. 7.1.6 of measurements using the 24 keV beam, the question was raised whether high energy TR-XSS experiments could be conducted with a beam of improved spectral purity at ID09. Despite considerably longer integration times, the data measured with 24 keV remained noisier than the 19 keV dataset, shown in Fig. 7.8 and Fig. 7.11. The individual integration times of the data sets are listed in tab 7.8. The presence of photons of another wavelength, in this case 16 keV, altered the shape of the difference scattering

Table 7.8: Integration times at ID09 for the different experiments of this chapter

Sample	n_{images}	$t_{integration}$
IrDimen in ACN 19keV	3755	10.6 h
IrDimen in ACN 24 keV	8705	24.6 h
IrDimen in DMSO 24 keV	3148	8.9 h

signal and, while not making the data uninterpretable, may have reduced the information content of the signal.

Simulation of the signal

To further analyze the spectral output the 24 keV beam profile of the setup was simulated using the software *XOP* [102] with the help of Michael Wulff, *Beamline Responsible* at ID09. Fig. 7.14 A) shows the result of this simulation at the undulator position and the sample position. Between the generation of the X-rays and the sample location, the beam was attenuated by 0.2 mm of beryllium and 1 mm of diamond, attenuation intrinsic to the beamline originating from windows that are used to maintain vacuum in the electron storage ring and the experimental hutch 1, and an additional 1.5 mm of diamond that was inserted into the beampath to attenuate X-rays of lower energies.

The 8 keV photons are very strongly attenuated by 96 %, but do show up in the spectrum as previously suspected from the analysis results. The 16 keV photons are attenuated by 38 %, the 24 keV photons are attenuated by 30 %. Because of the decreased detection probability of the detector for higher photon energies photons, photons of lower energies contribute disproportionally to the detector signal in relation to their number. This simulation confirmed that the measured spectral composition of the beam was indeed in line with the expected spectrum of the electron beam and not indicative of any misalignment of material problems that could have led to a relative amplification of the 2nd harmonic.
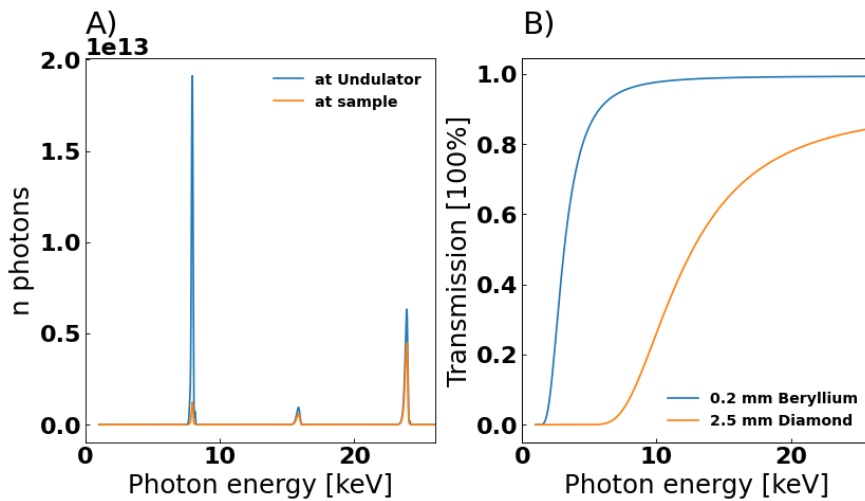
Figure 7.14: Simulated spectrum of the 24 keV beam generated by the third harmonic of the u27 undulator. A) depicts the simulated spectrum both during generation and at the sample location. B) depicts the major optical components in the beampath used to remove photons of undesired energy. 0.2 mm beryllium and 1.0 mm diamond are intrinsic to the beamline setup, 1.5 mm additional diamond was used as a filter for lower energy photons, as was done in the experiment. Simulation was done using the *XOP* [102] software with the help of Michael Wulff.

Beamline monochromators

As discussed in sec 5.1.1, the beamline has monochromators installed that can be used to further trim down the spectrum of the beam to generate pulses of photons with a single beam energy. A silicon monochromator is located in the experimental hutch 1 which is often used to scan the energy distribution of the beam. The beam is diffracted between two silicon crystals, in a way where only a single wavelength matches the Bragg condition, suppressing all other wavelengths. As the selectivity of the crystal is $\Delta E/E$ is $1.4e^{-4}$, the reduction in flux makes the application in TR-XSS experiments unfeasible. The fine selection of wavelengths however can be used to scan the transmissive properties of components further down the beam path.

Additional to this setup there are two multilayer monochromators, one using Ruthenium (Ru-ML) for lower energies and one using Tungsten (W-ML) for higher energies, and another crystal monochromator using Germanium in the experimental hutch 2. Rather than reflecting on crystal planes, the beam is reflected on the planes of the individual layers of the material, which are coated in an alternating way. The selectivity of multilayer systems $\Delta E/E$ is commonly 1-3 %, a factor of 100 larger than crystal monochromators.

Fig. 7.16 depicts the result of this investigation of the W-multilayer monochromator. The signal magnitude was scanned using the silicon monochromator measuring the transmitted intensity with and without the multilayer using a diode. The flux decreases at the peak at 24 keV by about 56 %, and in total the flux is decreased by 65 %. The multilayer removes the tail toward shorter energy, resulting in a more symmetric energy profile after the filtering.

Flux Comparison

In a secondary step the actual photon flux was determined by comparing number of photons detected by the detector in a given configuration. The experimental setup is depicted in Fig. 7.15 B). The ESRF synchrotron was operated in *continuous* mode during the flux measurements. As a result no single pulse could be selected and the pulse was defined by the 300 ns
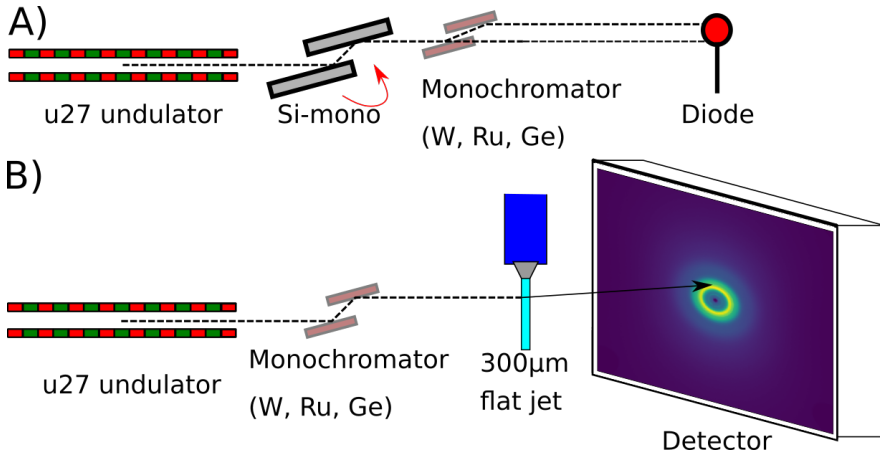
Figure 7.15: Simplified measurement setup for flux investigation at the ID09. A) depicts the setup for the measurement of the reflectivity of the monochromators in EH2. The silicon monochromator with its fine resolution is used to first scan the number of photons passing through the Si-mono for each wavelength, and then again after the insertion of a monochromator. The flux is recorded with diode. B) depicts the setup for the measurement of the flux using a liquid sample. The X-rays, filtered by the monochromator or not, scatter on the liquid jet. The flux is calculated through the magnitude of the scattering signal.
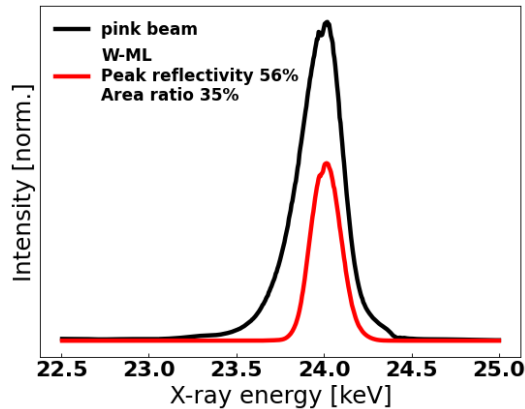

Figure 7.16: Comparison of signal shape and magnitude before and after filtering with the W-multilayer. The W-MI suppresses all photons of lower energy, but reduced the photon flux of the desired energy at 24 keV by about 65 %.

Table 7.9: Photon flux statistics measured in various configuration at the ID09 beamline for 18 keV and 24 keV

	18 keV	notes	24 keV	notes
Pink beam	3.5e9		6.6e8 (+3.3e8 16keV)	
Multilayer	1.6e9	Ru-ML	2.3e8	W-ML
Ge-Mono	5e7			

selection window of the high speed chopper. The X-rays that were used for the probing thus originated from $355000\,\text{Hz}\cdot300\text{e}^{-9}\,s\cdot200\,\text{mA} = 21.3\,\text{mA}$, instead of the 4 mA that were available from the single pulse during the IrDimen experiment discussed in sec. 7.1.4. The flux determined here are as a result a factor 5 larger than what would be available at a picosecond resolved experiment at ID09.

The flux can be determined by comparing the corrected detector and azimuthally integrated measured detector image to Eq. 4.6. The X-ray beam pathing through the 300 μm liquid water jet scatters on the equivalent of N_α 3.2e20 water molecules. The results of this analysis are tabulated in Tab 7.9 for 18 keV and 24 keV. The flux of the 18 keV, generated with the u17 undulator, is used as a reference in the pink beam configuration, as it is the standard X-ray solution scattering wavelength used at the beamline. In direct comparison, a switch to 19 keV reduced the flux by about 40 %. The Ruthenium-multilayer reduces the flux by a factor of 2, and the Germanium monochromator by a factor of 100. As shown in Fig. 7.4, the pink beam already has a narrow energy distribution since the EBS upgrade. As a result, neither options are likely to be useful for solution scattering experiments at that wavelength.

The flux of the 24 keV photons in the "pink beam", attenuated by 1.5 mm of diamond, is around a factor of 5 lower than the 18 keV reference. The reduction of photons by an additional factor of 3 is in good agreement with the reflectivity results shown in Fig. 7.16. The overall flux reduction is in good agreement with the results shown in sec. 7.1.5, where the 24 keV measurement appeared considerably more noisy despite longer integration times. The results show that the usage of higher energies from the u27 undulator is unfeasible for TR-XSS at ID09, due to the one order of magnitude reduced flux.

7.1.8 Conclusions

The recent EBS upgrade has brought a considerable improvement to the spectral purity of the beam both for the u17 undulator, providing photon energies up to 19 keV, and reducing the contribution from the second harmonic of the u27 undulator, where photons with energies up to 25 keV can be generated.

The improved spectral resolution and accessible q-range highlights problems modeling not observed in previous studies, where a considerably broader spectrum was used to measure in a small q-range. The ligand scaffolding in particular needs an improved description for ultrafine structural refinement such as this. The ligand scaffolding was approximated for each angle with a single structure, and disorder in the ensemble was simulated using an uncertainty u_{Ligand}. In practice, the uncertainty will not be identical for each of the ligand atoms, but instead be comparatively small for the cyanide groups bonding to the Iridium atoms and larger for the organic ring further apart. Overall, the signal at higher q appeared more structured than the measured data as a result of this.

An improvement to the modeling may be, instead of calculating the scattering signals from a fixed or blurred structures, to describe the distributions of interatomic distances with radial distribution functions using Eq. 4.9, possibly obtained from QM/MM MD simulations

An additional problem has shown to be the choice of normalization interval. If $\int_{q1}^{q2} \Delta S_0 \neq 0$ in the self-normalization interval, an image from unexcited sample will receive a different scaler in the self-normalization than otherwise identical excited sample when measured with identical X-ray pulses. While specific limits can be found to normalize a single defined excited state and ground state correctly, a single range is unlikely to be of equivalent quality for an entire range of signals arising from a time-evolution. Complimentary diodes or machine parameters measuring the beam intensity independently might be an option to address this problem.

The photon flux of 24 keV photons without suppression of the 16 keV mode is not sufficient for solution scattering experiments. The additional $\sim 2\,\text{Å}^{-1}$ come at the cost of considerably longer integration times, as shown in Tab. 7.8, and did not improve the structural resolution. Further suppression of the 16 keV mode reduces the amount of 24 keV by a factor

of 3, making very high energy X-ray solution scattering experiments at the ID09 unfeasible for the foreseeable future.

7.2 Transition dependent photodynamics in IrDimen

The dynamics following a photoexcitation depend on the induced electronic electronic transition and subsequent electronic structure. As shown in Tab. 7.1, the complexes IrDimen and PtPOP exhibit different optical transitions resulting in different electronic states following photoexcitation. Any excitations into energetically higher states are expected to relaxate within a few picoseconds into their lowest energetic state of their multiplicity, the Singlet S_1 or the the Triplet T_1. The dynamics of the structure until this point are however guided by the electronic state induced by the photoexcitation.

   This section will investigate this phenomenon by comparing two measurements of IrDimen in acetonitrile. In the first measurement the sample was excited with 400 nm photons, inducing a ^{3}dπdσ. In a subsequent experiment to study the distribution of structures following photoexcitation, IrDimen was measured with 480 nm laser inducing a ^{1}dσ*pσ transition from the HOMO into the LUMO. This resulted in a unique opportunity to compare the dynamics following a different electronic transition in the system. Previous TR-XSS experiments had also been conducted with 400 nm [101], but, as they were conducted at a synchrotron source, did not have the necessary time resolution to observe changes on the femtosecond scale.

   Fig. 7.17 highlights the excitation wavelength dependent electronic excitations in the complex. Excitation with 480 nm and 585 nm preferentially photoexcites the long and short conformer respectively into a high vibrational mode of the lowest lying singlet state ^{1}dσ*pσ. Excitation with higher photon energies, however, induces dπpσ transitions into a manifold of high-lying electronically excited states [95]. This manifold is not expected to maintain coherence within the distribution of d$_{IrIr}$ within the excited state ensemble, while the structure relaxes into the excited state
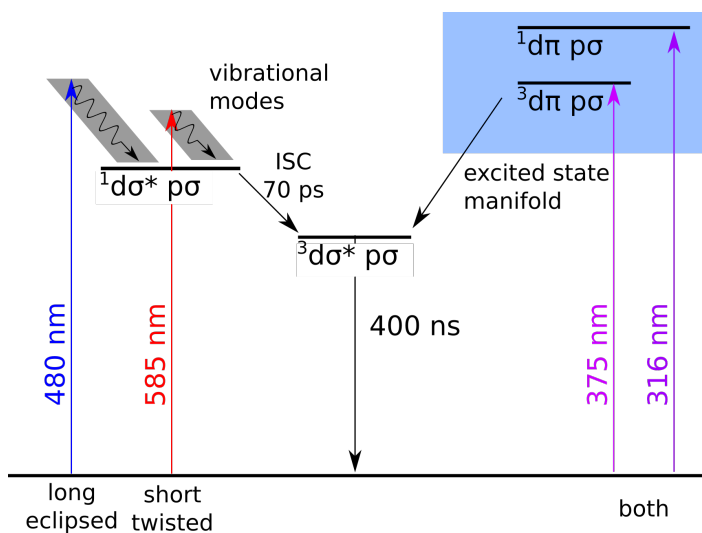
Figure 7.17: Wavelength dependent photodynamics scheme of IrDimen. Excitation with 480 nm and 585 nm excites electrons into higher vibrational states of ^{1}d$\sigma*$pσ. After vibrational relaxation, they intersystem cross into the triplet ^{3}d$\sigma*$pσ state. Excitation with UV-light excites the system into dπpσ states inside an excited state manifold, which decays into the ^{3}d$\sigma*$pσ state circumventing the lowest singlet. Simplified version of the model proposed by Pizl *et al.* [95]

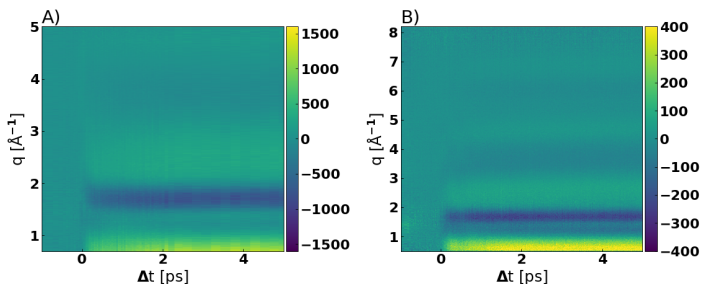**Figure 7.18:** Colorplots of the measurements of IrDimen with A) 400 nm and B) 480 nm. The 480 nm measurement was conducted at a later experiment in which access to higher q-ranges had become available due to upgrades to the facility.

equilibrium structure. This difference in dynamics induced by the different decay pathways can be investigated in these experiments.

The isotropic difference scattering signals are depicted in Fig. 7.18 for A) 400 nm and B) 480 nm. The facility was upgraded in between beamtimes, resulting in the increase in accessible q-range for the 480 nm measurement.

7.2.1 Structural refinement

The structural parameters obtained in sec. 7.1.4 were used for the analysis of these measurements. The fits are depicted in Fig. 7.19. The $\Delta S_0(400\,\text{nm}, \Delta t=4\,\text{ps})$ measurement is matched well by the fit except at the negative peak at $3.5\,\text{Å}^{-1}$ where the fit is systematically lower than the measured data. This is likely an artifact of the self-normalization. The $\Delta S_0((480\,\text{nm}, \Delta t=2\,\text{ps})$ is well matched by the fit through the entire q range.

7.2.2 Time resolved analysis

The analysis of IrDimen on ultra-fast timescales produces additional challenges compared to the equilibrated excited state analysis shown in sec. 7.1. As discussed previously, there are two ground state structures in solution which can be preferentially excited in and reequilibrate on the picosecond time scale [77]. To assess the change ground state population, the time

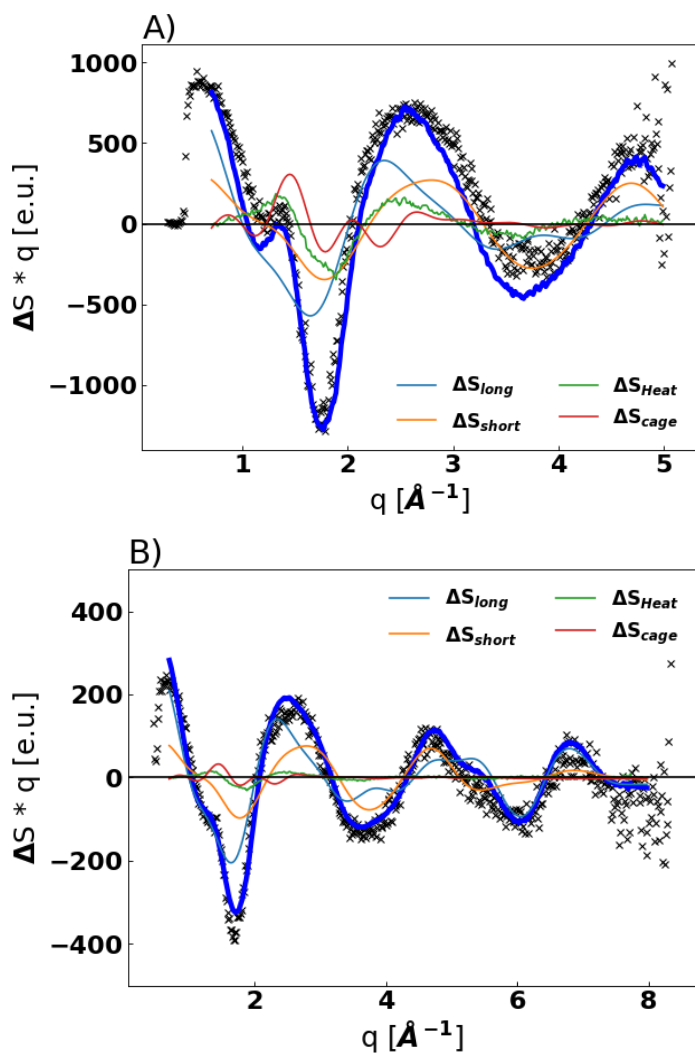**Figure 7.19:** Structural fit of A) $\Delta S(400\,\text{nm}, \Delta t{=}4\,\text{ps})$ and B) $\Delta S(480\,\text{nm},$ $\Delta t{=}2\,\text{ps})$. The structural parameters where used form sec. 7.1.4. In A) the fit matches the signal well except at the negative peak at $3.5\,\text{Å}^{-1}$. This is likely a result of the self-normalization. The 480 nm measurement is described well across the entire q-range.

bins are initially fit with the equilibrium structures used in the structural fit. The contraction is expected to occur on a timescale of ~100 fs [77]. As a result the solute scaler of such an analysis can be used to identify both the share of already contracted molecules as well as the distribution of the ground state conformers.

The investigation of these dynamics is shown in Fig. 7.20 for the 400 nm measurement. Panel A) shows the solute scaler α_{long} and α_{short} fitted with the equilibrated ground and excited state structures. Such an analysis is unable to describe the timescales shorter than the contraction time but can assess the longer population dynamics. Both excitation fraction increase abruptly at $\Delta t=0$ ps and with time constants of τ_{long} 1.2 ps and τ_{short} 1.3 ps. The share of excited molecules must be constant throughout the depicted timescale, as molecules are only excited at t_0 and the lifetime is in the nanosecond regime. As discussed in the last chapter, during the optimization of time-resolved data, it can be practical to keep the solute scaler constant even before t_0, as a finite solute scaler prevents the fitting of artifacts through ΔS_{Solute} with unrealistic structures. The similar timescale of increase suggests that the changes are not due to inter-conversion of the ground states. The excited state is assumed to have been formed from the ground state conformers according to their concentration in solution. A model that constrains the solute scaler defines α_{long} and α_{short} as constant.

The $d_{IrIr,ES}$ are determined using these solute scalers as constrains, shown in Fig. 7.20 B). A single excited state structure was used for IrDimen, despite the excitation from both ground states suggesting at least two ground states for very short delays, as the increase in degrees of freedom of a second ground state structure resulted in instabilities. This causes a most likely $d_{IrIr,ES}$ at $\Delta t <0$ ps between the two ground states. The parameter curve contracts after an unphysical delay of ~200 fs and converges slowly towards the excited state equilibrium. This suggests that the excited molecules do not contract in a coherent manor following photoexcitation. Fig. 7.20 C) shows the $d_{IrIr,ES}$ without a constrains on the solute scaler. This causes instabilities before t_0, but results in a contraction of $d_{IrIr,ES}$ with a step function at t_0.

An identical analysis was done for the 480 nm measurement, shown in Fig. 7.21. A) depicts the excitation fractions α_{long} and α_{short}. α_{long}
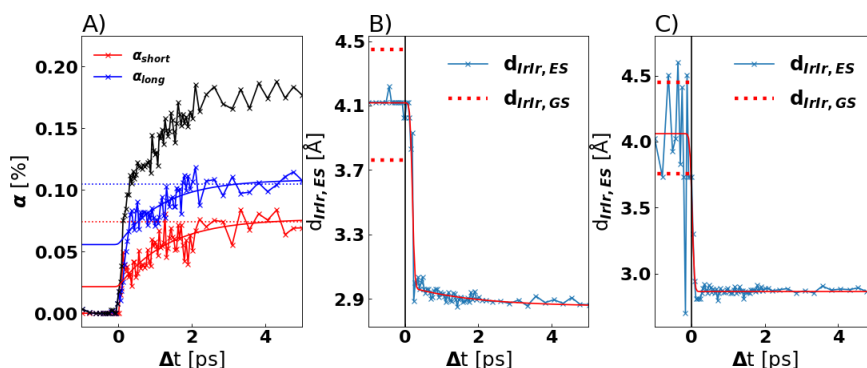
Figure 7.20: Time resolved structural analysis of the 400,nm measurement. A) shows the fitted solute scalers for every time bin using the equilibrium structures. Both α_{long} and α_{short} grow in with similar time constants τ_{long} 1.2 ps and τ_{short} 1.3 ps (solid lines), suggesting that this rise is depicting the formation of the excited state structure and does not represent inter-conversion between the ground states. As a result, the solute scalers are assumed to be constant in the ground state conformer equilibrium. B) shows d$_{IrIr,ES}$ parameter curve fitted with the solute scalers constrained according to A). d$_{IrIr,ES}$ contracts after a delay of ~200 fs and converges against the excited state equilibrium. C) depicts the same optimization without constrains of the excited state fraction, yielded a contraction at Δt=0 ps. The red lines depict kinetic fits.

rises sharply at t_0, while α_{short} rises on a much longer timescale. This could be explained through the preferential excitation of the long ground state and the interconversion of the ground states, which occurs through an energy barrier [94] and should follow a smooth curve. The ratio of $\alpha_{long}/\alpha_{short}$ becomes very large for short delays. The shapes suggest that not hole in ground state is generated from the photoexcitation and α_{long} must describe the entire solute scaler at t_0, shown through the solid lines. To constrain the solute scaler in the time-resolved optimization, a model $\alpha_{tot} = \alpha_{long} + \alpha_{short} = const.$ with the interconversion constant τ is used, shown by the solid lines in Fig. 7.21:

$$
\begin{aligned}
\alpha_{short}(\Delta t) &= IRF * (H(\Delta t) \cdot \alpha_{short,equi} \cdot (1 - \exp -\Delta t/\tau) \\
\alpha_{long}(\Delta t) &= \alpha_{tot} - \alpha_{short}(\Delta t)
\end{aligned}
\tag{7.1}
$$

Using these constrained solute scalers to determine the most likely excited state structure B) again produces a contraction of the d_{IrIr} parameter curve $\sim$200 fs delayed to t_0. The parameter curve exhibits a transient oscillation T_{osc} 0.57$\pm$0.05 ps with a fast decay time 0.21$\pm$0.08 ps. Lifting the constrained on the excitation fraction results in, as for the 400 nm measurement, instabilities before t_0 and a contraction at t_0. The oscillation T_{osc} is fitted with an amplitude of 0.28$\pm$0.11 Å dephasing with a lifetime of τ_{osc} 0.23$\pm$0.1 ps, using:

$$
\begin{aligned}
d_{IrIr}(\Delta t) =& IRF * (d_{IrIr,GS} + H(\Delta t + t') \cdot (\Delta d_{IrIr,1}) \\
&+ \Delta d_{IrIr,2}(1 - \exp(-\Delta t/\tau_{IrIr,1})) \\
&+ \Delta d_{osc} \cos(2\pi \cdot (\Delta t + t')/T_{osc}) \\
&\cdot \exp(-(\Delta t + t')/\tau_{osc})))
\end{aligned}
\tag{7.2}
$$

The short dephasing time and low amplitude compared to the contractions distance suggests that the coherence of the contraction of the excited molecules is limited, but present in opposition to the measurement with 400 nm excitation discussed earlier.
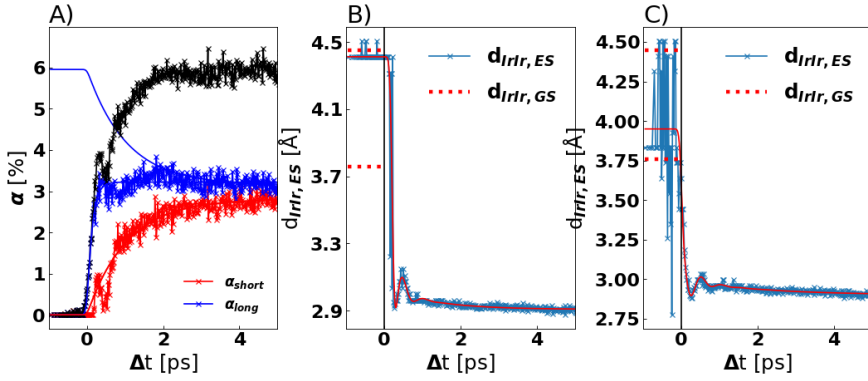
Figure 7.21: Time resolved structural analysis of the 480 nm measurement. A) shows the fitted excitation fractions for every time bin using the equilibrium structures. α_{long} grows in at $\Delta t=0$ ps, while α_{short} only grows in over time. This suggests that this rise depicts the inter-conversion, as α_{long} was preferentially excited. B) shows the $d_{IrIr,ES}$ parameter curve fitted with the excitation fractions constrained to according to A). $d_{IrIr,ES}$ contracts after a delay of $\sim$200 fs and converges against the excited state equilibrium. C) depicts the same optimization without constrains of the excited state fraction, yields a contraction at $\Delta t=0$ ps.

The ligand scaffolding twist parameter γ_{ES} of the 400 nm was determined as a very noise curve, likely a result of the choice to use the structural parameters from obtained from a different experiment. This caused the used ground state structure to not correspond with the minimum of the parameter space, leading to instabilities. The ligand scaffolding twisting of the 480 nm measurement will be discussed in sec. 7.3.3.

7.2.3 Conclusions

The TR-XSS measurements of IrDimen using 400 and 480 nm pump wavelengths did provide results in line with the model derived by Pizl *et al.* [95], in which electronic transition was linked to structural dynamics using transient absorption spectroscopy. Photoexcitation with 400 nm photons excites complexes from both ground states. Within the resolution of this analysis, both ground states are excited according to their presence in the equilibrated ground state. The $d_{IrIr,ES}$ parameter curve does not exhibit an oscillation, which is in line with an excitation into a higher lying manifold of excited states, in which the coherence in the ensemble structures is limited during the relaxation. The 480 nm excitation resulted in an oscillation, which is in line with the expectation of the vibrational relaxation observed in transient absorption spectroscopy [98].

In both cases, the fixation of the excitation fraction resulted in a delay in the $d_{IrIr,ES}$ contraction in the parameter curve compared to the onset of signal increase in the raw data. The removal of this constrained yielded parameter curves that contracted at $\Delta t=0$ and produced intermediate structures between ground state and excited state distances. In the 480 nm measurement, the total signal magnitude increases over the first picoseconds. The excitation resulted in a hole in the ground state population of the long conformer, which is regenerated during the equlibration of the ground states. This process shifts this hole from the *long* to the *short* population, which should decrease $\sum \Delta S$, which is not observed in the data. Both findings suggest that the modeling of the excited state population of IrDimen with a constant solute scaler is inadequate for short delays. A possibility to explain this behavior is that the complexes do not react coherently to the new electronic structure following photoexcitation. The flexible ligand could sterically hinder the contraction, as the Iridium

atoms are still bound to the cyanide groups. In this case, the contraction of the Iridium atoms could be faster than the average response time of the molecule. In a model where the excitation fraction is fixed, this would show up as the observed additional delay time highlighting the point where the majority of complexes have responded to the photoexcitation.

7.3 Parameter distributions in structural oscillations

As discussed in chap. 2, the distribution of a structural parameter in an excited state ensemble at t_0 depends on the interplay between the spectral width of the photon, the ground state population distribution and parameter dependent gap between ground and excited state potential surface $\Delta V(r) = V(r,ES) - V(r,GS)$. This distribution of parameters can be used to describe the motion of the excited state ensembles on the excited state potential surface. Generally, laser systems exhibit a Gaussian shaped spectrum, which makes it practical to approximate the distribution with a Gaussian shape. The distribution is thereby defined by its position r_i on the reaction coordinate and its width σ_i. For narrow distributions or approximations this model converges towards a single structure. The distribution propagates on the potential energy surface. If the distribution is sufficiently narrow and the potential sufficiently harmonic, the propagation yields an observable oscillation in the structural parameter, as seen in the last section.

This distribution of structures introduces changes to the structure factor in the measured systems. An economical way to calculate structure factors for a range of distributions is to use the Debye-Waller-esque positional uncertainty u_i introduced in Eq. 4.8.

Similar to motions on the excited state potential surface, these distributions can also be observed on the ground state potential surface. Under finite temperatures, the vibrational modes of the ground state are occupied, but are typically not observed as the vibrational modes in equilibrium cancel each other out. An off-resonance excitation can induce an imbalance into the equilibrium and result in an observed motion of the hole left behind by the photoexcitation, as discussed in the next section.

This section will investigate the shape and nature of distributions in structural oscillations induced in $d^8 d^8$ transition metal complexes by photoexcitation by both on-resonance and off-resonance photons.

7.3.1 Ground state dynamics

Preceeding time-resolved optical spectroscopic experiments by van der Veen *et al.* [103] had investigated the excited state dynamics of PtPOP, focusing on the Pt_2 stretching mode with a period of ~225 fs. PtPOP has been studied previously with TR-XSS [88], but the limited time resolution available at synchrotrons prevented any investigation of structural dynamics in the transition metal complex, due to dephasing times in the few-picoseconds regime [104]. With the improvement of the temporal resolution available at LCLS after the implementation of the timing-tool [64] such oscillations were resolvable in direct structural information for the first time.

Experimental parameters

The data was collected with the proposal *Charge transfer and vibrational coherence in a photocatalytic model system* at the LCLS XPP in 2015, alongside the systems discussed in sec. 8.1. This specific dataset has been intensively analyzed and discussed by Haldrup*et al.* 2019 and reanalyzed as part of this work. The sample was prepared as 80 mM PtPOP in water. The photoexcitation occurred with 395 nm, about 25 nm away from the absorption maximum (Fig. 7.3).

Model free analysis

The reduced data is shown in Fig. 7.22 Panel A) depicts the time resolved difference scattering data for the first 5 ps. The subplots B) and C) depict the first left singular component of the SVD decomposition of the reduced data and the associated time trace. The magnitude of the first SVD component $S_{1,1}$ is more than 7 times larger than any subsequent components, thus comprising a significant part of the data alone. Subplot D) depicts the Fourier transform of the OSS of the time trace depicted in C). A mode with a period of ~285 fs is dominant along the time trace.
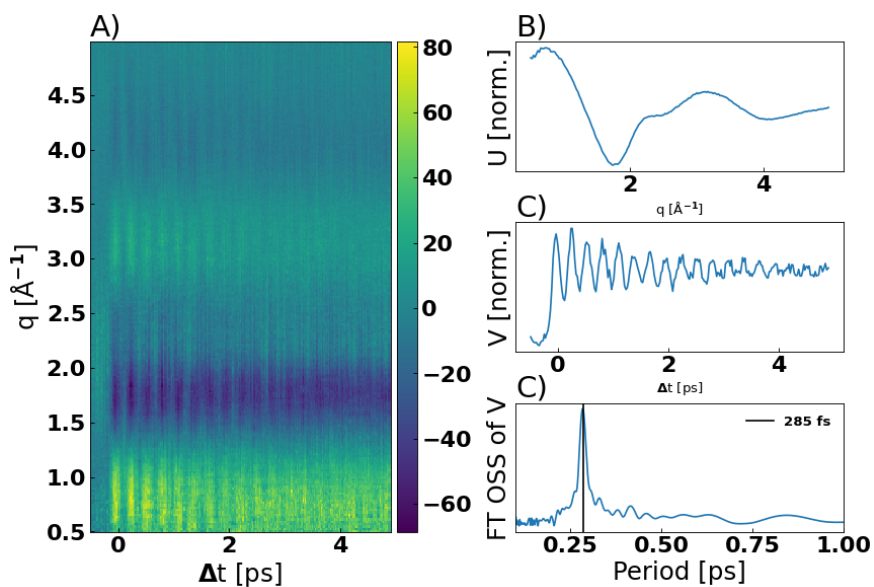
Figure 7.22: Colorplot of ΔS_0 and the analysis of its first SVD component. A) depicts ΔS_0 exhibiting an oscilating signal following Δt=0. The first right singular of the SVD B) depicts a strong positive peak at low q and a negative peak at $1.8\,\text{Å}^{-1}$. The right singular time-trace of this component C) depict at steep increase at t_0 followed by an oscillation dephasing over several picoseconds. The Fourier transform of the OSS of the time-trace indentifies the oscillation period as $285\,\text{fs}$

This frequency is much more in agreement with the ground state oscillation period of PtPOP, which has been determined for crystalline sample with low temperature absorption spectroscopy to be $110\,cm^{-1}$ [105], or 303 fs, and resonance Raman spectroscopy to be $117\,cm^{-1}$ [106], or 285 fs, than the excited state period of 225 fs. This indicates that the observed oscillation does not occur on the excited state potential surface, but the ground state potential surface instead. The strong off-resonance redshifted excitation with 395 nm laser, compared to the 370 nm absorption maximum in solution, resulted in the preferential excitation of groundstate complexes with a geometry closer to the excited state, due to their phase in the ground state oscillation. The excited ensemble of molecules is positioned near the bottom of the excited state potential. The low vibrational mode of this state results in only minor oscillations, limiting the magnitude in the scattered solution signal. Fig. 7.23 depicts this process. The photon preferentially excited PtPOP molecules with structures already close to the excited state structure, due to the off-resonance excitation. This left a hole in the ground state population of structures with a specific vibrational state. The observed oscillations in the signal originate from this hole oscillating on the ground state potential surface until it dephases [97].

Structural fitting

The initial structural optimization was conducted on the ΔS_2 signal, as shown in Fig. 7.24 A) using $\Delta S_2(\Delta t = 4\,ps)$. The structural parameter optimized d_{PtPt} is shown in Fig. 7.1. The excited state distance $d_{PtPt,ES}$ was frozen at 2.76 Å based on previous synchrotron experiments, in which a larger q-range $\leq 8\,Å^{-1}$ was accessible [88]. $d_{PtPt,GS}$ was determined at 2.93 ± 0.09 Å with an excitation fraction of α_{S2} $4\pm2\%$. The large error, determined with the Likelihood method, arises from the strong correlation between excitation fraction and contraction distance in the complex, which cannot be disentangled with the available q-space. These structural parameters were used to fit the structural signal of the isotropic ΔS_0 as depicted in Fig. 7.24 B).

As the dynamics occur on the ground state potential surface, as shown in Fig. 7.23, the dynamics are resolved by optimizing the structure of
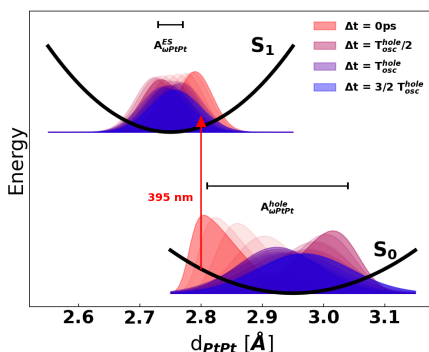
Figure 7.23: Oscillation of the excited state ensemble of molecules in the excited state potential surface S_1 and the ensemble of ground state holes on the ground state potential surface. Dephasing time decreased compared to actual sample for illustrative purposes. The amplitude of the motion of the hole $A_{\omega PtPt}^{hole}$ is considerably larger than any oscillation on the excited state potential surface after excitation with 395 nm. Adapted from [97]
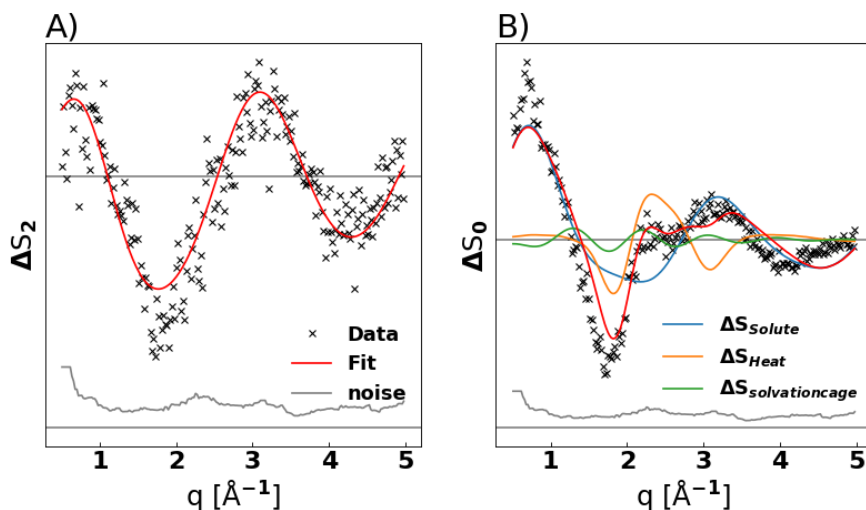
Figure 7.24: Fitting of PtPOP at a Δt 4 ps in the A) ΔS_2 and B) ΔS_0. The individual components of the ΔS_0 according to Eq. 6.5 are depicted independently. The error associated with each of the q-bins is depicted on the bottom of each of the fits.
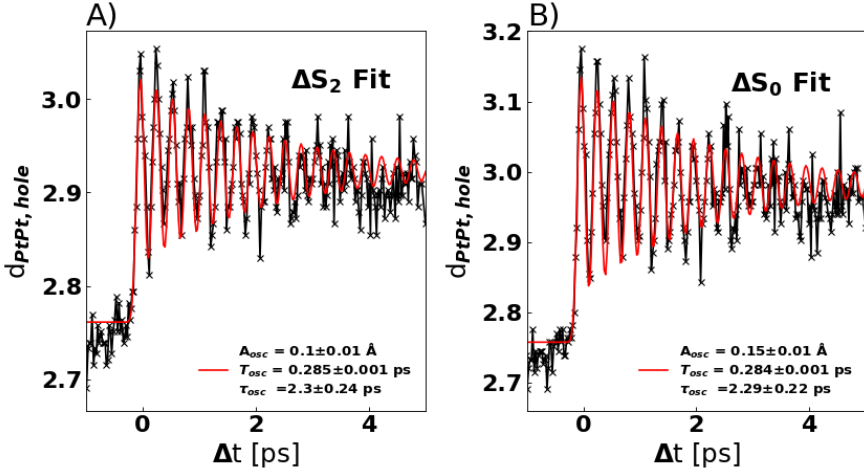
Figure 7.25: Structural optimization of the hole in A) ΔS_2 and B) ΔS_0. The parameters are fitted with Eq. 7.3 to derive the time-constants and oscillation magnitude

the hole for each of the time-bins. Fig. 7.25 depicts the time-resolved most likely $d_{PtPt,hole}$ for A) ΔS_2 and B) ΔS_0. The solute scaler was kept constant from the fits depicted in Fig. 7.24, resulting in the distance converting to the equilibrium distance of the excited state for $\Delta t < 0$. Both parameter curves are fitting with Eq. 7.3 to derive time constants:

$$
\begin{aligned}
d_{PtPt}(t) = d_{PtPt,0} + IRF \circledast H(t) \\
\cdot (\Delta d_{PtPt} + A_{\omega PtPt}^{hole} cos(2\pi \cdot t/T_{osc})) \cdot \exp(-\Delta t/\tau_{osc})
\end{aligned}
\tag{7.3}
$$

with the instrument response function RIF, the Heaviside function H(t), the ground state equilibrium distance $d_{PtPt,0}$, the amplitude of the oscillation $A_{\omega PtPt}^{hole}$ and the oscillation period T_{osc}. The oscillation frequencies T=0.285±0.001 ps and dephasing time of the oscillation $\tau_{osc} = 2.3±0.24$ ps are identical within the error bar.

Conclusions

In summary, the data has allowed the tracking of coherent oscillations of the femtosecond timescale in PtPOP. The off-resonance excitation yielded oscillations on the ground state potential energy surface The limitations in the accessible q-range limited the investigation of the actual shape of the distribution of d_{PtPt} in which the hole ensemble oscillates.

7.3.2 Parameter distributions in ensembles of PtPOP

Additional experiments studying the distribution of d_{PtPt} inside an oscillating excited state ensemble were conducted in 2021 after the ongoing upgrade towards LCLS-II had improved the machine.

The access to higher energies, and with it the additional q-range, would lead to two primary advantages during the analysis compared to the dataset presented in sec. 7.3.1. Firstly, the extended q-range would allow for a better separation of the solvent contribution, which is limited to the lower q-range, from solute contributions which exhibit oscillations in the difference scattering signal much further into the q-space. Secondly, the access to higher q-range would allow for the determination of not only the position of the Gaussian distribution along the d_{PtPt} axis but also the width. Depending on the width of the distribution, the distribution of the structures is spread out more widely, resulting in changes in the difference scattering signal according to Eq. 4.8. These changes are simulated for a contraction of d_{PtPt} from 2.95 to 2.75 Å in PtPOP in Fig. 7.26. The simulation predicts that the changes are most noticeable in the range from 4.5 to 8 Å^{-1}, which would have been unfeasible to resolve in the range available in previous experiment (<5Å^{-1}). In the 2021 experiment the sample was excited on-resonance with 370 nm photons, which resulted in the observation of motions on the excited state potential surface rather than the ground state potential surface discussed in the previous section.

The experiment was conducted PtPOP in the solvents water, acetonitrile and 2-propanols. The different solvents bond to the complex with different strength, and as such influence the potential energy surface, which governs the structural rearrangements following photoexcitation.
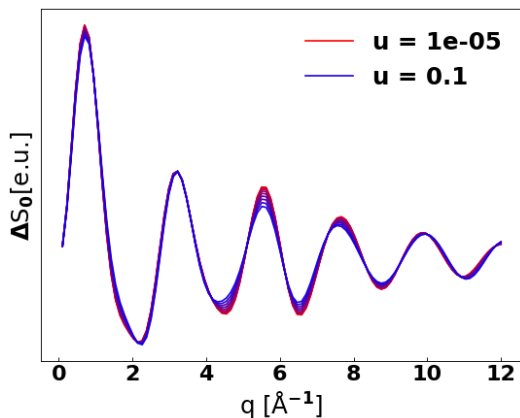
Figure 7.26: Influence of positional uncertainty on the ΔS_0 scattering signal. The simulated signal contraction in d_{PtPt} from 2.95 to 2.75 Å is imposed with a range of positional uncertainties according to Eq. 4.8 simulating the broadness of the d_{PtPt} distribution in the excited state ensemble. The largest changes occur in the range of 4.5 to 8 Å^{-1}.

The PtPOP potential energy surfaces in water are often depicted as parabolic in literature [104]. This approximation is supported by findings that the dephasing time is more dependent on the ligand flexibility than the solvent [107], showing the weak coupling to solvent modes. In practice, the platinum atom will experience some form of asymmetry in forces between the other platinum on one side and the solvent on the other [82]. To investigate the impact of such an asymmetric force, the width of the excited state ensemble parameter distribution was tracked following photoexcitation.

The temporal width of the laser limits the spectral resolution, resulting in a Gaussian distribution of molecular structures that are excited onto the excited state potential surface. This distribution experiences this anharmonicity and may broaden or sharpen, as molecules with different vibrational states move along the potential. [108]
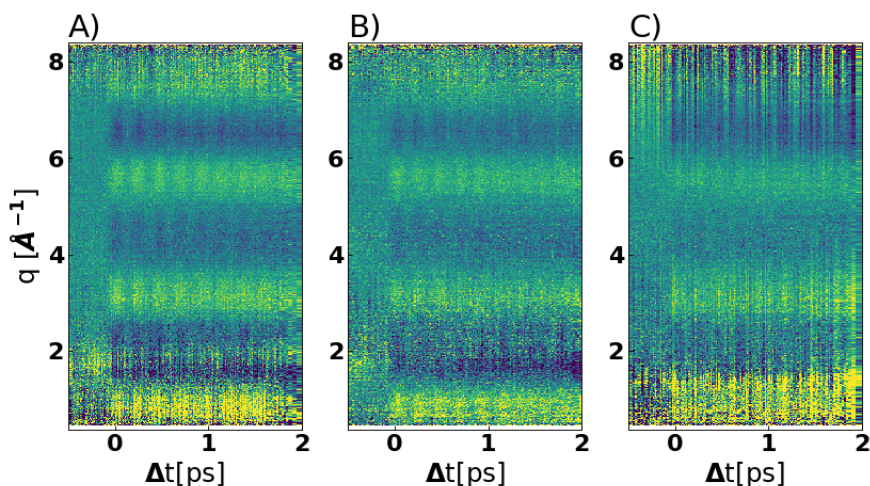
Figure 7.27: Colorplots of the isotropic difference scattering signal ΔS_0 for PtPOP in A) acetonitrile, B) water and C) 2-propanol.

Model independent analysis

The reduced and binned datasets are depicted in Fig. 7.27. The measurements in A) acetonitrile and B) water clearly exhibit oscillatory patters as expected in the experiment. The 2-propanol measurement C) has received the least amount of integration time and strong artifacts can be seen on either end of the q-range.

The datasets are analyzed with an SVD, shown in Fig. 7.28. The q-space was truncated to reduce the interference of artifacts from then ends of the q-axis. The left singular components all show the same oscillating pattern along the q range. The signals for the acetonitrile and water measurement appear identical within the noise, suggesting that the solvent dependent ΔS_{cage} term might be either very similar or relatively small. The right singular components all depict an increase in signal at t_0 followed by an oscillation. The oscillation is also present in the 2-propanol measurement, where it had previously obfuscated by noise and artifacts. The right singular components are fitted with Eq. 7.4,
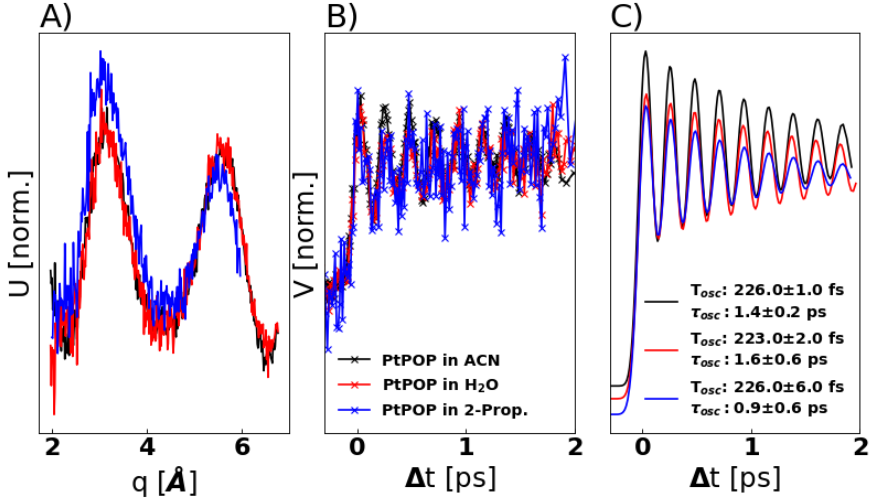
Figure 7.28: First left singular A) and first right singular B) of the SVD of the difference scattering data of PtPOP in acetonitrile, water and 2-Prop. The data was truncated in q-direction (A)) to reduce the impact of artifact contributions identified at either end. The strong similarity of the signal shape in A) suggests that the solvent contributions are minimal for $q > 2\,Å^{-1}$. All systems exhibit a similar shaped oscillation on the time-trace B). C) depicts the oscillation period and dephasing time according to Eq. 7.3. The time resolution appears unchanged to previous experiments, albeit with a larger error due greater noise at each data points

$$\Delta S(t) = IRF * H(t) \cdot (A + B \cdot \sin(2\pi \cdot t/T_{osc} + \phi) \cdot \exp(-t/\tau_{osc})) \quad (7.4)$$

describing the increase in signal at t_0 with an period T_{osc}, dephasing time τ_{osc} and the IRF. In all cases the oscillation period of $\sim$225 fs was found, as suggested by literature on the excited state oscillation. The dephasing times of 1.4 ± 0.2 ps (lit. 1.1 ± 0.1 ps [104]) for ACN and 1.6 ± 0.6 ps (lit. 1.76 ± 0.08 ps [103]) are in reasonable agreement with literature results.

The relative magnitudes of the first and subsequent SVD components are depicted in Fig. 7.29. The primary components is by far the largest
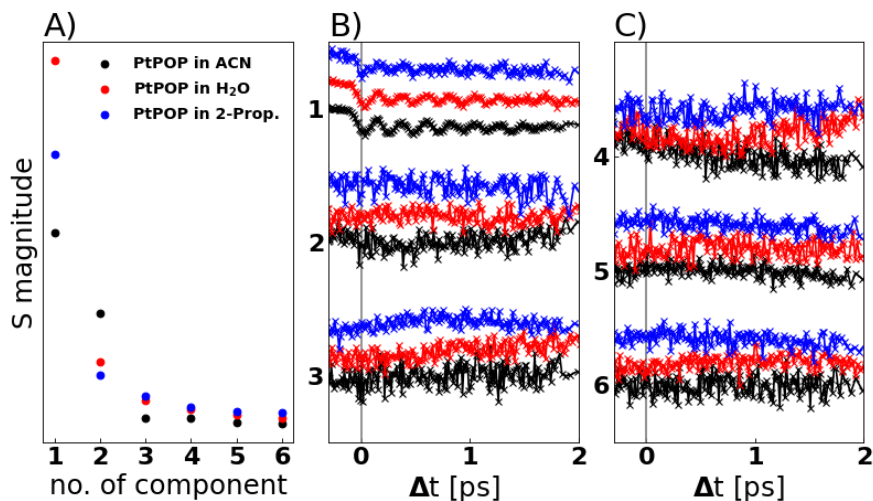
Figure 7.29: A) Magnitudes of the first six SVD-components and B) & C) their respective time traces for PtPOP in acetonitrile *(black)*, water *(red)* and 2-prop *(blue)*. Neither system has an additional component that exhibits a clear induction by the laser pulse at $\Delta t=0$ ps. Additional components are as as such primarily attributed to noise and artifacts.

contribution, with the acenonitrile measurement exhibiting one additional stronger component before the magnitudes begin to converge. Only the time-trace of the first component in B) exhibits a clear time dependency in regard to t_0 stronger than the noise level, suggesting that there is only a single dynamic component in the system.

Structural determination

Using the information from the SVD analysis, the structure was optimized using Eq. 6.5 at $\Delta t=2$ ps where the oscillation have dephased. The platinum atoms were constrained to symmetric positions for both ground and excited state. During the structural optimization the solvation cage scaler β was tied to the excitation fraction to stabilize the fit. $d_{PtPt,GS}$ was determined at 2.96 ± 0.17 Å, $d_{PtPt,ES}$ at 2.70 ± 0.14 Å. Fig 7.30 shows the fit and the individual components.
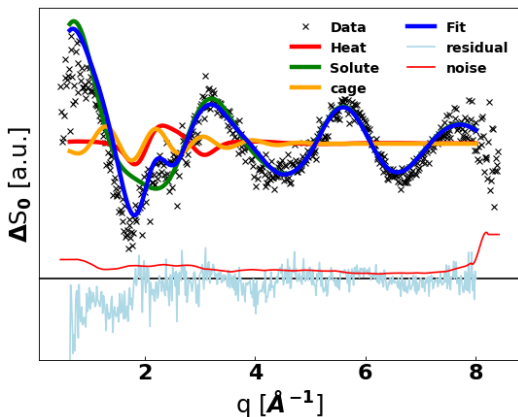
Figure 7.30: Structural optimization fit result of $\langle \Delta S(\Delta t=1.5{:}2\,\text{ps}) \rangle$ PtPOP in water. Signal averaged between Δt 1.5 and 2 ps

These equilibrium ground- and excited state distances were used as constrained parameters to determine the excitation fraction used in the acetonitrile and 2-propanol samples, where no solvation cage term was available. The strong similarity of the signal in Fig 7.28 suggested that the ΔS_{cage} has limited impact on the structural signal.

Time-resolved analysis

Using these ground state structure and determined solute scaler, the oscillations could be resolved in structural parameters across the entire experimental range.

For each time bin the most likely excited state distance $d_{PtPt,ES}$ and positional uncertainty u_{Pt} were fitted. The reduction artifacts were accounted for by taking the two strongest components of an SVD of the signal before -300 fs and using them as fit components in every time-step, as discussed in [76]. ΔS_{Cage} components were omitted to maintain parity between the systems, and heat contributions were used in accordance with the solvent. Fig. 7.31 depicts the results of the fit for the three solvents.

All three systems show a contraction of $d_{PtPt,ES}$ at t_0 followed by an oscillation with a frequency of $\sim$225 fs. The oscillations decrease in
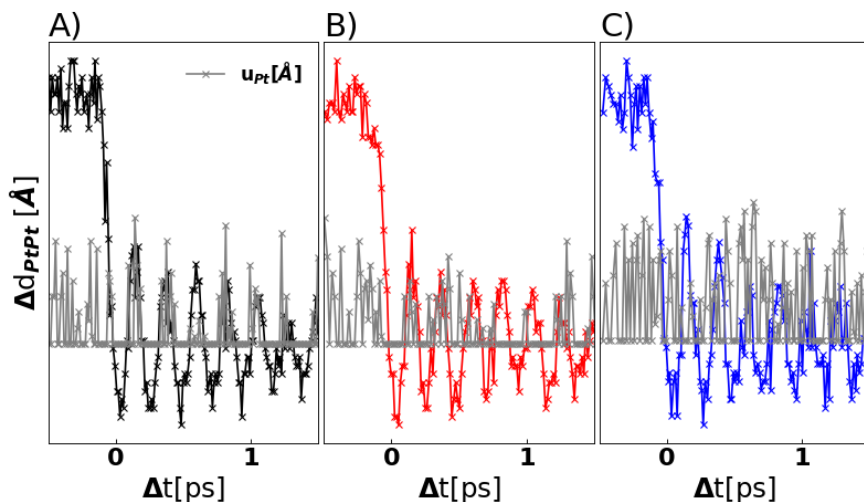
Figure 7.31: Time resolved structural fitting results in A) acetonitrile, B) water and C) 2-propanol. The ground state structure and excitation fraction were kept constant for all time-bins.

magnitude over time. The uncertainty u_{Pt} before t_0 can be noise and artifacts. In the acetonitrile sample, u_{Pt} appears to be maximal primarily at local maxima of $d_{PtPt,ES}$. This relationship is not as clearly seen in the water sample, and the 2-propanol sample exhibits a very noise uncertainty curve, which was expected from the strong noise in the data.

To determine patterns in the signal, an autocorrelation method was employed for the two parameter curves for the time range $\Delta t \geq 0$ ps. Fig 7.32 A) depicts the autocorrelation of the contraction of the PtPt-distance. The atoms undergo an oscillation resulting in strong positive correlation between the position at Δt and $\Delta t + n \cdot T_{osc}$ for all samples. In the uncertainties u_{Pt} this pattern is repeated for the acetonitrile sample, which exhibits a similar pattern, but nothing similar has been observed for the water and 2-propanol sample.
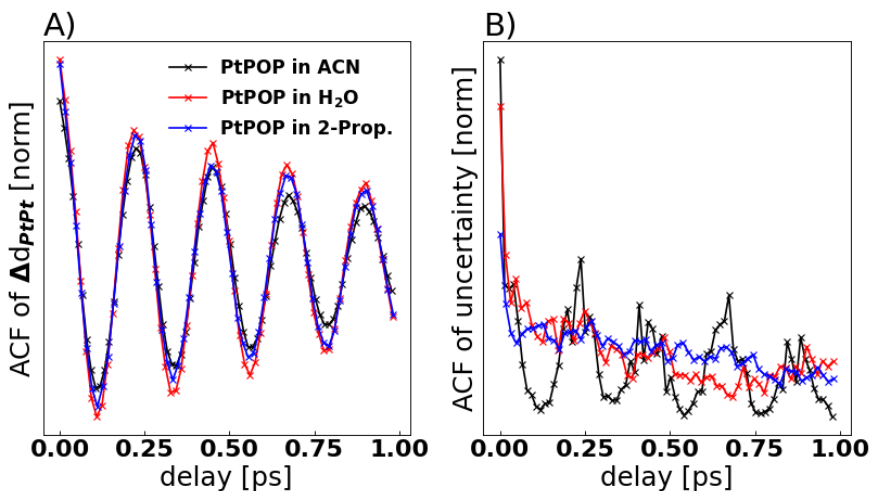
Figure 7.32: Autocorrelation of the fitted parameter curves A) platinum atoms contraction Δd_{PtPt} and B) positional uncertainty u_{Pt} for PtPOP in acetrnitrile, water and 2-propanol. In all 3 systems the Δd_{PtPt} curves depicts a clear correlation between the position at Δt and $\Delta t + n \cdot 0.225$ ps, as expected from the oscillations frequency. The uncertainty exhibits this relation only for the acetonitrile solution. In other systems, there is no clear correlation between local maxima and minima in the $u_{Pt}(t)$ distribution.
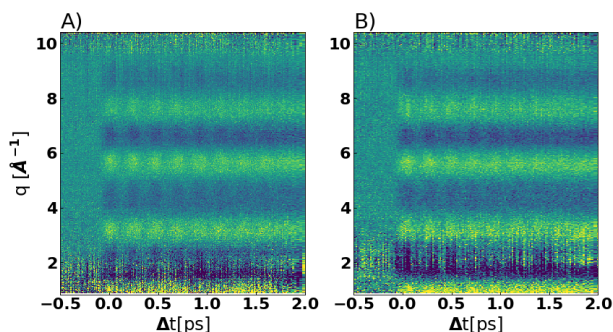
Figure 7.33: Colorplots of the A) acetonitrile and B) water measurements with the extended q-range until $10\,\text{Å}^{-1}$. The signal at lower $q<2.5\,\text{Å}^{-1}$ is strongly influenced by artifacts.

Extended q-range

During the experiment, additional measurements were taking for PtPOP in acetonitrile and water with access to a larger q-range. This was realized by moving the detector closer to the sample from $48\,\text{mm}$ to $43\,\text{mm}$, giving access to larger scattering angles and thereby a q until $10\,\text{Å}^{-1}$. The time dependent ΔS_0 are depicted in Fig. 7.33. Both solvents exhibit the characteristic oscillations observed in the previous measurements. However, the measurements also exhibit strong artifacts at $q<2.5\,\text{Å}^{-1}$.

The data was analyzed in an identical fashion to the data at low q. Fig. 7.34 A) depicts the structural optimization of the water measurement. The fit deviated from the data the strongest at around $2\,\text{Å}^{-1}$, where the fit is unable to produce a large enough signal. As in this particular section of the q-range the ΔS is notably larger than observed for the low q measurement, or previous PtPOP measurements in water, this can be attributed to a self-normalization artifact.

Using these structural parameters and excitation fraction, the most likely $\Delta d_{PtPt,ES}$ and u_i were determined for each binned delay. The aforementioned artifacts were treated identically as previously. The results are depicted in B) for acetonitrile and C) for water. Similar to the acetonitrile measurement in the lower q measurements, the uncertainty u_{PtPt} is correlated between Δt and $\Delta t + n \cdot T_{osc}$. The effect is also visible for water in

this q-region, albeit less pronounced than in the acetonitrile measurement.

Conclusions

The parameter curve of the uncertainty suggests a periodicity of the uncertainty $u_P t$ mirroring the dynamics of the platinum atoms reaching the outermost positions of the oscillation. This behavior can be explained with a solvent dependent anharmonicity in the potential, resulting in a difference in the parameter distribution at either turning point, resulting in a side with narrower and one with a wider average distribution. For a sufficiently narrow initial distribution, this has been proposed for anharmonic potentials [5, 109].

   An additional contribution to the uncertainty is that while the repulsive further from the other platinum atoms are identical between coherently oscillating complexes, the solvent fluctuates dynamically exhibiting a range of different forces onto the platinum atom for the ensemble.

   Fig. 7.35 sketches out the parameter distributions reaction to the anharmonic electronic potential surface. If a sufficiently narrow distribution of d_{PtPt} is generated by the photoexcitation, the Gaussian shaped distribution is sharpened up on the "inside" of the complex by the electrostatic repulsion. On the outside the attractive forces between the platinum atoms are counteracted by stabilizing forces from solvent interaction. The acetonitrile, as the stronger bonding solvent, stabilizes the platinum atoms stronger thus deforming the potential energy surface stronger, as seen in the autocorrelation plots. In contrast to the IrDimen discussed in sec. 7.2, the system is well described by a constant solute scaler, suggesting that molecules react more coherently to the changed electronic structure.

7.3.3 Parameter distributions in ensembles of IrDimen

The measurement of IrDimen with 480 nm discussed in sec 7.2 was conducted in the same experimental setup as the data presented in sec. 7.3.2. In the IrDimen analysis a single structure had, in combination with a constant excitation fraction, proven inadequate as a description of the system for very short time delays. In the PtPOP system, the Debye-Waller-esque
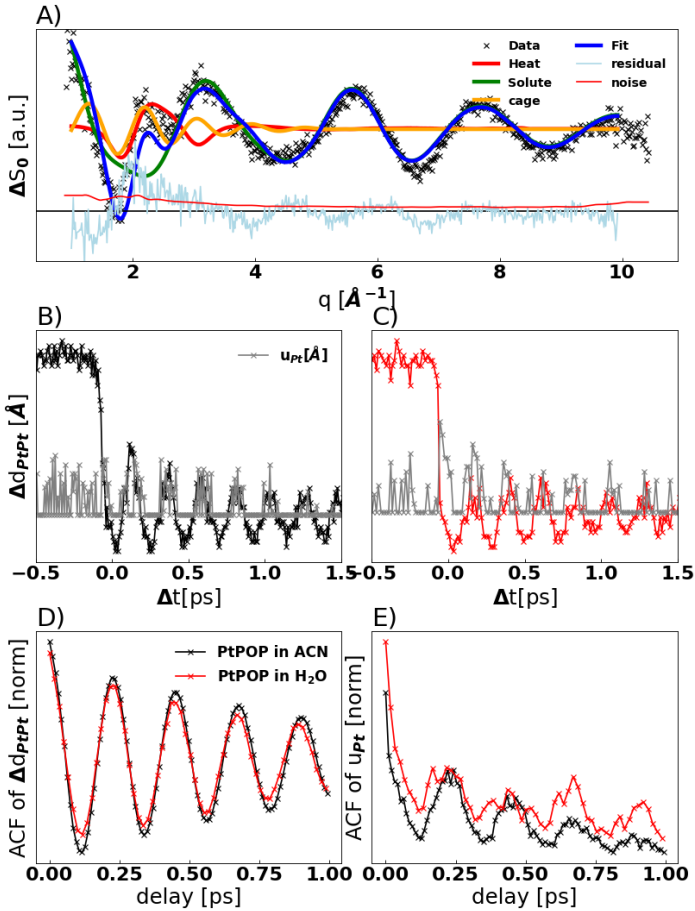
Figure 7.34: Analysis of the higher q-range data analogue to the previous steps. A) depicts the fit of $\Delta S_0(\Delta t = 2\,ps)$. The fit captures the oscillations of the data well, except for the peak at $2.2\,Å^{-1}$, where the data deviates from the low q data shown in Fig. 7.30. B) and C) depict the structural parameter curves d_{PtPt} and u_{Pt} for ACN and H_2O. The uncertainty overlaps in both cases with local maxima of the d_{PtPt} curve. This is also apparent in the autocorrelation E)
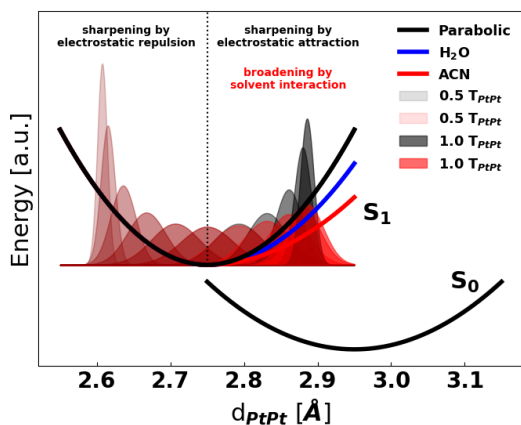
Figure 7.35: The excited state ensemble is generated at the outer turning point of the PtPt oscillation on the excited state potential surface. If the distribution along d_{PtPt} is narrower than the equilibrated distribution of the excited state, the distribution is expected to broaden up towards the center and narrow down towards the sides. In a harmonic potential this would be symmetric. A strong interaction with a solvent, such as acetonitrile, may break the symmetry by stabilizing longer distances. In such a case, the distribution would be sharper on one side than the other *(red)*.

positional uncertainty has given insight into the evolution of the distribution, and thereby the excited state potential energy surface. A similar increase in the parameter space introduces a distribution of structures into the analysis which could explain this behavior.

The structural optimization, constraining the excitation fractions to the values determined in Fig. 7.21, are depicted in Fig. 7.36 A). The $d_{IrIr,ES}$ parameter curve contracts after a delay of $\sim$200 fs, exhibiting one oscillations before converging to the excited state equilibrium. The Debye-Waller-esque factor u_{Ir} in B) increases sharply at t_0 to its maximum, from which it slowly decays over the first picoseconds.

The lifting of the constrained again produces a parameter curve where $d_{IrIr,ES}$ contracts at t_0 being followed by an oscillations. The Debye-Waller-esque factor u_{Ir} in D) experiences a similar shape but does not reach quite as high values compared to the previous analysis. In both analysis methods the ligand scaffolding twisted after a brief delay following photoexcitation. The large positional uncertainty directly following the photoexcitation highlights the broad distribution of structure that are electronically excited. While the observed collective oscillations only comprise a small part of the signal, the disorder suggests that the individual molecules are impacted by much larger oscillations, that nearly cancel out on average. As the system vibrationally relaxes, the molecules approach the excited state equilibrium and the positional uncertainty decreases.

The analysis shows that a Debye-Waller-esque factor u_{Ir} alone is not sufficient to describe the contraction of IrDimen with a constant solute scaler. The large uncertainty decreasing over time is consistent with complexes from a ground state with a relatively flat potential energy surface converging into a steeper excited state potential surface.

7.3.4 Conclusions

With femtosecond time resolution, parameter distributions in an ensemble and their width can be tracked if a sufficiently large q-range can be probed. The stiff pyrophosphit ligand scaffolding of the PtPOP effectively reduces the number of structural parameters to one. The dephasing time is long in comparison to the oscillation period and allows to observe the system over several oscillation periods. The excitation wavelength defines the
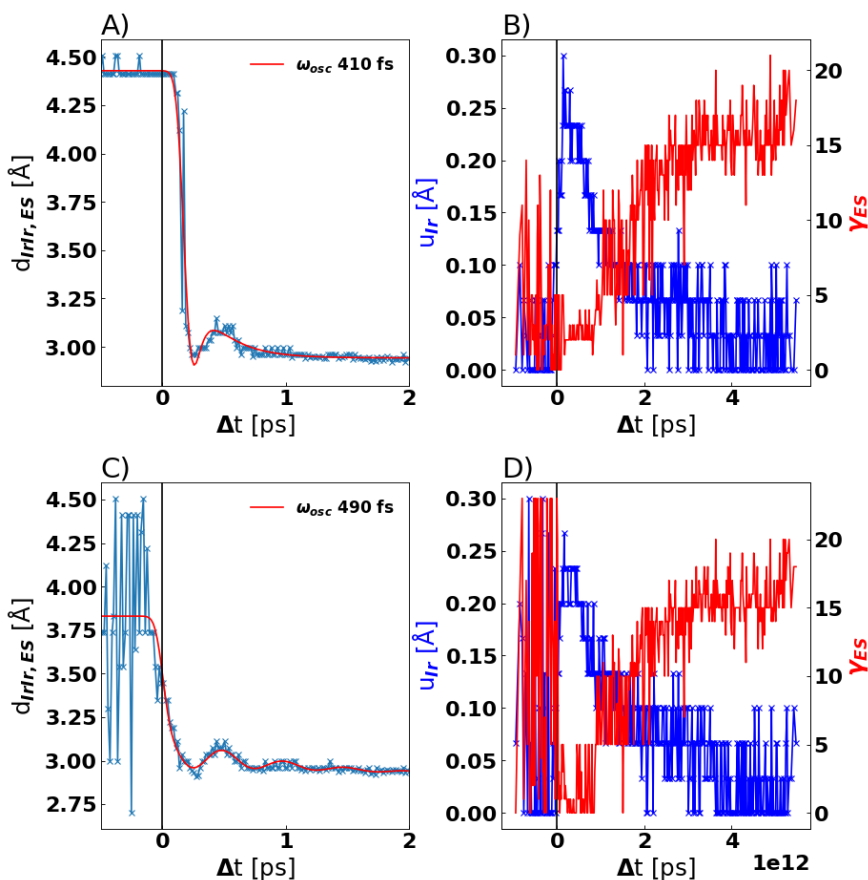
Figure 7.36: Structural parameters fitted for each individual Δt using the parameterized excitation fraction determined in Fig. 7.19. A) depicts $d_{IrIr,ES}$ fitted with Eq. 7.2. The contraction appear delayed by $\sim$200 fs and is superimposed by an oscillation with a period of 410 fs. The immediate onset is exhibited in B) through u_{Ir}, which rises sharply at Δt=0 ps and decays over the first picoseconds. The ligand scaffolding increases similarly to the previous analysis.

distribution of structural parameters in the excited state ensemble, which guides the observed oscillations on solvent dependent ground and excited state potential surface.

The IrDimen complex exhibits much more complicated potential energy surfaces, both for the ground and for the excited state. The additional degrees of freedom in ligand structure and ground state compositions create, as discussed in previous sections, a whole range of challenges. The dephasing time, which has been linked to ligand flexibility in d^8d^8-complexes [104], hinders the observation of more than one oscillation.

7.4 Summary

Bi-metallic d^8d^8 transition metal complexes have proven useful to the study of a range of fundamental photophysical properties. The improved spectral purity at modern X-ray sources and access to higher energies yields unprecedented insight into the systems, but also emphasizes problems in data treatment and modeling. Their wavelength and solvent dependent photodynamics have been analyzed and compared to complementary methods, linking the structural motions to electronic structures and solvent interactions. By exploiting the ever-advancing capabilities at large scale facilities, a fascinating new insight into systems can be achieved.

The *ultrafine structural refinement* analysis highlighted both problems through the choice of scaling interval as well as the modeling of flexible components. The self-normalization using the azimuthally integrated data has the fundamental problem that images of otherwise identical sample with and without photoexcitation measured with identical X-ray pulses (neglecting the quantum-physical element of chance in any scattering experiment) will be scaled with a differently, as long as the signal inside the scaling interval $\sum_{q1}^{q2} \Delta S$ does not add to zero. While q-values might be found where this is true for a single delay, a dynamically evolving system is unlikely to match this criterion with a single set of limits.

Nonetheless, the upgraded beam quality allowed for the study of the motion and width of a distance distribution across the potential energy surface. With improvement of X-ray sources to come, this form of studying

distributions and potentials may become accessible to broader groups of compounds.

The bi-metallic d^8d^8 transition metal complexes have long served as model systems both for studying fundamental photophysical dynamics as well as the bench-marking systems for method development. The complexes are can react with ions in solution to form, among other compounds, tri-metallic complexes. These systems will be discussed in the next chapter.

Chapter 8

Tri-metallic complexes

The previous chapter has discussed the electronic structure, physical structure and structural dynamics following photoexcitation of the $d^8 d^8$ transition-metal complexes PtPOP and IrDimen in great detail. Their reactive capabilities have not been discussed as much.

In addition to the catalytic activity discussed in the previous chapter d8d8-complexes have been shown to transfer charges to acceptors in solution [110] or associated with other compounds in both ground and excited state. This behavior has been observed for both PtPOP [111, 112] and IrDimen [43, 113]. Especially the PtPOP system has been reported to associate with a range of ions in solution [114], in particular thallium [44, 115], tin and lead [116], silver [117] , and anions [118]. Their formation in the ground state is generally observed through a shift of the absorption spectrum from the 370 nm of PtPOP towards longer wavelengths. The binding constant increases for many of these systems following photoexcitation, increasing the concentration of XPtPOP complexes and allowing the formation of X_2PtPOP formations, which are not present in the ground state [44].

The luminescence, both fluorescence and phosphorescence, is also affected by the bonding. Both shifts in the wavelength, depending on the type and amount of ions bonding to the complex [44], and quenching of the luminescence has been reported for Cu^{2+}, Gd^{3+} and Fe^{3+} [114]. The association of ions is commonly interpreted to occur along the PtPt axis [119], but configurations in which the bonding occurs on the ligand scaffolding have been proposed [120]. The mechanisms behind these processes are not well understood, and the bonding of the PtPOP with other components presents as a molecular playground for studying photophysical and bonding processes with transition metals.

The IrDimen system exhibits a similar reactivity in solution. $Ag(PPh_3)_2^+$ and $Au(PPh_3)_2^+$ ($PPh_3 =$ Triphenylphosphine) have been reported to associate along the Iridium axis in solution [113]. In addition to this, the increased flexibility of the dimen ligands allows for different bonding geometries than those possible in the PtPOP system. The complex has been shown to encapsulate an Ag^+ ion in solution, bonding the ion centrally in the complex. In direct opposition to the PtPOP system, where photoexcitation increases the binding constant, the ion is ejected following photoexcitation restoring the starting complex. [43] As a result the IrDimen

system offers opportunity to study bond breakage on ultrafast timescales, on top of the possibilities of the PtPOP molecule.

A unique commonality between these tri-metallic complexes is that the bonding relies solely on the formation of a metal-metal bond in the ground-state. The d^8d^8 complexes discussed in sec. 7 do not exhibit attractive forces between the metal atoms in the ground state, the bonding between metals and ligand scaffolding maintains the structure. The additional metal atoms, or ion, however bonds directly and solely to the metal atoms of the complex. The nature of this metal-metal bond is not well understood and will analyzed in this chapter.

This chapter will contain the investigation of three of tri-metallic complex systems. In the first section the bonding of MPtPOP (M= Ag^+, Tl^+) will be discussed in the ground state and following photexcitations. The second section will discuss the dissociation reaction of AgIrDimen.

8.1 Ultrafast structural dynamics in MPtPOP

The association process of metal ions to PtPOP can be tracked in both the absorption and the emission spectra. Fig. 8.1 depicts the absorption and emission spectra of PtPOP in the presence of 0 mM, 1.7 mM and 144 mM of Ag^+ ions in solution. A low concentration of silver ions induces only a small shoulder in the absorption spectrum, but the emission spectrum is nearly completely shifted towards the emission of the AgPtPOP* component at 556 nm. This can be attributed to the increasing bonding constant in the excited state resulting in considerable association following photoexcitation [44]. Under sufficiently high concentrations of Ag^+, the emission will shift towards the Ag_2PtPOP* emission at 610 nm, as the majority of the photoexcited complexes form bonds to two ions before emitting. The wavelenghts of absorption and emission maxima of M_nPtPOP (M=Ag,Tl) are summarized in Tab. 8.1.

The mechanism behind the formation of these metal-metal bonds, in which the ions in solution form a direct bond to the transition metal of the complex, is not well understood and will be discussed in this chapter. This chapter will summarize the key findings of **Paper I**, into which the majority of my analysis on this system was incorporated.
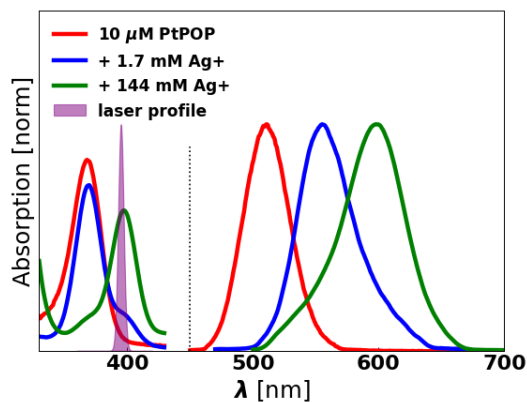
Figure 8.1: Absorption and emission spectra of PtPOP, AgPtPOP and Ag$_2$PtPOP. 10 μM solution of PtPOP are surrounded with 0 mM, 1.7 mM and 144 mM of Ag$^+$ ions in solution. In each solution there is 1 mM triflic acid per mM Ag$^+$ to suppress silver nanocluster formation. Small Ag$^+$ concentrations only lead to a small change in the absorption spectra, but change the emission considerably due to the significantly increased bonding constant in the excited state. Under sufficiently high concentrations Ag$_2$PtPOP* is formed in the solution resulting in emission with a wavelength shifted even further. The laser profile corresponds to the profile used during the X-ray solution experiment.

Table 8.1: Absorption and emission maxima wavelengths of PtPOP, Ag_nPtPOP and Tl_nPtPOP. The $d\sigma*p\sigma$ numbers correspond to the maxima of the broad peaks. The numbers in parenthesis correspond to spin forbidden transitions into the triplet state.

	PtPOP	Ag_nPtPOP	Tl_nPtPOP
Absorption [nm]		n = 1	n = 1
dσ*pσ	368, (452) [44]	400 [117]	390 [44]
dπpσ	284, (315) [96]		
Emission [nm]			
Flour.	400 [44]		
Phos.	513 [44]	560 [117]	559 [44]
Absorption [nm]		n = 2	n = 2
		(M_2PtPOP not	present in GS)
Emission [nm]			
Flour.			
Phos.		610 [117]	588 [44]

8.1.1 Sample systems

Previous TR-XSS studies on AgPtPOP [117] and TlPtPOP [115] were conducted at synchrotron sources and focused on the association of metal ions through the increase of the binding constant in PtPOP complexes following photexcitation. The metal ions associate along the platinum axis forming a metal-metal bond to the nearest platinum. Fig 8.2 depicts the structures of A) PtPOP, B) AgPtPOP and C) TlPtPOP, with indication of the metal-metal distances used as structural parameters. The sample systems were measured in identical circumstances during the same beamtime as the data presented in sec. 7.3.1. All 3 samples were excited with 395 nm 3 uJ laser pulses. As shown in Tab. 8.1, this laser wavelength is very close to the absorption peaks of AgPtPOP (400 nm) and TlPtPOP (390 nm), but excited the PtPOP far off resonance (370 nm).
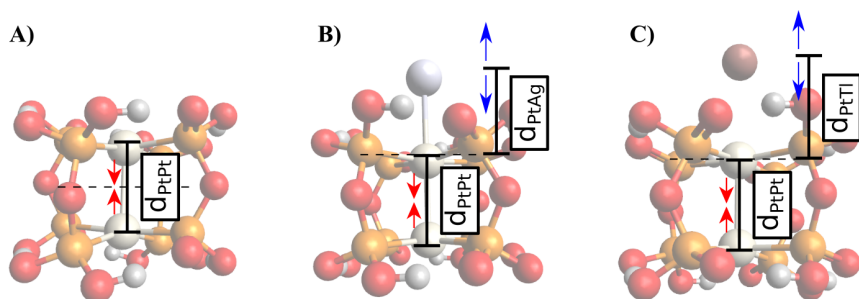
Figure 8.2: Atomic structures of A) PtPOP, B) AgPtPOP and C) TlPtPOP. The molecular structures correspond to the structurally optimized ground state structure discussed below. The marked distances d_{PtPt} and d_{PtM} correspond to the structural degrees of freedom of the complex. Made using Avogadro [93]. Adapted from **Paper I**
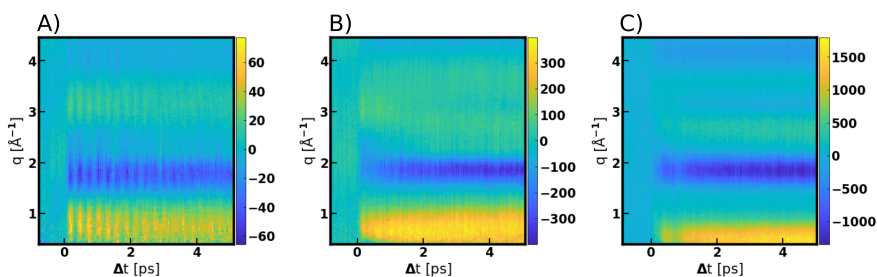
Figure 8.3: Colorpots of ΔS_0 for A) PtPOP, B) AgPtPOP and C)TlPtPOP. Adapted from **Paper I**

8.1.2 Model independent analysis

The measured data was reduced and separated into ΔS_0 and ΔS_2 as discussed in sec. 5.2. Fig 8.3 depicts the isotropic difference scattering signals for A) PtPOP, B) AgPtPOP and C)TlPtPOP. The details and the analysis of the PtPOP measurement has been reported by Haldrup *et al.* [97], and are summarized in sec. 7.3.1.

The Singular Value decomposition of the isotropic difference scattering signals ΔS_0 are depicted in Fig 8.4. Panel A) depicts the first left singular components of the three samples. They all share a strong positive peak at low q and a negative peak at $1.8\,\text{Å}^{-1}$, but differ above 2^{-1}.
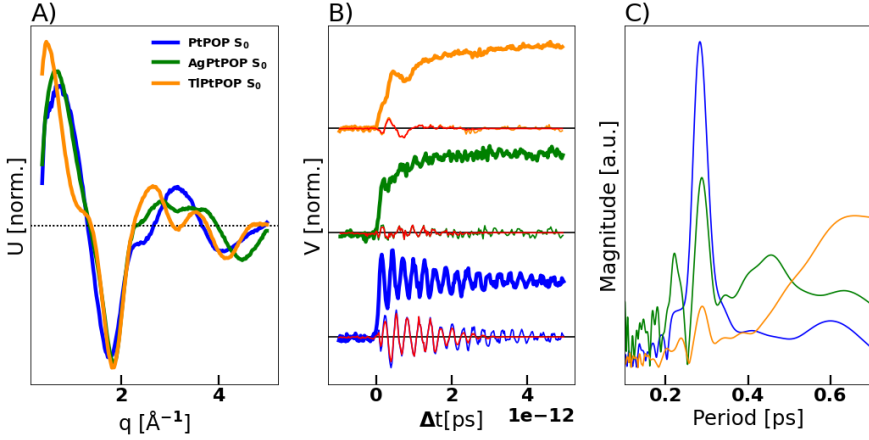
Figure 8.4: First component of the singular value decomposition for the data sets shown in Fig. 8.3. The left singular components A) all show a strong positive signal towards low q and a strong negative signal at $\sim 1.8\,\text{Å}^{-1}$, but differ in the oscillations following that peak. The right singular values time traces B) exhibit oscillations, which are transient for the MPtPOP systems and dephase over the first picoseconds for the PtPOP system. The oscillatory structural signal (OSS) is taken from all traces for further analysis and Furier transformed into C). A Gaussion window was applied (ref) to reduce the impact of artfacts in regions without oscillations. All 3 systems exhibit an oscillation at around $\sim 0.29\,\text{ps}$, the MPtPOP systems additionally exhibit longer periods at 0.4 ps (AgPtPOP) and 0.7 ps(TlPtPOP). Adapted from **Paper I**

The right singular time-traces are depicted in panel B), showing transient oscillations in the MPtPOP systems and an oscillations with longer coherence time in the PtPOP system. A Gaussian window with 1 ps fwhm centered at $\Delta t = 1$ ps is applied to the oscillatory structural signal is taken from the time-traces to focus on delays directly following photoexcitation. The Fourier transforms of these traces are depicted in C). A period of 0.29 ps is identified in all systems, and it is the nearly sole mode in the PtPOP measurement. The MPtPOP measurements exhibit additional periods, ~ 0.4 ps for AgPtPOP and ~ 0.7 ps for TlPtPOP. The time constant found in this analysis are expected to be resolved in the structural fitting further below.

8.1.3   Structural optimization

The structural parameters describing the inter-metal distances of the complexes, depicted in Fig 8.2, were optimized to match the simulated scattering signal against the data. $\Delta S_0(\Delta t=4\,\text{ps})$ was used for the structural optimization using Eq. 6.5. The platinum atoms were constrained to symmetric positions around the ligand scaffolding center of mass and the external metal atom was constrained to positions along the PtPt axis. The solvation cage scaler β was tied to the solute scaler $\beta=\alpha$ to stabilize the fit. Fig. 8.5 shows the result of the structural optimization for A) AgPtPOP and B) TlPtPOP.

   The first panel of A) depicts the fit using the optimized structure, the data and the residual. The residual is mostly structure-less for q<4.5 Å^{-1} . The second panel depicts the individual components to scale, highlighting that the difference scattering signal is primarily composed out of ΔS_{Solute} and ΔS_{Heat}. The third panel depicts the fit of $\Delta S_2(\Delta t=4\,\text{ps})$ using the structure obtained from the ΔS_0 optimization. The solute scaler had to be decreased by 32 % compared to the istropic fit to match the magnitude of the measured signal. The structural signal appears slightly shifted towards lower q-values in comparison to the data, resulting in an oscillation in the residual. The structural parameters are listed in Tab. 8.2. $d_{PtPt,Gs}$ decreases from 3.03±0.04 Å by $\Delta d_{\text{PtPt}}=0.25\pm0.08$ Å, which is comparable to results reported for PtPOP. $d_{\text{PtAg,GS}}$ increases following the photoexcitation from 2.87±0.12 Å by 0.19±0.04 Å.

   The TlPtPOP fit in the first panel of B) matches the shape of the data well, leaving only an unstructured residual. The second panel depicts the contributions of ΔS to scale, showing that ΔS_{Solute} comprises a larger part of the total signal, which is expected from the stronger scattering of the Thallium in comparison to silver. $d_{PtPt,Gs}$ contracts from 3.12±0.12 Å by 0.28±0.08 Å, the ground state distance being slightly longer than the ∼2.98 Å of PtPOP. $d_{PtTl,GS}$ is with 3.14±0.16 Å longer than the silver parameter, but contracts following photoexcitation by 0.31±0.24 Å. The ΔS_0 optimized structure matches the ΔS_2 leaving no structure in the residual, shown in the last panel, with the solute scaler reduced by 44 % compared to the isotropic one.

   In both cases α had to be reduced to match the ΔS_2 signal. The

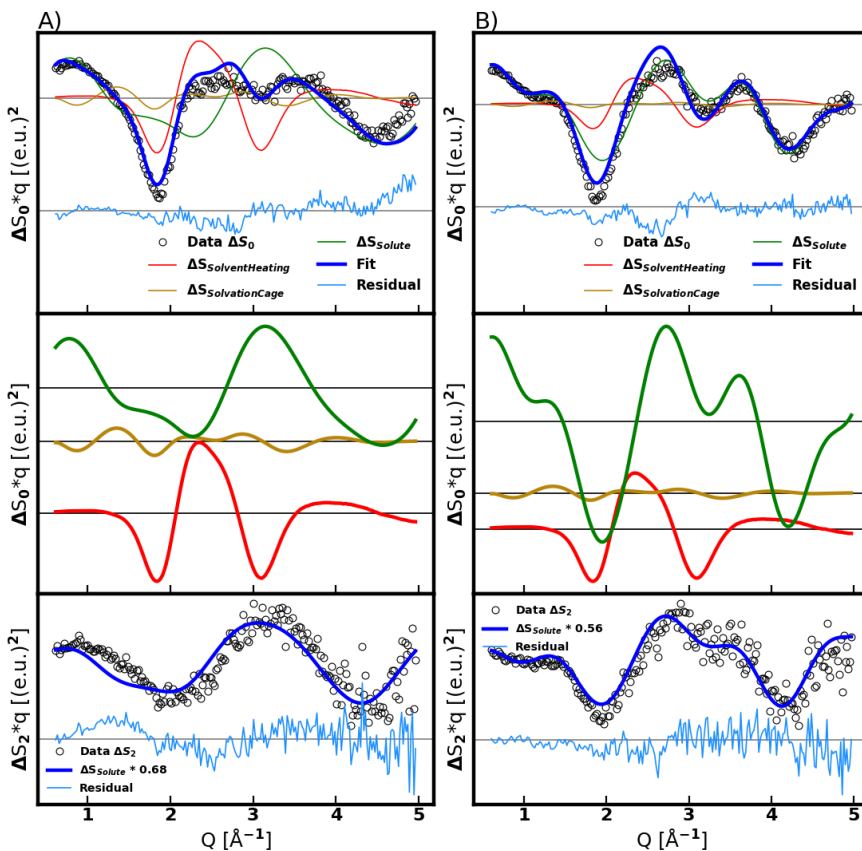**Figure 8.5:** Structural optimization results of A) AgPtPOP and B) TlPtPOP. The first panels show the fit on top of $\Delta S_0(\Delta t{=}4\,\text{ps})$. The second panels show the different model components to scale as in the fit. The last panels show the calculated anisotropic difference scattering signals using the optimized structure scaled to $\Delta S_2(\Delta t{=}4\,\text{ps})$. Adapted from **Paper I**

Table 8.2: Structural parameters of A) AgPtPOP and B) TlPtPOP optimized through a minimization of χ^2. Adapted from **Paper I**

Parameter	AgPtPOP	TlPtPOP
$d_{PtPt,GS}$ [Å]	3.03±0.04	3.12±0.12
Δd_{PtPt} [Å]	0.25±0.08	0.28±0.08
$d_{PtM,GS}$ [Å]	2.87±0.12	3.14±0.16
Δd_{PtM} [Å]	-0.19±0.04	0.31±0.24
α [%]	34±10	26±16

anisotropic signal only follows the $\cos^2$ distribution for perfectly linear transition dipole moments. If the transition dipole is less well defined, as might be the case through external metal atom, the observed effect will be reduced. Additionally, due to the temporal compression of the laser pulse, the laser might induce simultaneous multiphoton excitation events in the sample. As their transition dipole moment would likely not match the HOMO/LUMO transition, they would not contribute to the anisotropic signal but the isotropic one. Additional reductions may arise from the dephasing of the molecules rotating in solution.

In addition to the axial bonding of the external metal atom, as shown in Fig. 8.2, a structure has been proposed by Kruppa *et al.* [120] in which the external atom bonds to the ligand scaffolding in AgPtPOP. This configuration will be discussed as the *orthogonal* structure from now on, as opposed to the *axial* one. Fig 8.6 depicts these configuration for AgPtPOP and, TlPtPOP. The findings from DFT calculations by Kruppa *et al.* show a lower energy for the orthogonal configuration than the axial one.

The structure of the orthogonal configuration was optimized similar to the axial one. The platinum atoms were constrained to symmetric positions along the PtPt axis, while the external metal atom was constrained to positions orthogonal to this axis starting from the position optimized. A separate set of ΔS_{cage} was simulated for these structures.

Fig 8.7 depicts the result of this optimization. The AgPtPOP fit A) matches the structure of the signal well both for ΔS_0 and ΔS_2. The residual is slightly more structured in the isotropic and slightly less structure in the anisotropic, compared to the axial fit. This results in a reduction of χ^2 from χ^2_{axial}5.06 to χ^2_{ortho} 4.88, which is within the certainty range.
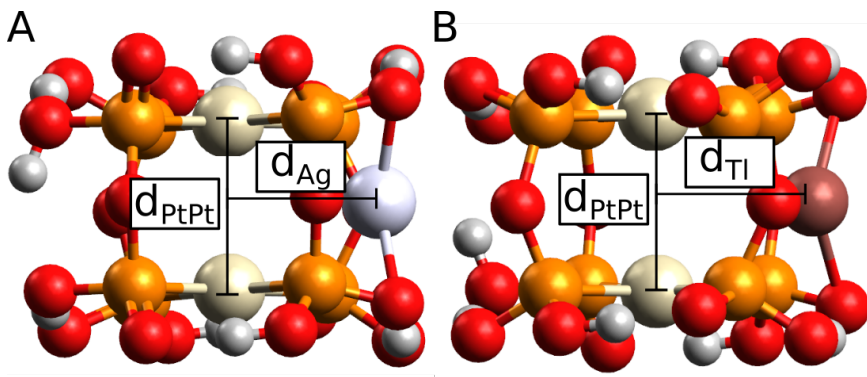
Figure 8.6: Molecular structures of A) AgPtPOP and B) TlPtPOP in the *orthogonal* configuration. The molecular structures correspond to the structurally optimized ground state structure discussed below. The marked distances d_{PtPt} and d_M correspond to the structural degrees of freedom of the complex. Made using Avogadro [93]. Adapted from **Paper I**

The residual TlPtPOP from the fit B) is notably more structured, as the model is unable to describe the kink in the curve at $1.3\,Å^{-1}$. This causes an increase from χ^2_{axial} 10.41 to χ^2_{ortho} 21.40, marking a substantial decrease in fit quality. The second panel shows that a much larger part of the signal is realized through the solvent ΔS_{Heat} than ΔS_{Solute}. The last panel shows that the model is unable to describe the anisotropic data well, and the excitation fraction had to be amplified in comparison to the ΔS_0, which is physically implausible.

The structural parameters for both system are listed in Tab. 8.3. The Δd_M distances of 2.75±0.33 Å (AgPtPOP) and 2.79±0.17 Å (TlPtPOP) are considerably shorter than the 4.12 Å predicted by Kruppa *et al.*, in a way that would likely be prohibited due to steric hindrance.

Based on these finding, the axial structure was deemed to be the more likely one for both systems.

8.1.4 Time-resolved analysis

The structural parameters of the ground state were used to optimize the excited state structure for every time-bin of $\Delta S_0(q,\Delta t)$. The ground state
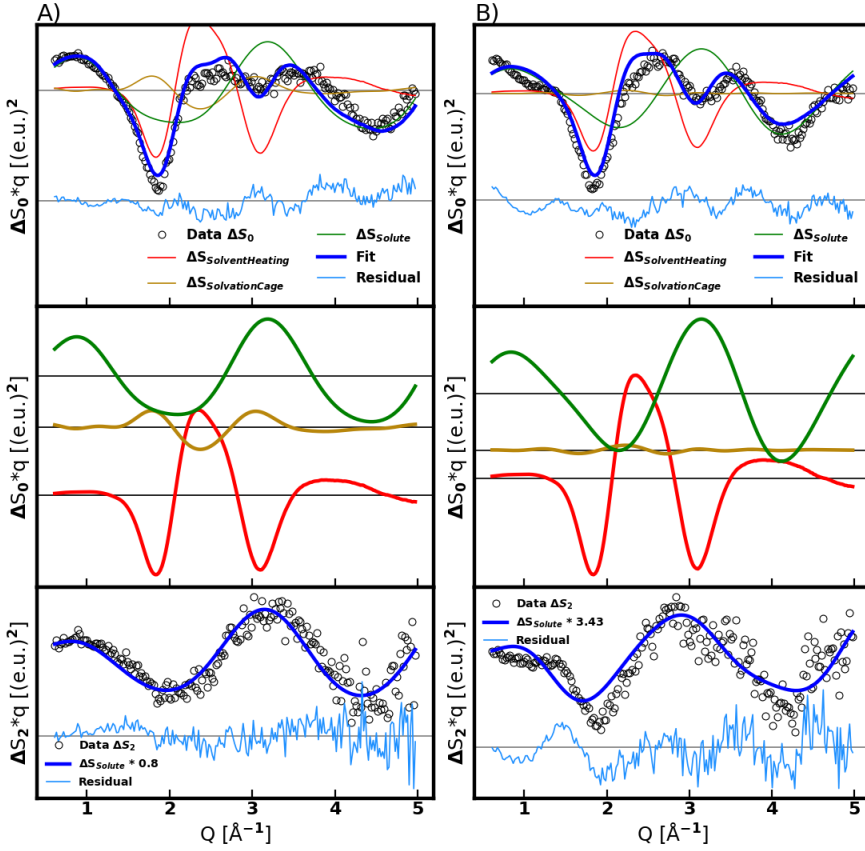
Figure 8.7: Structural optimization of A) AgPtPOP and B) TlPtPOP using orthogonal structures. Adapted from **Paper I**

Table 8.3: Orthogonal structure parameter. Adapted from **Paper I**

Parameter	AgPtPOP	TlPtPOP
$d_{PtPt,GS}$ [Å]	3.01±0.27	3.12±0.08
Δd_{PtPt} [Å]	0.30±0.27	0.30±0.17
$d_{M,GS}$ [Å]	2.75±0.33	2.79±0.17
Δd_M [Å]	-0.05±0.15	0.34±0.30
α [%]	14±4	12±7
ΔT [K]	0.83±0.08	0.77± 0.10

distances $d_{PtPt,GS}$ and $d_{PtM,GS}$ were kept constant alongside the solute scaler α. Fig. 8.8 depicts the time-resolved structural and solvent parameter curves of AgPtPOP.

The left panel shows the inter-metalic distances as a function of time alongside the kinetic functions describing functions describing them. The parameters of the metal atoms are described through Eq. 8.1 and Eq. 8.2:

$$
\begin{aligned}
d_{PtPt}(\Delta t) =& IRF * (d_{PtPt,GS} + H(\Delta t) \\
& \cdot (\Delta d_{PtPt,1} + \Delta d_{PtPt,2}(1 - \exp\left(-\Delta t/\tau_{PtPt,1}\right)) \\
& + \Delta d_{osc} \cos\left(2\pi \cdot \Delta t/T_{osc}\right) \exp\left(-\Delta t/\tau_{osc,Pt}\right)))
\end{aligned} \quad (8.1)
$$

$$
\begin{aligned}
d_{PtM}(\Delta t) =& IRF * (d_{M,GS} + H(\Delta t) \cdot (\Delta d_{PtM,1} \\
& + \Delta d_{PtM,2}(1 - \exp\left(-\Delta t/\tau_{PtM,1}\right)) \\
& + \Delta d_{osc} \cos\left(2\pi \cdot \Delta t/T_{osc}\right) \exp\left(-\Delta t/\tau_{osc,M}\right)))
\end{aligned} \quad (8.2)
$$

$d_{PtPt,ES}$ contracts following the photoexcitation and approaches the equilibrated distance over the first few picoseconds with $\tau_{PtPt,1}$ 1.58$\pm$0.18 ps. The parameter curve is superimposed with an oscillation T_1 0.28$\pm$0.01 ps dephasing with $\tau_{osc,Pt}$ 1.71$\pm$0.69 ps over the first picosecond. The $d_{PtAg,ES}$ exhibits similar dynamics, expanding with $\tau_{PtPt,1}$ 0.98$\pm$0.18 ps while oscillating with T_1 0.36$\pm$0.02 ps.

The temperature ΔT of the surrounding solvent increases with $\tau_{\Delta T}$ 1.24$\pm$0.04 ps, using Eq. 8.3. The solvation cage scaler ϵ reaches a maximum within the time-resolution of the experiment, determined with Eq. 8.4. The function was extended with a nonphysical linear term $m \cdot \Delta t$ to match the continued increase over the picoseconds following photoexcitation:

$$
\begin{aligned}
\Delta T(\Delta t) =& IRF * (\Delta T_{max} * H(\Delta t - t') \\
& * (1 - \exp\left(-(\Delta t - t')/\tau_{\Delta T}\right)))
\end{aligned} \quad (8.3)
$$

$$
\begin{aligned}
\epsilon_{AgPtPOP}(\Delta t) =& IRF * (\epsilon_{max} * H(\Delta t - t') \\
& * (1 - \exp\left(-(\Delta t - t')/\tau_\epsilon\right) + m \cdot t))
\end{aligned} \quad (8.4)
$$
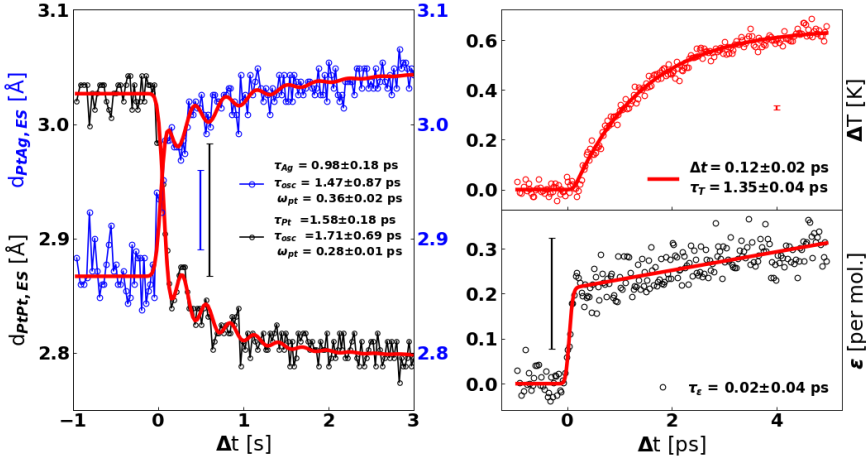
Figure 8.8: Time-resolved structural parameter optimization of AgPtPOP. The d$_{PtPt,ES}$ The parameter curves are fitted with functions (red lines) to derive time constants. Adapted from **Paper I**

The time-resolved structural optimization results for TlPtPOP are depicted in Fig. 8.9 alongside their kinetic fits using Eq. 8.5, Eq. 8.2, Eq. 8.3 and Eq. 8.6. An nonphysical exponential term with a short decay time was added to describe the cage for short delays. d$_{PtPt,ES}$ contracts within the time-resolution of the experiment and remains constant from thereon. d$_{PtPt,ES}$ contracts over several picoseconds oscillation with a period of T$_{PtTl}$ 0.80±0.04 ps:

$$d_{PtPt}(\Delta t) = IRF * (d_{PtPt,GS} + H(\Delta t) \cdot (\Delta d_{PtPt}))) \tag{8.5}$$

$$
\begin{aligned}
\epsilon_{TlPtPOP}(\Delta t) = & IRF * (\epsilon_{max} \cdot H(\Delta t - t') \\
& \cdot (1 - \exp\left(-(\Delta t - t')/\tau_\epsilon\right) \\
& - \exp\left(-(\Delta t - t')/\tau_{\epsilon,2}\right)))
\end{aligned}
\tag{8.6}
$$

The kinetic fit parameters for AgPtPOP and TlPtPOP are listed in
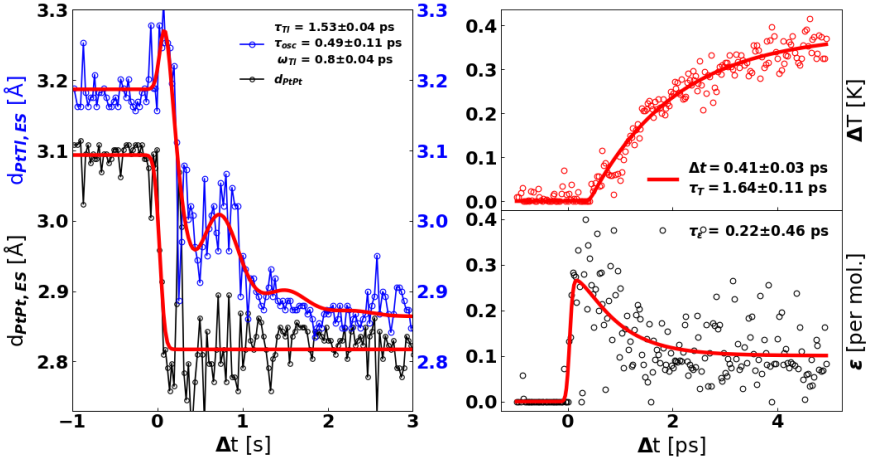
Figure 8.9: Time-resolved structural and solvent parameter for TlPtPOP as well as their kinetic fits. $d_{PtPt,ES}$ contracts within the time resolution of the experiment. $d_{PtM,ES}$ contracts with τ_{PtTl} 1.53±0.04 ps exhibiting a transients oscillation with T_{PtTl} 0.80±0.04 ps. Adapted from **Paper I**

Table 8.4: Summary of the kinetic fit parameters of A) AgPtPOP and B) TlPtPOP time-resolved structural fitting results. Adapted from **Paper I**

	A)	AgPtPOP	
	T_{osc} [ps]	τ_{osc} [ps]	τ_1 [ps]
d_{PtPt}	0.28±0.01	1.71±0.69	1.58±0.18
d_{PtAg}	0.36±0.02	1.47±0.87	0.98±0.18
ϵ			0.02±0.04
ΔT			1.35±0.04
	B)	TlPtPOP	
	T_{osc} [ps]	τ_{osc} [ps]	τ_1 [ps]
d_{PtPt}			
d_{PtTl}	0.8±0.04	0.49±0.11	1.53±0.04
ϵ			0.22±0.46
ΔT			1.64±0.11

127

Tab. 8.4. In both systems the longer oscillation period found in the SVD analysis was identified as a structural motion in the d_{MPt} parameter. The shorter $0.28\,ps$ mode, observed in the SVD anlysis for both MPtPOP systems, was only identified in the $d_{PtPt,ES}$ curve of AgPtPOP.

8.1.5   Electronic structure

Both complexes, AgPtPOP and TlPtPOP, appear similar but exhibit different dynamics following photoexcitation. The electronic structure of the systems should be able to elucidate these differences. The PtPOP electronic structure, shown in Fig. 8.10 A), can be described with a generic MO-scheme highlighting the $5d\sigma*$ HOMO and $6p\sigma$ LUMO. During the complexation with the external metal ion, these molecular orbitals mix with the metal ion orbitals. The filled 6s orbital of the Thallium ion mixes with the molecular orbitals of PtPOP, being positioned energetically lower than the PtPOP HOMO. This causes the nature of the HOMO/LUMO transition to remain from antibonding to bonding, causing the photoexcitation to yield a contraction. The silver ion on the other side provides an empty orbital and therefore providing space for electrons already within the system. The new orbital is positioned in the previous HOMO/LUMO gap. During photoexcitation the bonding does not unambiguously increase in the system, causing the silver atom to remain in place in relation to the molecule center of mass. This is supported by the shape and energetic levels of molecular orbitals calculated by Kong *et al.* [119] Similar argumentation strategies are used by Clodfelter *et al.* [44] to describe the orbital mixing of TlPtPOP and by Sykes & Mann [113] describing an externally bound ion to IrDimen.

8.1.6   Conclusions

PtPOP bonds with metal ions in solution, the metal atoms are bonded along the PtPt axis in the molecules as shown in this analysis. Their electronic structure is strongly influenced by the nature of the bonding ion. The Platinum atoms contract following photoexcitation is a comparable manner to the d_{PtPt} in PtPOP, but additional structural dynamics occur

A)   B)   C)

Figure 8.10: Molecular orbital scheme of the electronic structure of A) PtPOP, B) AgPtPOP and C) TlPtPOP. The PtPOP structure is the generic MO-scheme between two atoms as shown previously [38]. During the bonding with the Thallium atom the filled 6s orbital mixes with the electronic structure. The overall nature of the HOMO/LUMO $d\sigma*p\sigma$ transition is preserved, resulting in a contraction in the system following photoexcitation. The 5s of the silver ion is empty when bonding with the complex. The nature of the transition is changed and the bond order no longer increases unambiguously following photoexcitation, resulting in the expansion of d_{PtAg} . Taken from sec. 9

in the PtM axis. The metal atoms oscillate on the excited state potential surfaces as energy is dissipated while they approach the excited state equilibrium distance. The TR-XSS has helped to confirm and define the structure of the structure of MPtPOP, where theoretical calculations have led to ambivalent results. This information was then used to elucidate the electronic structure that would lead to such structures and dynamics following photoexcitation The metal-metal bonding and their perturbation through photoexcitation yield insight into the field of tri-metallic complexes as a whole.

8.2 Ultrafast deencapsulation in AgIrDimen

The association of metal ions with d^8d^8 transition metal complexes is limited to outward facing positions for PtPOP, due to the inflexible ligand scaffold and short d_{PtPt} distance of $\sim$2.95 Å. In transitions metal complexes with a more flexible structure, the additional metal ion is able
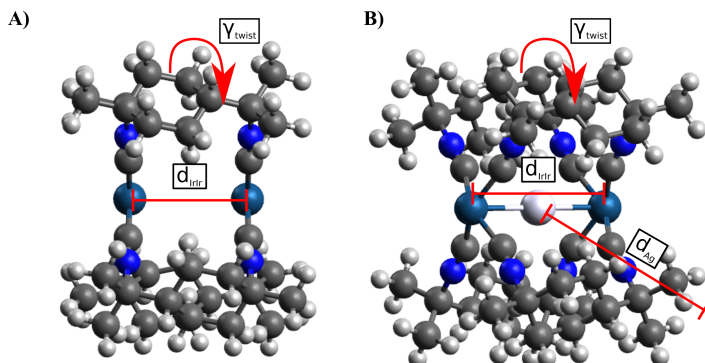
Figure 8.11: A) IrDimen and B) AgIrDimen complex structure visualized using Avogadro [93], together with their structural parameters.

to associate at the center of the complex, bonding to both metal atoms simultaneously.

This phenomenon was first described by Sykes and Mann 1988, synthesized this compound during an attempt to generate d8-d7 mixed metal transition metal complexes in DMSO. IrDimen encapsulates Ag^+ ions in solution, bleaching the characteristic absorption of IrDimen and turning the solution clear. The formed tri-metallic complex is sufficiently stable to be crystallized. Following photo-excitation with ultraviolet light, the Ag^+ is ejected restoring the characteristic absorption of IrDimen reversibly. [43]

The initial investigation was able to locate the position of the encapsulated ion but offered little insight on neither the electronic structure nor the reaction dynamics. The Ag^+ ion is located centrally in the complex between the two Iridium atoms, shown in Fig. 8.11 alongside the structural parameters.

The energetic parametrization of AgIrDimen in relation to IrDimen can be described in a Frank-Condon diagram, shown in Fig. 8.12 in relation to the d_{IrIr} coordinate. As discussed in section 7.1, IrDimen has two stable ground state conformers in solution with different d_{IrIr} which can be selectively excited with different wavelengths. The distance d_{IrIr} in the AgIrDimen expands to accommodate the encapsulated ion. The excitation with near-ultraviolet light is depicted to excite the complex onto
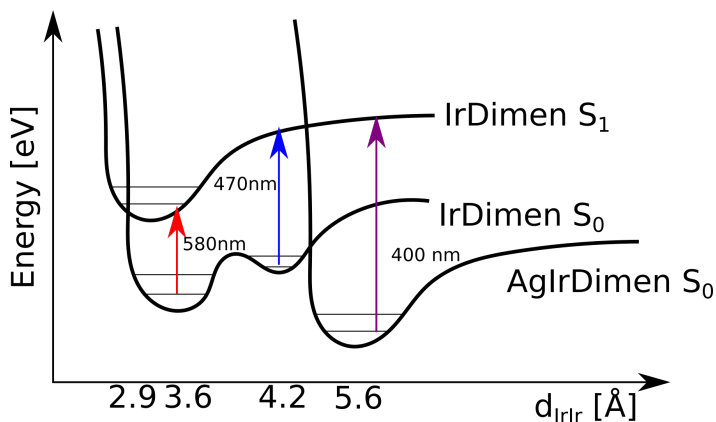
Figure 8.12: Frank-Condon Diagram of IrDimen and AgIrDimen in relation of d_{IrIr} against the energy in the system. The two ground states of IrDimen can be excited with different optical wavelenghts, while the AgIrDimen can be transferred into the IrDimen S_1 with ultraviolet excitation, ejecting the Ag^+.

the IrDimen S_1 excited state potential surface following the expulsion, but the process could also lead to the IrDimen relaxing into the ground state based on the information available at the time of the experiment. The excited state potential surface is depicted as a singlet, but the information available does not exclude spin-forbidden photoexcitation. The analysis of the system presented here is preliminary and further analysis has to be done for a full interpretation of the available data.

8.2.1 Experimental parameters

The experiment was conducted in 2018 at the LCLS facility under the proposal *Revealing the Ultrafast Dynamics and Hidden Symmetries During Ion- Release from a Transition-Metal Complex*. The sample was prepared as a 30 mM solution of IrDimen in acentonitrile. The data analyzed in this work reduced during the beamtime. The sample was excited with 400 nm 70 fs laser pulses.
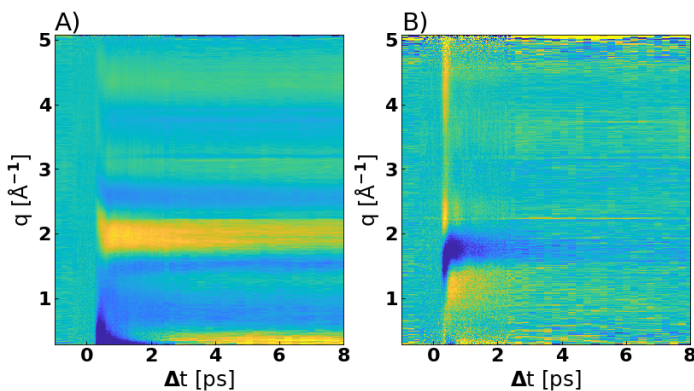
Figure 8.13: Difference scattering signal of AgIrDimen in acetonitrile, A) Isotropic difference scattering ΔS_0 and B) anisotropic difference scattering ΔS_2. The isotropic scattering signal features a strong transient negative signal at low q turning positive for longer delays. The rest of the q-range forms in the first $\sim$0.5 ps and remains stable. The anisotropoic signal B) is dominated by the optical Kerr effect but exhibits some additional signal for short delays.

8.2.2   Model independent analysis

The binned difference scattering signals separated into ΔS_0 and ΔS_2 are depicted in Fig. 8.13. The isotropic difference scattering signal A) exhibits a strong negative transient signal at low q for the first picosecond, which is later replaced by a strong positive signal. Additional oscillations along the q-axis, with notable maxima around 2, 3 and 4.5 Å^{-1}, appear within the first few hundreds of femtoseconds and remain stable. The isotropic signal also exhibits a weak sharp features around, amongst others, 3 Å^{-1}. These features can be attributed to silver nanocrystals that have formed in solution and are heated by the pump laser pulse.

The anisotropic signal primarily feature strong transient signals following photoexcitation, with a negative peak at around 1.8 Å^{-1}. Such as feature would be expected from the optical Kerr effect in acetonitrile. As this feature is expected to decay with a time constant of 1.5$\pm$0.5 ps [80]. There is longer lasting structure within the system. Going forwards, the analysis shown here will focus on ΔS_0.

Fig. 8.14 depicts the SVD of the AgIrDimen isotropic ΔS_0 scattering.
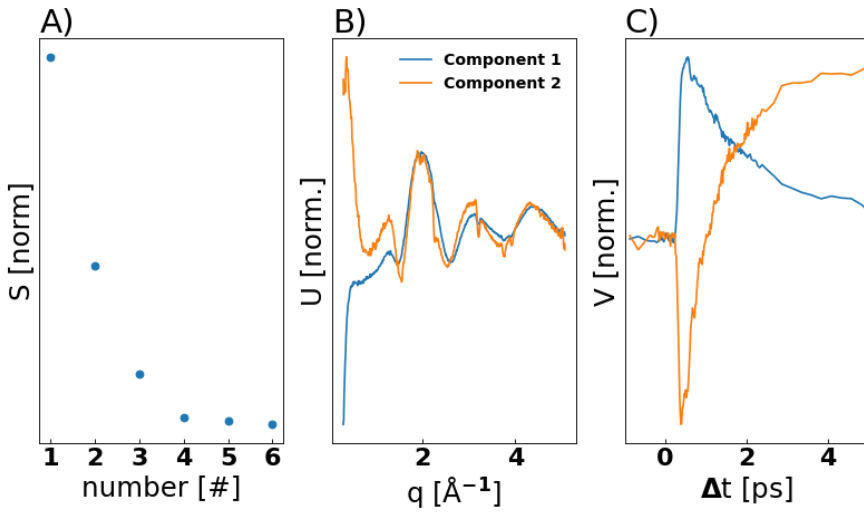
Figure 8.14: Singular Value Decomposition of the isotropic difference scattering signal ΔS_0 of AgIrDimen. A) depicts the component magnitudes S in descending order. The right singular components of the first two, which A) shows to be dominant, are depicted in B). They both show oscillations in the signal from q 2 to $5\,\text{Å}^{-1}$, and differ primarily in low q area. The time traces in C) highlight that the components are substituted from one another over the first 4 picoseconds.

The magnitude of the components in A) shows that the first two components comprise a large share of the total signal. These first components are depicted in B) and show great similarity in the q range larger than $\sim 2\,\text{Å}^{-1}$. The right singular time-traces of the components shown in C) suggests that the components are substituted for one another, describing the change in low q. As a result, the structure of the signal at larger q can be interpreted as growing in fast and remaining constant afterwards.

8.2.3 Structural optimization

The previous analysis has suggested that the signal at low q, which is generally strongly influence by solute-solvent interactions, changes strongly on the picosecond scale. However, at the time of analysis, no simulated ΔS_{cage} were available for the system. As a result the data q<$1\,\text{Å}^{-1}$ was omitted from further analysis. The results of the structural optimization of $\Delta S(\Delta t$=6 ps, 1<q <5) are depicted in Fig. 8.15. The optimized structural parameters are shown in Fig. 8.11.

The distance between the Iridium atoms $d_{IrIr,GS}$ was determined at 5.40±0.06 Å with the Ag$^+$ ion located at 0±0.25 Å. In the excited state, $d_{IrIr,ES}$ converges at 2.82±0.05 Å. $d_{IrIr,ES}$ matches the $d_{IrIr,ES}$ of IrDimen determined in previous studies [77] and this thesis sec. 7.1 resonable well. From these findings it can be reasoned that the complex remaining after the expulsion relaxes into the IrDimen excited state, as proposed by Fig. 8.12.

8.2.4 Time-resolved analysis

Having derived the structural parameters of the ground state and the equilibrated excited state, the next step is to track the atoms during the expulsion process.

In the previous analysis of IrDimen, shown in sec. 7.3.3, it was shown that the twisting of the ligand scaffolding to accommodate for the the decresed d_{IrIr} primarily occurs at Δt>2 ps. This parameter is thus omitted in the analysis for Δt<2 ps shown in this section.

A difficulty in the analysis is the distinguishing between movement along the d_{IrIr} and the d_{Ag} parameter. Fig. 8.16 depicts the fitting of
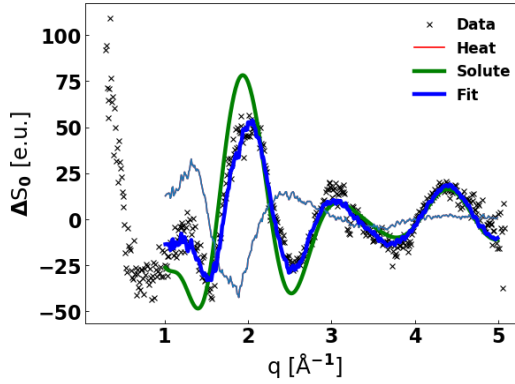
Figure 8.15: Fit of the higher q part of the isotropic scattering signal of AgIrDimen $\Delta S(\Delta t = 6\,ps)$. The data was fitted between 1 and $5\,\text{Å}^{-1}$ to avoid the strongly solvation dependent part observed in the model independent analysis.

A) $\Delta S(\Delta t=0.23\,ps)$ and B) $\Delta S(\Delta t=1\,ps)$ with structures in which either d_{IrIr} is expanded, or d_{IrIr} is contracted and the Ag^+-ion is expelled. In the fitted q-range $>1\,\text{Å}^{-1}$ the difference in ΔS for an identical solute scaler α is primarily in the position of the peak at $\sim 2\,\text{Å}^{-1}$. The shift of the peak at 2^{-1} towards hight q in comparison to the peak position in the equilibrated $\Delta S(\Delta t=1\,ps)$, could only be modelled by an expansion of d_{IrIr}.

The time-resolved structural optimization results are shown in Fig. 8.17 A). In the presented analysis the excited state the excited state ensemble is represented as a single structure. The inclusion of a range of more structures led to instabilities in the fitting parameters.

As discussed in sec. 7.3.3, IrDimen does not contract coherently following photoexcitation. Constraining the solute scaler led to the nonphysical appearance of a delay of 0.2 ps in the contraction of d_{IrIr} in the IrDimen analysis as a result. The AgIrDimen exhibits a similar behavior in the d_{IrIr} curve. The d_{IrIr} increases for short delays, after which d_{IrIr} abruptly decreases where, as discussed in Fig. 8.16, the structure with dissociated silver becomes the more probable.

The *Debye-Waller-esque* factor u_{Ag}, as used in Eq. 4.8, was dynamically chosen as $d_{Ag}/3$ to model and increase in spread of the distribution of
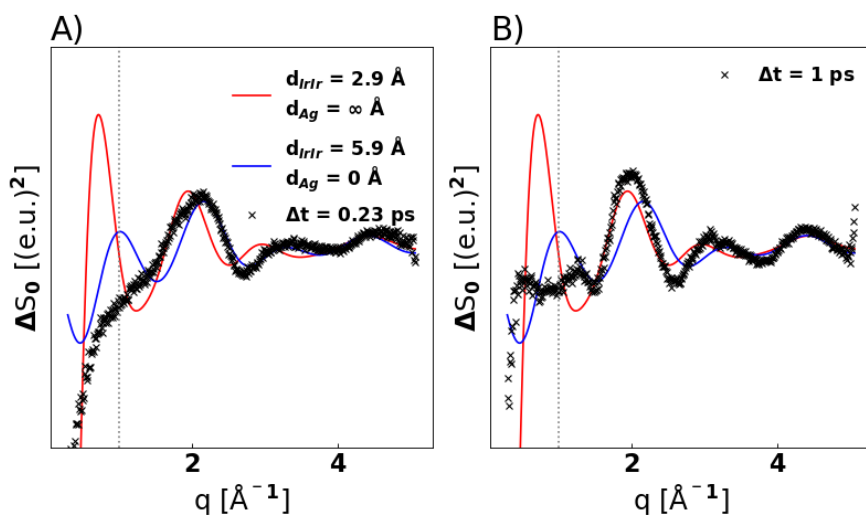
Figure 8.16: Comparison of the data to a model with expanded d_{IrIr} and a model with contracted d_{IrIr} with a dissociated Ag^+ for A) Δt=0.23 ps and B) Δt=0.23 ps. An expanded d_{IrIr} appears as the only way to model the peak at 2.3 $Å^{-1}$ for short delays, where it is shifted towards higher q-values in comparison to the excited state. For longer delays, the peak position approaches the shape of the dissociated structure. The ΔS_{Solute} differ the strongest for q $<1^{-1}$, where the analysis was omitted due to the lack of solvent terms.

distances with increasing d_{Ag}. The factor 3 was a compromise between too early delocalization of the ion, due to too large associated positional uncertainties, and nonphysical parameter curves due to artifacts of the form factor matching to the data in local minima. The convergence towards d_{Ag}=6 Å depicts such a minima, where the fit is only marginally better $\chi^2(d_{Ag}$=6 Å)=14.6 than for notably larger distances $\chi^2(d_{Ag}$=10 Å)=14.9.

The solute scaler is depicted in Fig. 8.17 B). The scaler was limited to values >0.25 $\cdot \alpha_{equi}$ to stabilized the fit and reaches its equilibrium value after ∼0.6 ps. With this information, the average speed of the Ag$^+$ was determined with a kinetic function comprising a linear fit convoluted with the IRF and a Heaviside function:

$$d_{PtPt}(\Delta t) = IRF * (H(\Delta t) \cdot v_{Ag} \cdot \Delta t) \qquad (8.7)$$

Omitting the data between 0.35 ps<Δt<0.6 ps, an average velocity of the Ag$^+$ of 1180 m/s was obtained. This speed is close to the speed of sound in acetonitrile (1278.01 m/s) [121]. Such as speed can only be realized in sufficient energy is deposited by the photon in the system by the excitation photon.

The encapsulation of the Ag$^+$-ion reduces the disorder in the liquid. For the association to occur with such a large reaction constant, as evident through the complete bleaching of a strongly absorbing solution, the free energy has to be reduced significantly in comparison to unbound IrDimen and silver in the solution. The 400 nm excitation delivers a total of 3.1 eV into the system upon absorption. The optical decay of IrDimen under emission of 710 nm [94] photons suggest that at least 1.74 eV remain in the excited state of the system following the structural rearrangement.

Accelerating an Ag$^+$-ion with a mass of 107.9 u to 1180 m/s requires 0.8 eV of total energy. This leaves 0.56 eV that can be dissipated into the solvent as the structure relaxes. This value is larger than the energy dissipated after an $S_{0,long}$ S_1 transition in IrDimen with 585 nm, where a total of 0.36 eV can be dissipated. The ejection of the Ag$^+$-ion at such speeds is therefore possible.
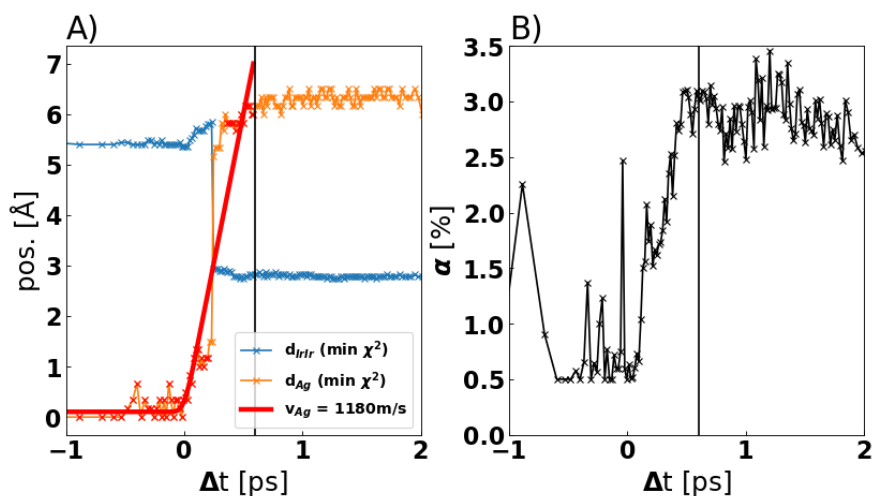
Figure 8.17: Time-resolved analysis of the photo dissociation of AgIrDimen. Panel A) depictes the structural parameter curves of $d_{IrIr,ES}$ and $d_{Ag,ES}$. The expulsion of the Ag^+ occurs perpendicular to the IrIr-axis and through a gap between the ligands. Structural parameters between $0.35\,ps < \Delta t < 0.6\,ps$, in which time the interconversion is likely to occur. B) depicts the solute scaler α. The scaler is limited to $\geq 0.5\,\%$ to stabilize the structures for short delays and reaches its excited state equilibrium at $0.6\,ps$.

8.2.5 Solvation shell

The description of solvation in this system has two main components, the solvation of the Ag^+, which forms a solvation shell with the solvent following ejection, the structure of which has been subject to debate [122, 123], and the solvation of the IrDimen unit. The acetonitrile surrounding the IrDimen interact with the solute and react to changes in structure and charge distribution.

The description of the Ag^+ ion itself also falls in principle into two components. In a first step, following the ejection, the ion is surrounded by solvent molecules. Until the ion has been slowed down sufficiently, and the adjacent molecules had enough to rearrange themselves, the ion experiences an average distribution of solvent molecules in its vicinity. In a secondary step the adjacent molecules align to form a solvation shell.

As discussed in the previous sections discussing IrDimen, the description of the solvation shell in both ground state and excited state has been subject to theoretical work [124] and proven difficult to apply in experimental analysis [77]. The encapsulation of the Ag^+ increases the charge of the from +2 to +3, would likely increase the order of the surrounding complexes. Future theoretical work on the solvation shell of this complexes could prove helpful in resolving the superposition of the excited state ensemble of AgIrDimen complexes.

8.2.6 Conclusions

In the analysis of this TR-XSS experiment, the structure of the ground state of AgIrDimen, the silver being encapsulated, was confirmed, and the electronic state after the ejection was identified as the excited state of IrDimen. The ejection of the Ag^+-ion was tracked, identifying the speed as close to the speed of sound. The analysis of the energy transfer in the individual processes suggested the plausibility of such as speed.

The large spread of the structural ensemble, also previously observed for pure IrDimen, resulted in some difficulties to describe the first 500 fs, but ultimately the measurement allowed the observation of the dissociative reaction.

8.3 Summary

The further complexation of d^8d^8 transition metal complexes leads, as already discussed in the introduction to this chapter, to a whole range of interesting properties and phenomena. The analysis of the MPtPOP system in sec. 8.1 investigated the association of metal ions in solution. The molecular and electronic structure of the complexes was determined, and oscillations in the data were linked to structural dynamics following photoexcitation. The analysis of the photophysical deencapsulation of AgIrDimen in sec. 8.2 found the structure of the ground and excited state following the photoexcitation, as well as derived the kinetics of the expelling of the ion.

Going forward, the association the field of tri-metallic complexes derived from d^8d^8 transition metal complexes allows for such a vast quantity of possible structures, that only a very small share could be investigated as part of this work.

Chapter 9

Future work

This thesis presents a broad spectrum of investigations of ultrafast structural dynamics and chemical reactions of IrDimen and PtPOP.

The structural implications of intersystem crossing have been investigated, and the distribution of structures in an ensemble of photoexcited molecules have been investigated with TR-XSS. The excitation wavelength dependent structural dynamics of PtPOP and IrDimen have been analyzed on the femtosecond timescale. The electronic transitions inducing oscillations in ground and exited state potential energy surfaces have been identified and linked to physical processes. By taking advantage of larger X-rays energies recently made available by the ongoing upgrade of the LCLS, this analysis was extended to investigate the parameter distributions inside an oscillation excited state ensemble and successfully linked to population dynamics in anharmonic potentials.

The formation, structure and structural dynamics of several tri-metallic complexes has been successfully identified. The structure, structural dynamics and electronic structure of TlPtPOP and AgPtPOP has been successfully identified with TR-XSS. The structure of AgIrDimen in solution has been determined and a preliminary analysis of the photodissociation reaction has been presented.

In the work done for this thesis, only a small share of the chemical reaction properties of d^8d^8 transition metal complexes and the metal-metal bonds they for could be investigated. As discussed in the introduction to chap. 8, the bonding occurs with a broad range different ions, which can be used to further study metal-metal bonds and to benchmark quantum chemical calculation tools.

In a broader sense, the continuous improvement of sources, such as the upcoming upgrade towards LCLS-II with its access to megahertz repetition rates, can extend this form of investigation towards more electron scarce materials and compounds. The methodology developed in this work for samples with strong scattering contrast can then be applied and used as a basis for the analysis of these sample systems. Ultrafast science as a whole will be able to answer interesting questions about fundamental problems for many years to come.

Bibliography

[1] A. H. Zewail, "Laser femtochemistry," *Science*, vol. 242, pp. 1645–1653, Dec. 1988.

[2] "The nobel prize in chemistry 1999." https://www.nobelprize.org/prizes/chemistry/1999/zewail/facts/. Accessed: 2022-10-14.

[3] W.C.Röntgen, "Über eine neue art von strahlen," *Annual report of the Physical-medical society*, 1985.

[4] J. R. Lakowicz, *Principles of fluorescence spectroscopy*. New York, NY: Springer, 3 ed., Aug. 2006.

[5] J. Petersen, N. E. Henriksen, and K. B. Møller, "Validity of the bersohn-zewail model beyond justification," *Chemical Physics Letters*, vol. 539-540, pp. 234–238, June 2012.

[6] P. D. D. Ziegenbalg, "Lumineszenz." http://www.chemie.uni-jena.de/ institute/oc/weiss/lumineszenz.htm. Accessed: 2022-10-14.

[7] V. S. Urban, W. T. Heller, J. Katsaras, and W. Bras, "Soft matter sample environments for time-resolved small angle neutron scattering experiments: A review," *Applied Sciences*, vol. 11, p. 5566, June 2021.

[8] G. Porter, "Flash photolysis and spectroscopy. a new method for the study of free radical reactions," *Proceedings of the Royal Society of London. Series A. Mathematical and Physical Sciences*, vol. 200, pp. 284–300, Jan. 1950.

[9] R. Geneaux, H. J. B. Marroux, A. Guggenmos, D. M. Neumark, and S. R. Leone, "Transient absorption spectroscopy using high harmonic generation: a review of ultrafast x-ray dynamics in molecules and solids," *Philosophical Transactions of the Royal Society A: Mathematical, Physical and Engineering Sciences*, vol. 377, p. 20170463, Apr. 2019.

[10] P. Beckman, R. P. Roy, V. Velidandla, and M. Capizzani, "An improved fast-response microthermocouple," *Review of Scientific Instruments*, vol. 66, pp. 4731–4733, Sept. 1995.

[11] V. Šrajer, T. yi Teng, T. Ursby, C. Pradervand, Z. Ren, S. ichi Adachi, W. Schildkamp, D. Bourgeois, M. Wulff, and K. Moffat, "Photolysis of the carbon monoxide complex of myoglobin: Nanosecond time-resolved crystallography," *Science*, vol. 274, pp. 1726–1729, Dec. 1996.

[12] M. Wulff, A. Plech, L. Eybert, R. Randler, F. Schotte, and P. Anfinrud, "The realization of sub-nanosecond pump and probe experiments at the ESRF," *Faraday Discussions*, vol. 122, pp. 13–26, Oct. 2002.

[13] M. Cammarata, L. Eybert, F. Ewald, W. Reichenbach, M. Wulff, P. Anfinrud, F. Schotte, A. Plech, Q. Kong, M. Lorenc, B. Lindenau, J. Räbiger, and S. Polachowski, "Chopper system for time resolved experiments with synchrotron radiation," *Rev. Sci. Instrum.*, vol. 80, p. 015101, Jan. 2009.

[14] H. Ihee, S. Rajagopal, V. Šrajer, R. Pahl, S. Anderson, M. Schmidt, F. Schotte, P. A. Anfinrud, M. Wulff, and K. Moffat, "Visualizing reaction pathways in photoactive yellow protein from nanoseconds to seconds," *Proceedings of the National Academy of Sciences*, vol. 102, pp. 7145–7150, May 2005.

[15] M. Cammarata, M. Levantino, F. Schotte, P. A. Anfinrud, F. Ewald, J. Choi, A. Cupane, M. Wulff, and H. Ihee, "Tracking the structural dynamics of proteins in solution using time-resolved wide-angle x-ray scattering," *Nature Methods*, vol. 5, pp. 881–886, Sept. 2008.

[16] H. Ihee, M. Lorenc, T. K. Kim, Q. Y. Kong, M. Cammarata, J. H. Lee, S. Bratos, and M. Wulff, "Ultrafast x-ray diffraction of transient molecular structures in solution," *Science*, vol. 309, pp. 1223–1227, Aug. 2005.

[17] C. J. Milne, V.-T. Pham, W. Gawelda, R. M. van der Veen, A. E. Nahhas, S. L. Johnson, P. Beaud, G. Ingold, F. Lima, D. A. Vithanage, M. Benfatto, D. Grolimund, C. Borca, M. Kaiser, A. Hauser, R. Abela, C. Bressler, and M. Chergui, "Time-resolved x-ray absorption spectroscopy: Watching atoms dance," *Journal of Physics: Conference Series*, vol. 190, p. 012052, Nov. 2009.

[18] G. Vanko, P. Glatzel, V.-T. Pham, R. Abela, D. Grolimund, C. Borca, S. L. Johnson, C. J. Milne, and C. Bressler, "Picosecond time-resolved x-ray emission spectroscopy: Ultrafast spin-state determination in an iron complex," *Angewandte Chemie International Edition*, vol. 49, pp. 5910–5912, July 2010.

[19] H. N. Chapman, A. Barty, M. J. Bogan, S. Boutet, M. Frank, S. P. Hau-Riege, S. Marchesini, B. W. Woods, S. Bajt, W. H. Benner, R. A. London, E. Plönjes, M. Kuhlmann, R. Treusch, S. Düsterer, T. Tschentscher, J. R. Schneider, E. Spiller, T. Möller, C. Bostedt, M. Hoener, D. A. Shapiro, K. O. Hodgson, D. van der Spoel, F. Burmeister, M. Bergh, C. Caleman, G. Huldt, M. M. Seibert, F. R. N. C. Maia, R. W. Lee, A. Szöke, N. Timneanu, and J. Hajdu, "Femtosecond diffractive imaging with a soft-x-ray free-electron laser," *Nature Physics*, vol. 2, pp. 839–843, Nov. 2006.

[20] R. A. P. Emma and J. A. *et al.*, "First lasing and operation of an ångstrom-wavelength free-electron laser," *Nature Photonics*, vol. 4, pp. 641–647, Aug. 2010.

[21] K. H. Kim, J. G. Kim, S. Nozawa, T. Sato, K. Y. Oang, T. W. Kim, H. Ki, J. Jo, S. Park, C. Song, T. Sato, K. Ogawa, T. Togashi, K. Tono, M. Yabashi, T. Ishikawa, J. Kim, R. Ryoo, J. Kim, H. Ihee, and S. ichi Adachi, "Direct observation of bond formation in solution with femtosecond x-ray scattering," *Nature*, vol. 518, pp. 385–389, Feb. 2015.

[22] C. Milne, T. Penfold, and M. Chergui, "Recent experimental and theoretical developments in time-resolved x-ray spectroscopies," *Coordination Chemistry Reviews*, vol. 277-278, pp. 44–68, Oct. 2014.

[23] C. Kupitz, S. Basu, I. Grotjohann, R. Fromme, N. A. Zatsepin, K. N. Rendek, M. S. Hunter, R. L. Shoeman, T. A. White, D. Wang, D. James, J.-H. Yang, D. E. Cobb, B. Reeder, R. G. Sierra, H. Liu, A. Barty, A. L. Aquila, D. Deponte, R. A. Kirian, S. Bari, J. J. Bergkamp, K. R. Beyerlein, M. J. Bogan, C. Caleman, T.-C. Chao, C. E. Conrad, K. M. Davis, H. Fleckenstein, L. Galli, S. P. Hau-Riege, S. Kassemeyer, H. Laksmono, M. Liang, L. Lomb, S. Marchesini, A. V. Martin, M. Messerschmidt, D. Milathianaki, K. Nass, A. Ros, S. Roy-Chowdhury, K. Schmidt, M. Seibert, J. Steinbrener, F. Stellato, L. Yan, C. Yoon, T. A. Moore, A. L. Moore, Y. Pushkar, G. J. Williams, S. Boutet, R. B. Doak, U. Weierstall, M. Frank, H. N. Chapman, J. C. H. Spence, and P. Fromme, "Serial time-resolved crystallography of photosystem II using a femtosecond x-ray laser," *Nature*, vol. 513, pp. 261–265, July 2014.

[24] K. H. Nam, "Serial x-ray crystallography," *Crystals*, vol. 12, p. 99, Jan. 2022.

[25] E. H. Choi, Y. Lee, J. Heo, and H. Ihee, "Reaction dynamics studied via femtosecond x-ray liquidography at x-ray free-electron lasers," *Chemical Science*, vol. 13, no. 29, pp. 8457–8490, 2022.

[26] H. Ihee, V. A. Lobastov, U. M. Gomez, B. M. Goodson, R. Srinivasan, C.-Y. Ruan, and A. H. Zewail, "Direct imaging of transient molecular structures with ultrafast diffraction," *Science*, vol. 291, pp. 458–462, Jan. 2001.

[27] S. P. Weathersby, G. Brown, M. Centurion, T. F. Chase, R. Coffee, J. Corbett, J. P. Eichner, J. C. Frisch, A. R. Fry, M. Gühr, N. Hartmann, C. Hast, R. Hettel, R. K. Jobe, E. N. Jongewaard, J. R. Lewandowski, R. K. Li, A. M. Lindenberg, I. Makasyuk, J. E. May, D. McCormick, M. N. Nguyen, A. H. Reid, X. Shen, K. Sokolowski-Tinten, T. Vecchione, S. L. Vetter, J. Wu, J. Yang, H. A. Dürr, and X. J. Wang, "Mega-electron-volt ultrafast electron diffraction at SLAC national accelerator laboratory," *Review of Scientific Instruments*, vol. 86, p. 073702, July 2015.

[28] M. Z. Mo, Z. Chen, R. K. Li, M. Dunning, B. B. L. Witte, J. K. Baldwin, L. B. Fletcher, J. B. Kim, A. Ng, R. Redmer, A. H. Reid, P. Shekhar, X. Z. Shen, M. Shen, K. Sokolowski-Tinten, Y. Y. Tsui, Y. Q. Wang, Q. Zheng, X. J. Wang, and S. H. Glenzer, "Heterogeneous to homogeneous melting transition visualized with ultrafast electron diffraction," *Science*, vol. 360, pp. 1451–1455, June 2018.

[29] K. Ledbetter, E. Biasin, J. P. F. Nunes, M. Centurion, K. J. Gaffney, M. Kozina, M.-F. Lin, X. Shen, J. Yang, X. J. Wang, T. J. A. Wolf, and A. A. Cordones, "Photodissociation of aqueous i 3 - observed with liquid-phase ultrafast mega-electron-volt electron diffraction," *Structural Dynamics*, vol. 7, p. 064901, Nov. 2020.

[30] M. M. Harding, M. W. Nowicki, and M. D. Walkinshaw, "Metals in protein structures: a review of their principal features," *Crystallography Reviews*, vol. 16, pp. 247–302, Oct. 2010.

[31] L. Thompson, "Preparation of prussian blue," *Journal of the Franklin Institute*, vol. 27, pp. 412–413, 1839.

[32] H. Machemer, "Die konstitution der metallkomplexe indigoider farbstoffe," *Journal fuer Praktische Chemie*, vol. 127, pp. 109–168, July 1930.

[33] J. V. Obligacion and P. J. Chirik, "Earth-abundant transition metal catalysts for alkene hydrosilylation and hydroboration," *Nature Reviews Chemistry*, vol. 2, pp. 15–34, Apr. 2018.

[34] W. Gawelda, C. Bressler, M. Saes, M. Kaiser, A. N. Tarnovsky, D. Grolimund, S. L. Johnson, R. Abela, and M. Chergui, "Picosecond TimeResolved XRay absorption spectroscopy of solvated organometallic complexes," *Physica Scripta*, p. 102, 2005.

[35] K. J. Gaffney, "Capturing photochemical and photophysical transformations in iron complexes with ultrafast x-ray spectroscopy and scattering," *Chemical Science*, vol. 12, no. 23, pp. 8010–8025, 2021.

[36] N. G. Connelly and T. Damhus, *Nomenclature of Inorganic Chemistry, IUPAC Recommendations*. IUPAC, 2005.

[37] E. L. Wehry, "Photochemical behaviour of transition-metal complexes," *Q. rev.*, vol. 21, no. 2, p. 213, 1967.

[38] H. B. Gray, S. Záliš, and A. Vlček, "Electronic structures and photophysics of d8-d8 complexes," *Coordination Chemistry Reviews*, vol. 345, pp. 297–317, 2017. Chemical Bonding: "State of the Art".

[39] V. W.-W. Yam, V. K.-M. Au, and S. Y.-L. Leung, "Light-emitting self-assembled materials based on d8 and d10 transition metal complexes," *Chemical Reviews*, vol. 115, pp. 7589–7728, July 2015.

[40] M. Norgett, J. Thornley, and L. Venanzi, "The visible and ultraviolet spectra of d6-, d7- and d8-metal ions in trigonal bipyramidal complexes," *Coordination Chemistry Reviews*, vol. 2, pp. 83–98, July 1967.

[41] D. C. Smith and H. B. Gray, "Photochemistry of binuclear d8 complexes," *Coordination Chemistry Reviews*, vol. 100, pp. 169–181, Apr. 1990.

[42] H. Furukawa, K. E. Cordova, M. O'Keeffe, and O. M. Yaghi, "The chemistry and applications of metal-organic frameworks," *Science*, vol. 341, Aug. 2013.

[43] A. Sykes and K. R. Mann, "Thermal encapsulation and photochemical deencapsulation of silver(i) by [ir2(dimen)4](PF6)2 (dimen = 1, 8-diisocyanomenthane). x-ray crystal structure of [AgIr2(dimen)4](PF6)3.cntdot.2dmso," *Journal of the American Chemical Society*, vol. 110, pp. 8252–8253, Nov. 1988.

[44] S. A. Clodfelter, T. M. Doede, B. A. Brennan, J. K. Nagle, D. P. Bender, W. A. Turner, and P. M. LaPunzina, "Luminescent metal-metal-bonded exciplexes involving tetrakis(.mu.-diphosphito)diplatinate(II) and thallium(i)," *Journal of the American Chemical Society*, vol. 116, pp. 11379–11386, Dec. 1994.

[45] J. Als-Nielsen and D. McMorrow, *Elements of modern X-ray physics*. Hoboken, NJ: Wiley-Blackwell, 2 ed., Mar. 2011.

[46] B. E. Warren, *X-ray Diffraction*. Courier Corporation, 1990.

[47] D. T. Cromer and J. B. Mann, "X-ray scattering factors computed from numerical Hartree–Fock wave functions," *Acta Crystallographica Section A*, vol. 24, pp. 321–324, Mar 1968.

[48] D. Waasmaier and A. Kirfel, "New analytical scattering-factor functions for free atoms and ions," *Acta Crystallographica Section A*, vol. 51, pp. 416–431, May 1995.

[49] J. G. Kim, S. Nozawa, H. Kim, E. H. Choi, T. Sato, T. W. Kim, K. H. Kim, H. Ki, J. Kim, M. Choi, Y. Lee, J. Heo, K. Y. Oang, K. Ichiyanagi, R. Fukaya, J. H. Lee, J. Park, I. Eom, S. H. Chun, S. Kim, M. Kim, T. Katayama, T. Togashi, S. Owada, M. Yabashi, S. J. Lee, S. Lee, C. W. Ahn, D.-S. Ahn, J. Moon, S. Choi, J. Kim, T. Joo, J. Kim, S.-I. Adachi, and H. Ihee, "Mapping the emergence of molecular vibrations mediating bond formation," *Nature*, vol. 582, pp. 520–524, June 2020.

[50] H. Ki, T. W. Kim, J. Moon, J. Kim, Y. Lee, J. Heo, K. H. Kim, Q. Kong, D. Khakhulin, G. Newby, J. Kim, J. Kim, M. Wulff, and H. Ihee, "Photoactivation of triosmium dode-cacarbonyl at 400 nm probed with time-resolved x-ray liquidography," *Chemical Communications*, vol. 58, no. 53, pp. 7380–7383, 2022.

[51] A. O. Dohn, E. Biasin, K. Haldrup, M. M. Nielsen, N. E. Henriksen, and K. B. Møller, "On the calculation of x-ray scattering signals from pairwise radial distribution functions," *Journal of Physics B: Atomic, Molecular and Optical Physics*, vol. 48, p. 244010, nov 2015.

[52] F. Zernike and J. A. Prins, "Die beugung von röntgenstrahlen in flüssigkeiten als effekt der molekülanordnung," *Zeitschrift für Physik A Hadrons and nuclei*, vol. 41, pp. 184–194, Jun 1927.

[53] E. Biasin, T. B. V. Driel, G. Levi, M. G. Laursen, A. O. Dohn, A. Moltke, P. Vester, F. B. Hansen, K. S. Kjaer, T. Harlang, R. Hartsock, M. Christensen, K. J. Gaffney, N. E. Henriksen, K. B. Møller, K. Haldrup, and M. M. Nielsen, "Anisotropy enhanced x-ray scattering from solvated transition metal complexes," *Journal of Synchrotron Radiation*, vol. 25, pp. 306–315, 3 2018.

[54] A. H. Compton, "A quantum theory of the scattering of x-rays by light elements," *Physical Review*, vol. 21, pp. 483–502, May 1923.

[55] F. Hajdu, "Revised parameters of the analytic fits for coherent and incoherent scattered x-ray intensities of the first 36 atoms," *Acta Crystallogr. A*, vol. 28, pp. 250–252, May 1972.

[56] G. Pálinkás, "Analytic approximations for the incoherent x-ray intensities of the atoms from ca to am," *Acta Crystallogr. A*, vol. 29, pp. 10–12, Jan. 1973.

[57] T. Shintake, "Review of the worldwide SASE FEL development," in *2007 IEEE Particle Accelerator Conference (PAC)*, IEEE, 2007.

[58] R. P. Walker, "Calculation of undulator radiation spectral and angular distributions," *Review of Scientific Instruments*, vol. 60, pp. 1816–1819, jul 1989.

[59] "Esrf find a beamline." https://www.esrf.fr/home/UsersAndScience/ find-a-beamline.html. Accessed: 2022-10-17.

[60] S. A. W. Decking and P. A. *et al.*, "A MHz-repetition-rate hard x-ray free-electron laser driven by a superconducting linear accelerator," *Nature Photonics*, vol. 14, pp. 391–397, May 2020.

[61] T. S. Christopher Milne and M. A. *et al.*, "SwissFEL: The swiss x-ray free electron laser," *Applied Sciences*, vol. 7, p. 720, July 2017.

[62] H. A. Tetsuya Ishikawa and T. A. *et al.*, "A compact x-ray free-electron laser emitting in the sub-ångström region," *Nature Photonics*, vol. 6, pp. 540–544, June 2012.

[63] J. A. Howard, H. A. Sparkes, P. R. Raithby, and A. V. Churakov, eds., *The Future of Dynamic Structural Science*. Springer Netherlands, 2014.

[64] M. Harmand, R. Coffee, M. R. Bionta, M. Chollet, D. French, D. Zhu, D. M. Fritz, H. T. Lemke, N. Medvedev, B. Ziaja, S. Toleikis, and M. Cammarata, "Achieving few-femtosecond time-sorting at hard x-ray free-electron lasers," *Nature Photonics*, vol. 7, pp. 215–218, 3 2013.

[65] M. Levantino, Q. Kong, M. Cammarata, D. Khakhulin, F. Schotte, P. Anfinrud, V. Kabanova, H. Ihee, A. Plech, S. Bratos, and M. Wulff, "Structural dynamics probed by x-ray pulses from synchrotrons and XFELs," *C. R. Phys.*, vol. 22, pp. 75–94, Dec. 2021.

[66] S. Herrmann, S. Boutet, B. Duda, D. Fritz, G. Haller, P. Hart, R. Herbst, C. Kenney, H. Lemke, M. Messerschmidt, J. Pines, A. Robert, M. Sikorski, and G. Williams, "Cspad-140k: A versatile detector for lcls experiments," *Nuclear Instruments and Methods in Physics Research, Section A: Accelerators, Spectrometers, Detectors and Associated Equipment*, vol. 718, pp. 550–553, 2013.

[67] R. A. Doyle and R. L. Justin Anderson, *High Speed Series X-ray Detector Manual*. Rayonix, 2015.

[68] G. Hura, J. M. Sorenson, R. M. Glaeser, and T. Head-Gordon, "A high-quality x-ray scattering experiment on liquid water at ambient conditions," *The Journal of Chemical Physics*, vol. 113, no. 20, pp. 9140–9148, 2000.

[69] P. Bösecke and O. Diat, "Small-angle x-ray scattering at the ESRF high-brilliance beamline," *J Appl Crystallogr*, vol. 30, no. 5, pp. 867–871, 1997.

[70] B. R. Pauw, "Everything SAXS: small-angle scattering pattern collection and correction," *Journal of Physics: Condensed Matter*, vol. 25, p. 383201, aug 2013.

[71] L. B. Skinner, C. Huang, D. Schlesinger, L. G. Pettersson, A. Nilsson, and C. J. Benmore, "Benchmark oxygen-oxygen pair-distribution function of ambient water from x-ray diffraction measurements with a wide q-range," *Journal of Chemical Physics*, vol. 138, 2 2013.

[72] L. Sandberg, "Ultrafast dynamics in photoexcited iron-carbene molecules - an x-ray study," Master's thesis, University of Copenhagen, Niels Bohr Institute, 2017.

[73] T. B. V. Driel, K. S. Kjær, E. Biasin, K. Haldrup, H. T. Lemke, and M. M. Nielsen, "Disentangling detector data in xfel studies of temporally resolved solution state chemistry," *Faraday Discussions*, vol. 177, pp. 443–465, 4 2015.

[74] U. Lorenz, K. B. Møller, and N. E. Henriksen, "On the interpretation of time-resolved anisotropic diffraction patterns," *New Journal of Physics*, vol. 12, 11 2010.

[75] W. H. Press, S. A. Teukolsky, W. T. Vetterling, and B. P. Flannery, *Numerical Recipes 3rd Edition: The Art of Scientific Computing*. Cambridge University Press, 3 ed., 2007.

[76] K. Haldrup, "Singular value decomposition as a tool for background corrections in time-resolved xfel scattering data," *Philosophical Transactions of the Royal Society B: Biological Sciences*, vol. 369, 7 2014.

[77] T. B. van Driel, K. S. Kjær, R. W. Hartsock, A. O. Dohn, T. Harlang, M. Chollet, M. Christensen, W. Gawelda, N. E. Henriksen, J. G. Kim, K. Haldrup, K. H. Kim, H. Ihee, J. Kim, H. Lemke, Z. Sun, V. Sundström, W. Zhang, D. Zhu, K. B. Møller, M. M. Nielsen, and K. J. Gaffney, "Atomistic characterization of the active-site solvation dynamics of a model photocatalyst," *Nat. Commun.*, vol. 7, p. 13678, Dec. 2016.

[78] K. S. Kjær, T. B. V. Driel, J. Kehres, K. Haldrup, D. Khakhulin, K. Bechgaard, M. Cammarata, M. Wulff, T. J. Sørensen, and M. M. Nielsen, "Introducing a standard method for experimental determination of the solvent response in laser pump, x-ray probe time-resolved wide-angle x-ray scattering experiments on systems in solution," *Physical Chemistry Chemical Physics*, vol. 15, pp. 15003–15016, 9 2013.

[79] M. Cammarata, M. Lorenc, T. K. Kim, J. H. Lee, Q. Y. Kong, E. Pontecorvo, M. Lo Russo, G. Schiró, A. Cupane, M. Wulff, and H. Ihee, "Impulsive solvent heating probed by picosecond x-ray diffraction," *The Journal of Chemical Physics*, vol. 124, no. 12, p. 124504, 2006.

[80] H. Ki, S. Choi, J. Kim, E. H. Choi, S. Lee, Y. Lee, K. Yoon, C. W. Ahn, D.-S. Ahn, J. H. Lee, J. Park, I. Eom, M. Kim, S. H. Chun, J. Kim, H. Ihee, and J. Kim, "Optical kerr effect of liquid acetonitrile probed by femtosecond time-resolved x-ray liquidography," *Journal of the American Chemical Society*, vol. 143, pp. 14261–14273, Aug. 2021.

[81] A. Montoya-Castillo, M. S. Chen, S. L. Raj, K. A. Jung, K. S. Kjaer, T. Morawietz, K. J. Gaffney, T. B. van Driel, and T. E. Markland, "Optically induced anisotropy in time-resolved scattering: Imaging molecular-scale structure and dynamics in disordered media with experiment and theory," *Physical Review Letters*, vol. 129, July 2022.

[82] G. Levi, M. Pápai, N. E. Henriksen, A. O. Dohn, and K. B. Møller, "Solution structure and ultrafast vibrational relaxation of the ptpop complex revealed by delta scf-qm/mm direct dynamics simulations," *Journal of Physical Chemistry C*, vol. 122, pp. 7100–7119, 4 2018.

[83] A. O. Dohn, E. O. Jónsson, G. Levi, J. J. Mortensen, O. Lopez-Acevedo, K. S. Thygesen, K. W. Jacobsen, J. Ulstrup, N. E. Henriksen, K. B. Møller, and H. Jónsson, "Grid-based projector augmented wave (GPAW) implementation of quantum mechanics/molecular mechanics (QM/MM) electrostatic embedding and application to a solvated diplatinum complex," *Journal of Chemical Theory and Computation*, vol. 13, pp. 6010–6022, Nov. 2017.

[84] A. O. Dohn, "Multiscale electrostatic embedding simulations for modeling structure and dynamics of molecules in solution: A tutorial review," *International Journal of Quantum Chemistry*, vol. 120, July 2020.

[85] M. Abedi, G. Levi, D. B. Zederkof, N. E. Henriksen, M. Pápai, and K. B. Møller, "Excited-state solvation structure of transition metal complexes from molecular dynamics simulations and assessment of partial atomic charge methods," *Physical Chemistry Chemical Physics*, vol. 21, no. 7, pp. 4082–4095, 2019.

[86] A. Filipponi, "Statistical errors in x-ray absorption fine-structure data analysis," *Journal of Physics: Condensed Matter*, vol. 7, pp. 9343–9356, nov 1995.

[87] D. I. Svergun, V. V. Volkov, M. B. Kozin, and H. B. Stuhrmann, "New Developments in Direct Shape Determination from Small-Angle Scattering. 2. Uniqueness," *Acta Crystallographica Section A*, vol. 52, pp. 419–426, May 1996.

[88] K. Haldrup, M. Christensen, and M. Meedom Nielsen, "Analysis of time-resolved X-ray scattering data from solution-state systems," *Acta Crystallographica Section A*, vol. 66, pp. 261–269, Mar 2010.

[89] A. P. Zipp, "The behavior of the tetra-μ-pyrophosphito-diplatinum(II) ion pt2(p2o5h2)4-4 and related species," *Coordination Chemistry Reviews*, vol. 84, pp. 47–83, Mar. 1988.

[90] D. M. Roundhill, H. B. Gray, and C. M. Che, "Pyrophosphito-bridged diplatinum chemistry," *Accounts of Chemical Research*, vol. 22, pp. 55–61, Feb. 1989.

[91] J.-J. Zhong, W.-P. To, Y. Liu, W. Lu, and C.-M. Che, "Efficient acceptorless photo-dehydrogenation of alcohols and n/i-heterocycles with binuclear platinum(scpii/scp) diphosphite complexes," *Chemical Science*, vol. 10, no. 18, pp. 4883–4889, 2019.

[92] S. C. Cheng, C. A. Blaine, M. G. Hill, and K. R. Mann, "Electrochemical and IR spectroelectrochemical studies of the electrocatalytic reduction of carbon dioxide by [ir(dimen)4](dimen = 1, 8-diisocyanomenthane)," *Inorganic Chemistry*, vol. 35, pp. 7704–7708, Jan. 1996.

[93] M. D. Hanwell, D. E. Curtis, D. C. Lonie, T. Vandermeersch, E. Zurek, and G. R. Hutchison, "Avogadro: an advanced semantic chemical editor, visualization, and analysis platform," *Journal of Cheminformatics*, vol. 4, Aug. 2012.

[94] R. W. Hartsock, W. Zhang, M. G. Hill, B. Sabat, and K. J. Gaffney, "Characterizing the deformational isomers of bimetallic ir 2(dimen)42+ (dimen = 1,8-diisocyano-p-menthane) with vibrational wavepacket dynamics," *Journal of Physical Chemistry A*, vol. 115, pp. 2920–2926, 4 2011.

[95] M. Pižl, B. M. Hunter, I. V. Sazanovich, M. Towrie, H. B. Gray, S. Záliš, and A. Vlček, "Excitation-wavelength-dependent photophysics of d_8d_8 di-isocyanide complexes," *Inorganic Chemistry*, vol. 61, pp. 2745–2759, Dec. 2021.

[96] S. Záliš, Y.-C. Lam, H. B. Gray, and A. Vlček, "Spin–orbit TDDFT electronic structure of diplatinum(II, II) complexes," *Inorganic Chemistry*, vol. 54, pp. 3491–3500, Mar. 2015.

[97] K. Haldrup, G. Levi, E. Biasin, P. Vester, M. G. Laursen, F. Beyer, K. S. Kjær, T. B. V. Driel, T. Harlang, A. O. Dohn, R. J. Hartsock, S. Nelson, J. M. Glownia, H. T. Lemke, M. Christensen, K. J. Gaffney, N. E. Henriksen, K. B. Møller, and M. M. Nielsen, "Ultra-fast x-ray scattering measurements of coherent structural dynamics on the ground-state

potential energy surface of a diplatinum molecule," *Physical Review Letters*, vol. 122, 2 2019.

[98] M. Pižl, B. M. Hunter, G. M. Greetham, M. Towrie, S. Záliš, H. B. Gray, and A. Vlček, "Ultrafast wiggling and jiggling: Ir2(1,8-diisocyanomenthane)42+," *Journal of Physical Chemistry A*, vol. 121, pp. 9275–9283, 12 2017.

[99] A. C. Durrell, G. E. Keller, Y. C. Lam, J. Sýkora, A. Vlček, and H. B. Gray, "Structural control of 1a 2u-to- 3a 2u intersystem crossing in diplatinum(ii,ii) complexes," *Journal of the American Chemical Society*, vol. 134, pp. 14201–14207, 8 2012.

[100] K. Kjaer, "Photophysics of metal metal bonded exciplexes between tetrakis μ pyrophosphitodiplatinate(ii) and silver(i)," Master's thesis, Technical University of Denmark, 2010. master's thesis.

[101] K. Haldrup, T. Harlang, M. Christensen, A. Dohn, T. B. V. Driel, K. S. Kjær, N. Harrit, J. Vibenholt, L. Guerin, M. Wulff, and M. M. Nielsen, "Bond shortening (1.4 Å) in the singlet and triplet excited states of [ir2(dimen)4]2+ in solution determined by time-resolved x-ray scattering," *Inorganic Chemistry*, vol. 50, pp. 9329–9336, 10 2011.

[102] M. S. del Río and R. J. Dejus, "XOP v2.4: recent developments of the x-ray optics software toolkit," in *SPIE Proceedings* (M. S. del Rio and O. Chubar, eds.), SPIE, Sept. 2011.

[103] R. M. V. D. Veen, A. Cannizzo, F. V. Mourik, A. Vlček, and M. Chergui, "Vibrational relaxation and intersystem crossing of binuclear metal complexes in solution," *Journal of the American Chemical Society*, vol. 133, pp. 305–315, 1 2011. PtPOP.

[104] R. Monni, G. Capano, G. Auböck, H. B. Gray, A. Vlcek, I. Tavernelli, and M. Chergui, "Vibrational coherence transfer in the ultrafast intersystem crossing of a diplatinum complex in solution," *Proceedings of the National Academy of Sciences of the United States of America*, vol. 115, pp. E6396–E6403, 7 2018.

[105] S. F. Rice and H. B. Gray, "Electronic absorption and emission spectra of binuclear platinum(ii) complexes. characterization of the lowest singlet and triplet excited states of tetrakis(diphosphonato)diplatinate(4-) anion (pt2(h2p2o5)44-)," *Journal of the American Chemical Society*, vol. 105, pp. 4571–4575, Jul 1983.

[106] C. M. Che, F. H. Herbstein, W. P. Schaefer, R. E. Marsh, and H. B. Gray, "Binuclear platinum diphosphite complexes. crystal structures of tetrapotassium bromotetrakis(diphosphito)diplatinate trihydrate (k4[pt2(pop)4br].3h2o), a new linear chain semiconductor, and tetrapotassium dichlorotetrakis(diphosphito)diplatinate dihydrate (k4[pt2(pop)4cl2].2h2o)," *Journal of the American Chemical Society*, vol. 105, pp. 4604–4607, Jul 1983.

[107] R. Monni, G. Auböck, D. Kinschel, K. M. Aziz-Lange, H. B. Gray, A. Vlček, and M. Chergui, "Conservation of vibrational coherence in ultrafast electronic relaxation: The case of diplatinum complexes in solution," *Chemical Physics Letters*, vol. 683, pp. 112–120, 9 2017.

[108] S. Yang, J. Cao, and R. W. Field, "A semiclassical study of wave packet dynamics in anharmonic potentials," *The Journal of Chemical Physics*, vol. 121, pp. 6599–6607, Oct. 2004.

[109] Z. xian Wang and E. J. Heller, "Semiclassical investigation of the revival phenomena in a one-dimensional system," *Journal of Physics A: Mathematical and Theoretical*, vol. 42, p. 285304, June 2009.

[110] J. R. Peterson and K. Kalyanasundaram, "Energy- and electron-transfer processes of the lowest triplet excited state of tetrakis(diphosphito)diplatinate(II)," *The Journal of Physical Chemistry*, vol. 89, pp. 2486–2492, jun 1985.

[111] S. A. Bryan, R. H. Schmehl, and D. M. Roundhill, "Electrochemical oxidation of the tetrakis(.mu.-pyrophosphito-p, p)diplatinum(II) complex pt2(p2o5h2)44- both in the presence and the absence of halide ions and reduction of the axially substituted halodiplatinum(III) complexes pt2(p2o5h2)4x2-1," *Journal of the American Chemical Society*, vol. 108, pp. 5408–5412, Sept. 1986.

[112] J. K. Nagle and B. A. Brennan, "Luminescent exciplex formation involving tetrakis(.mu.-diphosphito)diplatinate(II) and -thallium(i) in aqueous solution," *Journal of the American Chemical Society*, vol. 110, pp. 5931–5932, Aug. 1988.

[113] A. G. Sykes and K. R. Mann, "X-ray crystal structure and phosphorus-31 nmr solution studies of [ir2(dimen)4(pph3)au(pph3)] (pf6)3 (dimen = 1,8-diisocyano-p-menthane). observation of particle site preference in the formation of "outside" silver and gold adducts," *Journal of the American Chemical Society*, vol. 112, pp. 7247–7254, Sep 1990.

[114] N. T. Satumtira, A. Mahdy, M. Chehbouni, O. ElBjeirami, and M. A. Omary, "Novel method for waste analysis using a highly luminescent diplatinum(II) octaphosphite complex as a heavy metal detector," in *Ceramic Transactions Series*, pp. 279–288, John Wiley & Sons, Inc., Sept. 2011.

[115] K. Haldrup, M. Christensen, M. Cammarata, Q. Kong, M. Wulff, S. O. Manager, K. Bechgaard, R. Feidenhans'l, N. Harrit, and M. M. Nielsen, "Structural tracking of a bimolecular reaction in solution by time-resolved x-ray scattering," *Angewandte Chemie - International Edition*, vol. 48, pp. 4180–4184, 5 2009.

[116] D. P. Bender and J. K. Nagle, "Metal-metal interactions of aqueous lead(II) and tin(II) ions with the ground and excited states of tetrakis(μ-diphosphito)diplatinate(II)," *Inorganica Chimica Acta*, vol. 225, pp. 201–205, Oct. 1994.

[117] M. Christensen, K. Haldrup, K. S. Kjær, M. Cammarata, M. Wulff, K. Bechgaard, H. Weihe, N. H. Harrit, and M. M. Nielsen, "Structure of a short-lived excited state trinuclear ag-pt-pt complex in aqueous solution by time resolved x-ray scattering," *Physical Chemistry Chemical Physics*, vol. 12, pp. 6921–6923, 2010.

[118] C. N. Pettijohn, E. B. Jochnowitz, B. Chuong, J. K. Nagle, and A. Vogler, "Luminescent excimers and exciplexes of PtII compounds," *Coordination Chemistry Reviews*, vol. 171, pp. 85–92, Apr. 1998.

[119] Q. Kong, K. S. Kjaer, K. Haldrup, S. P. Sauer, T. B. V. Driel, M. Christensen, M. M. Nielsen, and M. Wulff, "Theoretical study of the triplet excited state of ptpop and the exciplexes m-ptpop (m = tl, ag) in solution and comparison with ultrafast x-ray scattering results," *Chemical Physics*, vol. 393, pp. 117–122, 1 2012.

[120] S. V. Kruppa, Y. Nosenko, M. O. Winghart, S. P. Walg, M. M. Kappes, and C. Riehn, "Fragmentation pathways of dianionic [pt2(μ-p2o5h2)4 + x,y]2- (x,y = h, k, ag) species in an ion trap induced by collisions and uv photoexcitation," *International Journal of Mass Spectrometry*, vol. 395, pp. 7–19, 2 2016.

[121] G. C. Benson, P. J. DArcy, and Y. P. Handa, "Thermodynamics of aqueous mixtures of nonelectrolytes. v. isobaric heat capacities and ultrasonic speeds for water + ethanenitrile mixtures at 25°c," *Thermochimica Acta*, vol. 46, pp. 295–301, July 1981.

[122] T. Ichikawa, H. Yoshida, A. S. W. Li, and L. Kevan, "Solvation structure of silver ions and atoms in acetonitrile," *Journal of the American Chemical Society*, vol. 106, pp. 4324–4327, Aug. 1984.

[123] T. Shoeib, H. E. Aribi, K. W. M. Siu, and A. C. Hopkinson, "A study of silver (i) ion-organonitrile complexes: ion structures, binding energies, and substituent effects," *The Journal of Physical Chemistry A*, vol. 105, pp. 710–719, Jan. 2001.

[124] A. O. Dohn, E. Örn Jónsson, K. S. Kjær, T. B. V. Driel, M. M. Nielsen, K. W. Jacobsen, N. E. Henriksen, and K. B. Møller, "Direct dynamics studies of a binuclear metal complex in solution: The interplay between vibrational relaxation, coherence, and solvent effects," *Journal of Physical Chemistry Letters*, vol. 5, pp. 2414–2418, 7 2014.

Appendix A

Paper included in the thesis

Paper I

Ultrafast photoexcitation dynamics in tri-nuclear metal-metal bonded M-PtPOP (M = Ag, Tl) transition-metal complexes
Philipp Lenzen, Kristoffer Haldrup, Asmus O. Dohn, Elisa Biasin, Kasper Steen Pedersen, Peter Vester, Mads Goldschmidt Laursen, Frederik Beyer, Kasper Skov Kjær, Tim B. van Driel, Tobias Harlang, Robert J. Hartsock, Silke Nelson, James M. Glownia, Henrik T. Lemke, Morten Christensen and Kelly J Gaffney, Klaus B. Møller, Martin M. Nielsen
Contribution: Data treatment and reduction for all X-ray solution scattering measurements, as well as the analysis and the lead of the interpretation of the data. I did the vast majority of the drafting of the manuscript, created all of the figures and implemented the majority of changes suggested by Co-authors.

Ultrafast photoexcitation dynamics in tri-nuclear metal-metal bonded M-PtPOP (M = Ag, Tl) transition-metal complexes

December 31, 2022

The diplatinum complex PtPOP associates with free metal ions (M=Ag+, Tl+) in solution forming tri-nuclear metal-metal bonded MPtPOP complexes. These complexes, their structural dynamics and their electronic behavior are not well understood and afford a unique opportunity to study metal-metal bonds. Here, we present an X-ray solution scattering study of the ultrafast structural dynamics of AgPtPOP, TlPtPOP and PtPOP in water after photoexcitation. We carry out model-independent analysis of the observed dynamics as well as an analysis incorporating time-resolved structural refinements of the PtPt and MPt bond lengths with <100 fs time resolution. Based on the observed structural dynamics we propose an electronic structure model that describes the metal-metal bonding behavior in both the ground and excited state. The model classifies the MPtPOP molecular orbital schemes by the electronic configuration of the association ion which defines the HOMO and LUMO of the resulting complex. The similarities and differences observed in the dynamics of AgPtPOP, TlPtPOP and PtPOP complex are discussed on the basis of this model.
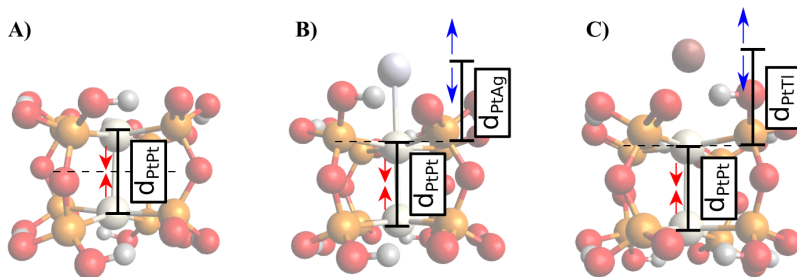
Figure 1: DFT-calculated structures of PtPOP (A), AgPtPOP (B) and TlPtPOP (C) with the structural parameters investigated in the present study indicated by arrows.

.

1   Introduction

Transition-metal complexes have been objects of interest for their photochemical and photophysical properties for several decades[1]. Their ability to absorb and convert energy from as well as into photons makes them interesting for potential applications such as catalysis and electrically driven light emitting diodes [2]. They consist of a core comprising of one or more metal-atoms, which are enclosed by a ligand scaffold composed of often organic compounds. The complexes are regularly classified based on the number of electrons in the outermost d-orbital of the metal atoms. Following photo-excitation the single-metal d6, d8, and d10 metal ion complexes often undergo metal-to-ligand charge transfer [1, 3, 4] whereas for the bimetallic d8-d8 complexes metal-metal (MM) and metal-metal-to-ligand charge transfer (MMLCT) often dominates and this leads to large changes in the metal-metal bond length and overall geometry of the complexes as recently reviewed by Gray, Zanis and Vlcek [5]. However, despite decades of investigation, the interrelationship between electronic transitions, structural change, and catalytic activity is not yet completely understood.

Fig. 1 A depicts the structure of the tetrakis (diphosphito) diplatinate(II) anion $[Pt_2(H_2P_2O_5)_4]^{4-}$, or PtPOP. Within the field of ultra-fast structural dynamics PtPOP, has

been intensively investigated due to its interesting photophysical properties[1, 6, 7], its photodehydrogenation capabilities [8] as well as its comparative simplicity with respect to other d8-d8-complexes such as Ir_2(1,8-diisocyano-p-menthane)$_4$ (Ir_2Dimen_4)[9, 10, 11]. In the PtPOP system, the four pyrophosphite ligand subunits are known to form a symmetrical scaffold around the platinum atoms as depicted in Figure 1. In the ground state (GS) the platinum-platinum distance (d_{PtPt}) was determined from crystallography to be 2.92 Å [12] with later studies based on L-edge X-ray Absorption Spectroscopy in solution suggesting d_{PtPt} to be around 2.88 Å [13] whereas a study based on Time-Resolved X-ray Solution Scattering suggested a distance of slightly above 2.95 Å [14]. Simulation studies based on Density FUnctional Theory (DFT) have found d_{PtPt} to be in the range from 2.8 Å to 3.1 Å with higher levels of theory trending towards longer distances [15, 16, 17].

From early single-crystal spectroscopic studies [18] the photoexcitation of PtPOP in the intense absorption band centered at 370 nm was concluded to involve a significant contraction of Δd_{PtPt} = 0.2-0.3 Å along the Pt-Pt axis. This was later confirmed with Raman Spectroscopy [19] and steady-state X-ray diffraction [20] and in two studies with 100 picosecond time resolution based on Time-Resolved X-ray Solution Scattering (TR-XSS) [14] and L-edge EXAFS [21]. From the spectroscopic data, this contraction was determined to arise from a $d\sigma^* \rightarrow p\sigma$ transition along the Pt-Pt axis, where one electron is promoted from an anti-bonding orbital to a bonding orbital located between the two Pt atoms. More recently, and beginning with a landmark study by van der Ween *et al.* [22], Transient Optical Absorption Spectroscopy (TOAS) has been extensively used to elucidate the details of the electronic and structural dynamics following photo-excitation. Following excitation, the molecules start out in a vibrationally hot state on the potential energy surface of the S_1 electronic excited state. The structure dissipates energy with impulsive vibrational cooling

during the first Pt-Pt oscillation. This is followed by solvent dependent vibrational cooling for 1-2 ps into the lowest vibrational state [22, 23]. On slightly longer time scales, the intersystem crossing (ISC) time has been determined to be strongly solvent dependent for PtPOP, ranging from 0.7 in Acetonitrile to 30 ps in Ethylen Glycol, whereas for water it is 13.7 ± 0.2 ps [22] and we note that also the properties of the ligand scaffolding have been shown to impact ISC times [7]. Under excitation with higher photon energies the electrons are initially excited to the higher lying state manifold above the lowest singlet, an excitation process which has been attributed to ligand-to-metal charge transfer states [24]. From these states the PtPOP molecules rapidly ($\sim$ 100 femtoseconds) decay into the lowest triplet state, bypassing the singlet while maintaining structural coherence upon ISC to the triplet state.[23]

Focusing next on the solution-phase chemistry, PtPOP forms complexes in solution in the presence metal-ions, $PtPOP + M \rightleftharpoons MPtPOP$ and $PtPOP + 2M \rightleftharpoons M_2PtPOP$, where the metal ion M can be Ag, Tl or a range of other metal ions [25]. As discussed in detail by Clodfelter et al. [26] this complexation most likely takes place in the axial position and both in ground state and in the photoexcited state, where the interaction is enhanced by several orders of magnitude. As such, the metal-PtPOP complexes 1 B and C, afford a unique opportunity for studying metal-metal bonding. The TlPtPOP complex was investigated first in the optical studies by Nagle&Brennan [27] and Clodfelter et al.[26], where the association reaction constants (see below) were determined and the Pt-Tl distance estimated to be 2.7-3.0 Å assuming a Δd_{PtPt} Pt-Pt distance contraction from 2.92 Å to 2.71 Å, which was estimated from measurements on PtPOP alone. Taking advantage of the much increased bonding affinity in the excited state, the structure and lifetime of TlPtPOP* and $Tl_2PtPOP*$ was later studied using TR-XSS by Haldrup et al. [28] determining a $d_{PtTl,ES}$ of 2.92 Å. In the case of AgPtPOP* Christensen et al., [29] determined a $d_{PtPt,ES}$ of 2.84 and a $d_{PtAg,ES}$

of 2.47 Å for the AgPtPOP complex. These studies however did not include the ground state association in the structural refinement, a shortcoming which was later adressed by the same authors in a study by Kong et al., reporting on excited state quantum chemical calculations[16]. In this study, $d_{PtPt,ES}$ was calculated to be 2.78 and 2.79 Å for axially-coordinated TlPtPOP and AgPtPOP, respectively, with a polarizable-continuum model of the solvent environment. The excited state distances $d_{PtM,ES}$ were determined to be 3.0 and 2.9 Å for Tl and Ag, respectively. This study also discussed the shape and nature of the HOMO and LUMO molecular orbitals used to support the MO-scheme suggested from the structural results presented here. In contrast to these studies, Kruppa et al. [30] reported on time-resolved mass spectrometry in combination with (vacuum) DFT, based on which a side-binding motif was suggested for AgPtPOP, as discussed further below.

1.1   Electronic structure

Fig. 2 shows the electronic structure of PtPOP, AgPtPOP and TlPtPOP as molecular orbital (MO) energy diagrams. The diagrams for AgPtPOP and TlPtPOP are derived from previous work on d8-transition metal complexes[5] and previous quantum-chemical calculations on these samples[16], and will be discussed below. In PtPOP, the electrons fill up the orbitals to the antibonding highest occupied molecular orbital (HOMO) $5\sigma^*$. The optical transition of an electron into the bonding, lowest unoccupied molecular orbital (LUMO) 6σ orbital increases the bonding order between the platinum atoms, resulting in a bond-length contraction[5]. When a metal ion associates with the PtPOP anion, the valence s-orbitals, filled 6s for Tl+ and empty 5s for Ag+, mix with both the HOMO and the LUMO[26]. This process decreases the overall energy of the system by decreasing the energy of the $5d\sigma^*$ electrons in AgPtPOP and the 6s electrons for TlPtPOP. In the TlPtPOP system the interaction yields a Tl 6s type
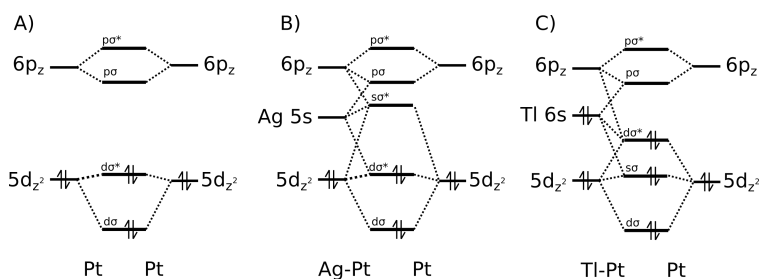
Figure 2: Molecular orbital (MO) scheme of A) PtPOP, B) AgPtPOP and c) TlPtPOP

MO energetically below the PtPOP 5d, resulting in the nature of the HOMO and LUMO being largely preserved.[16] In the AgPtPOP system, the interaction results Ag 5s type MO being energetically between the PtPOP 5d and 6p type MOs, as is shown in Fig. 2 B. This changes the nature of the transition and the bond order no longer unambiguously increases during excitation. In fact, we have tentatively made the new MO anti-bonding, following the argumentation of Sykes and Mann 1990[31], who discuss the MO-scheme of the d8-d8 complex Ir_2Dimen_4 in crystals after externally binding a silver. We will return to this point in the discussion of our results.

In this work, we use time-resolved X-ray solution scattering with an X-ray Free Electron Laser (XFEL) source to investigate the structural rearrangements, dynamics and energy dissipation with 50 fs time resolution following photo-excitation of Ag- and Tl-PtPOP in solution. The difference scattering signals $DeltaS(q,t)$ acquired for both the metal-PtPOP systems as well as for the PtPOP anion alone are analyzed using first Singular Value Decomposition (SVD) and Fourier analysis of $DeltaS(q,t)$, followed by time-resolved structural model refinement. Based on the structural dynamics observed, we propose a molecular orbital scheme for the metal-PtPOP systems investigated

6

2 Methods

Experimental

The experiments presented here were all carried out the Linac Coherent Light Source (LCLS) XFEL facility at SLAC. The PtPOP sample was prepared as an aqueous solution of K_4PtPOP (81 mM) via direct mixing of the bright yellow-green K_4PtPOP powder into the aqueous solvent under inert atmosphere to form a bright yellow solution exhibiting green fluorescence under phosphoresecent ceiling lights. The AgPtPOP sample was similarly prepared as an aqueous solution with K_4PtPOP (20 mM), CF_3SO_3Ag (30 mM) and CF_3SO_3H (40 mM). The excess triflic acid increased the stability of the sample by preventing the formation of silver clusters in solution. The TlPtPOP sample was prepared as an aqueous solution of K_4PtPOP (14 mM) and Tl_2SO_4 (105 mM Tl^+). The samples were prepared on-site and validated with optical absorption spectroscopy.

Eq. 1 depicts the law of mass actions determining the concentration of $[MPt_2POP_4]^{3-}$ as a function on the metal ion concentration M^+, the PtPOP concentration $[Pt_2POP_4]^{4-}$ and the equilibrium constants $K_{MPt_2POP_4}$.

$$K_{AgPt_2POP_4} = \frac{[AgPt_2(H_2P_2O_5)_4^{3-}]}{[Ag^+][Pt_2(H_2P_2O_5)_4^{4-}]} \qquad K_{TlPt_2POP_4} = \frac{[TlPt_2(H_2P_2O_5)_4^{3-}]}{[Tl^+][Pt_2(H_2P_2O_5)_4^{4-}]} \qquad (1)$$

From previously determined reaction constants of $K_{AgPt_2POP_4} = 320\,M^{-1}$[32] and $K_{TlPt_2POP_4} = 6\,M^{-1}$[26] we estimate the AgPtPOP concentration to be 16.3 mM, and the TlPtPOP concentration to be 5.2 mM. As such, some residual uncomplexed PtPOP remains
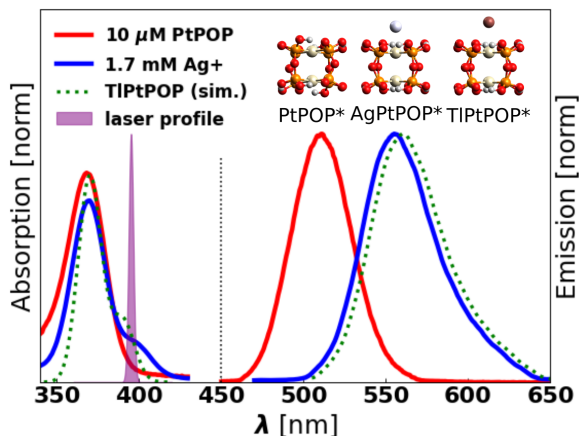
Figure 3: Ground state absorption and excited state emission spectra of PtPOP, AgPtPOP and TlPtPOP. All samples were prepared with $10\,\mu$M PtPOP in aqueous solution with either Ag^+ or Tl^+ ions added. The spectrum depicted in purple shows the position and spectral width of the excitation laser used in the X-ray scattering experiments, chosen to preferentially excite the Ag- and TlPtPOP species. The TlPtPOP spectra are a preliminary simulation based on literature.

in the solution for both metal-PtPOP samples (4 mM for AgPtPOP, 9 mM for TlPtPOP) as discussed in more detail below.

Figure 3 shows the changes in the absorption and emission spectra arising from the addition of Ag^+ and Tl^+ ions in excess to a dilute PtPOP solution. For both metal ions the absorption spectrum shifts towards longer wavelengths with concommittant shift of the emission spectrum also towards longer wavelengths. Also shown in Figure 3 is the spectral profile of the excitation laser pulse centered at 395 nm, indicating how this choice of wavelength will lead to preferential excitation of the Ag- and Tl-PtPOP species compared to the PtPOP anions also present in the sample solutions.

The laser-pump/X-ray probe experiments presented here were conducted at the XPP instrument at the LCLS. The facility delivered sub 50 fs 9.5 keV X-ray pulses at 120 Hz focused to 30 x 30 μm^2 at the sample position. The sample solutions were supplied under

helium atmosphere as a 50 μm diameter cylindrical jet with a flow speed of 3 m/s to ensure the sample was replaced between consecutive X-ray pulses. The X-rays scattered from the sample we detected by the Cornell–SLAC Pixel Array Detector (CSPAD)[33] positioned ∼5 cm behind the sample jet. We define the resulting scattering data as $S(q, \phi)$, with the scattering vector $q = (4\pi/\lambda)\sin\theta$ depending on the X-ray wavelength λ and the scattering angle θ, and the azimuthal angle ϕ in the detector plane. The detector position ∼5 cm behind the sample jet allowed the detection of scattering patterns up to a maximum scattering vector of $q = 5\text{Å}^{-1}$. The excitation laser delivered <50 fs 395(5) nm pulses of 3 μJ, focused to a ∼150 μm circular spot and set to arrive with known delays Δt with respect to the X-ray pulses.

Data reduction

To determine the structural changes following the laser excitation it is most often convenient to perform the analysis on the difference-scattering data $\Delta S(q, \phi, \Delta t)$, where $\Delta S(q, \phi, \Delta t) = S(q, \phi, \Delta t)_{\text{LaserOn}}$- $S(q, \phi)_{\text{LaserOff}}$. As such, scattering images without laser excitation were acquired for every N'th X-ray pulse and the (scaled) average of the nearest two such Laser-off images were subtracted from each Laser-On image. The difference scattering images thus formed were time-stamped and sorted according to the delay Δt, with the nominal time delay individually corrected by the timing tool information [34]. These difference scattering image arise from and therefore contain information about the structural changes in the sample arising as a consequence of the laser excitation.

To enable analysis of the acquired difference images, several data correction and reduction steps are necessary and the full data reduction process and filtering procedures are

described in detail in the supplementary information but are outlined inj the following. As an inital step, applied before forming the difference images, the 2D-images were corrected for effects of X-ray polarization, electronic noise and solid-angle coverage of the individual pixels. Nonlinear responses to changes in X-ray intensity and wavelength were corrected for following the SVD-based methodology presented in van Driel *et al*. [35]. The corrected scattering images were subsequently scaled to the simulated scattering from what is know as the Liquid Unit Cell, representing the stoichiometry of the sample. This removes the changes in scattered intensity arising from changes in incident intensity before the 2D difference scattering images are calculated and further allows for quantitative estimates of e.g. excitation fractions and temeprature increases [36]

The preferential excitation of complexes with a well-defined transition dipole moment with respect to the laser polarization causes the 2D difference scattering images to be anisotropic. As such, the 2D difference scattering images are integrated in 17 individual azimuthal bins, which are then used for the decomposition of $\Delta S(q, \phi, \Delta t)$ into the so-called isotropic $\Delta S_0(q, \Delta t)$ and anisotropic $\Delta S_2(q, \Delta t)$ components as previously described by Biasin *et al.* and Lorenz *et al*. [37, 38].

In the final step of the data reduction the difference scattering signals are binned according to Δt into equistatistical groups, meaning the same number of difference scattering images per time bin. This leads to an average temporal bin size of 30 fs for the first 5 ps. Fig. 4 depicts the measured isotropic difference scattering signals $\Delta S_0(q, \Delta t)$ of PtPOP (A), AgPtPOP (B) and TlPtPOP (C) with the corresponding anisotropic signals $\Delta S_2(q, \Delta t)$ shown in the supplementary online information. The analysis reported here focuses on the isotropic
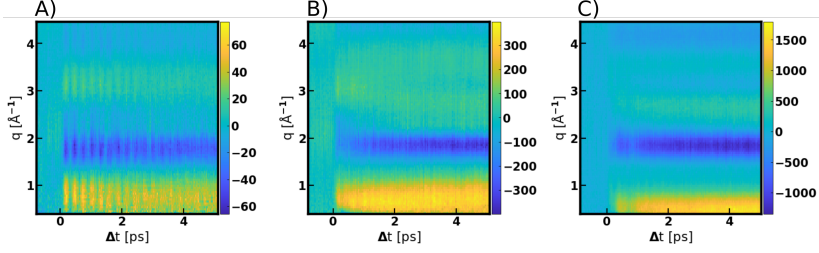
Figure 4: Isotropic difference scattering signals $\Delta S_0(q, \Delta t)$ of PtPOP (A), AgPtPOP (B) and TlPtPOP (C) for the first 5 ps after excitation. Common to all data sets are an increased difference signal at low Q which indicates a contraction along the Pt-Pt axis and an oscillatory behaviour along the time direction.

difference scattering signal ΔS_0 and uses the anisotropic signal to independently assess the structural model quality.

We note that the analysis of the PtPOP data has previously been reported[39], and that from analysis of the rise time of this difference signal the time resolution (Instrument Response Function, σ_{IRF}) of the experiment could be estimated to be $\sigma_{IRF} = 50 \pm 6$ fs.

Data analysis

The isotropic difference scattering signal ΔS_0 arises from the laser induced structural changes in the sample. In this work, we model this as arising from three contributions: Structural changes in the solute $\Delta S(q, \Delta \mathbf{r})_{Solute}$, structural changes in the solvent "shell" immediately around the solute $\Delta S(q)_{Shell}$ and changes in the bulk solvent structure due to the temperature increase ΔT following energy dissipation from the solute to the bulk solvent $\Delta S_{\Delta T}(q)$. Eq.2 depicts how the contributions are used to assemble the full model of the difference scattering

signal with the excitation fraction α, the solvation cage scaler ε, and the solvent temperature increase ΔT.

$$\Delta S_0(q, \Delta t)_{sim} = \alpha \Delta S_{Solute}(q, \mathbf{r}(\Delta t)) + \varepsilon(\Delta t)\Delta S_{Shell}(q) + \Delta T(\Delta t)\Delta S_{\Delta T}(q) \qquad (2)$$

We here note that the changes in solute structure (denoted $\Delta \mathbf{r}$) are explicitly time dependent (see below), as are the scalers on the Δs_{Shell} and $\Delta S_{\Delta T}$ terms. $\Delta S_{Solute}(q, \mathbf{r}(\Delta t))$ denotes the difference scattering between excited and ground state structures arising from a given vector of bond-length changes $\Delta \mathbf{r}$. Eq. 3 shows the calculation of the solute difference scattering signal by subtracting the ground-state scattering signal from the excited state scattering signal. The solute scattering signals, which may generally depend on all bond lengths in the ground- and excited state molecules, are in the present investigation parameterized as a function of only changes in the Pt-Pt and the metal-Pt distances in the two states, $(d_{PtPt,GS}\ d_{M,GS})$ and $(d_{PtPt,ES}\ d_{M,ES})$ as indicated in Fig. 1. $d_{PtPt,GS}$ and $d_{PtPt,ES}$ describe the distance between the platinum atoms in the ground- and excited-state, respectively. $d_{M,GS}$ and $d_{M,ES}$ describe the distances between the external metal ion and the nearest platinum atom in ground- and excited state. The ligand scaffold is assumed to be rigid, as in our prior work on PtPOP [14, 39].

$$\Delta S(q, \Delta t)_{Solute} = S(q, \Delta t)[d_{PtPt,ES}, d_{M,ES}] - S(q)[d_{PtPt,GS}, d_{M,GS}] \qquad (3)$$

The isotropic solute terms are calculated using the rotationally averaged Debye equation. Eq. 4 from which the coherent X-ray scattering from a given molecular structure consisiting of N atoms can be straighforwardly calculated:

$$S(q,\Delta t) = \sum_{m,n}^{N,N} f_n(q)f_m(q)\frac{\sin\left(qr_{mn}(\Delta t)\right)}{qr_{mn}(\Delta t)} \tag{4}$$

Here, the scattering signal $S(q,t)$ depends on the the atomic form factors $f_{n,m}$ of the various atoms and the positional vectors between atoms n and m, r_{mn}. The atomic form factors are calcualted using the Cromer-Mann approximation.[40].

The bulk solvent heat term $\Delta S_{\Delta T}(q)$ in Eq. 2 was obtained from a set of measurements utilizing photoexcitation of a short-lived dye reference sample with detection of the difference scattering signal at a time delay of 100 ps as described by Kjær et al. [41]. The time evolution of this contribution is assumed to be described by a scaling only, here denoted $\Delta T(t)$ as the scaling mentioned above yields this in degree K at thermodynamic equilibrium.

The solvation cage difference scattering term Δs_{Shell} describes the changes in scattering arising from changes in the interatomic distances between atoms in the solute and solvent molecules following photoexcitation from the ground state (GS) tot he excited state (ES), i.e. $\Delta S(q)_{Shell} = S(q)_{\text{Shell, ES}} - S(q)_{\text{Shell, GS}}$. These changes can be due to both solute structural change as well as changes in the solute electronic charge distribution [42]. For the analysis presented here, Δs_{Shell} was calculated from equilibrium Molecular Dynamics simulations of the ground- and excited state species [43] and with the time evolution of the cage term assumed to be described by a simple scaling factor, here denoted $\varepsilon(\Delta t)$. These MD simulations are described in detail in the SI.

For both AgPtPOP and TlPtPOP data sets, the best-fit structural parameters were determined based on Likelihood-estimation in a multidimensional grid of $d_{PtPt,GS}$, $d_{PtPt,ES}$, $d_{PtM,GS}$ and $d_{PtM,ES}$. The platinum atoms were constrained to take symmetric positions with respect to the Center of Mass of the ligand scaffold while the external metal atoms were constrained to positions along the PtPt bond axis. The ligand scaffold was approximated as rigid. An alternative geometry, where the complexating metal atom is located outside the ligand scaffold on an axis orthogonal to the PtPt- axis has been proposed by Kruppa *et al.*[30]. Result using this model are discussed in detail in the supplementary online information.

The likelihood of any given structural model was assessed in a χ^2 framework, where $\chi^2 = \sum(\Delta S_{Model} - \Delta S_{data})^2/\sigma^2$ using Eq. 2 to calculate the $\Delta S(q)$. From this we estimated the (relative) model likelihoods L via $L \sim \exp(-\chi^2/2)$, projecting the N-dimensional likelihood distribution onto each parameter axis [44], with N being the set of optimization parameters $(d_{PtPt}, d_{PtM}, \alpha, \varepsilon, \Delta T)$.

The full optimization of the structural and solvent fit parameters was done as a two-step process. Initially the structural parameters of the ground state solute and the equilibrated excited state solute are determined along with the excitation fraction α at Δt 4 ps, at which the structural changes in the solute are expected to be completed. The fit was further stabilized by constraining $\varepsilon = \alpha$ during this optimization process, as the relative magnitude of the ΔS_{Shell} contribution scaled via ε is expected to be determined by the excitation fraction α in the excited state equilibrium obtained after a few picoseconds. In the second step of the analysis the ground state structure and excitation fraction were kept constant while the excited-state structural parameters as well as ε and ΔT were optimized for each time bin individually.

Modelling

To provide a starting point for the structural analysis described above, initial ground- and excited-state structures of PtPOP, AgPtPOP and TlPtPOP were calculated with DFT using the B3LYP functional with a D3(BJ) dispersion correction. The structure was first determined with the def2-SVP basis set and refined using the def2-TZVP set. The solvent was approximated with the polarizable continuum CPCM-model and all calculations were done using the ORCA framework[45]. Determining the structure of loosely bound transitions metal complexes can be a significant challenge for DFT-based methods [16] and therefore the geometry optimizations were carried out while constraining the Pt-metal distances.

To calculate contributions to the difference scattering signal arising from changes in the solute-solvent interactions and structure, ΔS_{Shell}, the aqueous solvent was included in the modelling via molecular dynamics (MD) simulations by extending the GAFF force field based on the partial charges calculated from the DFT simulations. These simulations were done for the ground- and excited state solute structures and with 2872 Water molecules in the MD simulations and with the corresponding difference scattering signals calculated from the resulting Radial Distribution Functions using the approach outlined by Dohn *et al.* [43]. The simulation methods used are further described in the supplementary online information.

3   Results

3.1   Model-independent analysis

As a first step in the analysis of the three $\Delta S(q,t)$ data sets presented in Figure 4 we apply a Singular Value Decomposition. By this approach, the data matrix $\Delta S(q,t)$, now denoted **X**, is decomposed into an orthonormal set of vectors via $X = SUV^T$, where T here denotes the transpose of V. Within this framework, the columns of S describe the characteristic shape(s) of the signal in X, the colums of V described the (time) evolution of the signal and the diagonal values of U encode the relative magnitude of the individual components described the columns of S. Figure 5 A) shows the first column of S as a function of q, and the characteristic shapes with a positive feature at low-q followed by an oscillatory pattern as also seen is Figure 4 is immediately recognized for all three data sets with TlPtPOP in orange, AgPtPOP in green and PtPOP in blue. This characteristic shape of the difference scattering signal can be directly interpreted as arising from a contraction of electron density, and based on the know structural dynamics of PtPOP we assign this as arising primarily from a contraction along the Pt-Pt axis. Figure Sx in the SI shows SVD components 2-5 for the three data sets.

Figure 5 B) shows the time evolution (rows of V) for these three components, which all show a prompt increase at $\Delta t = 0$. In particular for the PtPOP data set (blue lines) a clear oscillatory pattern is seen, as expected from the full data sets shown in Figure 4. To enhance these features, we follow the approach presented by Biasin *et al.* [46] where an IRF-broadened exponential grow-in is substracted from the signal to isolate the Oscillatory
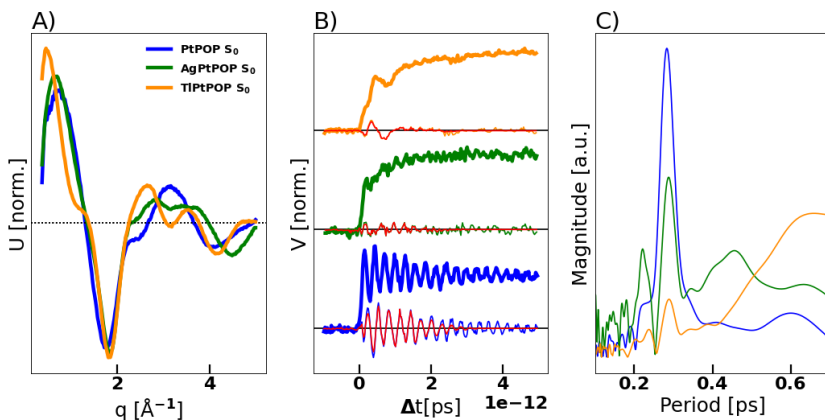
Figure 5: Analysis of the first SVD-component of $\Delta S0$. A) depicts the first U vector of each system along the q-axis. They are comparatively similar between the samples. B) shows the V vector along Δt corresponding to the depicted U vectors, as well as its oscillatory structural signal (OSS) along the time-axis. The red lines show the OSSs after application of a $\sigma=1$ ps Gaussian window centered at $\Delta t = 1$ ps to suppress artifacts. C) shows the Fourier-transformation a of said windowed OSSs. The Fourier magnitudes are normalized to the magnitude of the OSS.

Structural Signal, OSS. Figure 5 B) shows the OSS with thinner lines, with the color coding again corresponding to TlPtPOP (orange), AgPtPOP (green) and PtPOP (blue).

Fig. 5 C) shows Fourier Transformations (FT) of the three OSS as a function of period T following application of a gaussian window function centered at $\Delta t = 1$ ps and with $\sigma=1$ ps, as shown with red lines in Fig. 5 B) Common to all three data sets, a mode with a period of $T = 0.29$ ps is present and while this completely dominates the PtPOP spectrum, it is less pronounced for AgPtPOP and even more so for TlPtPOP. In contrast to the PtPOP data set, both M-PtPOP data sets exhibit significant contributions at other vibrational periods, with AgPtPOP having peaks at $T = 0.2$ ps and $T=0.4$ ps and TlPtPOP exhibiting broader feature around $T=0.7$ ps as discussed in further detail below. To investigate the dynamics observed in Fig. 5 C) in more detail, we next consider time-resolved Fourier spectra taken at two differen regions of q-space highlight different structural motions in the solute. The

Fourier Transforms of the OSS from ΔS_0 averaged between $q = 0.4 - 0.8\,\text{Å}^{-1}$ and q= 1.0 - $1.2\,\text{Å}^{-1}$ are taken with a sliding $\sigma = 0.4\,\text{ps}$ Gaussian window. The q-ranges have been chosen based on their ability to separate the periods determined via the analysis shown in Fig. 5 C.

The time-resolved Fourier transform of the PtPOP OSS (Fig.6 A1) exhibits a strong $\sim 0.29\,\text{ps}$ mode decaying over several picoseconds. As discussed in the recent paper by Haldrup *et al.*[39], at 395 nm excitation this mode corresponds to the ground state oscillation in the PtPt distance of PtPOP, due to off-resonanence excitation. The fourier analysis of the difference signal in the higher q-range exhibits the same period, but with reduced amplitude (Figure 6 A2). Figures 6 A3 and A4 show the two OSS (blue) for PtPOP along with a fit (red line) of a single, damped harmonic function to the OSS data, and we find that the OSS signal is very well described by single oscillating signal with a period of T = 0.29(1) ps and a damping time of ??? ps. This model-independent analysis is thus in good agreement with the results of structural modelling presented in [39] where the T=0.285 ps mode with a decay time was found to arise from ground-state dynamics of the Pt-Pt bond length.

Focusing next on the high-q signals for AgPtPOP and TlPtPOP, the time-resolved Fourier transform of the AgPtPOP OSS (Fig.6 B1) exhibits a short-lived (<1 ps) broad feature at a period T=0.4-0.6ps. In a similar fashion, the TlPtPOP system (Fig.6 C1) exhibits a broad, short-lived feature centered at 0.6 ps. From the fits to the OSS data (B3, C3) we find best-fit periods of T=0.44 ps and T=0.6 ps, respectively, with decay times of 0.9±0.2 and 1.1±0.3 ps. The Fourier maps indicate that these oscillations frequencies change slightly over time, as the 0.44 ps mode of AgPtPOP moves towards shorter period times and the 0.6 ps mode moves towards longer period times over the first picosecond.

In the time-resolved fourier analysis in the higher q-range (B2 and C2), both M-PtPOP systems exhibit oscillations with periods at around T=0.29 ps. The corresponding features in the OSSs can be again be described through a single 0.29±0.01 ps oscillation (B4,C4), even if the fit quality is considerably poorer than in the PtPOP system.

The oscillation magnitudes are fitted on the relative difference signal between the self normalized images, to prevent biasing from the liquid unit cell scaling. The amplitudes are depicted as normalized to both the residual PtPOP concentration and the sample concentration, to assess whether or not the 0.29 ps oscillatory mode is a feature of the MPtPOP systems. The amplitudes of the oscillations are about 3 times stronger for TlPtPOP and 8 times stronger for AgPtPOP than expected from the residual PtPOP in solution, as shown by the oscillation amplitudes in the fits of the panel 4's, which we shall return to in the discussion section. We observe a phase shift of less than $0.3\,\pi$ between the three systems on the other in the 0.29 ps mode when fitting the OSS between 1.0 and $1.2\,\text{Å}^{-1}$. The 0.29 ps mode normalized to the sample concentration depicts that the oscillation is nearly 3 times as strong per TlPtPOP molecule than it is per AgPtPOP molecule in the sample solutions. The oscillations revealed in the SVD analysis have been attributed to different parts of the q-space, which suggests they arise from different parts of the structure. The 0.29 ps mode is too strong in the MPtPOP datasets as to be explained by residual PtPOP.

3.2   Structural model fitting

3.2.1   Ground state and excited state equilibrium fit

To further investigate the direct complex structure, the sample systems are analyzed with a modeling approach to determine structural parameters. Fig. 7 depicts the best fit result
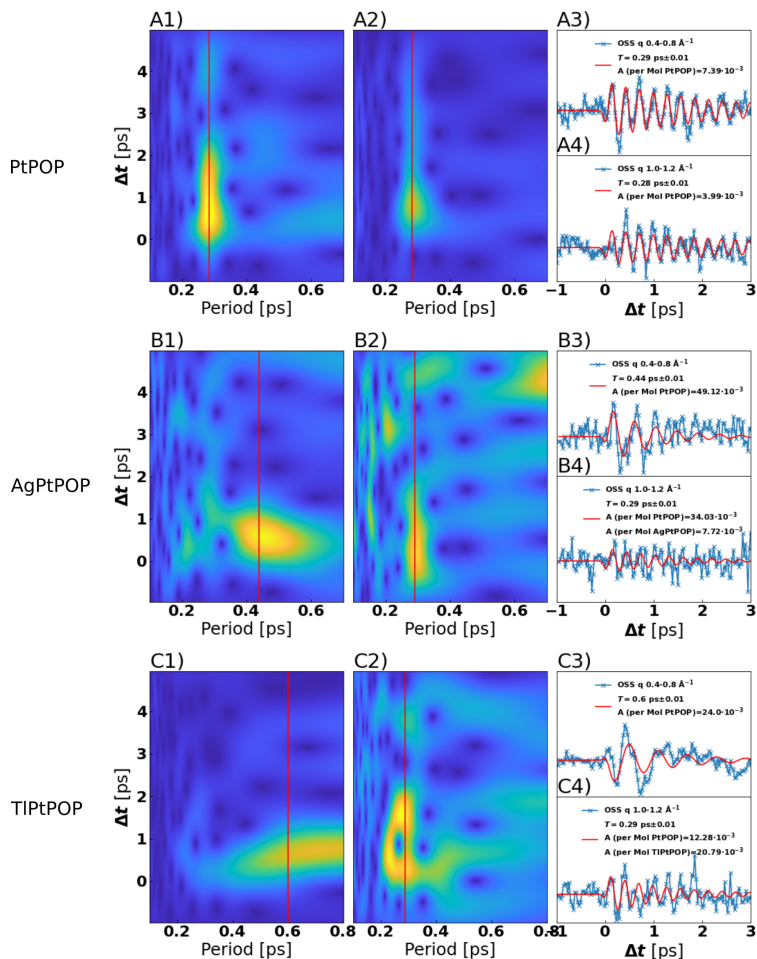
Figure 6: Fourier map of the PtPOP (A), AgPtPOP (B), and TlPtPOP (C) oscillatory structural signals of the averaged data signal between 0.4 and 0.8 Å^{-1} (column 1) and between 1.0 and 1.2 Å^{-1} (column 2). The time and frequency resolution is given by a gaussian window function with $\sigma = 0.425$ ps. A $\sim$0.29 ps mode is visible in the PtPOP (A1 & A2) and appears for the M-PtPOP in q range 2 (B2 & C2). The M-PtPOP systems exhibit strong transient oscillations at 0.45 ps and 0.6-0.7 ps respectively in q range A (B1 & C1). The signals in the Fourier space are fitted to the corresponding signals in the images 3 and 4 for A-C. The amplitude fit parameter is normalized to the amount of uncomplexed PtPOP in solution to assess whether or not the oscillation arises from MPtPOP. The red lines in the first 2 columns corresponds to the fitted periods in the third column.

Table 1: Fitting results of the ground state structural parameters and changes after excitation

Parameter	AgPtPOP	TlPtPOP
$\mathbf{d_{PtPt,GS}}$ [Å]	3.03±0.04	3.12±0.12
$\mathbf{\Delta d_{PtPt}}$ [Å]	0.25±0.08	0.28±0.08
$\mathbf{d_{PtM,GS}}$ [Å]	2.87±0.12	3.14±0.16
$\mathbf{\Delta d_{PtM}}$ [Å]	-0.19±0.04	0.31±0.24
α [%]	34±10	26±16

from the structural optimization for both AgPtPOP (A) and TlPtPOP (B) as well as the heat and solvation contributions in accordance with Eq. 2 for $\Delta t = 4$ ps. The determined structural parameters are listed in Tab. 1. In both cases the ground state distances between the platinum atoms are determined to be slightly larger than 3 Å and are associated with a contraction of around 0.25 Å after excitation. However, in opposition to one another, d_{PtTl} contracts after excitation while d_{PtAg} expands. Fig. 7 depicts the fits using the parameters. The models reproduces the broader features of the signals well. The residual of the AgPtPOP fit does not show much structure. The TlPtPOP fit also follows the broader features of the data well, but leave some structured residual around the peaks at 1.8 and 2.3 Å^{-1}.

The panels III of both samples depict the anisotropic scattering of the structures optimized on the isotropic signal ΔS_0 scaled onto ΔS_2. The TlPtPOP fit describes the data well. The AgPtPOP signal follows shape of the data but exhibits some offsets to the curve towards lower q. In both cases the excitation fraction had to be decreased in order to match the signal.

3.2.2 Time resolved fitting

By first identifying the the ground state structure and excited state fraction of the system the temporal development of the structural parameters can be tracked as a function of time. Fig. 8 shows the results obtained by analyzing the AgPtPOP data in such a manner.
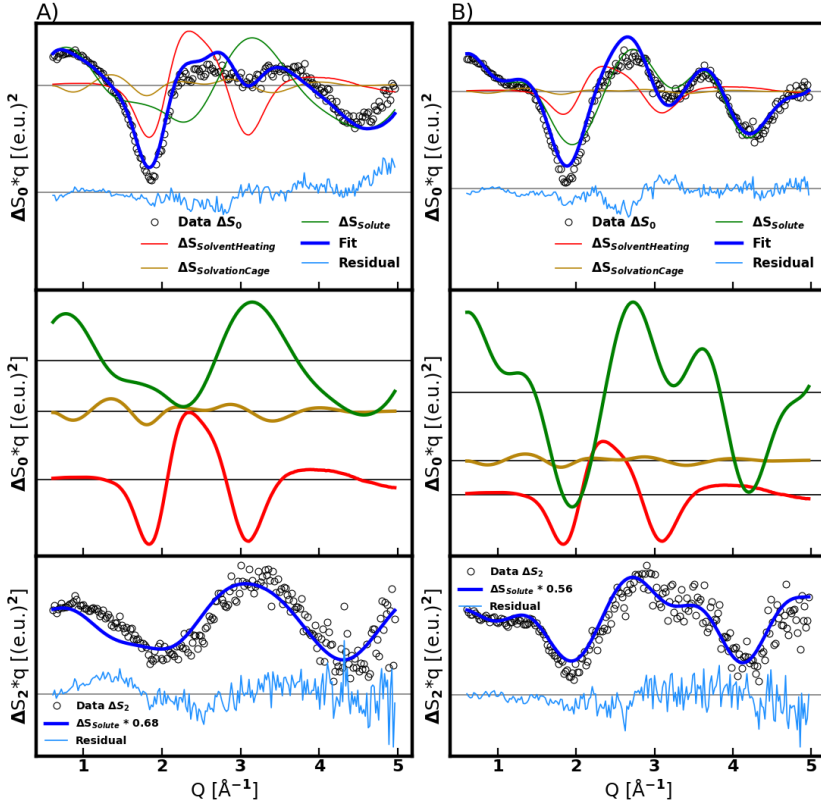
Figure 7: Fit of the signal for AgPtPOP (A) and TlPtPOP (B) at Δt = 4 ps. The panels I) show signal, fit and individual fit components to scale on top of one another. The light blue lines at the bottom show the residual of the fit. II) depicts the solute, heat and solvation fit components separated from one another. III) depicts ΔS_2 and the simulated signal of the structure optimized on the ΔS_0 signal.

Table 2: Comparison of the kinetic fit parameters between the AgPtPOP and TlPtPOP time-resolved structural fitting results

	A)	AgPtPOP		B)	TlPtPOP	
Parameter	T_1 [ps]	τ_ω [ps]	τ_1 [ps]	T_1 [ps]	τ_ω	τ_1 [ps]
d_{PtPt}	0.28±0.01	1.71±0.69	1.58±0.18			
d_{PtM}	0.36±0.02	1.47±0.87	0.98±0.18	0.8±0.04	0.49±0.11	1.53±0.04
ε			0.02±0.04			0.22±0.46
ΔT			1.35±0.04			1.64±0.11

Figure 8: Structural Parameters and solvent temperature increase fitted for the isotropic signal of AgPtPOP. The left panel shows the optimized structural parameters for every time bin. The solid red lines depict the kinetic fits. $d_{PtPt,ES}$ describes the distance between the two platinum atoms and $d_{PtAg,ES}$ describes the distance of the silver atom to the complex center, as is shown in Fig. 1, The right panels show the solvation cage and temperature scaler along with the fits.

The most likely parameters for each time step were connected through the time bins using kinetic functions. These functions consist out of terms for increases and decreases as well as an oscillations with a dampening term convoluted with a Heaviside function and the IRF. The functions used for each specific parameter curve are discussed in the supplementary online information. The time constants describing the dynamics can be extracted by using these functions. The functions are described in the supplementary online information.

The kinetic parameters for the AgPtPOP dataset are depicted in Tab. 2 A), with the oscillation period T_1, the oscillation dampening time τ_ω, and the exponential convergence term τ_1.

Both the d_{PtPt} contraction and d_{PtAg} could only be described well by expanding a step function with an exponential terms describing the atom movements. The motions are superimposed with oscillations with periods of 0.28 ± 0.01 ps and 0.36 ± 0.02 ps. The
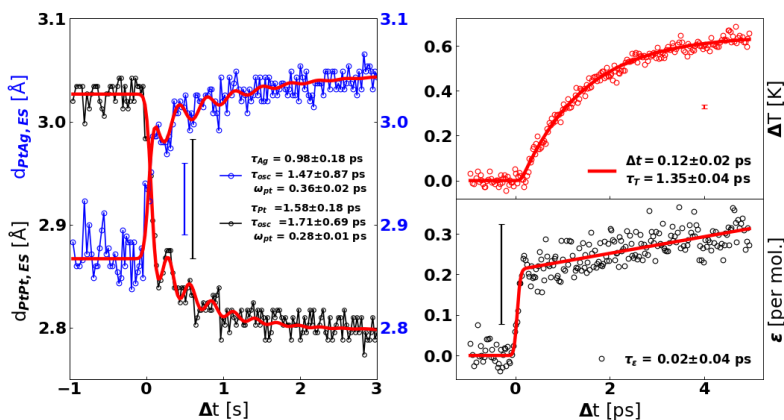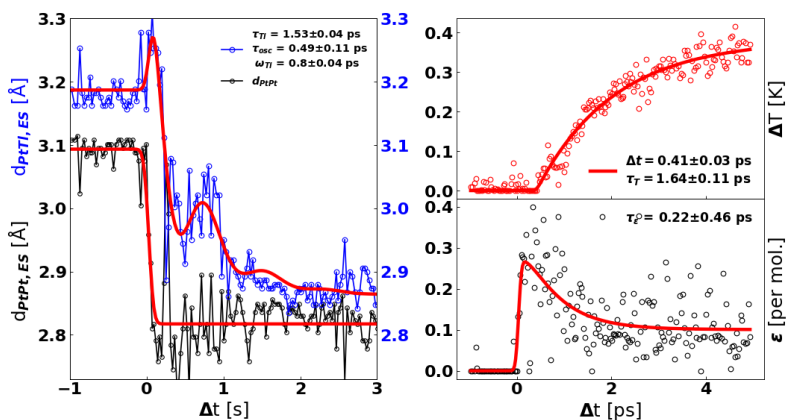
Figure 9: Structural Parameters and solvent temperature increase fitted for the isotropic signal of TlPtPOP. The left panel shows the optimized structural parameters for every time bin. The solid red lines depict the kinetic fits. $d_{PtPt,ES}$ describes the distance between the two platinum atoms and $d_{PtTl,ES}$ describes the distance of the Thallium atom to the complex center, as is shown in Fig. 1. The right panels show the solvation cage and temperature scaler along with the fit.

solvation cage scaler reaches is maximum immediately. The function had to be extended with a linear term to match the result. The energy is dissipated with a time constant of 1.35 ± 0.04 ps after a delay of 0.12 ps.

The TlPtPOP temporal analysis results are depicted in Fig. 9 with the associated time constants displayed in Tab. 2 B). The contractions of d_{PtPt} is well described with a broadened step function, d_{PtTl} is adequately described with a single exponential convergence term. The Thallium motion is superimposed with as oscillation with the period of 0.8 ± 0.04 ps. The solvation cage scaler reaches its maximum with a time constant of 0.22 ± 0.46 ps. The function had to be extended by an exponentially decaying term to match the larger values at short time delays. The temperature approaches its maximum with a time constant of 1.65 ± 0.11 ps after a delay 0.4 ps.

24

Individual data curves and the corresponding fits are depicted in the SI for short time delays for both systems.

4   Discussion

The SVD analysis, the Fourier analysis, and the structural model fit have three oscillation periods in common: 0.28-29 ps for both MPtPOP systems (for TlPtPOP only in the SVD and Fourier analyses), 0.36-0.44 ps for AgPtPOP, and 0.6-0.8 ps for TlPtPOP. These similarities give confidence to the structural model and we, therefore, continue the discussion based on the structural model.

4.1   Steady state structural fitting (Table 1) discussion

The ground state Pt-Pt distances of 3.03 and 3.12 Å for AgPtPOP and TlPtPOP are slightly longer than distances proposed for PtPOP ranging from 2.88 Å[13] to 2.96 Å[39] but could be explained with the external bond stabilizing platinum positions further away from the center.

The final contractions in Pt-Pt distances of 0.25 and 0.28 Å for AgPtPOP and TlPtPOP are in good agreement with previous work on the PtPOP system, which estimate the contraction between 0.2 and 0.31 Å[39, 36, 18, 21, 13, 19, 47, 20]

The ground state distances $d_{PtTl,GS}$ 3.14 Å and $d_{PtAg,GS}$ 2.87 Å are plausible in comparison to previous work on transition metal complexes.[5] The excited state PtTl distance of 2.83 Å is shorter than the 3.0 Å previously predicted by DFT calculations[16] and the 2.92 Å estimated with solution scattering[28] but still comparable and within the range

of 2.7-4.0 Å initially assessed by Clodfelder et al.[26]. In the AgPtPOP system the excited

state PtAg distance of 3.06 Å is longer than the 2.86 Å predicted by DFT calculations[16].

The MO-scheme Fig. 2 attributes the contraction of d_{PtPt} in both systems after

excitation to the depopulation of the antibonding orbital $5d\sigma*$. In the TlPtPOP system, like

in PtPOP, the electron is promoted into a bonding $6p\sigma$ orbital, resulting in an increase in

bonding order, which is consistent with our observed decrease of d_{PtTl}. In AgPtPOP the

electron is promoted into the an $5s\sigma$-type orbital, which we tentatively made anti-bonding

in the figure. This is consistent with our observed increase of d_{PtAg}, resulting in the Ag to

complex center distance $d_A g$ not changing within the error bar.

The ΔS_2 signal in both system can best be described through a decrease in excitation

fraction in comparison to the ΔS_0 result. This difference can be explained through either a

not well defined transition dipole moment, resulting in the anisotropy being smeared out, or

multiphoton excitation which does not necessarily follow the ΔS_2 symmetry.

Due to distortions in the signal shape due to artifacts there may be an offset to the

structural parameters to covered by the statistical error determined through goodness-of-fit

estimations.

4.2 Time dependent structural fitting (Table 2) discussion

The fitted changes in structural parameters occur as one motion on the potential energy

surface, but are subject to dampening on several timescales. The primary ones are impul-

sive cooling within the first hundreds of femtoseconds, vibrational cooling over the first 2

picoseconds as well as (very slight) dephasing.[22] As such, the motion is split during the

kinetic fitting into at least a fast contraction and an oscillatory term. The impulse cooling is faster than the IRF for both systems. The additional time constant τ_1 needed to describe the d_{PtPt} is AgPtPOP is likely the result of multiphoton excitation, in which higherlying states are populated, which decay within the first picoseconds into the lowes singlet or triplet state. The oscillations with a T_1 of 0.29 ps, determined also from the SVD and Fourier analyses, were resolved in the the $d_{PtPt,ES}$ of AgPtPOP, but not for TlPtPOP. This is likely due to the oscillations being weak and the model being much more sensitive to details of the analysis than a Fourier transformation.

d_{PtAg} expands within the time resolution and exhibits the 0.36±0.02 ps mode, the d_{PtTl} exhibits a 0.8±0.04 ps mode, which supports the conclusion from the Fourier analysis that these are indeed dynamics of the excited state. The slower contraction of d_{PtTl} supports the argument of a reasonable amount of multiphoton excitation suggested by the scaling onto the ΔS_2 signal.

In both systems, the solvation cage response reaches its maximum faster than solvent response time of water of 0.6(2) ps[48]. This behavior is in line in the platinum atoms and possibly metal atom moving away from the closest solvent molecules during the fast contraction process, causing the majority of changes between the solvation shell in ground and excited state equilibrium. In both systems the $\varepsilon(t)$ fits had to be expanded to include an additional term as an ajustment, a linear for AgPtPOP and a shortlived decay for TlPtPOP,

The heat dissipation time constants of 1.35 ps for AgPtPOP and 1.65 ps for TlPtPOP are notably slower than the timescale of the solvent. The heat dissipation is therefore not only limited to the first hundreds of femtoseconds following the excitation, but energy continues to be dissipated due to vibrational cooling over the first few picoseconds[22]. The delays

of the arise of the heat signal of 0.12 ps and 0.41 ps are comparable with previous studies [39] and simulated energy dissipation time for PtPOP[17]. The delay can be attributed to the transfer of energy from central modes to those coupling to solvent molecules

The temperature increase of 0.61 K for AgPtPOP and 0.31 K of TlPtPOP are notably larger than 0.25 K[39] reported for PtPOP. The values are in line with the heat dissipated from single photon excitation as well as the added heat from additional multiphoton excitation, in relation to the change in excitation fraction needed to describe the ΔS_2 signal, as described in the supplementary online information.

4.3   Discussion of the 0.29 ps oscillation

Both the SVD analysis and the fitting of the low q signal with a dampened oscillator show oscillations with a period of 0.29 ps as part of the responses of both AgPtPOP and TlPtPOP difference scattering. This mode shows up in the Fourier analysis, alongside the stronger modes at longer periods with short decay times. The fitted magnitude of the oscillation is 3-8 times stronger than would be expected from the residual PtPOP present in the sample solutions. Thus oscillation is too strong to be explained by residual PtPOP and must originate from the M-PtPOP systems.

In the structural model, this period is assigned to Pt-Pt vibrations in the excited state. However, no PtPt vibrations are included in the ground state so the model fit could also try to compensate for PtPt vibrations in the ground state. Below, we discuss two pictures that would give rise to observed either excited- or ground-state PtPt vibrations.
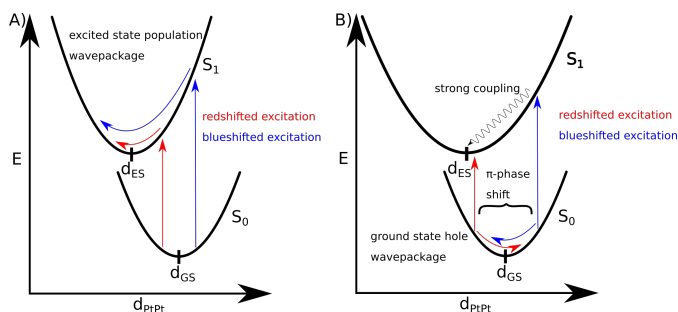
Figure 10: Ground- and excited state potential energy surfaces for d_{PtPt}, depicting a possible oscillation in the excited state A and the ground state B

Excited-state oscillations only: The observed oscillations can be explained through motion of the excited state population on the excited state potential energy surface shown in Fig. 10 A. After excitation d_{PtPt} oscillates around the equilibrium excited-state distance d_{ES} dissipating energy into the surroundings. The (slightly) blue shifted excitation of the AgPtPOP (395 nm laser, 400 nm absorption maximum) would result in an excitation to a higher vibrational state, resulting in a relatively larger oscillation amplitude, compared to the TlPtPOP system. At the same time, the blue shift for AgPtPOP and the red shift for TlPtPOP (395 nm laser, 400 nm absorption maximum) are both small and would result in little visible ground-state vibration. This model results in no phase shift in the oscillation between both the MPtPOP systems and the PtPOP system.

Ground-state oscillations only: A model with strongly coupled d_{PtPt} excited state vibrational modes, such as to the external metal modes observed, also explains the observed dynamics, as depicted in Fig. 10 B. This model describes the larger relative change per solvent molecule observed in the fitting for TlPtPOP due to the larger scattering power of the heavier external atom. This model is also supported by the similarity of oscillation frequencies in PtPOP and MPtPOP systems This is supported by shape of the ground state molecular

orbitals calculated by Kong et al.[16], which describes a similar electronic potential surface describing the ground state Pt-Pt distance should be similar between the MPtPOP and the PtPOP systems, thereby explaining the same frequency to oscillations in the ground state potential surface of PtPOP.[39]. The model results in a phase shift of π between the red shifted excitations PtPOP and TlPtPOP on one side and the blue shifted excitation of AgPtPOP on the other side, as observed by Van der Veen *et al.*[22] for PtPOP.

Due to the low signal to artifact ratio for the weak oscillation, both t_0 and thereby phase are difficult to determine accurately.

We thus tentatively assign this mode to arise from ground state oscillations of the M-PtPOP systems between the Pt atoms, in which, similar to the PtPOP system[39], the hole in ground state from where the molecules have been excited on the ground state potential oscillates. The decreased coherence time in comparison to pure PtPOP can be attributed to the influence of the external metal atom.

The several picosecond rise-time seen in the temporal evolution of the M-PtPOP systems in the SVD analysis indicate that there is at least some degree of either electronic or steric hindrance preventing the equilibration of the excited state structure (Fig. 5). Multi-photon excitation in PtPOP results in the population of short-lived higher lying states, that directly decay into the triplet state over the with a time constant of 0.3 ps.[49] As the bonding MO between the platinum atoms is not occupied in these higher lying states, the preferred platinum-distance may be longer than the one of the lowest singlet or triplet state. As such the excited state signal grows in over said time instead of developing fully immediately after the excitation. As the signal is strongest in a different part of the q-range as the previously identified PtPt motion, we tentatively assign the slow grow-in of the primary component of

the M-PtPOP systems to arise from similar higher order population effects. The changes

of frequency over the first picoseconds in the $d_{M,Pt}$ modes over the first picosecond can be

attributed to anharmonicity in the potential energy surface.

4.4 What we have learned

We have determined the structures to of AgPtPOP and TlPtPOP. We see the metal atom

distance change following excitation and observe oscillations around the new equlibrium

positions. We believe this is due to the changes in bond strength following the promotion of

the electron and subsequent change of electronic structure. The structural fitting also grants

insight into the structural rearrangement and non-equilibrium structural dynamics occurring

on ultrafast timescales shortly after the excitation. This work gives insight into the larger

class to trimetallic transition metal complexes as well as the nature of metal-metal bonding.

4.4.1 open data

The reduced data files, containing the data binned in q and Δt dimension, as well as reference
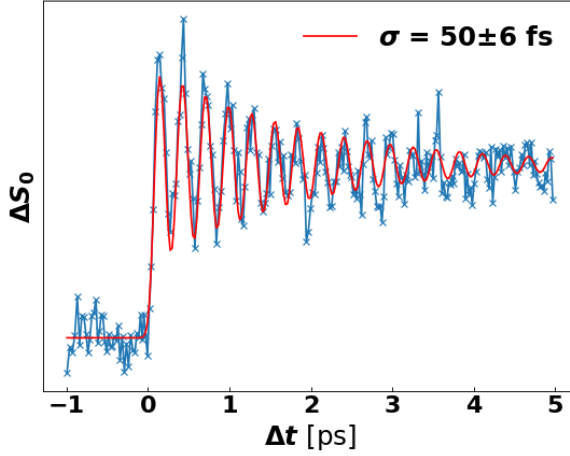
files and analysis code is available online [cite final DOI]

Figure 11: Determination of the IRF with the Pt_2POP_4 sample. The ΔS_0 of the PtPOP dataset averaged in the q range between 0.8 and 1.2 Å^{-1} is taken and fitted with Heaviside function convoluted with a dampened oscillation and a Gaussian Instrument response function.

Supplementary online information

5 Instrumental response function and two-photon excitation

The temporal resolution of the Pt_2POP_4 measurement was assessed by fitting the time-depedence of the signal averaged between 0.8 and 1-2 Å^{-1}. The signal shows evolution arising from coherent dynamics to the Pt-Pt distances in the ground state population after off-resonance excitation[39], and can be described through a convolution of a Heaviside function describing t=0, a sine function describing the oscillations and an exponential decay describing the decreasing coherence, as shown in Eq. 5.

$$\Delta S(t) = IRF * H(t) \cdot (A + B \cdot \sin(\omega t + \phi) \cdot \exp(-t/\tau)) \tag{5}$$

$$IRF = \frac{1}{\sqrt{2\pi}\sigma} \cdot \exp\frac{-t^2}{2\sigma^2} \qquad (6)$$

For the fit, this function was convoluted with the instrument response function (IRF), which yielded a σ_{IRF} of 50 ± 6 fs when fitted using the gaussian distribution shaped IRF shown in Eq. 6. This is within expectation for a 50μm jet thickness, resulting in a temporal smearing of 50 fs due to the different speed of optical and X-ray pulse, a pulse width of 30 fs, and 10 fs uncertainty on the timing tool, adding up to a total expected smearing of 59 fs.

The peak height of oscillation maxima and minima after the first rise exceeding the first peak hints and the presence of two-photon excitation[39], leading to the formation of higher-order states that directly decay into the triplet state T_1 over the course of 2 ps[49]. As a same excitation energy was used for the MPt_2POP_4, which exhibits a larger absorbance at the excitation wavelength, experiments, multiphoton effects cannot be ruled out.

Complexes excited into higher order states decay within hundreds of femtoseconds into the lowest triplet or singlet states. As such the structural parameters determined for the equilibrium after several picoseconds are not effected by the occurrence of multiphoton excitation. The dynamics however at short time delays would be smeared out, as complexes in different electronic states posses different potential energy surfaces in atom position resulting in different vibrational modes.

6 MD Simulations of solvent shell structural changes

The overarching strategy for sampling solvent shell changes is described in detail elsewhere[50]. We attempt to sidestep issues inherent in developing force fields for exotic complexes and electronic states[51] by restraining DFT-optimized geometries of the involved complexes and their states while sampling the solvent structure as a result of custom partial charge sets obtained through the DFT calculations, to obtain an average response from the changes in the solvent shell.

First, the bonded interatomic force field terms of the AgPtPOP complex were parametrized within the GAFF model[52] in the ground state using 'MCPB.py' following the procedure reported elsewhere[53], using the Gaussian16 program[54] for the required QM simulations. This preliminary solute structure was solvated and the total simulation cell was charge-neutralized using the LEaP code from the AmberTools suite[55]. The cell was initially equilibrated in the NPT ensemble, resulting in a 44.49 Å x 44.00 Å x 44.52 Å box containing 2871 water molecules, described by the TIP4PEW potential[56]. All MD simulations were carried out using OpenMM[57]. Molecular ES and GS geometries containing metal-metal distances structurally fitted without solvent cage contributions were then re-relaxed, constraining the 3 metal atom distances to the values obtained from the initial, solvent-free structural fit. The geometric relaxation was carried out at the B3LYP/def2-TZVP[58, 59, 60, 61, 62] level with the CPCM polarizable continuum model for water[63], using the ORCA program with its standard geometry convergence criteria[64]. We name the the two resulting geometries $\mathbf{R}_{\text{initial}}^{\text{ES}}$ and $\mathbf{R}_{\text{initial}}^{\text{GS}}$. Then, sets of RESP-charges were created by scanning the vdw radii of the Pt and the Ag/Tl metals in the range of 1-3 Å, using Gaussian which allows the user to manually set this parameter, using the same functional, basis set and solvation model

as previously. Then, for each set of partial charges, the solvation shell of the complex was sampled using the MD procedure described below.

For each of the partial charge sets for each of the previously optimized structures, the ES and GS solute geometries in the initial MD box were reset to the $\mathbf{R}_{initial}^{ES}$ and $\mathbf{R}_{initial}^{GS}$ geometries, and its charges changed. For the TlPtPOP runs, the Lennard-Jones parameters were changed accordingly[65]. The solute atoms were restrained with 2000 kcal/mol Hookean potentials, and the solvent shell was allowed to re-equilibrate around this new structure and set of charges for 200 ps in the NVT ensemble. The production runs sampling the solvent shells were then sampled for 10 ns each, also in the NVT ensemble, using a Langevin thermostat in both cases. The radial distribution functions were sampled using the VMD program[66], and difference-RDFs (ES - GS) were calculated for all possible combinations of ES and GS vdw radii-runs, and the resulting cage-scattering from these distributions were calculated as described elsewhere[43].

6.1   Radial distribution functions

Radial distribution functions (RDFs) describe correlation of atomic distances between 2 atoms of specific types, being separated both by atomic number and affiliation with either solvent or solute. In solution, the correlation is defined as the amount of molecules within a given spherical shell in comparison to the density of bulk solvent.

Fig. 12 depicts the radial distribution function between the silver atom and the solvent atoms for both ground and exited state for the simulated solvation cage used in the structural analysis. In the ground state, the water molecules are strongly coordinated with the silver atom. The positive charge of the complex results in the oxygen atoms directing
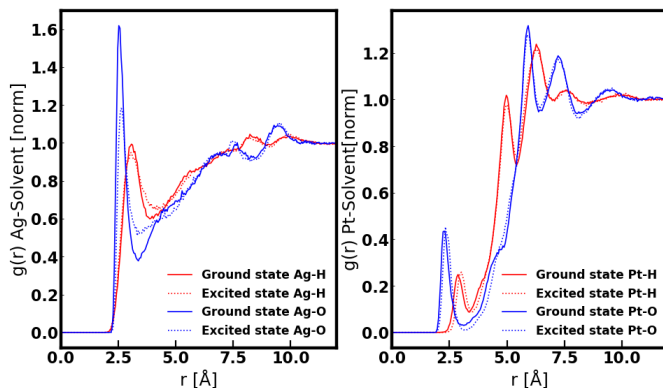
Figure 12: Radial distribution functions of Ag and Pt for the solvent atoms

themselves towards the atom, with the hydrogen atom point outwards. After the excitation, the coordination becomes weaker as the first peak is softened and shifts to greater distances. The simulation suggests that the excitation results in a desolvation of the silver.

In direct comparison to the ground state, the RDFs are shifted towards larger distances in the excited state especially in the Pt-distances, which can be explained with the contraction of the Pt atoms away from the solvent. Additionally there is a considerably decrease in order especially in the Ag-solvent distributions.

The same cage was used for the $TlPt_2POP_4$ system due to problems with the simulations of solvation cages with this system. The solvation cage was chosen out of several simulated with different partial charge distribution. Solvation cages were rejected for exhibiting discrete peaks in the radial distribution functions of either ground and excited state or by exhibiting an increased difference scattering signal towards higher q. The remaining solvation cages produced similar results.

7 Calorimetry

We report a temperature increase of 0.68±0.07 K in the AgPtPOP measurement and 1.08±0.32 K for the TlPtPOP. With an excitation wavelength of 395 nm and emission wavelengths of 560 nm for AgPtPOP and 550 nm for TlPtPOP, 0.92 eV and 0.88 eV are deposited in the form of heat in the solvent per single photon excitation. This deposited energy per liquid unit cell multiplied with the determined excitation fractions of $\alpha_{Ag} = 0.34$ and $\alpha_{Tl} = 0.26$ both serves as a minimum possible temperature as well as a starting point to assess how much multiphoton excitation may have occurred during the experiment.

$$n_{Multiphoton} = \frac{\Delta T \cdot C_{T,Water} \cdot n_{water} - (e_i - e_f) \cdot \alpha}{e_i} \tag{7}$$

The amount of multiphoton absorption events in a liquid unit cell can be assessed with Eq. 7, with the heat capacity $C_{T,Water}$, the absorbed energy e_i and the emitted energy e_f. The energy that is dissipated in the form of heat is attributed to two sources, single-photon and multiple-photon absorption events. The single photon absorption per liquid unit cell occurs according to the excitation fraction, dissipating the difference in energy between absorbed and emitted photons in heat. During multi-photon events, one or more additional inciting photons are absorbed by an already excited complex, or at the same time as another photon, resulting in the entirety of the photon energy being dissipated into the solvent heat. To assess the amount of multi-photon absorption in the system, the dissipated energy $\Delta T \cdot C_{T,water} \cdot n_{water}$ is contrasted to the expected heat from single photon absorption $(e_i - e_f) \cdot \alpha$.

We determine that to reach the fitted temperature 0.48 photons have to be absorbed in a multiphoton processes in the AgPtPOP sample and 0.75 in the TlPtPOP sample per

liquid unit cell. This is in line with the magnitude of the scaler needed to match the scattering signal from structure and excitation fraction determined from the ΔS_0 signal onto the ΔS_2 signal, 0.85 for AgPtPOP and 0.66 for TlPtPOP.

8   Data Reduction

8.1   Information sources

The following primary information for the data analysis are taken from the hdf5-files of the experiment:

- Machine motor positions

- Detector images saved for each x-ray pulse with the CSPAD detector[33]

- LCLS accelerator information, which are saved for each shot along the detector data

- Timing tool, which delivers information both about the delay between the pulses as well as their shape. It was developed and is extensivly discussed by Harmand et al.[34].

8.2   Correction and masking of the detector images

The beam center position was found by optimizing the overlap of the solvent total scattering peak between 17 azimuthal slices. The detector distance was found by comparison of the solvent total scattering peak to its literature position. The q-axis was additionally corrected for small distance changes during the model fitting using a χ^2 minimization after most likely

ground and excited state distance for the Platinum atoms where determined. As such the solvent heat signal was matched as good as possible to the well characterized reference.

The first corrections applied to every image can be summarized as Eq. 8, with the corrected image $I_{Corrected}$, the detector image I_{Image}, the detector noise correction I_{Dark}, the omitting of untrustworthy detector pixels C_{mask}, and solid angle correction $C_{SolidAngle}$, and the polarization correction $C_{Polarization}$.

$$I_{Corrected} = (I_{Image} - I_{Dark}) \cdot C_{mask} \cdot C_{SolidAngle} \cdot C_{Polarization} \tag{8}$$

To account for electronic background, 30 dark images per scan, meaning detector images with neither x-ray nor laser pulses, are averaged and subtracted from every used detector image.

$$I_{DarkCorrected} = I_{Image} - I_{Dark} \tag{9}$$

Areas of the detector in which scattered x-rays are shadowed by part of the setup such as the nozzle removed from all images. Pixels that are within 5 pixels of the edges for any given detector image are omitted. Unbonded pixels, which are a diagonal line of pixels through every detector panel that are not electronically connected, are removed from the analysis together with their adjacent pixels. Additionally pixels that exhibit a standard deviation of 3.35 times the mean standard deviation in their electronic readout are omitted from the analysis. Fig. 13 depicts the assembled detector image, the area after masking as well as the mask used during the integration. In total around 39.8 % of the $\sim$2.3 million pixels are removed in this step through application of C_{mask}.
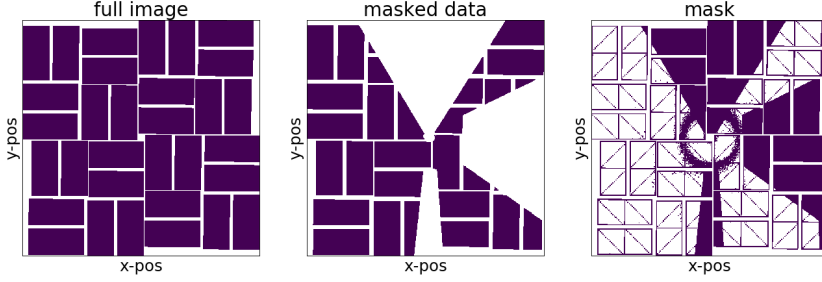
Figure 13: Assembled detector image, detector image after mask application and applied mask for every detector image

$$C_{mask} = \begin{cases} \text{NaN}, & \text{if masked} \\ 1, & \text{otherwise} \end{cases} \tag{10}$$

A solid angle correction is used to correct for the relative area covered by a pixel in a projection of the scattering sphere, with θ being the scattering angle, as discussed by Boesecke et al.[67]

$$C_{SolidAngle} = \frac{1}{\cos(2\theta)^3} \tag{11}$$

Lastly, a polarization correction is made to account different scattering probabilities depending on the angle between x-ray polarization and azimuthal scattering angle,[37, 38]

$$C_{Polarization} = P[1 - (\sin(2\theta)\sin(\phi))^2] + (1-P)[1 - (\cos(2\theta)\sin(\phi))^2] \tag{12}$$

with the x-ray polarization P, the x-ray scattering angle θ, and the azimuthal angle ϕ, as discussed by Hura et al.[68]

8.3 Correction for nonlinear detector response

In a second correction step, the data set is tested and corrected for nonlinear behaviour in regards to X-ray energy or intensity, according to the SVD-based methodology in van Driel et. al. 2015[35]. For this each of the individual scans is analyzed with Singular Value Decomposition (SVD). The strongest signal yielded by the decomposition is the scattering signal of the sample system, additional contributions can be either due to electronic detector behaviour or changes in the measurement setup such as crystal formation or pressure changes in the gas chamber. Each non signal contribution is plotted and fitted against beam intensity and x-ray energy. Contributions that show a clear correlation with said parameters and contribute significantly to the system are determined as nonlinear contributions, and subtracted according to fit and machine parameters.[35] Eq. 13 shows the correction, with the already once corrected data $I_{Corrected}$, the x-ray energies and intensities for each shot $\gamma_{x-ray\,energy}$ and $\gamma_{x-ray\,intensity}$, and the identified nonlinear responses $I_{Fit\,energy}$ and $I_{Fit\,intensity}$.

$$I_{SVD\,corrected} = I_{Corrected} - \sum_{X-ray\,energy}^{n} I_{Fit\,energy} \cdot \gamma_{X-ray\,energy} - \sum_{X-ray\,intensity}^{n} I_{Fit\,intensity} \cdot \gamma_{X-ray\,intensity}$$

$$(13)$$

8.4 Image normalization

The signal measured on the detector fluctuates stronger as a result of the photon count than due to laser induced changes. To reduce the impact of fluctuations each corrected detector image is self normalized by dividing the detector counts by the average intensity between 2.5 and 5 Å^{-1}.
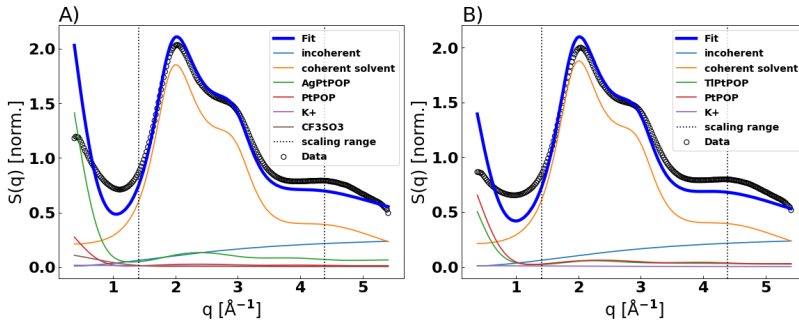
Figure 14: Scaling of the data to the liquid unit cell for AgPtPOP A) and TlPtPOP B)

During the self normalization process the analogue detector units saved in the file are converted into arbitrary units. To reconvert the fit parameters into physical properties, most notably excitation fraction and temperature, the signal magnitude is scaled to the liquid unit cell. The liquid unit cell consists of one sample molecule of interest, solvent molecules according to the sample concentration and other components such as counter ions and stabilizing detergents. The sum of simulated coherent and incoherent desolved molecules, as well as a measured reference[69] of the solvent to scale is the scaled onto the azimuthal integrated total scattering signals of off-images. This process is seen in Fig. 14. The fitted scaling parameter is applied to the difference scattering curves and transforms the arbitrary units into electron units squared of the liquid unit cell.

8.5   Filtering

Tab. 3 shows the number of scattering images taken, filtered and used for each dataset. X-ray pulse shots with X-ray intensities less than 20% of the median are removed together with images with which the timing tool-detector registered an invalid position, defined as within 10 pixels from the edge of the detector or no registration at all.

	Pt_2POP_4	$AgPt_2POP_4$	$TlPt_2POP_4$
Total Scattering images	554154	458346	361788
low X-ray intensity	4877	8901	18402
Deviating X-ray energy	26955	26107	20129
Invalid position on timing-tool detector	76644	64369	51225
Error on timing tool position too large	143638	132269	95790
Scattering signal deviating from mean	17133	3926	3857
Scattering images after filtering	284907	222774	172385
Difference scattering images after filtering	208706	161001	125144

Table 3: Filtering statistics for the analysed datasets

The shots were additionally filtered based on the X-ray energy, as measured through the energy of the electrons for a given shot, and the fit error determined by the fit of the position on the timing tool detector. In both cases the density kernel distribution was estimated using a prodecure proposed by Botev et al.[70], and images rejected that deviate too much from the center using a triangular filter.

The majority of shots rejection occurs based on information from the timing-tool, rejecting shots in the fringe region of the timing-tool detector and determination of the actual temporal delay was associated with a too large error.

In a final step scattering images whose azimuthally integrated signal deviate from the mean are rejected using the triangular filtering algorithm.

These filtered scattering images are then used to calculate the difference scattering images used on the analysis. 600 difference scattering images were averaged for each time bin to ensure equivalent counting statistic in each of the temporal bins.

9 Anisotropic scattering signals

The angular distribution of molecules excited molecules after a one photon absorption process with linear polarized is described by a cosine-squared distribution centered around the laser polarization. Eq. 14 separates this distribution $D(\alpha)$ into an isotropic term with the 0th order Legendre polynomial $P_0(x) = 1$ and 2nd order Legendre polynomial $P_2 = (3x^2 - 1)/2$.

$$D(\alpha) \propto P_0(cos\alpha) + 2 \cdot P_2(cos\alpha) \tag{14}$$

The scattering cross section $\frac{d\sigma}{d\omega}$ of such a distribution is described through Eq. 15 with the isotropic coherent scattering S_0 and the anisotropic coherent scattering S_2.

$$\frac{d\sigma}{d\omega}(q,\theta_q,t) \propto S_0(q,t) + P_2(cos\theta_q)S_2 \tag{15}$$

The contributions can be separated by doing a linear fit through the 17 azimuthal slides for each of the q-bins using Eq. 16. Each azimuthal slide represents a specific angle α between laser polarization and transition dipole moment of the molecule. The actual angle between laser polarization and x-ray polarization θ_q is refined by testing a large range of possible angles and choosing the one that produces the largest absolute anisotropic difference scattering signal. This process was described in great detail Biasin et al.[37] based on work by Lorenz et al.[38].

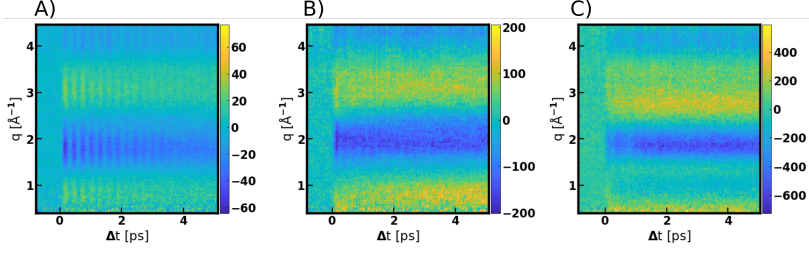$$\Delta S(q,\theta_q,\alpha) = m_q \cdot P_2(cos(\theta_q + \alpha)) + b_q \tag{16}$$

Figure 15: $\Delta S_2(Q,t)$ for Pt_2POP_4 (A), $AgPt_2POP_4$ (B) and $TlPt_2POP_4$ (C)

Fig.15 depicts the anisotropic difference scattering signal of Pt_2POP_4, $AgPt_2POP_4$ and $TlPt_2POP_4$.

The anisotropic solute scattering signal can be calculated with Eq. 17[37], with the vector r_{ij} between the atoms i and j, the angle ξ_{ij} between said vector and the transition dipole moment, the atomic form factor f, and the second order Legendre polynomial P_2.

$$S_2(Q) = -c_2 \sum_{i,j}^{N} f_i(Q)f_j(Q)P_2[cos(\xi_{ij})]j_2(r_{ij}) \tag{17}$$

10   SVD of S2

11   Artifacts

The difference scattering curves are superimposed with artifacts that were not be removed in the data reduction. They are most noticeable in time bins with $\Delta t < 0$ for AgPtPOP where the signal should be 0 superimposed with counting noise. The artifacts posed a problem in the time-resolved fit. As such they were assessed by doing an SVD decomposition of the signal $\Delta t < -0.3$ ps, and the two strongest components were used as fitting components. Fig. 17
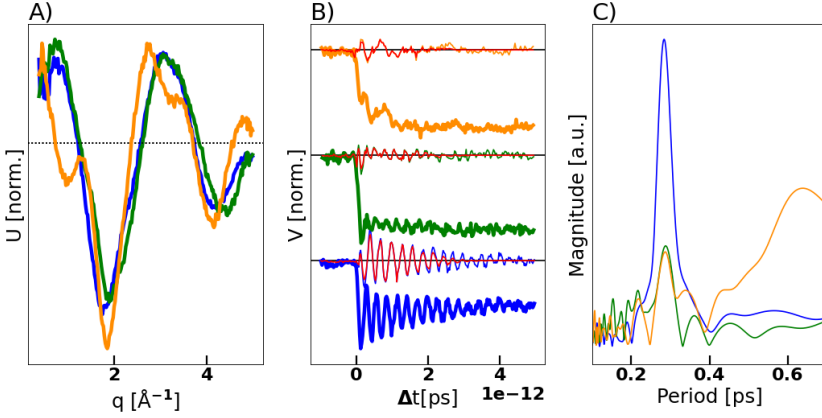
Figure 16: Analysis of the first SVD-component of ΔS_2 . A) depicts the first U vector of each system along the q-axis. They are comparatively similar between the samples. B) shows the V vector along Δt corresponding to the depicted U vectors, as well as its oscillatory structural signal (OSS) along the time-axis. The red lines show the OSSs after application of a σ =1 ps Gaussian window centered at Δt = 1 ps to suppress artifacts. C) shows the Fourier-transformation a of said windowed OSSs. The Fourier magnitudes are normalized to the magnitude of the OSS

depicts these components and their temporal evolution through all time bins. While the first components exhibits very little time dependents, the second one exhibits a clear jump at $\Delta t = 0$. As the variance in the scaler afterwards is much greater than any additional structure, we estimate that while some of the concrete parameters might be slightly altered by this, the dynamics are expected to remain untouched.

12   Errors

The error associated with the data is each q-bin for a given time step is estimated based on a local low order polynomial fit method proposed by A. Filipponi[71]. The error is the averaged error of all time steps with a delay of larger than 4 ps and smoothed with a Savitzky-Golay-Filter, independently for the ΔS_0 and ΔS_2 signal.
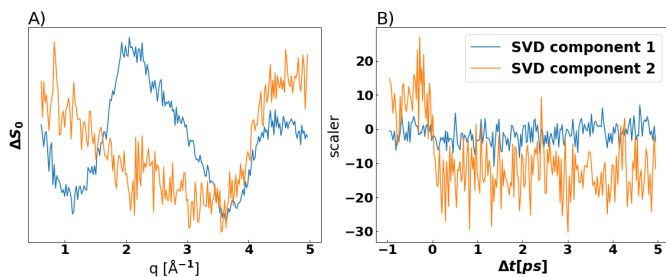
Figure 17: Artifact SVD components and temporal development in the time-resolved fits for AgPtPOP
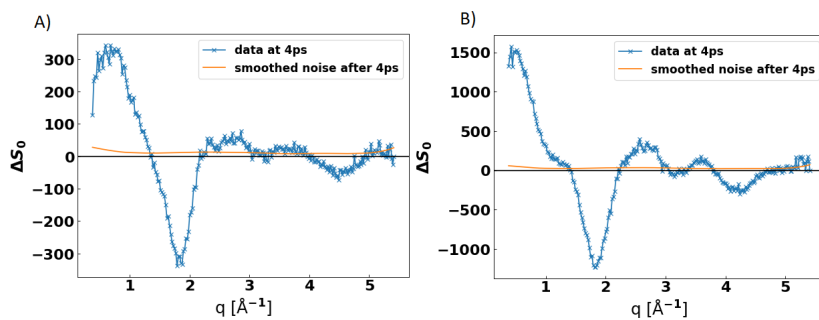

Figure 18: Data and estimated noise of a single time bin at 4 ps for AgPtPOP A) and TlPtPOP B)

The structural optimization was conducted on the data from a single time step, binning 600 difference scattering images, to reduce the error being dominated by counting statistics. The errors associated with a structural parameters were estimated in two ways based on a χ^2 goodness-of-fit estimation, as shown in Eq. 18 with the error σ^2, the number of data points N and the number of free parameters M. We note that the number of data points are the result of our choice of binning during the data reduction and exceeds the number of independent data points considerably, resulting in N » M.

$$\chi^2_{red} = \sum \frac{(\Delta S_{fit} - \Delta S_{data})^2}{\sigma^2} / (N - M - 1) \tag{18}$$

The error of a given parameter was determined with a constant χ^2 boundary[44]. A 6 dimensional parameter space, consisting of ground state Pt-Pt distance, Pt-M distance, Pt-Pt contraction, Pt-M-position change, excitation fraction and temperature was fitted. The n-dimensional hull, consisting of parameter combinations for which $\chi^2_{red} <= \chi^2_{red,min} + 1$, is projected onto each axis, thus determining the confidence interval in each direction. The errors were taken in symmetric approximation.

The errors were compared against those determined with the Likelihood-method[44], which has been used in previous work in X-ray solution scattering[36, 28] and provided similar results. For the Likelihood-method, the likelihood of a given point in an n-dimensional parameter space is $P(x_1, x_2, ...) \sim \exp(-\chi^2/2)$. The results for both methods are comparable and shown in tab. 4

The error bars on the time constants in the time-resolved fitting were determined from the covariance matrix.

	AgPtPOP			TlPtPOP		
Parameter		χ^2-hull error	Likelihood error		χ^2-hull error	Likelihood error
$d_{PtPt,Gs}$ [Å]	3.03	0.04	0.08	3.12	0.12	0.1
$d_{PtM,Gs}$ [Å]	2.87	0.12	0.2	3.14	0.16	0.12
Δd_{PtPt} [Å]	0.25	0.08	0.08	0.28	0.15	0.12
Δd_{PtM} [Å]	-0.19	0.04	0.1	0.31	0.24	0.2
α	0.34	0.1	0.07	0.26	0.16	0.07
ΔT [K]	0.68	0.07	0.14	1.08	0.32	0.27

Table 4: Comparison of the confidence intervals for AgPtPOP and TlPtPOP

13   Fits over time

Fig. 19 depicts every other time bin and fit for the first 1.5 ps of the reaction.

14   Kinetic functions

The most likely parameters for each time step were connected by fitting of a kinetic function to derive time constants of the processes at play. Eq. 19 and Eq. 20 show the function used for the kinetic fit, which connects the changes in structural parameters to parameters in functions describing the motion of the atoms, with the contraction time scales $\tau_{PtPt,1}$, $\tau_{PtPt,2}$ and τ_{Ag}, the Heaviside function H, the oscillation frequencies ω_{PtPt} and ω_{Ag}, the oscillation dephasing times $\tau_{\omega,Pt}$ and $\tau_{\omega,Ag}$, and the distances between excited-state and ground-state equilibrium positions $\Delta d_{PtPt,1}$, $\Delta d_{PtPt,2}$ and Δd_{Ag}

$$d_{PtPt}(\Delta t) = IRF * (d_{PtPt,GS} + H(\Delta t) \cdot (\Delta d_{PtPt,1} + \Delta d_{PtPt,2}(1 - \exp(-\Delta t/\tau_{PtPt,1}))$$
$$+ \Delta d_{osc} \cos(2\pi \cdot \Delta t/T_1) \exp(-\Delta t/\tau_\omega))) \tag{19}$$
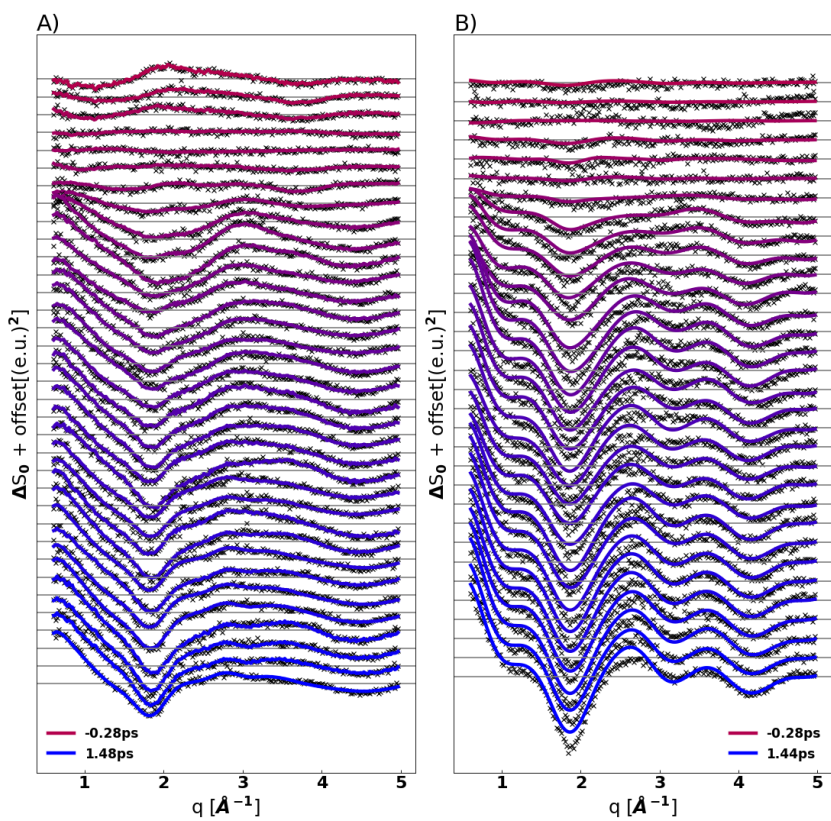
Figure 19: Data points and fit for every second time bin between -0.3 ps and 1.5 ps for A) AgPtPOP and B) TlPtPOP

$$d_{Ag}(\Delta t) = IRF * (d_{Ag,GS} + H(\Delta t) \cdot (\Delta d_{PtAg,1}) + \Delta d_{PtAg,2}(1 - \exp(-\Delta t/\tau_{PtAg,1}))$$
$$+ \Delta d_{osc} \cos(2\pi \cdot \Delta t/T_{Ag}) \exp(-\Delta t/\tau_{\omega Ag}))) \tag{20}$$

Eq. 21 and Eq. 22 describe the kinetic fits of the solvation cage and the heat dissipation, with the excited state equilibrium parameters ΔT_{max} and ε_{max}, the time constants $\tau_{\Delta T}$ and τ_ε and the temporal offset t'.

$$\varepsilon(\Delta t) = IRF * (\varepsilon_{max} * H(\Delta t - t') * (1 - \exp(-(\Delta t - t')/\tau_\varepsilon) + m \cdot t)) \tag{21}$$

$$\Delta T(\Delta t) = IRF * (\Delta T_{max} * H(\Delta t - t') * (1 - \exp(-(\Delta t - t')/\tau_{\Delta T}))) \tag{22}$$

The kinetic for the structural parameters of TlPtPOP are described through Eq. 23, Eq. 24 and Eq. 25.

$$d_{PtPt}(\Delta t) = IRF * (d_{PtPt,GS} + H(\Delta t) \cdot (\Delta d_{PtPt}))) \tag{23}$$

$$d_{Tl}(\Delta t) = IRF * (d_{PtTl,GS} + H(\Delta t) \cdot (\Delta d_{Tl}(1 - \exp(-\Delta t/\tau_{Tl}))$$
$$+ \Delta_{osc} \cos(2\pi \cdot \Delta t/T_{PtTl,1}) \exp(-\Delta t/\tau_{\omega Tl}))) \tag{24}$$
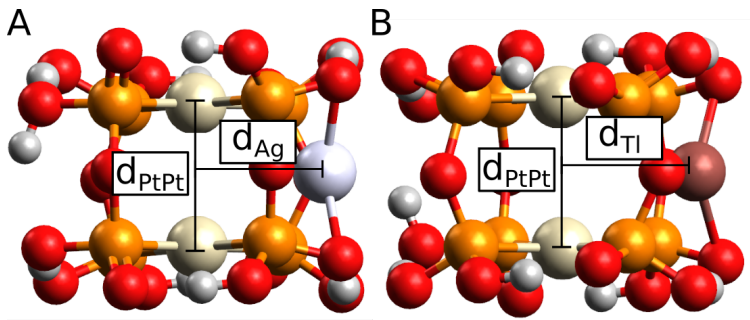
Figure 20: Optimized ground state structures of AgPtPOP A) and TlPtPOP B) based on the model of Kruppa et al.[30]. The structures corresponds to the structurally optimized ground states.

$$\varepsilon(\Delta t) = IRF * (\varepsilon_{max} * H(\Delta t - t') * (1 - \exp(-(\Delta t - t')/\tau_\varepsilon) - \exp(-(\Delta t - t')/\tau_{\varepsilon,2}))) \quad (25)$$

15 Orthogonal structures

15.1 Introduction

Kruppa et al.[30] suggested a structure for AgPtPOP and KPtPOP with the metal atom bonding to the ligand scaffold, perpendicular to the Platinum-Platinum axis. This structure is based on their calculation using density functional theory (DFT), which predicted a lower energy of the complex compared to isomers with axially oriented silver atoms.

We constructed a model structure based on the published scaffold bonded structure for AgPtPOP and, through simple exchange of atoms, for TlPtPOP (Kruppa et al. 2016 [30] SI p. 33). The structures were optimized in a similar way as axial structures, with the Platinum atoms being allowed to move symmetrically along their bond axis and the external
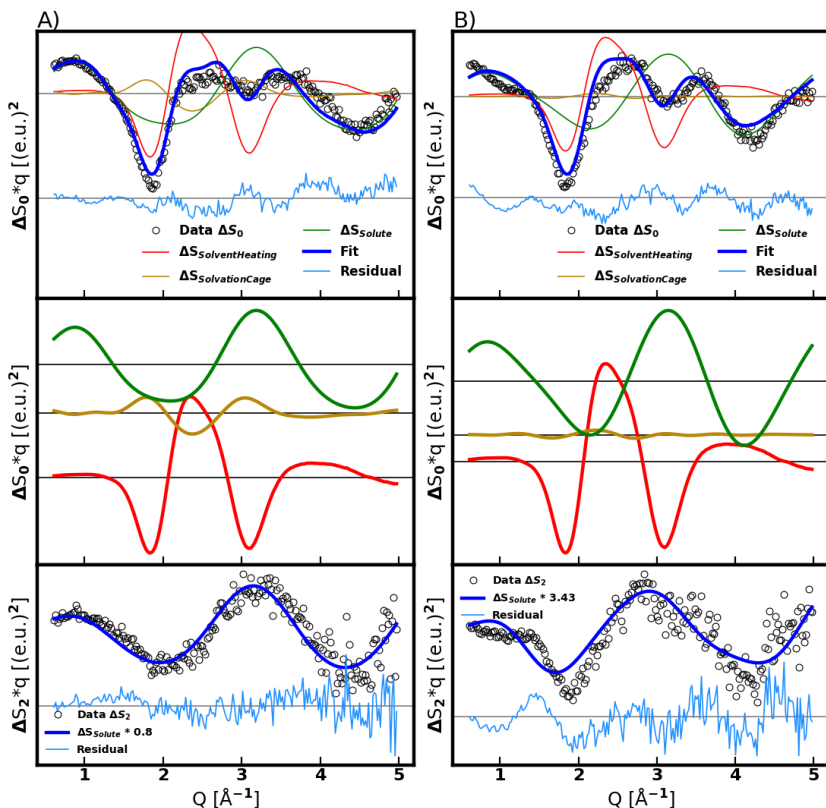
Figure 21: Fit of the data, $AgPt_2POP_4$ A) and $TlPt_2POP_4$ B), with the additional metal atom being positioned orthogonal to the Pt-Pt axis

metal atom perpendicular to said axis. The cage terms used have been simulated for the orthogonal structures. The optimized ground state structures are depicted in Fig. 20.

15.2 Fits

Tab. 5 contains the fitting results. A ground state d_{PtPt} of slightly above 3 Å was determined for both systems, equally associated with a contraction of 0.3 Å. The excitation fractions of 14 ± 4 and 12 ± 7 are about half those obtained from the axial model. The additional metal

Table 5: Fiting results of the ground state structural parameters and changes after excitation

Parameter	AgPtPOP	TlPtPOP
$d_{PtPt,GS}$ [Å]	3.01±0.27	3.12±0.08
Δd_{PtPt} [Å]	0.30±0.27	0.30±0.17
$d_{M,GS}$ [Å]	2.75±0.33	2.79±0.17
Δd_M [Å]	-0.05±0.15	0.34±0.30
α [%]	14±4	12±7
ΔT [K]	0.83±0.08	0.77± 0.10

atoms are positioned at d_{Ag}2.75±0.33 and at d_{Tl} 2.79±0.17 Å away from the center of the complex. These are considerably shorter distances than calculated by Kruppa et al., which predict a distance of 4.12 Å to the molecule center. After excitation the d_{Ag} expands by 0.05±0.15 Å while d_{Tl} contracts by 0.34±0.30.

Fig. 21 III depicts the anisotropic ΔS_2 signal using the anisotropic solute scattering signal calculated from the ΔS_0 optimized structure. The calculation of the the anisotropic scattering using Eq. 17 was tested with a range of possible transition dipole moments ξ_{ij}, as the transition dipole moment of the orthogonal structure may not be identical to the axial one. Transition dipole moments were tested along the Pt-Pt axis, the metal atom axis and perpendicular to both. The calculation with the transition dipole moment along the Pt axis produces the best results and is depicted here for both systems. The best result was chosen on the lowest χ^2 while producing positive excitation fractions. For AgPtPOP the magnitude of the excitation fraction is about the same for ΔS_0 and ΔS_2, while for TlPtPOP the excitation fraction is a factor of 4 larger, which is implausible.

15.3   Discussion

The goodness-of-fit χ^2 improves slightly for AgPtPOP when optimizing the orthogonal structure for ΔS_0 from 5.06 to 4.88. For TlPtPOP the fit quality declines from χ^2 10.41

to 21.40. The ΔS_2 fit quality increases for AgPtPOP from 5.95 to 2.48. For TlPtPOP it declines from χ^2 3.06 to 9.28. The larger excitation fraction in the ΔS_2 signal for TlPtPOP is physically implausible.

In both cases the metal atom is considerably closer to the center of the metal atom than predicted by DFT, about 1.3-1. Å for both systems. The atom is no longer binding to the outside, but is instead integrated into the ligand scaffolding in a way that is likely prohibited due to steric hindrance. Based on these consideration we find the axial configuration to be more likely than the orthogonal configuration.

These findings are in line with estimations about changes in the lifetime that would be associated with binding to the ligand scaffold but do not occur in $TlPt_2POP_4$, as discussed by Clodfelter $et\ al.$ [26].

References

[1] D. Max Roundhill, Harry B. Gray, and Chi Ming Che. Pyrophosphito-bridged diplatinum chemistry. *Accounts of Chemical Research*, 22(2):55–61, February 1989.

[2] Maya Chaaban, Chenkun Zhou, Haoran Lin, Brandon Chyi, and Biwu Ma. Platinum(ii) binuclear complexes: Molecular structures, photophysical properties, and applications. *Journal of Materials Chemistry C*, 7:5910–5924, 2019.

[3] Michael G. Hill, James A. Bailey, Vincent M. Miskowski, and Harry B. Gray. Spectroelectrochemistry and dimerization equilibria of chloro(terpyridine)platinum(II). nature of the reduced complexes. *Inorganic Chemistry*, 35(16):4585–4590, January 1996.

[4] Vivian Wing-Wah Yam and Keith Man-Chung Wong. Luminescent metal complexes of d6, d8 and d10 transition metal centres. *Chem. Commun.*, 47:11579–11592, 2011.

[5] Harry B. Gray, Stanislav Záliš, and Antonín Vlček. Electronic structures and photophysics of d8-d8 complexes. *Coordination Chemistry Reviews*, 345:297–317, 2017. Chemical Bonding: "State of the Art".

[6] S. J. Milder and B. Brunschwig. Factors affecting nonradiative decay: temperature dependence of the picosecond fluorescence lifetime of tetrakis(dihydrogen diphosphate)diplatinum(4-). *The Journal of Physical Chemistry*, 96:2189–2196, 1992.

[7] Alec C. Durrell, Gretchen E. Keller, Yan Choi Lam, Jan Sýkora, Antonín Vlček, and Harry B. Gray. Structural control of 1a 2u-to- 3a 2u intersystem crossing in diplatinum(ii,ii) complexes. *Journal of the American Chemical Society*, 134:14201–14207, 8 2012.

[8] Jian-Ji Zhong, Wai-Pong To, Yungen Liu, Wei Lu, and Chi-Ming Che. Efficient acceptorless photo-dehydrogenation of alcohols and n/i-heterocycles with binuclear platinum(scpii/scp) diphosphite complexes. *Chemical Science*, 10(18):4883–4889, 2019.

[9] Christopher L. Exstrom, Doyle Britton, Kent R. Mann, Michael G. Hill, Vincent M. Miskowski, William P. Schaefer, Harry B. Gray, and William M. Lamanna. Structures of [m2(dimen)4](y)2 (m = rh, ir; dimen = 1,8-diisocyanomenthane; y = pf6, tetrakis[3,5-bis(trifluoromethyl)phenyl]borate, b(c6h5)4) crystals featuring an exceptionally wide range of metal−metal distances and dihedral twist angles. *Inorganic Chemistry*, 35(3):549–550, Jan 1996.

[10] Robert W. Hartsock, Wenkai Zhang, Michael G. Hill, Bridgett Sabat, and Kelly J. Gaffney. Characterizing the deformational isomers of bimetallic ir 2(dimen)42+ (dimen = 1,8-diisocyano-p-menthane) with vibrational wavepacket dynamics. *Journal of Physical Chemistry A*, 115:2920–2926, 4 2011.

[11] Tim B. Van Driel, Kasper S. Kjaer, Robert W. Hartsock, Asmus O. Dohn, Tobias Harlang, Matthieu Chollet, Morten Christensen, Wojciech Gawelda, Niels E. Henriksen, Jong Goo Kim, Kristoffer Haldrup, Kyung Hwan Kim, Hyotcherl Ihee, Jeongho Kim, Henrik Lemke, Zheng Sun, Villy Sundstroöm, Wenkai Zhang, Diling Zhu, Klaus B. MØller, Martin M. Nielsen, and Kelly J. Gaffney. Atomistic characterization of the active-site solvation dynamics of a model photocatalyst. *Nature Communications*, 7, 11 2016.

[12] M. A. Filomena Dos Remedios Pinto, Peter J. Sadler, Stephen Neidle, Mark R. Sanderson, Arun Subbiah, and Reiko Kuroda. A novel di-platinum(scpII/scp) octaphosphite

complex showing metal–metal bonding and intense luminescence; a potential probe for basic proteins. x-ray crystal and molecular structure. *J. Chem. Soc., Chem. Commun.*, 0(1):13–15, 1980.

[13] Renske M. Van der Veen, Christopher J. Milne, Van-Thai Pham, Amal El Nahhas, Julia A. Weinstein, Jonathan Best, Camelia N. Borca, Christian Bressler, and Majed Chergui. EXAFS structural determination of the pt2(p2o5h2)44– anion in solution. *Chimia*, 62(4):287, 2008.

[14] Morten Christensen, Kristoffer Haldrup, Klaus Bechgaard, Robert Feidenhans'l, Qingyu Kong, Marco Cammarata, Manuela Lo Russo, Michael Wulff, Niels Harrit, and Martin Meedom Nielsen. Time-resolved x-ray scattering of an electronically excited state in solution. structure of the (3)a(2u) state of tetrakis-μ-pyrophosphitodiplatinate(II). *Journal of the American Chemical Society*, 131(2):502–508, December 2008.

[15] Irina V. Novozhilova, Anatoliy V. Volkov, and Philip Coppens. Theoretical analysis of the triplet excited state of the $[pt_2(h_2p_2o_5)_4]^{4-}$ ion and comparison with time-resolved x-ray and spectroscopic results. *Journal of the American Chemical Society*, 125(4):1079–1087, January 2003.

[16] Qingyu Kong, Kasper S. Kjaer, Kristoffer Haldrup, Stephan P.A. Sauer, Tim Brandt Van Driel, Morten Christensen, Martin M. Nielsen, and Michael Wulff. Theoretical study of the triplet excited state of ptpop and the exciplexes m-ptpop (m = tl, ag) in solution and comparison with ultrafast x-ray scattering results. *Chemical Physics*, 393:117–122, 1 2012.

[17] Gianluca Levi, Mátyás Pápai, Niels E. Henriksen, Asmus O. Dohn, and Klaus B. Møller. Solution structure and ultrafast vibrational relaxation of the ptpop complex revealed

by delta scf-qm/mm direct dynamics simulations. *Journal of Physical Chemistry C*, 122:7100–7119, 4 2018.

[18] Steven F. Rice and Harry B. Gray. Electronic absorption and emission spectra of binuclear platinum(ii) complexes. characterization of the lowest singlet and triplet excited states of tetrakis(diphosphonato)diplatinate(4-) anion (pt2(h2p2o5)44-). *Journal of the American Chemical Society*, 105(14):4571–4575, Jul 1983.

[19] King Hung Leung, David Lee Phillips, Chi-Ming Che, and Vincent M. Miskowski. Resonance raman intensity analysis investigation of metal–metal bonded transitions: an examination of the 1a2u - 1a1g (5dσ - 6pσ) transition of pt2(p2o5h2)44−. *Journal of Raman Spectroscopy*, 30(11):987–993, 1999.

[20] Nobuhiro Yasuda, Hidehiro Uekusa, and Yuji Ohashi. X-ray analysis of excited-state structures of the diplatinum complex anions in five crystals with different cations. *BCSJ*, 77(5):933–944, 2004.

[21] Renske M. van der Veen, Chris J. Milne, Amal El Nahhas, Frederico A. Lima, Van-Thai Pham, Jonathan Best, Julia A. Weinstein, Camelia N. Borca, Rafael Abela, Christian Bressler, and Majed Chergui. Structural determination of a photochemically active diplatinum molecule by time-resolved exafs spectroscopy. *Angewandte Chemie International Edition*, 48(15):2711–2714, 2009.

[22] Renske M. Van Der Veen, Andrea Cannizzo, Frank Van Mourik, Antonín Vlček, and Majed Chergui. Vibrational relaxation and intersystem crossing of binuclear metal complexes in solution. *Journal of the American Chemical Society*, 133:305–315, 1 2011. PtPOP.

[23] Roberto Monni, Gerald Auböck, Dominik Kinschel, Kathrin M. Aziz-Lange, Harry B. Gray, Antonín Vlček, and Majed Chergui. Conservation of vibrational coherence in ultrafast electronic relaxation: The case of diplatinum complexes in solution. *Chemical Physics Letters*, 683:112–120, 9 2017.

[24] Stanislav Záliš, Yan-Choi Lam, Harry B. Gray, and Antonín Vlček. Spin–orbit TDDFT electronic structure of diplatinum(II, II) complexes. *Inorganic Chemistry*, 54(7):3491–3500, March 2015.

[25] Nisa T. Satumtira, Ali Mahdy, Mohamed Chehbouni, Oussama ElBjeirami, and Mohammad A. Omary. Novel method for waste analysis using a highly luminescent diplatinum(II) octaphosphite complex as a heavy metal detector. In *Ceramic Transactions Series*, pages 279–288. John Wiley & Sons, Inc., September 2011.

[26] Sarah A. Clodfelter, Tina M. Doede, Bridget A. Brennan, Jeffrey K. Nagle, David P. Bender, Warren A. Turner, and Paul M. LaPunzina. Luminescent metal-metal-bonded exciplexes involving tetrakis(.mu.-diphosphito)diplatinate(II) and thallium(i). *Journal of the American Chemical Society*, 116(25):11379–11386, December 1994.

[27] Jeffrey K. Nagle and Bridget A. Brennan. Luminescent exciplex formation involving tetrakis(.mu.-diphosphito)diplatinate(II) and -thallium(i) in aqueous solution. *Journal of the American Chemical Society*, 110(17):5931–5932, August 1988.

[28] Kristoffer Haldrup, Morten Christensen, Marco Cammarata, Qingyu Kong, Michael Wulff, Simon O. Manager, Klaus Bechgaard, Robert Feidenhans'l, Niels Harrit, and Martin M. Nielsen. Structural tracking of a bimolecular reaction in solution by time-resolved x-ray scattering. *Angewandte Chemie - International Edition*, 48:4180–4184, 5 2009.

[29] Morten Christensen, Kristoffer Haldrup, Kasper S. Kjær, Marco Cammarata, Michael Wulff, Klaus Bechgaard, Høgni Weihe, Niels H. Harrit, and Martin M. Nielsen. Structure of a short-lived excited state trinuclear ag-pt-pt complex in aqueous solution by time resolved x-ray scattering. *Physical Chemistry Chemical Physics*, 12:6921–6923, 2010.

[30] Sebastian V. Kruppa, Yevgeniy Nosenko, Marc Oliver Winghart, Simon P. Walg, Manfred M. Kappes, and Christoph Riehn. Fragmentation pathways of dianionic [pt2(μ-p2o5h2)4 + x,y]2- (x,y = h, k, ag) species in an ion trap induced by collisions and uv photoexcitation. *International Journal of Mass Spectrometry*, 395:7–19, 2 2016.

[31] Andrew G. Sykes and Kent R. Mann. X-ray crystal structure and phosphorus-31 nmr solution studies of [ir2(dimen)4(pph3)au(pph3)] (pf6)3 (dimen = 1,8-diisocyano-p-menthane). observation of particle site preference in the formation of "outside" silver and gold adducts. *Journal of the American Chemical Society*, 112(20):7247–7254, Sep 1990.

[32] Kasper Kjaer. Photophysics of metal metal bonded exciplexes between tetrakis μ pyrophosphitodiplatinate(ii) and silver(i). Master's thesis, Technical University of Denmark, 2010. master's thesis.

[33] Sven Herrmann, Sébastien Boutet, Brian Duda, David Fritz, Gunther Haller, Philip Hart, Ryan Herbst, Christopher Kenney, Henrik Lemke, Marc Messerschmidt, Jack Pines, Aymeric Robert, Marcin Sikorski, and Garth Williams. Cspad-140k: A versatile detector for lcls experiments. *Nuclear Instruments and Methods in Physics Research, Section A: Accelerators, Spectrometers, Detectors and Associated Equipment*, 718:550–553, 2013.

[34] M. Harmand, R. Coffee, M. R. Bionta, M. Chollet, D. French, D. Zhu, D. M. Fritz, H. T. Lemke, N. Medvedev, B. Ziaja, S. Toleikis, and M. Cammarata. Achieving few-femtosecond time-sorting at hard x-ray free-electron lasers. *Nature Photonics*, 7:215–218, 3 2013.

[35] Tim Brandt Van Driel, Kasper Skov Kjær, Elisa Biasin, Kristoffer Haldrup, Henrik Till Lemke, and Martin Meedom Nielsen. Disentangling detector data in xfel studies of temporally resolved solution state chemistry. *Faraday Discussions*, 177:443–465, 4 2015.

[36] Kristoffer Haldrup, Morten Christensen, and Martin Meedom Nielsen. Analysis of time-resolved X-ray scattering data from solution-state systems. *Acta Crystallographica Section A*, 66(2):261–269, Mar 2010.

[37] Elisa Biasin, Tim B. Van Driel, Gianluca Levi, Mads G. Laursen, Asmus O. Dohn, Asbjørn Moltke, Peter Vester, Frederik B.K. Hansen, Kasper S. Kjaer, Tobias Harlang, Robert Hartsock, Morten Christensen, Kelly J. Gaffney, Niels E. Henriksen, Klaus B. Møller, Kristoffer Haldrup, and Martin M. Nielsen. Anisotropy enhanced x-ray scattering from solvated transition metal complexes. *Journal of Synchrotron Radiation*, 25:306–315, 3 2018.

[38] U. Lorenz, K. B. Møller, and N. E. Henriksen. On the interpretation of time-resolved anisotropic diffraction patterns. *New Journal of Physics*, 12, 11 2010.

[39] Kristoffer Haldrup, Gianluca Levi, Elisa Biasin, Peter Vester, Mads Goldschmidt Laursen, Frederik Beyer, Kasper Skov Kjær, Tim Brandt Van Driel, Tobias Harlang, Asmus O. Dohn, Robert J. Hartsock, Silke Nelson, James M. Glownia, Henrik T. Lemke, Morten Christensen, Kelly J. Gaffney, Niels E. Henriksen, Klaus B. Møller, and Mar-

tin M. Nielsen. Ultrafast x-ray scattering measurements of coherent structural dynamics on the ground-state potential energy surface of a diplatinum molecule. *Physical Review Letters*, 122, 2 2019.

[40] D. T. Cromer and J. B. Mann. X-ray scattering factors computed from numerical Hartree–Fock wave functions. *Acta Crystallographica Section A*, 24(2):321–324, Mar 1968.

[41] Kasper Skov Kjær, Tim B. Van Driel, Jan Kehres, Kristoffer Haldrup, Dmitry Khakhulin, Klaus Bechgaard, Marco Cammarata, Michael Wulff, Thomas Just Sørensen, and Martin M. Nielsen. Introducing a standard method for experimental determination of the solvent response in laser pump, x-ray probe time-resolved wide-angle x-ray scattering experiments on systems in solution. *Physical Chemistry Chemical Physics*, 15:15003–15016, 9 2013.

[42] Habiburrahman Zulfikri, Matyas Papai, and Asmus Ougaard Dohn. Simulating the solvation structure of low- and high-spin [fe(bpy)(3)](2+): long-range dispersion and many-body effects. *PHYSICAL CHEMISTRY CHEMICAL PHYSICS*, 24(27):16655–16670, JUL 13 2022.

[43] Asmus O Dohn, Elisa Biasin, Kristoffer Haldrup, Martin M Nielsen, Niels E Henriksen, and Klaus B Møller. On the calculation of x-ray scattering signals from pairwise radial distribution functions. *Journal of Physics B: Atomic, Molecular and Optical Physics*, 48(24):244010, November 2015.

[44] William H. Press, Saul A. Teukolsky, William T. Vetterling, and Brian P. Flannery. *Numerical Recipes 3rd Edition: The Art of Scientific Computing*. Cambridge University Press, 3 edition, 2007.

[45] Frank Neese, Frank Wennmohs, Ute Becker, and Christoph Riplinger. The ORCA quantum chemistry program package. *J. Chem. Phys.*, 152(22):224108, 2020.

[46] Elisa Biasin, Tim Brandt Van Driel, Kasper S. Kjær, Asmus O. Dohn, Morten Christensen, Tobias Harlang, Pavel Chabera, Yizhu Liu, Jens Uhlig, Mátyás Pápai, Zoltán Németh, Robert Hartsock, Winnie Liang, Jianxin Zhang, Roberto Alonso-Mori, Matthieu Chollet, James M. Glownia, Silke Nelson, Dimosthenis Sokaras, Tadesse A. Assefa, Alexander Britz, Andreas Galler, Wojciech Gawelda, Christian Bressler, Kelly J. Gaffney, Henrik T. Lemke, Klaus B. Møller, Martin M. Nielsen, Villy Sundström, György Vankó, Kenneth Wärnmark, Sophie E. Canton, and Kristoffer Haldrup. Femtosecond x-ray scattering study of ultrafast photoinduced structural dynamics in solvated [co (terpy)2] 2+. *Physical Review Letters*, 117, 6 2016.

[47] Renske M. van der Veen, Joshua J. Kas, Christopher J. Milne, Van-Thai Pham, Amal El Nahhas, Frederico A. Lima, Dimali A. Vithanage, John J. Rehr, Rafael Abela, and Majed Chergui. L-edge XANES analysis of photoexcited metal complexes in solution. *Phys. Chem. Chem. Phys.*, 12(21):5551, 2010.

[48] Kristoffer Haldrup, Wojciech Gawelda, Rafael Abela, Roberto Alonso-Mori, Uwe Bergmann, Amélie Bordage, Marco Cammarata, Sophie E. Canton, Asmus O. Dohn, Tim Brandt Van Driel, David M. Fritz, Andreas Galler, Pieter Glatzel, Tobias Harlang, Kasper S. Kjær, Henrik T. Lemke, Klaus B. Møller, Zoltán Németh, Mátyás Pápai, Norbert Sas, Jens Uhlig, Diling Zhu, György Vankó, Villy Sundström, Martin M. Nielsen, and Christian Bressler. Observing solvation dynamics with simultaneous femtosecond x-ray emission spectroscopy and x-ray scattering. *Journal of Physical Chemistry B*, 120:1158–1168, 2 2016.

[49] Roberto Monni, Gloria Capano, Gerald Auböck, Harry B. Gray, Antonín Vlcek, Ivano Tavernelli, and Majed Chergui. Vibrational coherence transfer in the ultrafast intersystem crossing of a diplatinum complex in solution. *Proceedings of the National Academy of Sciences of the United States of America*, 115:E6396–E6403, 7 2018.

[50] Mostafa Abedi, Gianluca Levi, Diana B. Zederkof, Niels E. Henriksen, Mátyás Pápai, and Klaus B. Møller. Excited-state solvation structure of transition metal complexes from molecular dynamics simulations and assessment of partial atomic charge methods. *Physical Chemistry Chemical Physics*, 21(7):4082–4095, 2019.

[51] Oliviero Andreussi, Ingrid G. Prandi, Marco Campetella, Giacomo Prampolini, and Benedetta Mennucci. Classical force fields tailored for QM applications: Is it really a feasible strategy? *Journal of Chemical Theory and Computation*, 13(10):4636–4648, September 2017.

[52] Junmei Wang, Romain M. Wolf, James W. Caldwell, Peter A. Kollman, and David A. Case. Development and testing of a general amber force field. *Journal of Computational Chemistry*, 25(9):1157–1174, 2004.

[53] Pengfei Li and Kenneth M. Merz. Mcpb.py: A python based metal center parameter builder. *Journal of Chemical Information and Modeling*, 56:599–604, 4 2016.

[54] M. J. Frisch, G. W. Trucks, H. B. Schlegel, G. E. Scuseria, M. A. Robb, J. R. Cheeseman, G. Scalmani, V. Barone, G. A. Petersson, H. Nakatsuji, X. Li, M. Caricato, A. V. Marenich, J. Bloino, B. G. Janesko, R. Gomperts, B. Mennucci, H. P. Hratchian, J. V. Ortiz, A. F. Izmaylov, J. L. Sonnenberg, D. Williams-Young, F. Ding, F. Lipparini, F. Egidi, J. Goings, B. Peng, A. Petrone, T. Henderson, D. Ranasinghe, V. G. Zakrzewski, J. Gao, N. Rega, G. Zheng, W. Liang, M. Hada, M. Ehara, K. Toyota, R. Fukuda, J. Hasegawa,

M. Ishida, T. Nakajima, Y. Honda, O. Kitao, H. Nakai, T. Vreven, K. Throssell, J. A. Montgomery, Jr., J. E. Peralta, F. Ogliaro, M. J. Bearpark, J. J. Heyd, E. N. Brothers, K. N. Kudin, V. N. Staroverov, T. A. Keith, R. Kobayashi, J. Normand, K. Raghavachari, A. P. Rendell, J. C. Burant, S. S. Iyengar, J. Tomasi, M. Cossi, J. M. Millam, M. Klene, C. Adamo, R. Cammi, J. W. Ochterski, R. L. Martin, K. Morokuma, O. Farkas, J. B. Foresman, and D. J. Fox. Gaussian˜16 Revision C.01, 2016. Gaussian Inc. Wallingford CT.

[55] D.A. Case, H.M. Aktulga, K. Belfon, I.Y. Ben-Shalom, J.T. Berryman, S.R. Brozell, D.S. Cerutti, III T.E. Cheatham, G.A. Cisneros, V.W.D. Cruzeiro, T.A. Darden, R.E. Duke, G. Giambasu, M.K. Gilson, H. Gohlke, A.W. Goetz, R. Harris, S. Izadi, S.A. Izmailov, K. Kasavajhala, M.C. Kaymak, E. King, A. Kovalenko, T. Kurtzman, T.S. Lee, S. LeGrand, P. Li, C. Lin, J. Liu, T. Luchko, R. Luo, M. Machado, V. Man, M. Manathunga, K.M. Merz, Y. Miao, O. Mikhailovskii, G. Monard, H. Nguyen, K.A. O'Hearn, A. Onufriev, F. Pan, S. Pantano, R. Qi, A. Rahnamoun, D.R. Roe, A. Roitberg, C. Sagui, S. Schott-Verdugo, A. Shajan, J. Shen, C.L. Simmerling, N.R. Skrynnikov, J. Smith, J. Swails, R.C. Walker, J Wang, J. Wang, H. Wei, R.M. Wolf, X. Wu, Y. Xiong, Y. Xue, D.M. York, S. Zhao, and P.A. Kollman. Ambertools 20, 2020.

[56] Hans W. Horn, William C. Swope, Jed W. Pitera, Jeffry D. Madura, Thomas J. Dick, Greg L. Hura, and Teresa Head-Gordon. Development of an improved four-site water model for biomolecular simulations: TIP4p-ew. *The Journal of Chemical Physics*, 120(20):9665–9678, May 2004.

[57] Peter Eastman, Jason Swails, John D. Chodera, Robert T. McGibbon, Yutong Zhao, Kyle A. Beauchamp, Lee-Ping Wang, Andrew C. Simmonett, Matthew P. Harrigan,

Chaya D. Stern, Rafal P. Wiewiora, Bernard R. Brooks, and Vijay S. Pande. OpenMM 7: Rapid development of high performance algorithms for molecular dynamics. *PLOS Computational Biology*, 13(7):e1005659, July 2017.

[58] Axel D. Becke. Density-functional thermochemistry. III. the role of exact exchange. *The Journal of Chemical Physics*, 98(7):5648–5652, April 1993.

[59] P. J. Stephens, F. J. Devlin, C. F. Chabalowski, and M. J. Frisch. Ab initio calculation of vibrational absorption and circular dichroism spectra using density functional force fields. *The Journal of Physical Chemistry*, 98(45):11623–11627, 1994.

[60] Benjamin P. Pritchard, Doaa Altarawy, Brett Didier, Tara D. Gibsom, and Theresa L. Windus. A new basis set exchange: An open, up-to-date resource for the molecular sciences community. *J. Chem. Inf. Model.*, 59:4814–4820, 2019.

[61] David Feller. The role of databases in support of computational chemistry calculations. *J. Comput. Chem.*, 17:1571–1586, 1996.

[62] Karen L. Schuchardt, Brett T. Didier, Todd Elsethagen, Lisong Sun, Vidhya Gurumoor-thi, Jared Chase, Jun Li, and Theresa L. Windus. Basis set exchange: A community database for computational sciences. *J. Chem. Inf. Model.*, 47:1045–1052, 2007.

[63] Maurizio Cossi, Nadia Rega, Giovanni Scalmani, and Vincenzo Barone. Energies, structures, and electronic properties of molecules in solution with the c-PCM solvation model. *Journal of Computational Chemistry*, 24(6):669–681, April 2003.

[64] Frank Neese. The ORCA program system. *WIREs Computational Molecular Science*, 2(1):73–78, June 2011.

[65] Pengfei Li, Lin Frank Song, and Kenneth M. Merz. Systematic parameterization of monovalent ions employing the nonbonded model. *Journal of Chemical Theory and Computation*, 11(4):1645–1657, March 2015.

[66] Benjamin G. Levine, John E. Stone, and Axel Kohlmeyer. Fast analysis of molecular dynamics trajectories with graphics processing units—radial distribution function histogramming. *Journal of Computational Physics*, 230(9):3556–3569, May 2011.

[67] P. Bösecke and O. Diat. Small-angle x-ray scattering at the ESRF high-brilliance beamline. *J Appl Crystallogr*, 30(5):867–871, 1997.

[68] Greg Hura, Jon M. Sorenson, Robert M. Glaeser, and Teresa Head-Gordon. A high-quality x-ray scattering experiment on liquid water at ambient conditions. *The Journal of Chemical Physics*, 113(20):9140–9148, 2000.

[69] Lawrie B. Skinner, Congcong Huang, Daniel Schlesinger, Lars G.M. Pettersson, Anders Nilsson, and Chris J. Benmore. Benchmark oxygen-oxygen pair-distribution function of ambient water from x-ray diffraction measurements with a wide q-range. *Journal of Chemical Physics*, 138, 2 2013.

[70] Z. I. Botev, J. F. Grotowski, and D. P. Kroese. Kernel density estimation via diffusion. *The Annals of Statistics*, 38(5):2916 – 2957, 2010.

[71] A Filipponi. Statistical errors in x-ray absorption fine-structure data analysis. *Journal of Physics: Condensed Matter*, 7(48):9343–9356, nov 1995.